

UNIVERSITY OF
NEWCASTLE



The Effects of Corrosions and Fatigue Induced Cracks on Strength Degradation in Ageing Ships

By

Duo Ok

Submitted for the degree of Doctor of Philosophy

**School of Marine Science and Technology
University of Newcastle upon Tyne
United Kingdom**

September 2006

Abstract

Over the past decades there have been many losses of the merchant vessels due to either accidents or exposure to large environmentally induced forces. The potential for the structural capability degrading effects of both corrosion and fatigue induced cracks are profoundly important and must be fully understood and reflected in vessel's inspection and maintenance programme. Corrosion has been studied and quantified by many researchers, however its effect on structural integrity is still subject to uncertainty, particularly with regards to localized corrosion. The present study is focused on assessing the effects of corrosion and fatigue induced cracks on the strength degradation in marine structures. Various existing general corrosion models for tanker structures have been studied and compared for time variant neutral axis, section modulus at deck and section modulus at keel based on various years of service. Simplified formulae to estimate time variant vertical/horizontal section modulus degradation and stress change at upper deck and keel are developed based on the double hull tanker. A fatigue assessment study which considers the new corrosion degradation model has also been carried out for the side shell stiffened plates of a North Sea operating shuttle tanker and of a world wide operating tanker.

In addition, over 265 non-linear finite element analyses of panels with various locations and sizes of pitting corrosion have been carried out. The results indicate that the length, breadth and depth of pit corrosion have weakening effects on the ultimate strength of the plates while plate slenderness has only marginal effect on strength reduction. Transverse location of pit corrosion is also an important factor determining the amount of strength reduction. When corrosion spreads transversely on both edges, it has the most deteriorating effect on strength. In this study, The multi-variable regression method and the Artificial Neural Network (ANN) method are applied to derive new formulae to predict ultimate strength of both uncorroded and locally corroded plate. It is found out that the proposed formulae can accurately predict the ultimate strength of both uncorroded and locally corroded plate under uni-axial compression.

It is certain that undetected defects and developing cracks may lead to catastrophic fracture failure. Fracture control is necessary to prevent the ship's structure safety not to fall down below a certain safety limit. It is very important to calculate how the structural strength is affected by cracks and to calculate the time in which a crack growth to the unacceptable limits. Fatigue analysis can estimate the elapsed time and locations where cracks could develop, whereas fracture mechanic approach can estimate crack growth times and response of structural strength as a function of crack size. In this study, the linear elastic fracture mechanics (LEFM) method based on stress intensity factor (K) and the elastic plastic fracture mechanics (EPFM) approach based on J-Integral and crack tip opening displacement (CTOD) have been investigated under different loads and crack sizes and material properties by using finite element analyses method. The finite element modelling and calculation for stress intensity factor (K) and J-computation are not easy tasks for most of engineers and researchers who do not have enough experiences. Accordingly some useful macro

programs are developed for automatic creation of geometry, mesh details, boundary condition and applying loads, for automatic calculation of stress intensity factor (K) and computation of J-integral value.

Proposed formulae based on multi-variable regression method and ANN might be useful to assess structural integrity during the initial design, on-site inspection and maintenance. In addition the developed macro programs for stress intensity factors (K) and J-computation could save time and efforts from time consuming finite element analyses.

Copyright © 2006 by Duo Ok

The Copyright of this Thesis rests with the author. The information derived from the Thesis should be acknowledged properly and no question from it should be published without prior consent of the author.

Acknowledgements

I must start to express my most sincere gratitude to my Supervisor, Dr. Yongchang Pu, for guidance, patience, wisdom, encouragement and support throughout the entire research at the University of Newcastle upon Tyne during the period of 2003 to 2006, without which the successful completion of this research would not have been possible. Secondly, I must thank Professor Atilla Incecik for his encouragement and financial supports in Overseas Research Students Award Scheme (ORSAS) and MARSTRUCT scholarship which was invaluable.

I would like to thank to Mr. John Garside for his sharing knowledge over 45 years engineering experiences and discussing this work, proof reading of my publications and this thesis. His knowledge, advice and encouragement are obviously invaluable to complete this research and thesis successfully.

I also would like to thank to the internal examiner Professor Robert S. Dow and the external examiner Professor Purnendu K. Das for their review, comments and suggestions on my PhD work.

My thanks also must go to Professor Hanwon Shin at Korea Maritime University for his encouragement and supports during my PhD period.

I would like to thank to Dr. Nigel Witts for his advice and support in fracture mechanics area.

I would also like to gratefully acknowledge the Government of the U.K. for Overseas Research Students Award Scheme (ORSAS) and would like to acknowledge the partial financial support by the project "Network of Excellence on Marine Structures (MARSTRUCT), which is financed by the European Union through "the 6th Framework Programme on Research, Technological Development and Demonstration", under Contract No. TNE3-CT-2003-506141 throughout my research.

Several people helped move my research forward. Thanks to my friends and colleagues in School of Marine Science and Technology.

Finally, I would like to express my sincere appreciation and gratitude to my wife Jung-sun Joo for her endless support and understanding and unlimited patience, and to my children Seul-chan and Ga-on for their smile and love, and to mother Duk-soon Yim for her pray and devotion for me and the late my father Hyung-seuk Ok, and to my parents-in-law Chel-won Joo and Cha-im Won for their support and understanding, and to my family members, This thesis is dedicated to them. I love you all.

Contents

Abstract	Ab-1
Acknowledgements	Ack-1
Contents	C-1
Nomenclature	Nom-1
List of Figures	LF-1
List of Tables	LT-1
Declaration	D-1

Chapter 1 : Introduction

1.1	General	1-1
1.2	Objectives and scope of thesis	1-5
1.3	Structure of the thesis	1-7
	References for Chapter 1	1-9

Chapter 2 : Corrosion and Corrosion Prevention in Ageing Ships

2.1	Introduction	2-1
2.2	Principles of corrosion	2-4
2.3	Physical forms of corrosion	2-4
	2.3.1 General corrosion	2-5
	2.3.2 Local corrosion	2-5
	2.3.3 Pitting corrosion	2-5
	2.3.4 Weld metal corrosion	2-6
	2.3.5 Microbial attack corrosion	2-6
	2.3.6 Galvanic corrosion	2-8
	2.3.7 Erosion corrosion	2-8
	2.2.8 Stress corrosion cracking	2-8
2.4	Causes of accelerated corrosion	2-9
2.5	Various corrosion protection methods and guidelines	2-9

2.5.1	Crude oil washing effects on cargo tanks	2-10
2.5.2	Temperature effects of cargo oil heating in cargo tanks	2-11
2.5.3	Inert gas system	2-17
2.5.3.1	Types of inert gas systems	2-17
2.5.3.2	Inert gas system for ballast tank and ship structures	2-21
2.5.3.3	Optimized anti-corrosion design by inert gas generator	2-24
2.6	Concluding remarks	2-27
	References for Chapter 2	2-29

Chapter 3 : Corrosion Rate Estimation Model

3.1	Introduction	3-1
3.2	Existing general corrosion rate estimation models for tanker	3-3
3.2.1	Melcher's model	3-3
3.2.2	Guedes Soares and Garbatov's model	3-5
3.2.3	Paik and Thayamballi's model	3-7
3.2.4	Qui and Cui's model	3-9
3.2.5	Average model for marine immersed general corrosion	3-9
3.3	Pitting corrosion estimation model	3-11
3.3.1	Hutchison and Bea's model	3-11
3.3.2	Daidola and Parente's model	3-11
3.3.3	Paik's model	3-12
3.3.4	TSCF's model	3-14
3.3.5	IACS recommendation	3-15
3.4	General corrosion estimation models for specific regions	3-15
3.5	Section modulus degradation model	3-19
3.5.1	Vertical section modulus degradation model	3-21
3.5.1.1	Section modulus at deck	3-21
3.5.1.2	Section modulus at keel	3-23
3.5.2	Horizontal section modulus degradation model at shipside shell	3-24
3.6	Estimated section modulus degradation model with I.G.G system	3-25
3.7	Stress changes based on section modulus degradation model	3-27
3.8	Concluding remarks	3-28
	References for Chapter 3	3-31

Chapter 4 : Fatigue Assessment of Corroded Ship Structures

4.1	Introduction	4-1
4.2	Fatigue assessment methods	4-3
4.2.1	S-N curve	4-4
4.2.2	Cumulative damage model	4-6
4.3	Stress and load analysis	4-8
4.3.1	DNV model	4-8
4.3.2	ABS model	4-13
4.4	Spectral based fatigue analysis	4-14
4.4.1	Statistical description of wave	4-14
4.4.2	Wave spectrum	4-16
4.4.2.1	ITTC spectrum	4-16
4.4.2.2	JONSWAP spectrum	4-16
4.4.3	Short-term statistical analysis	4-17
4.4.4	Long-term statistical analysis	4-18
4.5	Time variant fatigue assessment of AFRAMAX shuttle tanker	4-19
4.6	Fatigue assessment based on corrosion degradation model	4-25
4.7	Concluding remarks	4-29
	References for Chapter 4	4-31

Chapter 5 : The Effects of Localized Corrosion on Strength Degradation of Unstiffened Plates

5.1	Introduction	5-1
5.2	The parameters which influence the strength	5-3
5.2.1	Deflection due to welding	5-3
5.2.2	Welding induced residual stresses	5-5
5.3	Ultimate strength of plates under uni-axial compression	5-7
5.3.1	Faulkner's formula	5-8
5.3.2	Guedes Soares's method	5-9
5.3.3	Fujikubo's formula	5-10
5.3.4	NK's formula	5-10
5.3.5	DNV's formula	5-10
5.3.6	Paik's methods	5-11

5.4	Ultimate strength of plates with cracks	5-12
5.5	Computation of ultimate strength of plates with localized corrosion	5-15
5.5.1	Modelling details for finite element analysis	5-17
5.5.1.1	Material properties	5-17
5.5.1.2	Boundary conditions	5-17
5.5.1.3	Element type	5-18
5.5.1.4	Material plasticity model	5-19
5.5.1.5	Non-linear control	5-19
5.5.2	Evaluation of results from FE analysis	5-21
5.5.3	FE analysis of plate under uniaxial compression	5-22
5.5.3.1	Unstiffened plates without residual stresses	5-22
5.5.3.2	Unstiffened plates with residual stresses	5-24
5.5.4	Modelling strategy for rectangular plate with pitting corrosion	5-26
5.5.5	Finite element analysis of typical square plates with pitting corrosion	5-28
5.6	Proposed formulae for predicting ultimate strength reduction	5-34
5.7	Application of artificial neural networks to ultimate strength of plates with pitting corrosion	5-37
5.7.1	Biological neurons	5-38
5.7.2	Artificial neural network	5-39
5.7.2.1	ANN fundamentals	5-40
5.7.3	Types of neural networks	5-41
5.7.3.1	Single layer feedforward network	5-41
5.7.3.2	Multi-layer feedforward network	5-41
5.7.3.3	Recurrent network	5-42
5.7.4	Learning algorithm	5-43
5.7.4.1	Output layer weight update	5-44
5.7.4.2	Hidden layer weight update	5-44
5.7.5	Design of ANN model	5-45
5.7.5.1	Determine structure of ANN	5-46
5.7.5.2	Training & cross validation	5-48
5.7.5.3	Testing ANN models	5-48

5.7.6	ANN based formulae for ultimate strength of plate with pitting corrosion	5-51
5.7.6.1	ANN (Tanh) based output for single end pitting corrosion	5-52
5.7.6.2	ANN (Tanh) based output for both ends pitting corrosion	5-54
5.8	Concluding remarks	5-56
	References for Chapter 5	5-58

Chapter 6 : The Effects of Localized Corrosion on Strength Degradation of Stiffened Plate

6.1	Introduction	6-1
6.2	Ultimate strength of stiffened panels	6-2
6.2.1	LRS methods	6-2
6.2.2	Pu and Das's method	6-3
6.2.3	Paik & Thayamballi's methods	6-4
6.3	F.E. model for stiffened plate without pitting corrosion	6-6
6.3.1	Material properties	6-6
6.3.2	Dimension and details of F.E. models	6-7
6.3.3	Mesh size	6-8
6.3.4	Boundary condition	6-8
6.4	Results of finite element analysis for stiffened plate	6-9
6.5	Ultimate strength of stiffened plate with general overall corrosion	6-11
6.6	Ultimate strength of stiffened plate with pitting corrosion	6-13
6.6.1	Dimension and details of F.E. models	6-13
6.6.2	Mesh size	6-13
6.6.3	Location of pits and FEA results	6-14
6.7	Ultimate strength of stiffened plate with simultaneous pitting corrosion on both plate and stiffener web	6-17
6.8	Concluding remarks	6-19
	References for Chapter 6	6-21

Chapter 7 : Crack and Crack Propagation on Marine Structures

7.1	Introduction	7-1
7.2	Concept of fracture mechanics design	7-5

7.2.1	General	7-5
7.2.2	Modes of crack extension	7-6
7.3	Linear elastic fracture mechanics design	7-7
7.4	Stress intensity factor (K)	7-9
7.5	Elastic plastic fracture mechanics design	7-13
7.5.1	Crack tip opening displacement	7-13
7.5.2	Irwin's plastic zone correction	7-15
7.5.3	The Dugdale approach	7-16
7.5.4	J-Integral approach	7-17
7.6	Crack propagation threshold and crack closure	7-19
7.7	General concept of crack propagation	7-19
7.8	Stress cycle and amplitude	7-21
7.9	Parameters to calculate crack propagation	7-22
7.9.1	Threshold stress-intensity factor	7-23
7.9.2	Material constant	7-23
7.10	Prediction of crack propagation and fatigue life	7-24
7.11	Fracture control and inspection	7-25
7.12	Prediction of Stress intensity factors using finite element analysis	7-27
7.12.1	Finite element modelling details and methods for plate with crack	7-28
7.12.1.1	Size and material properties	7-28
7.12.1.2	Element type and K calculation	7-29
7.12.1.3	Computation of J-Integral theory	7-31
7.12.1.4	Computation of crack tip opening displacement	7-32
7.12.2	Modelling results by LEFM	7-33
7.12.3	Modelling results by EPFM	7-36
7.13	Concluding remarks	7-41
	References for Chapter 7	7-44

Chapter 8 : Conclusions and Recommendations for Further Works

8.1	Conclusions	8-1
8.2	Recommendations for further researches	8-7
	References for Chapter 8	8-10

Author's Publication	P-1
-----------------------------	-----

Appendixes

Appendix A	Geometric properties of shipside longitudinal stiffener in ballast tank	AP-A-1
Appendix B	FEM Macro	AP-B-1
Appendix C	Summary of FEA results for higher strength steel with pitting	AP-C-1
Appendix D	Summary of FEA results and Multi-Variable Regression output	AP-D-1
Appendix E	Summary of ANN inputs and outputs	AP-E-1
Appendix F	MATLAM programs for ultimate strength of plate with pitting corrosion	AP-F-1
Appendix G	Macro programs for stress intensity factor (K)	AP-G-1
Appendix H	Summary of stress intensity factors (K) for centre cracked plate	AP-H-1

Nomenclature

Chapter 2

- A_i = area of surface (m^2)
- C_{F-I} = cost of installation for boiler flue gas uptake based inert gas system
- C_{F-M} = cost of material/equipment for boiler flue gas uptake based inert gas system
- C_{F-MT} = cost of maintenance for boiler flue gas uptake based inert gas system
- C_{F-O} = cost of operation for boiler flue gas uptake based inert gas system
- C_{G-I} = cost of installation for inert gas generator system
- C_{G-M} = cost of material/equipment for inert gas generator system
- C_{G-MT} = cost of maintenance for inert gas generator system
- C_{G-O} = cost of operation for inert gas generator system
- C_{MT} = total maintenance cost for whole design life
- K_i = heat transfer coefficient ($kcal/m^2h\ ^\circ C$)
- S_M = required steam consumption to maintain oil temperature (kg/h)
- S_U = required steam consumption to raise-up oil temperature (kg/h)
- T_k = oil maintaining temperature ($^\circ C$)
- T_s = surrounding media temperature ($^\circ C$)
- T_a = temperature of cargo oil after heating up ($^\circ C$)
- T_b = temperature of cargo oil before heating ($^\circ C$)
- V = oil volume (m^3)
- c = specific heat of cargo oil ($kcal/kg\ ^\circ C$)
- i_1 = heating coil steam enthalpy at inlet ($kcal/kg$)
- i_2 = heating coil condensate enthalpy at outlet ($kcal/kg$)
- $\alpha = \frac{\sum K_i A_i}{\gamma V c}$
- γ = specific gravity of cargo oil (kg/m^3)

Chapter 3

- A_o = original cross sectional area of the intact member
- A_r = cross sectional area involved by pit corrosion at the smallest cross section
- A_{pi} = surface area of the i th pit.
- A_{plate} = plate area
- C_1, C_2 = coefficient
- D = depth of ship (m)

H_{NA0} = initial distance of the neutral axis above base line (=9.142 m)
 H_{NA} = distance of the neutral axis allowing for corrosion
 M_s = longitudinal bending moment in still water
 M_U = moment capacity of hull transverse section
 M_w = a wave-induced longitudinal bending moment in extreme sea conditions
 N = number of pits in the 300 x 300mm sample square
 R_{xr} = a factor of ultimate compressive strength reduction due to pitting corrosion
 $R_{\tau r}$ = a factor of ultimate shear strength reduction due to pitting corrosion
 T = age of vessel in years
 T_c = life of coating in years
 T_e = exposure time in years, after breakdown of coating = $T - T_c - T_t$
 T_0 = original plate thickness
 $T_{REDUCED}$ = equivalent reduced plate thickness with uniform pit distribution
 T_t = duration of transition in years (= pessimistically 0)
 V = volume loss of steel due to pitting
 V_{PIT} = average volume of pits
 Z_{DC} = reduced section modulus at deck
 Z_{DO} = initial section modulus at deck (=28.86 m³)
 Z_{KC} = reduced section modulus at keel
 Z_{KO} = initial section modulus at keel (=38.379 m³)
 a = plate length
 a_i = cross sectional area of the *i*th structural member
 a_i = area of pit 'i'
 b = plate breadth
 c_i = cylinder coefficient, defined as the actual pit volume divided by the corresponding cylinder of depth d_i , and top area a_i
 d_1 = corresponding depth of corrosion penetration at t_1
 d_2 = depth of corrosion penetration at annual mean temperature t_2
 d_i = depth of pit 'i'
 d_∞ = long term thickness of the corrosion wastage
 $d_w(t)$ = mean value of corrosion
 $d(t)$ = thickness of the corrosion wastage at time t
 $\dot{d}(t)$ = corrosion rate
 d_{ri} = diameter of *i*th pit
 h_i = distance of *i*th structural member from the base line
 k_i = local moment of inertia for each member
 n = number of pits
 n^{av} = the average number of responses per unit time
 r_s = the corrosion rate under anaerobic conditions

t_0	= the annual mean temperature below which there is ‘no’ corrosion throughout the year
t_1	= the corresponding temperature
t_2	= the annual mean temperature
t_{\min}	= minimum acceptable remaining thickness
t_0	= original thickness or rule thickness
t_r	= corrosion depth in mm
w	= pit width
α	= degree of pitting intensity (DOP)
η	= safety factor
μ_c	= mean value of $\ln T_c$ in years
$\mu_d(t)$	= mean value of corrosion
$\rho_{A_{PT}}$	= average area density of pits
σ_c	= standard deviation of $\ln T_c$
$\sigma_d(t)$	= standard deviation function of corrosion
σ_{DC}	= the changed stress level due to overall hull section corrosion at deck
σ_{DO}	= original stress level at deck
σ_{KC}	= the changed stress level due to overall hull section corrosion at keel
σ_{KO}	= original stress level at keel
σ_{xu}	= ultimate compressive strength for a member with pitting corrosion
σ_{xuo}	= ultimate compressive strength for an intact (uncorroded) member
τ_c	= coating life
τ_t	= transition time
τ_u	= ultimate shear strength for a pitted plate
τ_{uo}	= ultimate shear strength for an intact (uncorroded) plate
DOP	= the ratio percentage of the corroded surface area to the original plate surface area

Chapter 4

A_j	= the j -th component of wave amplitude
B	= the greatest moulded breadth of the ship
C_B	= block coefficient
C_w	= wave coefficient
D	= cumulative damage ratio
D_1	= cumulative fatigue damage for the loaded condition
D_2	= cumulative fatigue damage for the ballast condition
D_{corr}	= corrosion environment factor
D_{Depth}	= moulded depth of ship

H	= response amplitude operator
$H_{N.A}$	= neutral axis above keel
H_s	= significant wave height
I_C	= the hull section moment of inertia about the vertical neutral axis
I_N	= moment of inertia of hull cross-section in m^4 about transverse axis
K	= intercept of the design S-N curve with the log N axis
K_{R-Bal}	= roll radius of gyration in ballast condition
K_{R-Load}	= roll radius of gyration in loaded condition
K_{St}	= stress concentration factor for considered detail and loading
L	= ship's length, in m
M_H	= horizontal wave bending moment amplitude
$M_{w0,S}$	= vertical wave sagging bending moment amplitude
$M_{w0,h}$	= vertical wave hogging bending moment amplitude
N	= the number of responses in a given storm = $3600 n^{av} T$
N_i, N	= number of total cycles to failure
N_L	= total number of stress cycles over the design life $\left(= \frac{\alpha_0 T}{4 \log L} \right)$
N_R	= number of cycles corresponding to the probability level of $1/N_R$
P_{Load}	= fraction of time in load condition
P_{Load_Bal}	= fraction of time in ballast condition
P_{risk}	= the risk of probability
Q	= probability of exceedance of the stress range $\Delta\sigma$
Q_D^{Extr}	= design extreme value of response amplitude
R	= the mean square value of peak to peak random variable (= $2m_0$)
S	= stress range
S_q	= stress range at the intersection of the two segments of the S-N curve
S_{Ri}	= stress range, in MPa, for the basic case considered, at the probability level of $1/N_R$
T	= design life, in seconds
T_{Load}	= scantling draft (moulded)
T_{Bal}	= ballast draft
T_{ac}	= the draught in m of the considered load condition
T_{act}	= the actual draught
T_{Wave}	= wave period
U	= vessel's forward speed
U_w	= wind velocity
V	= vessel's design speed in knots
X	= fetch length

- Y_r = target value in years of “design fatigue life” set by the applicant in five (5) year increments
 Z_h = horizontal sectional modulus at ship side
 Z_s = stiffener sectional modulus at top of flange
 Z_v = vertical sectional modulus at deck line
 a = life intercept of the mean S-N curve
 a_s = scale parameter
 a_l = acceleration in longitudinal direction (m/s^2)
 a_t = acceleration in transverse direction (m/s^2)
 a_v = acceleration in vertical direction (m/s^2)
 b = shape parameter
 b_{br} = length of bracket side
 b_f = width of flange
 c_f = adjustment factor to reflect a mean wasted condition = 0.95
 c_w = coefficient for the weighted effects of the two paired loading patterns = 0.75
 f = vertical distance from the waterline to the top of the ship’s side at transverse section considered (m) = maximum $0.8 C_w (m)$
 f_{d1vi}, f_{d1vj} = wave induced component of the primary stresses produced by hull girder vertical bending moment, in N/cm^2 , for load case i and j of the selected pairs of combined load cases, respectively
 f_{d1hi}, f_{d1hj} = wave induced component of the primary stresses produced by hull girder horizontal bending moment, in N/cm^2 , for load case i and j of the selected pairs of combined load cases, respectively
 f_{d2i}, f_{d2j} = wave induced component of the secondary bending stresses produced by the bending of cross-stiffened panels between transverse bulkheads, in N/cm^2 , for load case i and j of the selected pairs of combined load cases, respectively
 f_{d2i}^*, f_{d2j}^* = wave induced component of the additional secondary stresses produced by the local bending of the longitudinal stiffener between supporting structures (e.g., transverse bulkheads and web frames), in N/cm^2 , for load case i and j of the selected pairs of combined load cases, respectively
 f_{d3i}, f_{d3j} = wave induced component of the tertiary stresses produced by the local bending of plate elements between the longitudinal stiffeners in, N/cm^2 , for load case i and j of the selected pairs of combined load cases, respectively
 f_{RG} = global dynamic stress range, in $N/cm^2 = \left| (f_{d1vi} - f_{d1vj}) + (f_{d1hi} - f_{d1hj}) \right|$
 f_{RL} = local dynamic stress range, in $N/cm^2 = c_w \left| (f_{d2i} + f_{d2i}^* + f_{d3i}) - (f_{d2j} + f_{d2j}^* + f_{d3j}) \right|$

f_a	= factor to transform the load effect to probability level 10^{-4} , when the accelerations are specified at the 10^{-8} probability level = $0.5^{1/h}$
f_e	= the operation route reduction factor
f_m	= the mean stress reduction factor
f_r	= factor to transform the load from 10^{-8} to 10^{-4} probability level = $0.5^{1/\xi_0}$
g	= acceleration due to gravity = 9.81 m/s^2
h	= height of stiffener
h_s	= vertical distance from point considered to surface inside the tank (m)
k	= wave number = ω^2 / g for deep water
k_j	= wave number = $2\pi / \lambda$
k_{wm}	= moment distribution factor = 1.0 between 0.40L and 0.65L from A.P
l_s	= web frame spacing
m	= the negative inverse slope of S-N curve
Δm	= slope range at the upper to lower segment of the S-N curve
n^{av}	= the average number of responses per unit
n_i	= number of applied cycles in stress block i
p	= number of stress blocks
p_1	= pressure due to vertical acceleration
p_2	= pressure due to transverse acceleration
p_3	= pressure due to longitudinal acceleration
p_{ij}	= weighting factor for the joint probabilities of significant wave height and zero crossing period given in the wave scatter diagrams for a specific trade routes
p_k	= weighting factor for wave spectrum
p_l	= weighting factor for heading to waves in a given sea state
p_m	= weighting factor for ship speed in a given sea state and heading
q	= Weibull scale parameter = $\frac{\Delta\sigma_0}{(\ln N_R)^{1/\xi}}$
r_p	= reduction of pressure amplitude in the surface zone
s_f	= stiffener spacing
s	= standard deviation of log N
t_b	= thickness of bracket
t_f	= thickness of flange
t_{fr}	= thickness of transverse frame plating
t_p	= thickness of ship sideshell plate
t_w	= thickness of web
v_i	= $\left(\frac{S_q}{S_{Ri}}\right)^\xi \ln N_R$

- x = the longitudinal distance from the origin to the load point of the considered structural detail
 x_s = longitudinal distance from centre of free surface of liquid in tank to pressure point considered (m)
 x^{Extr} = the most probable extreme value
 y = the transverse distance from the origin to the load point of the considered structural detail
 y_s = transverse distance from centre of free surface of liquid in tank to the pressure point considered (m)
 z = the location height above the keel
 z_{01} = distance from neutral axis to top flange
 z_{wl} = distance in m measured from actual water line
 Γ = Gamma function
 α_0 = factor taking into account the time needed for loading / unloading operations, repairs, etc. (=0.85)
 α_1 = part of the ship's life in loaded condition (= 0.5 for tanker)
 α_2 = part of the ship's life in ballast (=0.5 for tanker)
 β = angle of wave attack
 ε = bandwidth parameter = $\sqrt{1 - \frac{m_2^2}{m_0 m_4}}$
 γ = peakedness parameter
 $\gamma(a, x)$ = incomplete gamma function, Legendre form
 η = target cumulative fatigue damage for design
 λ = wave length
 θ_j = phase angle
 μ_i = coefficient taking into account the change in slope of the $S-N$ curve

$$= 1 - \frac{\left[\gamma\left(1 + \frac{m}{\xi}, v_i\right) - v^{-\Delta m / \xi} \gamma\left(1 + \frac{m + \Delta m}{\xi}, v_i\right) \right]}{\Gamma\left(1 + \frac{m}{\xi}\right)}$$

 ξ = Weibull shape parameter $\left(= 1.1 - 0.35 \frac{L - 100}{300} \right)$
 $\xi(t)$ = wave elevation
 ρ = density of water = 1.025 (ton / m³)
 ρ_{vh} = average correlation between vertical and horizontal wave induced bending stress (= 0.10)
 σ = the standard deviation (r.m.s. value) of the water surface = $\sqrt{m_0} = H_s / 4$
 σ_e = the external sea pressure induced stress amplitude
 σ_i = the internal inertia pressure induced stress amplitude

$\Delta\sigma_0$ = reference stress range value at the local detail exceeded once out of N_R cycles

$\Delta\sigma_v$ = wave induced vertical hull girder bending stress ranges

$\Delta\sigma_{hg}$ = horizontal hull girder bending stress ranges = $2\sigma_h$

τ = shape parameter (τ_a for $\omega \leq \omega_0$ and τ_b for $\omega > \omega_0$)

ϕ = rolling angle, single amplitude (rad)

ω = wave frequency

ω_e = the encountered wave frequency = $|\omega - kU \cos \beta|$

ω_j = the j -th component of wave frequency = $2\pi/T$

ω_0 = the peak wave frequency

ω_z = zero crossing frequency = $\sqrt{\frac{m_2}{m_0}}$

$\log K$ = the life time intercept of the S-N curve (= $\log a - 2s$)

GM_{Load} = metacentric height in loaded condition

GM_{Bal} = metacentric height in ballast condition

$PS[Y_r]$ = permissible stress ranges for the target design fatigue life of Y_r

Chapter 5

A_{om} = amplitude of the response buckling mode initial deflection for axial compressive loading

A_m = amplitude of the added deflection function

B = plate width

B_{0ij} = welding-induced initial deflection amplitude

E_t = material tangent modulus

I = internal activation

L = member length between supports

M_p = the fully plastic moment

N = number of exemplars in the data set

P = number of output processing elements

R^2 = the multiple coefficient of determination

W = weight value

$W1$ = first layer weight matrix

$W2$ = second layer weight matrix

Y = value of matrix based equation

a = plate length

a_p, a_s = crack length for the plating and the stiffener

$a(t)$ = crack length at given time t

b	= plate breadth
b_e	= effective width
$b1$	= first layer bias vector
$b2$	= second layer bias vector
d_{ij}	= desired output for exemplar i at processing element j
f	= neuron output
i, j	= half wave numbers in the x and y directions
r	= correlation coefficient
t	= target output value
w_0	= initial deflection function = $\delta_0 \sin \frac{\pi x}{L}$
w_{0pl}	= value of maximum initial deflection
x_1	= plate slenderness parameter (β)
x_2	= the ratio of pit breadth to plate width
x_3	= the ratio of pit length to plate length
x_4	= the ratio of pit depth to plate thickness
y_i	= arbitrary data point
y_{ij}	= network output for exemplars i at processing element j
\bar{y}	= the mean of the data points
\hat{y}_i	= the predicted value of Y_i for the model
Γ_F	= strength of an unwelded plate
$\Delta\Gamma_F$	= reduction of strength due to the weld induced residual stress
α	= momentum constant.
δ_0	= initial deflection amplitude
ε	= error term
η	= function of welding
λ_e	= equivalent reduced slenderness
ρ_x	= correction factor
σ_C	= the ultimate strength of plate with localized corrosion
σ_E	= elastic buckling resistance
σ_0	= ultimate strength of plate without welding induced residual stress
σ_R	= ultimate strength of plate with welding induced residual stress
σ_{av}	= average stress
σ_e	= maximum membrane stress at plate/web junction
σ_r	= residual stress
σ_{rx}	= tensile residual stresses in the x direction
σ_{ry}	= tensile residual stresses in the y direction
σ_{Ult}	= ultimate strength or compressive strength of plate

- σ_x = non-uniform membrane stress
 σ_Y = the yield strength of the material
 σ_{Yp}, σ_{Ys} = yield strength of the plating and the stiffener, respectively.
 $\phi_{cux}(t)$ = nominal ultimate strength of plate under tensile load at given time t with centre crack
 $\phi_{eux}(t)$ = nominal ultimate strength of plate under tensile load at given time t with edge crack
 $\phi_{u-x}(t) = \sigma_u(t) / \sigma_Y$ is the nominal ultimate strength of the cracked plate under compressive load
 SM_p = plastic section modulus
MSE = mean squared error

 $[K^T]$ = the tangent stiffness matrix
 $\{\Delta u\}$ = the incremental displacement
 $\{F_a\}$ = the applied load vector
 $\{F_i^{nr}\}$ = the internal load vector calculated from element stress
i = subscript representing the current equilibrium iteration
 λ = load factor
 $\{\Delta u_i^I\}$ = displacement due to a unit load factor = $\{K_i^T\}^{-1} \{F_a\}$
 $\{\Delta u_i^{II}\}$ = displacement increment from the Newton-Raphson method = $\{K_i^T\}^{-1} \{R_i\}$
 $\{R_i\}$ = residual vector
 β = scaling factor
 Δu_n = the sum of all the displacement increments Δu_i of this iteration

Chapter 6

- A* = total sectional area
 A_e = effective sectional area
I = total second moment of area of section
 I_e = effective second moment of area of section
K = the secant stiffness of the plate panel
 M_q = The moment resulting from lateral pressure at mid span
 P_c = maximum compressive force
 P_e = Euler load ($= \pi^2 EI_e / L^2$)
 b_{fx}, t_{fx} = the breadth and thickness of flange, respectively
 h_{wx}, t_{wx} = the height and thickness of web, respectively
 n_{sx} = the number of x stiffeners
 t_{eq} = equivalent plate thickness

- y_p = the distance between its centroid and the middle plane of the plate
 y_s = the distance between the centroid of the cross-section and the extreme stiffener fibre
 Δ = the eccentric of load at mid-span
 δ_0 = initial plate deflection
 η = welding residual stress factor
 σ_{yeq} = equivalent yield stress = $\left(= \frac{Bt\sigma_{yp} + n_{sx}A_{sx}\sigma_{ys}}{Bt + n_{sx}A_{sx}} \right)$
 σ_{yp}, σ_{ys} = the material yield stress for plate and stiffener, respectively
 $\sigma_{xav}, \sigma_{yav}$ = average axial stress applied in the x or y direction
 $\sigma_{x\max}$ = maximum axial membrane stress applied in the x direction
 $\sigma_{x\min}$ = minimum axial membrane stress applied in the x direction
 σ_{xu}, σ_{yu} = ultimate longitudinal or transverse axial strength components
 $\sigma_{y\max}$ = maximum axial membrane stress applied in the y direction
 $\sigma_{y\min}$ = minimum axial membrane stress applied in the y direction

Chapter 7

- C, m = material constants
 F_C = a crack shape factor
 F_S = a crack surface factor
 F_W = a finite width factor
 F_G = a non-uniform stress factor
 G = strain energy release rate ($= \pi a\sigma^2 / E$)
 J = J integral value
 K = stress intensity factor
 Kc = fracture toughness under plane stress
 K_{IC} = fracture toughness under plane strain
 K_I, K_{II}, K_{III} = stress intensity factors for *Mode I, II and III*.
 ΔK = stress-intensity factor
 ΔK_{th} = threshold values of stress intensity factor
 M_k = free-surface correction factor
 N = number of cycles
 N_O = reference number of the stress cycles
 Q = flaw-shape parameter
 R = K ratio defined by ($= K_{min} / K_{max}$).
 T_i = the time to crack initiation

- T_p = the subsequent time to crack propagation
 W = the strain energy density = $\int \sigma_{ij} d\epsilon_{ij}$
 $Y(a)$ = geometric factor
 a = a half the crack length
 a_{cr} = critical crack size
 a_d = depth of surface crack
 $a_{d,0}$ = limit size of detection under which a crack will not be detected.
 ds = arc length along the path Γ
 $f_{ij}^I, f_{ij}^{II}, f_{ij}^{III}$ = stress functions of θ for *Mode I, II and III*.
 $g_i^I, g_i^{II}, g_i^{III}$ = displacement functions of θ for *Mode I, II and III*.
 n = unit outward normal vector to path Γ
 r, θ = the stress components and the coordinates
 r_y = the size of the plastic zone
 t = thickness of plate
 t = time
 t_x = traction vector along x-axis ($= \sigma_x n_x + \tau_{xy} n_y$)
 t_y = traction vector along y-axis ($= \sigma_y n_y + \tau_{xy} n_x$)
 u, v, w = the displacements in the x, y and z directions, respectively
 Γ = arbitrary path surrounding crack tip
 $\Gamma[]$ = the incomplete *Gamma function*
 $\alpha_{\Delta\sigma}$ = the shape parameter
 $\gamma_{\Delta\sigma}$ = the scale parameter of the Weibull distribution of the stress range
 μ = the shear modulus of elasticity = $\frac{E}{2(1+\nu)}$
 ν = Poisson's ratio
 ν_0 = the mean zero up-crossing rate
 σ = applied load (tensile stress)
 $\Delta\sigma$ = stress range

List of Figures

Fig. 2.1	The loss of the ship	2-1
Fig. 2.2	Corroded bulkhead in an oil tanker	2-3
Fig. 2.3	Typical types of corrosion damage	2-4
Fig. 2.4	Pitting intensity diagrams	2-6
Fig. 2.5	Corrosion of steel surface caused by <i>SRB</i>	2-7
Fig. 2.6	Single nozzle type fixed tank cleaning machine	2-10
Fig. 2.7	Increase of corrosion rate with increase in temperature	2-12
Fig. 2.8	Corrosion rates correspond to various temperature	2-12
Fig. 2.9	Performance curve of cargo oil pump	2-14
Fig. 2.10	Total steam consumption (kg/hour)	2-16
Fig. 2.11	Total required heating coil length (m)	2-16
Fig. 2.12	Typical schematic of a boiler flue gas uptake inert gas plant	2-18
Fig. 2.13	Typical schematic of an inert gas generator based system for tanker	2-19
Fig. 2.14	Typical arrangement for N_2 generator	2-20
Fig. 2.15	New anticorrosion method by using nitrogen gas	2-22
Fig. 2.16	Percent oxygen in the nitrogen treated ballast tanks during 18 months of operations of the coal/ore vessel	2-23
Fig. 2.17	Corrosion levels on steel plates placed in ballast tanks during the 18 months shipboard study	2-24
Fig. 2.18	Inert gas supply to double hull space during laden voyage	2-25
Fig. 3.1	Five years of corrosion as a function of annual mean water temperature	3-4
Fig. 3.2	Corrosion data points for field exposed specimens	3-4
Fig. 3.3	Multiphase corrosion time model	3-5

Fig. 3.4	Thickness of corrosion wastage as a function of time	3-6
Fig. 3.5	A schematic of the corrosion process for steel structure	3-7
Fig. 3.6	The 95% and above band for corrosion wastage model	3-8
Fig. 3.7	Corrosion rate formulations and data for sea water ballast tanks	3-9
Fig. 3.8	Time dependant average general corrosion degradation model	3-10
Fig. 3.9	A representative sample square of the typical inspected pitted Panel	3-12
Fig. 3.10	The name of individual double hull tanker structural components	3-16
Fig. 3.11	Corrosion rate in each structural component	3-18
Fig. 3.12	Time variant section modulus changes at deck	3-22
Fig. 3.13	Time variant section modulus changes at keel	3-23
Fig. 3.14	Time variant section modulus changes at ship side shell	3-24
Fig. 3.15	Time variant section modulus changes at deck	3-26
Fig. 3.16	Time variant section modulus changes at keel	3-27
Fig. 3.17	Time variant stress changes pattern based on various models	3-27
Fig. 4.1	New HSE basic design S-N curves	4-5
Fig. 4.2	IIW S-N curve	4-5
Fig. 4.3	Typical fatigue crack locations in tanker structures	4-20
Fig. 4.4	Typical midship section	4-21
Fig. 4.5	Details of longitudinal stiffener on ship sideshell	4-21
Fig. 4.6	Cumulative fatigue damage ratio of North Sea operating shuttle Tanker (DSD)	4-24
Fig. 4.7	Cumulative fatigue damage ratio of North Sea operating shuttle Tanker (DSP)	4-24
Fig. 4.8	Cumulative fatigue damage ratio of World Wide operating crude oil tanker	4-25
Fig. 4.9	Fatigue Life in Years for various cases	4-25
Fig. 4.10	Comparison of fatigue life	4-28

Fig. 5.1	Classification of welding deformation	5-3
Fig. 5.2	A typical idealized welding-induced residual stress distribution inside a rectangular steel plate element Comparison of fatigue life	5-6
Fig. 5.3	Effective width and stress distribution in plate under uniaxial compression	5-7
Fig.5.4	Membrane stress distribution under longitudinal loads	5-11
Fig.5.5	Various types of typical cracks in plates	5-13
Fig.5.6	A stiffened plate with a crack	5-14
Fig.5.7	Typical procedure of finite element analysis (FEA)	5-15
Fig.5.8	Typical procedure of macro programs for FEA	5-16
Fig.5.9	Meshes and constraint details	5-17
Fig.5.10	Shell181 geometry	5-18
Fig.5.11	Arc-length approach with full Newton-Rapson Method	5-19
Fig.5.12	The <i>Von Mises</i> stress distribution at the ultimate limit state	5-22
Fig.5.13	The average stress-strain curves under uni-axial compressive load	5-23
Fig.5.14	The effect of plate slenderness parameter on strength reduction under uni-axial compressive loads without consideration of residual stresses	5-24
Fig.5.15	The welding induced residual stress distribution	5-25
Fig.5.16	The stress distribution (σ_x) of an unstiffened plate with residual stresses at the ultimate limit state	5-26
Fig.5.17	The effect of plate slenderness parameter on strength reduction under uni-axial compressive loads considering residual stresses	5-26
Fig.5.18	Typical localized corrosion in ballast tank	5-27
Fig.5.19	Patterns of pitting corrosion	5-27
Fig.5.20	Shell layers with nodes at midplane	5-28
Fig.5.21	Finite element analysis modelling detail for pitting corrosion	5-29

Fig.5.22	Mesh details of the plate with typical pitting corrosion at central region	5-30
Fig.5.23	A comparison of the average stress-strain curves	5-30
Fig.5.24	Effects of pitting corrosion length	5-31
Fig.5.25	A comparison of the FEA results with those of Eq.3.26	5-32
Fig.5.26	Effects of pit length, breadth and depth on the ultimate strength	5-33
Fig.5.27	Correlation of FEM results and Multi-Variable Regression based outputs for single edge pitting corrosion	5-36
Fig.5.28	Correlation of FEM results and Multi-Variable Regression based outputs for both edges pitting corrosion	5-36
Fig.5.29	The basic features of a biological neuron and chemical signal at synapse	5-38
Fig.5.30	Outline of the basic model of artificial neuron	5-40
Fig.5.31	Multi-layer feed-forward neural network	5-42
Fig.5.32	Multi-layer back-propagation neural network	5-43
Fig.5.33	Procedures to establish ANN models	5-46
Fig.5.34	Average MSE versus epoch for trained data based on various numbers of hidden layer processing elements	5-47
Fig.5.35	Mean square error versus epoch for pitting corrosion on single edge location by using a logistic activation function	5-49
Fig.5.36	Mean square error versus epoch for pitting corrosion on single edge location by using a hyperbolic tangent (Tanh) activation function	5-50
Fig.5.37	Comparison of desired output and ANN output for pitting on single edge location as obtained using logistic (sigmoid) activation function	5-51
Fig.5.38	Comparison of desired output and ANN output for pitting corrosion on single edge location as obtained using hyperbolic tangent (Tanh) activation function	5-51
Fig.5.39	Correlation of FEM results and ANN (Tanh) based outputs	5-52

	for single edge pitting corrosion	
Fig.5.40	Correlation of FEM results and ANN (Tanh) based outputs for both edges pitting corrosion	5-54
Fig.6.1	Bacteria influenced corrosion in ballast tank	6-2
Fig.6.2	Typical three(3) bay panel model with L-type stiffeners	6-7
Fig.6.3	Typical of one stiffened plate component with mesh details	6-8
Fig.6.4	Various buckling modes and <i>Von-Mises</i> stress distribution	6-10
Fig.6.5	A comparison of the average stress-strain curves for stiffened Plates	6-12
Fig.6.6	Mesh details for stiffened plate with pitting corrosion model	6-13
Fig.6.7	The alternative location of pits on stiffened plate	6-14
Fig.6.8	Mesh detail of stiffened plate with pitted area	6-15
Fig.6.9	Various finite element results for stiffened plate with pitting Corrosion	6-15
Fig.6.10	Average stress-strain curves for stiffened plates under various pitting location	6-16
Fig.6.11	Detail location of pitting corrosion on plate and web	6-17
Fig.6.12	Average stress-strain curves for stiffened plates with combined pitting corrosion on both stiffener web and plate	6-18
Fig.6.13	<i>Von Mises</i> stress distribution	6-19
Fig.7.1	Cracked deck in tanker ‘Castor’	7-2
Fig.7.2	Typical crack growth for stiffened and unstiffened panel	7-3
Fig.7.3	Typical load path lines with crack	7-6
Fig.7.4	The three basic modes of crack surface extensions	7-7
Fig.7.5	Local coordinate system and components ahead of a crack	7-8
Fig.7.6	The effect of plate thickness on fracture toughness	7-10
Fig.7.7	Effects of temperature on fracture toughness	7-11

Fig.7.8	Residual strength curves for two steel	7-11
Fig.7.9	Typical crack geometries under tensile load	7-12
Fig.7.10	Crack opening displacement and CTOD	7-14
Fig.7.11	Irwin plastic zone correction for plane stress condition	7-15
Fig.7.12	The strip yield model for a through crack	7-16
Fig.7.13	Arbitrary contour around a crack tip	7-18
Fig.7.14	A schematic of the fatigue crack growth rate curve	7-20
Fig.7.15	Constant-amplitude loading	7-21
Fig.7.16	Random stress loading	7-22
Fig.7.17	Time dependant crack growth curve	7-26
Fig.7.18	Element type for 2D and 3D models	7-29
Fig.7.19	Nodes and stress details around 2D crack tip	7-30
Fig.7.20	Mesh details and stress details around 3D crack tip	7-30
Fig.7.21	Typical procedure of macro program for K calculation	7-31
Fig.7.22	J integral path based on 4 nodes	7-31
Fig.7.23	Typical procedure of macro program for J computation	7-32
Fig.7.24	K values against different loads ($2a/W=0.2$)	7-34
Fig.7.25	The von Mises stress distribution near the crack tip	7-35
Fig.7.26	J-integral values with different crack size and loads ($\sigma_y = 235 \text{ N/mm}^2$)	7-38
Fig.7.27	J-integral values with different crack size and loads ($\sigma_y = 315 \text{ N/mm}^2$)	7-39
Fig.7.28	J-integral values with different crack size and loads ($\sigma_y = 355 \text{ N/mm}^2$)	7-39
Fig.7.29	CTOD values with different crack size and loads ($\sigma_y = 235 \text{ N/mm}^2$)	7-40
Fig.7.30	CTOD values with different crack size and loads ($\sigma_y = 315 \text{ N/mm}^2$)	7-40

Fig.7.31	CTOD values with different crack size and loads ($\sigma_y = 355 \text{ N/mm}^2$)	7-41
-----------------	--	------

List of Tables

Table 2-1	Large scale oil spill accident by tanker	2-2
Table 2-2	Galvanic series in sea water	2-8
Table 2-3	Typical design criteria for cargo oil tank heating	2-11
Table 2-4	Illustrative design criteria of cargo oil tank heating temperature	2-15
Table 2-5	Steam consumption and heating coil length	2-15
Table 2-6	Typical boiler flue gas and corresponding inert gas composition	2-18
Table 2-7	The composition of gas contents	2-20
Table 3-1	Guidance on minimum remaining plate thickness in pits	3-14
Table 3-2	Experience with bottom pitting (maximum depth)	3-14
Table 3-3	Experience with bottom pitting (average depth)	3-14
Table 3-4	Comparison of existing general corrosion models	3-17
Table 3-5	Corrosion of structural members in Post-MARPOL and Pre-MARPOL ships	3-19
Table 3-6	Summary of plate thickness diminution	3-19
Table 3-7	Comparisons of the section modulus at deck	3-21
Table 3-8	Equations of section modulus degradation models at deck	3-22
Table 3-9	Comparison of the section modulus at keel	3-23
Table 3-10	Equations of section modulus degradation models at keel	3-23
Table 3-11	Comparison of the horizontal section modulus at ship side shell	3-24
Table 3-12	Equations of section modulus degradation models at ship side shell	3-25
Table 3-13	Assumed different corrosion rates under high quality inert gas system	3-26

Table 4-1	Fatigue lives of ship sideshell longitudinal stiffeners	4-23
Table 4-2	Time variant design values based on <i>WANG's et al.</i> model	4-26
Table 4-3	Time variant design values based on average (<i>PW</i>) model	4-27
Table 4-4	The accumulated fatigue life based on <i>DNV</i> model assuming 5 years effective corrosion protection period	4-27
Table 4-5	The accumulated fatigue life based on <i>WANG's et al.</i> model	4-28
Table 4-6	The accumulated fatigue life based on average (<i>PW</i>) model	4-28
Table 5-1	Boundary conditions for unstiffened plate	5-18
Table 5-2	Comparison of existing methods versus ANSYS FEA results	5-21
Table 5-3	Ultimate strength of unstiffened plates without residual stresses	5-22
Table 5-4	Ultimate strength of unstiffened plates with residual stresses	5-25
Table 5-5	Effects of transverse location of pitting corrosion on ultimate strength	5-30
Table 5-6	Effects of pitting corrosion length on ultimate strength	5-31
Table 5-7	Effects of plate slenderness parameter on ultimate strength	5-33
Table 5-8	Comparison of ultimate strength of plates based on different pit length	5-34
Table 5-9	Comparison of ANN outputs and desired output for single end pitting corrosion	5-49
Table 5-10	Comparison of the performance of sigmoid and hyperbolic tangent activation function	5-50
Table 5-11	Comparison of ANN outputs and desired output for single edge pitting corrosion	5-55
Table 6-1	Boundary conditions for stiffened plate component	6-9
Table 6-2	Comparison of ultimate strength of stiffened plates	6-10
Table 6-3	Time variant corrosion degradation rates	6-12

Table 6-4	The results of finite element analysis for stiffened plate with pitting corrosion	6-16
Table 6-5	The results of finite element analysis for stiffened plate with combined pitting corrosion on web and plate	6-18
Table 7-1	Comparison of K calculation for plate with centre crack	7-33
Table 7-2	Comparison of K calculation for plate with single edge crack	7-35
Table 7-3	J-integral and crack tip opening displacement (CTOD) values	7-37

Declaration

Except where reference is made to the works of others,
this Thesis is believed to be original

Chapter 1

Introduction

1.1 General

Over the past decades there have been many losses of the merchant vessels due to either accidents such as grounding, collision, explosion and sinking or exposure to large environmentally induced forces. Such casualties represent considerable financial loss of both the vessel and its cargo and also, possibly more importantly, to loss of life and of damage to the marine environment. The structural condition of a vessel, when it is entering a period of higher than normal risk, particularly in heavy weather, is clearly very important. The potential for the structure capability degrading effects of both corrosion and fatigue induced cracks are profoundly important. Improperly maintained ageing ship structures could finally lead to disastrous casualties in rough seas and heavy weather. The complex effects of both corrosion and fatigue cracking manifest themselves at both local and global structure performance levels. It is probable that subsequent structural degradation, for example buckling failure, will develop in a progressive form and spread with both further corrosion and cracking in time dependent manner, subject to continuing environmental and operational demands.

Ships operate over a life of 20 years and more in an extremely demanding and aggressive environment. The objective of classification society rules is to establish requirements to reduce the risks of structural failure in order to improve the safety of life, environment and property and to provide adequate durability of the hull structure during the design life [1]. The classification societies attempt to allow for the average effects of overall corrosion by incorporating a component related corrosion margin in their minimum scantling requirements and actively maintain an observation of the levels of corrosion throughout the life of the vessel, replacing steel where the corrosion is found to have exceeded the renewal criteria. Recently IACS [1] published “Common Structural Rules for Double Hull Tanker” for the double hull oil tankers of 150m length and upward classed with the Society and contracted for construction on or after 1 April 2006, based on a nominal design life of 25 years and defines the criteria for the local/overall hull girder wastage allowable thickness diminution of the ships’ hull structures.

One of the most important considerations in controlling corrosion is to minimise cost of both first and through life. There are many materials that are used for ship’s structure, outfitting and piping etc. Often corrosion problems arise due to the materials or coatings that are originally selected, are being suitable to its surrounding operational conditions. Generally the designer selects material considering costs and the proper level of corrosion resistance for the intended service requirements. This does not necessarily mean the use of a material which is the most resistant to the operational environment but that is based on cost-benefit considerations.

Among the factors which could accelerate corrosion, the effects of tank cleaning washing, temperature changing in cargo oil tanks and ballast tanks due to crude oil tank heating, and inert gas have not been investigated well and should be studied more in order to define what are the different corrosion effects and behaviours at different tank heating temperatures, outlet pressure of tank cleaning machines and inert gas effect to reduce corrosion rates of structural members. In this study, the possible effects of tank cleaning washing, temperature changing in cargo oil tanks and ballast tanks due to crude oil tank heating, and inert gas on the corrosion rates have been investigated.

Many methods can be employed in order to protect marine structures from corrosion, such as paints, other forms of coatings and cathodic protection, etc. However there are no perfect long lived corrosion protection systems or methods which are used in the marine environment and it is inevitable for vessels to experience some corrosion to some greater or lesser extent. Of course, corrosion control is very important so as not to lead to leakage of cargo oil, pollution, structural failure or expensive steel renewals of structures during a ship's lifetime. Careful attention and consideration to the potential corrosion should be provided during a ship's design stage, fabrication, subsequent in-service maintenance and inspection. In this study, the useful clean inert gas system will be introduced as one of effective corrosion control methods in marine structures.

The most important role of a corrosion model is to enable an operator to be able to estimate when at some time in the future ship's structures will require some maintenance by replacing corroded plates, renewing coating and anodes etc. If plate thickness or coating condition is below the level required by classification rules then the replacement or upgrade must be carried out. An economical decision for the next maintenance and replacement period can be planned and facilitated when the rate of future corrosion degradation can be estimated properly. Uniform corrosion is the most common form of corrosion found in the many grades of mild steel that are mainly used for marine structures. Normally uniform corrosion is calculated from weight loss or sampled thickness measurement from test plate coupons. Many researches have been carried out and considerable efforts have been made to develop time-based predictive mathematical models. Many data have been obtained from large numbers of thickness measurements made on many vessels that have been in-service for some years. Such thickness measurements are typically made using ultrasonic techniques and several point measurements may be made over the surface of a plate in order to arrive at an assumed average value. Comparisons would then be made between as-built scantling thicknesses. Obviously thickness measurements must be made by approved technicians and using approved methods in order to ensure that there is a good degree of confidence in the obtained data. Such measurements would also be made for the web and flange element thicknesses of hull structures. Much difference was often found in each sets of corrosion data, even though corrosion data was sampled in same type of vessels [2-8]. This means that any generalised models will have a fairly high level of uncertainty. Most of recent corrosion models are based on actually measured data. Normally we can consider that the most reliable corrosion models are those that are based on actual measurement in hundreds of vessels, this means that a large degree of scattered data is unavoidable in sampled values. The

reason is that there are many factors which accelerate individual levels of corrosion such as type of cargoes, frequency of cleaning and sediment removal, type of coating, humidity, temperature, inert gas quality, ballast frequency and presence of sacrificial anodes, etc. It is apparent that slow and progressive corrosion and fatigue are weakening the structure of ageing ships. Thus reliability and safety assessment considering corrosion degradation is very important in ageing ships. This is clearly very significant especially when the level of corrosion exceeds the corrosion margins that are mandated by the relevant classification society.

The designer may need to consider if each panel is fully effective for contribution to hull girder strength and undertake full hull girder cross-section area property calculations. Hull girder section modulus represents a measure of the ship's longitudinal strength and the section modulus should be always greater than the rule requirement. The value of hull girder section modulus will be decreased with time due to corrosion progress in ageing ship structures, accordingly stress levels of local members will also be increased over the design life. However it is time consuming and routine work to calculate the section modulus repeatedly, so it is advantageous to develop a model to estimate time dependent section modulus degradation which considers annual corrosion degradation in ageing ships for initial corrosion margins in design stage and for decision of future maintenance period.

As previously mentioned, ship and offshore structures frequently suffer from the fatigue damage mainly caused by cyclic wave induced loads and both external and internal hydrodynamic pressures. Fatigue thus becomes the cause of various cracks in welded and unwelded ship structural components. Eventually fatigue damage affects not only costly replacement or repair of ship structures but also potential damage to cargo and environment, serviceability and safety of ageing ships. According to recent reports, many cracks have been found in relatively new crude oil tankers which were constructed of high strength materials. This means that the use of higher strength steel (HTS) leads to higher stresses in ship's structure due to reduced thickness but there is little difference between mild steel and higher strength steel with regard to corrosion and fatigue properties and hence more careful study is necessary during design stage. The purpose of the fatigue assessment process is to estimate the fatigue life of individual details of the hull structure and to ensure that the structure is well designed for its intended service, operational and environmental loads over its required lifetime. The estimated length of fatigue life can be a basis for initial scantling design and the selection of appropriate design details and shall be used for future developing a maintenance and inspection programme throughout the life of a ship. Actually verification of an adequate fatigue life is now becoming part of the classification society approval process. Generally, fatigue failure can be prevented by controlling the local cyclic stress amplitude. The designer should ensure that the hull section modulus is large enough considering corrosion degradation of the ageing ship and its ability to continue to withstand wave induced hull girder bending stresses and seek to reduce stress concentrations at local areas by increasing local scantling or suitably modifying the local detail geometry.

Pitting corrosion is a highly localized form of damage, caused by severe chemical and biological factors rather than physical contact, and its effects on structural integrity

have not been adequately evaluated. However during the life of a vessel detailed structural survey may detect and quantify the existence of pits. The problem for the owner would then be to ascertain that the pits could not, at sometime in the foreseeable future, be the source for initiating local structural failure which could result in leakage or larger scale failure, etc. This requires knowledge of the strength of pitted plate members, general stress distributions in the local hull structure associated with various ship loading conditions and environmental factors, etc. The latter is now covered, to a certain degree, by the structural response data that is typically assessed during the classification process. Frequently concentrated patterns of localized corrosion can be found in ageing ship structures. Excessively deep pits and a large grouping of pitting corrosion may lead to a loss of local strength, thus degrading hull integrity and may result in serious pollution by eventual perforation of the plate. In the case of uniform corrosion, the buckling or ultimate strength of stiffened and unstiffened plates can be easily estimated by reducing the plate thicknesses from their original values. Several empirical formulae are available to obtain the ultimate strength of plates under general corrosion [9-14]. However the calculation of strength degradation due to localized defects, such as pitting corrosion, are more difficult and complicated than general area-wide corrosion and there have been relatively few research activities and guidelines have been published until now [15-21]. Accordingly it is necessary to develop and propose accurate methodologies to predict the ultimate strength of unstiffened plates with localized corrosion or local defects in order to develop proper inspections, maintenance periods and rational repair decisions.

Fracture is initiated by structural flaws or cracks subject to high local stress levels. The size of flaw and crack is typically increased slowly with repeated service loads. Fracture control is intended to prevent fracture due to previously undetected defects and cracks at the loads anticipated to be experienced during operational service. To determine the permissible crack size and the safe operational life, it is necessary to know the effect of crack on the structural strength and to calculate the operational time in which a crack grows to a permissible size. Based on damage tolerance analysis, periodic inspections should be scheduled so that cracks can be repaired or components can be replaced when critical cracks are detected. Fracture control is a combination of measurements and analyses. It may include damage tolerance analysis, material selection, design improvement, determination of maintenance and inspection schedule etc. The mathematical tool for damage tolerance analysis is called fracture mechanics. It provides the concepts and equations to determine how cracks grow and how cracks affect the local strength of a structure. The prediction of fatigue crack propagation rates and propagation time of a cracked structure requires the input values of relevant crack propagation data, geometry factors and stress history etc. Actually most ship and offshore structural components are subjected to a variety of load histories either constant amplitude loading or variable amplitude loading. The load sequence on a ship is different in each loading and ballast voyage. The fluctuating loads on a ship occur from hogging and sagging response across various waves. In wave conditions, the buoyancy forces of ship are unevenly distributed, causing bending of ship, and shows the compression in the deck and tension in the keel during the sagging condition and vice-versa in a hogging condition. The loads on offshore structure depend on winds, currents and waves.

Obviously, local and overall structural strength tends to decrease with time through the effects of corrosion and cracks. The total useful life of a structural component, which is subject to variable loading, is determined by the time, which is required to initiate a crack and then to propagate the crack from sub-critical size to a critical size. There are many factors that influence crack propagation and permissible residual strength, such as the magnitude and fluctuation of the applied stresses, fracture toughness of the material at a particular service temperature, plate thickness, crack size and shape, discontinuity at possible locations of fracture initiation, the magnitude of stress intensity factor, stress-corrosion susceptibility, the fatigue characteristics, etc. It is very important to evaluate the critical crack size at design loads and to estimate the time or cycles to reach the critical crack size from existing crack size. Once critical crack size and amplitude of load are known, the inspection intervals on the basis of analysis results can be determined based on the most economic interval and reliability, probability of detection and safety of structure, etc. Obviously undetected defects and developing cracks may lead to catastrophic fracture failure. Fracture control is necessary to prevent the ship's structure safety not to fall down to below a certain safety limit. It is very important to calculate how the structural strength is affected by cracks and to calculate the time in which a crack grows to the unacceptable limits. Fracture mechanic approach can be used to estimate crack growth times and response of structural strength as a function of crack size. In this study some methodologies which are based on linear elastic fracture mechanic method (LEFM) and elastic plastic fracture mechanic methods (EPFM) are investigated to predict crack propagation on damaged marine structures.

It is very important that the structural designers and operators should have a better understanding of the causes of corrosion and fatigue cracks, the proper corrosion prevention methods, the corrosion rate estimate models, the fatigue and fatigue induced cracks and the location and extent of structural damage formed during operation of the structure and how it can affect the structural capacity. One reason is to facilitate repair decisions for a vessel's inspection and maintenance programme. Another possible broad reason may be to support a structural life extension decision later in life.

In this study, the corrosion and corrosion prevention methods, corrosion rate estimation models, fatigue assessment of ship structures, the effects of localized corrosion on strength degradation of ship structures, and crack and crack propagation on ship structures will be fully discussed.

1.2 Objectives and scope of thesis

The objective of the present study will be focused on assessing the effects of general surface and localized pitting corrosion, and fatigue cracks on the structural integrity of ship hull structures. The contributions of this study could be summarised as follows:

- Causes of corrosion acceleration in marine structures have been reviewed and investigated.

- Existing corrosion models in marine structures have been reviewed.
- The effects of high pressure tank cleaning washing, temperature changing due to cargo oil tank heating and clean inert gas system on corrosion have been investigated.
- Various existing general corrosion models and variations due to corrosion in neutral axis of a hull girder, section modulus at deck and keel based on various years of service for tanker structures have been investigated and compared.
- Optimised corrosion control methods by using clean inert gas system have been proposed.
- General historical background and development of fatigue damage assessment methodologies and the guidances of the Classification Societies (IACS, DNV, ABS) have been reviewed
- Fatigue assessment studies which considered existing corrosion degradation models are carried out for the side shell stiffened plates of a North Sea operating shuttle tanker and of a world wide operating tanker.
- General reviews of existing formulae and recommendations to estimate elastic buckling strength and ultimate strength of unstiffened and stiffened plates have been investigated. Some recent research activities and guidelines for the strength degradation due to localized corrosion have also been reviewed.
- The effects of pitting corrosion width, depth, length and its transverse location on ultimate strength have been systematically studied. A total of 256 nonlinear finite element analyses have been carried out which is the full combination of two cases of transverse pitting locations, four cases of plate slenderness, four cases of pitting breadths, four cases of pitting lengths and two cases of pitting depths.
- A limited study into the ultimate strength of stiffened plates with pitting corrosion has been investigated by using nonlinear finite element analyses. The effects of different buckling modes based on half wave number, pitting corrosion width, transverse location and combined pitting corrosion on the plate and web on ultimate strength have been studied.
- Linear elastic fracture mechanic method (LEFM) and elastic plastic fracture mechanic methods (EPFM) are used to predict crack propagation on damaged marine structures. Stress intensity factors (K) and J and crack tip opening displacement (CTOD) values have been investigated based on plate with a central crack under various loads, crack sizes and material properties.

Consequently some useful mathematical formulae and useful programs have been developed as follows:

To estimate corrosion degradation rate, section modulus and stress change for crude oil tankers:

- Average model for marine immersed general corrosion
- Time variant vertical section modulus degradation model for crude oil tankers
- Time variant horizontal section modulus degradation model for crude oil tankers
- Time variant stress change models at upper deck and at the keel

To predict ultimate strength of locally corroded plates by using multi-variable regression method and artificial neural network method:

- Multi-variable regression model based formulae to predict the ultimate strength reduction of unstiffened plates with localized corrosion
- Artificial neural networks based formulae to predict the ultimate strength of unstiffened plates with localized corrosion

To calculate a stress intensity factor (K) by linear elastic fracture mechanic method (LEFM) and the J-integral value by elastic plastic fracture mechanic method (EPFM):

- FEA macro program for automatic creation of geometry, mesh details, symmetric boundary condition and applying loads
- FEA macro program for automatic calculation of stress intensity factor (K)
- FEA macro program for automatic calculation of J-integral computation

Proposed formulae and programs might be useful to assess structural integrity during the initial design, on-site inspection and maintenance in order to save time and efforts from time consuming finite element analyses (FEA) and actual experimental test.

1.3 Structure of the thesis

The thesis is divided into following eight chapters. A list of reference will be presented at the end of each chapter.

Chapter One introduces the general overviews of research area, background and objectives of this research.

Chapter Two reviews the various corrosion theories and factors which cause the accelerated corrosion in ship structures. Especially the effect of pitting corrosion, inert gas effect on ballast tanks, temperature effect due to tank heating by heating coil and the effect on corrosion degradation of tank cleaning operation by high pressure tank cleaning machine are originally issued.

Chapter Three discusses the existing probabilistic corrosion rate estimation models. In addition, time variant vertical/horizontal section modulus degradation and stress change at upper deck and keel are investigated for double hull tanker based on various existing general corrosion models for tanker structures. The effects of clean inert gas on the corrosion degradation rates and time variant section modulus changes have also been discussed.

Chapter Four examines various fatigue assessment methods and models. Actual lifetime prediction based on fatigue crack propagation for side shell stiffened plates allowing for yearly progressive corrosion wastage has been performed in North Atlantic Sea operating shuttle tanker and world wide operating crude oil tanker.

Chapter Five investigates the ultimate strength and post buckling behaviour of unstiffened plates. New empirical formulae to predict the ultimate strength of unstiffened plates with localized corrosion under uniaxial compression are proposed

and developed by using the multi-variable regression method and the artificial neural network method

Chapter Six discusses the ultimate strength of stiffened plates with pitting corrosion by using nonlinear finite element analyses. The effects of different buckling modes based on half wave number, pitting corrosion width, transverse location and combined pitting corrosion on plate and web on ultimate strength have been studied.

Chapter Seven reviews theoretical and historical development of the fracture mechanic methodologies to assess and predict crack propagation on damaged marine structures. Finite element modelling analyses for the linear elastic fracture mechanics (LEFM) approach using stress intensity factor (K) and the elastic plastic fracture mechanics (EPFM) approach using the J-integral and the crack tip opening displacement (CTOD) values have been performed based on plates with a centre crack under various loads, crack sizes and material properties. Some useful FEA macro programs have been developed for automatic calculation of the stress intensity factor (K) and the J-integral computation.

Chapter Eight concludes this research and recommends the future works.

References (Chapter 1)

1. IACS, *Common Structural Rules for Double Hull Oil Tankers*. 2006.
2. Wang, G., J. Spencer, and H. Sun, *Assessment of corrosion risks to ageing ships using an experience database*. 22nd International Conference on Offshore Mechanics and Arctic Engineering, 2003.
3. TSCF, *Condition Evaluation and Maintenance of Tanker Structures*. Tanker Structure Cooperative Forum, May, 1992.
4. TSCF, *Guidance Manual for Tanker Structures*. Tanker Structure Co-Operative Forum, 1997.
5. Bergesen, D.Y.A., *Experience with Double Hull Tankers: an Owner's ViewPoint*. Tank Structure Co-Operative Forum, October 2000, Tokyo.
6. TSCF, *Corrosion Protection of Cargo Tanks*. Tanker Structure Co-Operative Forum, 2000. **TSCF Working Group #2, Chevron, Shipping Company**.
7. Paik, J.K., et al., *A Time-Dependent Corrosion Wastage Model for the Structures of Single and Double-Hull Tankers and FSOs and FPSOs*. Marine Technology, 2003. **Vol.40, No.3**: p. 201-217.
8. Wang, G., J. Spencer, and T. Elsayed, *Estimation of Corrosion Rates of Structural Members in Oil Tankers*. International Conference on Offshore Mechanics and Arctic Engineering, CANCUN, MEXICO, 2003c. **22nd**.
9. Faulkner, D., *A review of effective plating for use in the analysis of stiffened plating in bending and compression*. Journal of Ship Research, 1975. **19(1)**: p. 1-17.
10. Soares, C.G., *Design equation for the compressive strength of unstiffened plate elements with initial imperfections*. Journal of Constructional Steel Research, 9, 1988: p. 287-310.
11. Fujikubo, M., T. Yao, and M.R. Khedmati, *Estimation of Ultimate Strength of Ship Bottom Plating under Combined Transverse Thrust and Lateral Pressure*. Journal of the Society Naval Architects of Japan, Vol.186., 1999.
12. Class NK, *Guidelines for Tanker Structures*. 2001.
13. DNV, *Buckling strength analysis*. Det Norske Veritas, Classification Notes No.30.1, 1995.
14. Paik, J.K. and A.K. Thayamballi, *Ultimate Limit State Design of Steel Plated Design*. 2003: John Wiley & Sons Ltd.
15. Chapkis, D.T., *Simulation of pitting corrosion of hull plating under static loading*. Trudy TSNIIMF, 1967. **No.82**: p. 34-50.
16. Flaks, V.Y., *Correlation of pitting corrosion of aluminium plates and reduction of load-bearing capacity under tension*. Fiziko-Khimicheskaya Mekhanika Materialov, 1978. **14(1)**: p. 89-93.
17. TSCF, *Experimental and theoretical investigation of the strength of corroded hull elements*. 1984, Tanker Structure Co-operative Forum, Project 300, Report No. 84-3438.
18. Daidola, J.C., et al., *Residual strength assessment of pitted plate panels*. Ship Structure Committee, SSC-394, 1997.
19. Paik, J.K., et al., *Time-dependent risk assessment of ageing ships accounting for general/pit corrosion, fatigue cracking and local dent damage*. SNAME,

- Annual Meeting in San Francisco (World Maritime Technology Conference), 2003.
20. Paik, J.K., J.M. Lee, and M.J. Ko, *Ultimate compressive strength of plate elements with pit corrosion wastage*. Journal of Engineering for the Maritime Environment, 2003. **217(M4)**: p. 185-200.
 21. Paik, J.K., J.M. Lee, and M.J. Ko, *Ultimate shear strength of plate elements with pit corrosion wastage*. Thin-Walled Structures, 2004. **vol.42**: p. 1161-1176.

Chapter 2

Corrosion and Corrosion Prevention in Ageing Ships

2.1 Introduction

Sea water is an aggressive corrosive environment because it is a good electrolyte and contains corrosive salts. The marine environment is a sea water environment and this means that corrosion in marine structures, which are generally fabricated with various grades of mild steel and low alloy steel, is very severe not only under immersed conditions in ballast tanks but also under general exposure to atmospheric conditions.

Corrosion eventually reduces the thickness of a ship's structure and which results in a corresponding reduction in both local and overall strength of the structure. Improperly maintained ageing ship structures could finally lead to disastrous casualties in rough seas and heavy weather. Fig. 2.1 pictures "ERICA" incident in 1999 and Table 2-1 shows some large scale oil spill accidents that have occurred since 1967.



Fig. 2.1. The loss of the ship "ERICA" [1]

There are many methods that can be employed in order to protect marine structures from corrosion, such as paints and other forms of coatings and cathodic protection, etc. However there are no perfect long lived corrosion protection systems or methods which are used in a marine environment and it is inevitable for vessels to experience some corrosion to some greater or lesser extent.

Of course, corrosion control is very important so as not to lead to leakage of cargo oil, pollution, local structural failure or expensive steel renewals of structure during a ship's lifetime. Careful attention and consideration to the potential for corrosion should be provided during a ship's design stage, fabrication, subsequent in-service maintenance and inspection.

Table 2-1
Large scale oil spill accident by tanker [2]

Year	Ship Name	Flag State	Volume (10^3 kL)	Causes
1967	Torrey Canyon	Liberia	119	Grounding
1972	Sea Star	Korea	120	Collision & fire
1976	Urquiola	Spain	100	Grounding
1977	Hawaiian Patriot	Liberia	95	Foundered at 12 yrs
1978	Amoco Cadiz	Liberia	223	Grounding
1979	Atlantic Empress	Greece	287	Collision & fire
1979	Independenta	Rumania	95	Collision & fire
1983	Castillo de Bellver	Spain	252	Fire
1988	Odyssey	Greece	132	Foundered at 17 yrs
1989	Exxon Valdez	USA	37	Grounding
1991	ABT Summer	Liberia	260	Fire
1993	Braer	Liberia	85	Grounding
1996	Sea Empress	Liberia	72	Grounding
1997	Nakhodka	Russia	6.2	Foundered at 26 yrs
1999	Erika	Malta	> 10	Foundered at 25 yrs
2001	Baltic Carrier	Marshall Is.	2.5	Collision & fire
2002	Prestige	Bahama	5	Foundered at 26 yrs

One of the most important considerations in controlling corrosion is to minimise cost both first and through life. Many materials are used for ship's structure, outfitting and piping etc. Often corrosion problems arise due to the materials or coatings that are originally selected not being suitable to its surrounding operational conditions. Generally the designer selects the materials considering costs and the proper level of corrosion resistance for the intended service requirements and based on cost-benefit considerations.

Chandler [3] introduced six elements which should be considered during material selection as follows;

- Material
- Fabrication and transport to site
- Installation
- Quality control and testing
- Monitoring
- Maintenance and repair

All merchant vessels are built under *Classification Society Design Rules* and each *Classification Society* requires some extent of corrosion allowance that is based on a certain amount or degree of corrosion wastage. If the corrosion degradation rate is greater than anticipated in rule requirement and continuously unchecked and

undetected due to difficulties in access during routine inspection, this will potentially be the cause of a disastrous structural failure of ageing ships.

Many investigations and research studies [4-7] show that the mean value of the annual corrosion degradation in typical ballast tanks varies from 0.027mm to 0.21mm per annual and in cargo oil tanks varies from 0.004mm to 0.21mm per annual. Furthermore the maximum annual corrosion degradation can reach up to 0.807mm [6]. Fig. 2.2 pictures a typical example of a heavily corroded bulkhead.



Fig. 2.2. Corroded bulkhead in an oil tanker [6]

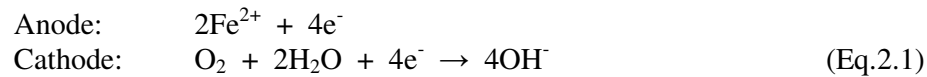
Similarly some excessive pitting corrosion of up to 2.0mm per year was found in the uncoated bottom plating in cargo tanks and this was considered to be due to a complex microbial induced corrosion process [8].

It is very important to know the basis and background of corrosion theory and of the various factors which accelerate corrosion in marine structures, not only for designers but also for operators and surveyors. This is the way to understand corrosion behaviour and from there to give good and reasonable guidance and to fundamental concepts in maintenance and inspection activities during the lifetime of a ship.

2.2 Principles of corrosion

Corrosion is basically a chemical reaction process and which results in surface wastages on metals and can be defined “The destruction of a metal by chemical or electrochemical reaction with its environment” [9].

Carbon steel is a very reactive material in a marine environment and the most common material in marine structures. If the corrosion of carbon steel is considered this can be explained by noting that steel is not homogeneous and at the initiation of corrosion localized anodic and cathodic sites are formed on the surface of the alloy. In the presence of an electrolyte, small corrosion cells are set up on the surface and at the anodic areas iron goes into solution as ferrous ions. Various reactions can occur at the cathode. The cathodic reaction under ordinary atmosphere or immersed conditions results in the production of hydroxyl ions and the two chemical reactions can be written as follows:



The two products Fe^{2+} and OH^{-} react together to form ferrous hydroxide which eventually is oxidised further to form what is generally referred to as rust:



If rust is formed at the steel surface, it will eventually stifle the process so, despite the availability of moisture and oxygen, the subsequent corrosion rate may be reduced. In practice, on carbon steels, the anodic process at one place is stifled and corrosion begins at new sites thus gradually spreading to the overall area.

The details of corrosion theory and basic principles can be found in many textbooks [3, 9-13].

2.3 Physical forms of corrosion

The rusting of ordinary carbon steels is generally called corrosion. This form of attack attributes to the major part of the maintenance and repair costs for its control. The costs may arise from a huge amount of steel renewals, or from the repair/renewal of coating. Typically the physical forms of corrosion in the cargo and ballast tanks of oil tankers can generally be classified as follows [8];

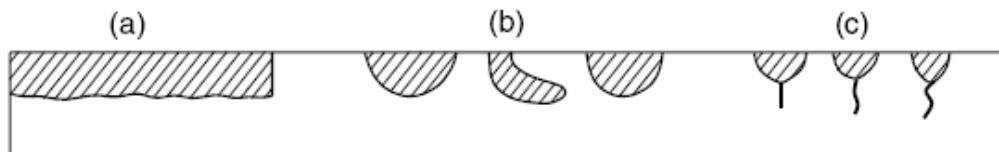


Fig. 2.3. Typical types of corrosion damage [14]: (a) general area corrosion (b) localized corrosion (c) fatigue cracks arising from localized corrosion

2.3.1 General corrosion

This form of corrosion is the most common and is typified by steel rusting in air, and generally appears in cargo and ballast tanks. General corrosion means that it proceeds at more or less at the same average rate over the whole surface of the metal that is exposed to the corrosive environment, but actually the loss of metal is not completely uniform and there is typically a slight difference over the surface. It is usually a less dangerous than ‘pitting’ because this kind of corrosion can be easily detected and controlled. The loss of thickness leads to the loss of local strength and integrity of structure. Although this kind of corrosion usually takes place slowly it should be inspected at regular intervals in order to ensure that it does not exceed any critical values in the structure which is assumed in the rules.

However it is difficult to investigate and judge the thickness loss until there is excessive metal loss on the structure. One of popular method to measure corroded thickness is through thickness measurements by using ultra-sonic equipment. Typically several measurements would be made over the surface of a discrete plate element. The corrosion degradation rate varies according to operating sea area, ship’s type and corrosion location. The various corrosion degradation rates at each location within a hull are described in Chapter 3.

2.3.2 Local corrosion

These are the types of corrosion in which there is intense attack at localized sites on the surface of a component whilst the rest of the surface is corroding at a much lower rate due to an inherent property of the component material (such as the formation of a protective oxide film) or some environmental effect. This type of corrosion is usually complex and unpredictable, so it is not usually possible to predict exactly where the attack will occur or even its extent. However normally localized corrosion in ship structure can be found at structural intersections where water collects or flows. Localized corrosion can also occur on the vertical structural members at the water flow path or on the flush sides of bulkheads in way of flexing of plating, at welds, area of stress concentration, etc. and there are many other possibilities.

2.3.3 Pitting corrosion

Pitting is a special form of very highly localized corrosion which results in pits in the metal surface. Once it has been initiated its continuation is determined by reactions within the pit itself, which at the point of attack is anodic, and with the outer surface being cathodic. Sometimes pits penetrate to a certain depth and then the downward attack stops or may continue horizontally within the metal.

This phenomenon is more commonly found in the bottom plating, particularly the aft bays of tank bottoms, welds of seams, stiffeners, horizontal surfaces or side shell plating where the way of water flow and place of water and sediment accumulation. Generally natural coatings such as a residual waxy oil coating from previous cargoes and rust tend to protect bare steel plates and painting break down area in cargo tanks from heavy corrosion and possibly delay corrosion degradation. But localized breakdown of these natural tank coatings, particularly in way of turbulent fluid flow

areas such as cargo bellmouths or tank cleaning medium impingement areas, can quickly cause very severe pitting where sea water collects and electrolytic and/or microbial induced corrosion can occur. If pitting corrosion is left unchecked, it can cause severe problems such as loss of structural strength and integrity and resulting in hull penetration, leakage and eventually leading to a serious pollution incident.

Hutchinson et al. [15], *Laycock and Scarf* [16], *Daidora et al.* [17] and *Paik et al.* [18] developed various mathematical models of pitting corrosion. A detailed review of each model is described in Chapter 3.

If pitting intensity area is higher than 15% in area, *the International Association of Classification Societies* [19] requires thickness measurements to check the severity of the pitting corrosion.

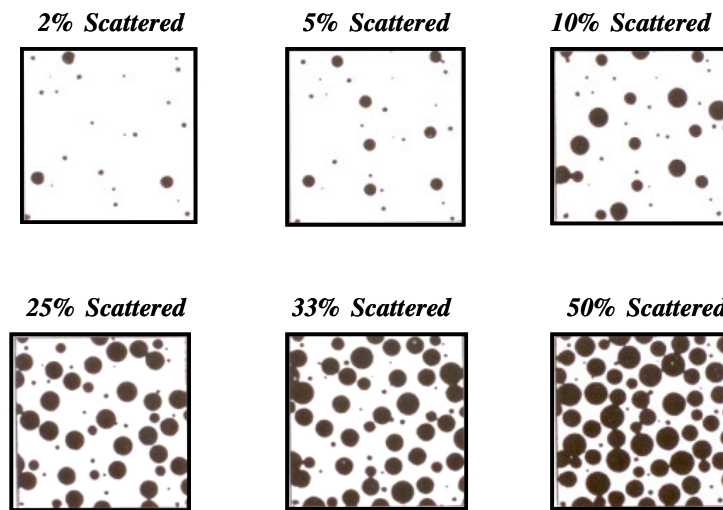


Fig. 2.4. Pitting intensity diagrams [20]

2.3.4 Weld metal corrosion

Various welds cause micro-level discontinuities in the surface of the alloy steel and these can lead to local metallurgical variations and to potential sites for coating breakdown. Weld metal corrosion is the result of a galvanic action between the base metal and the added weld material which can result in pitting or grooving corrosion. To overcome and minimise these kinds of corrosion problems it is necessary to make sure that the weld metal has a higher corrosion potential than the surrounding base metal. This means that a more noble electrode should be used for the weld metal than for the base metal. Eventually the weld metal will be the cathode and the base metal will be the anode in a galvanic circuit.

2.3.5 Microbial attack corrosion

Microbiologically Influenced Corrosion (MIC) is caused by one celled living organisms including bacteria, fungi and algae. The most common types of these

bacteria are called *Sulphate-reducing bacteria* (SRB) and *Acid Producing Bacteria* (APB).

Sulphate-reducing bacteria (SRB) are able to cause corrosion of steel under anaerobic conditions. Oxygen is an essential element in the corrosion of steel, but in the presence of these bacteria, the corrosion process differs from that experienced in normal oxygenated sea water. SRB obtains their needs of sulphurs by a complex chemical reaction.

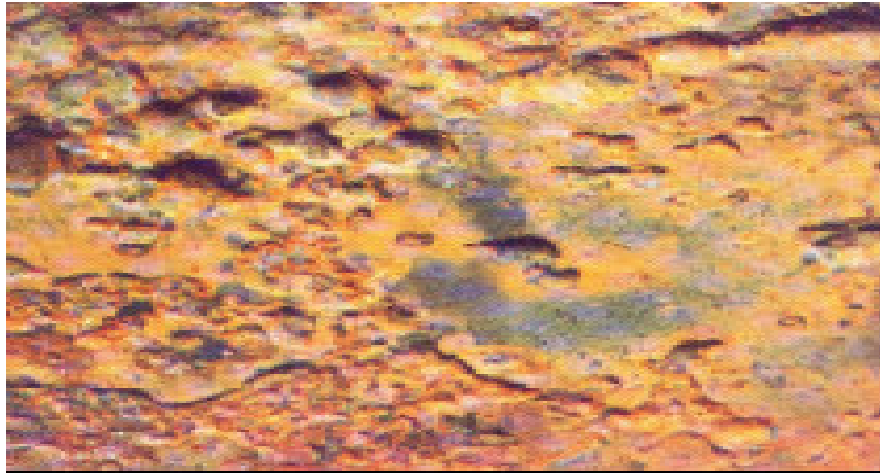


Fig. 2.5. Corrosion of steel surface caused by *SRB* [21]

The environmental conditions preferred by *SRB* include zero dissolved oxygen, water and the presence of soluble organic nutrients. Aerobic micro-organisms use up oxygen and the oxygen deficient zone formed anodic in relation to adjacent relatively oxygen rich zones thus causing anodic corrosion pits to develop.

During their life-cycle, the anaerobic *SRB* extracts the oxygen from sulphates found in the cargo to oxidise their organic food source and form sulphides, including hydrogen sulphide. These sulphides may be re-oxidised to form acidic sulphates during the ballast voyage when the cargo tanks are normally empty. This sulphate corrosion cycle requires the existence of aerobic → anaerobic → aerobic conditions. The cycle is continuous as the cargo tanks alternate between empty and loaded conditions.

APB uses the small quantity of oxygen of the water to metabolise hydrocarbons and produce organic acids. Since the *APB* consumes the residual oxygen present in the sediment, they produce a suitable and ideal environment for the *SRB*.

The corrosion degradation rates for these types are extremely fast and can reach 1.5 ~ 3 mm per year and can be highly irregular as Fig.2.5 illustrates. Generally the overview of microbial attack corrosion is referred from *OCIMF* [8] and *RINA* [21].

2.3.6 Galvanic corrosion

Galvanic corrosion occurs when two electrochemically dissimilar metals are physically connected and exposed to a corrosive environment. The less noble metal (anode) suffers accelerated attack and the more noble metal (cathode) is cathodically protected by galvanic current. The tendency of a metal to corrode in a galvanic cell is determined by its position in the ‘galvanic series’ of metals as listed in Table 2-2.

Table 2-2
Galvanic series in sea water [21]

	Metal	Potential mV
More anodic - Less Noble - Higher Corrosiveness 	Sodium (Na)	- 2,300
	Magnesium (Mg)	- 1,400
	Zinc (Zn)	- 760
	Aluminium (Al)	- 530
	Steel-Iron (Fe)	- 400
	Nickel (not passivated) (Ni)	- 30
	Copper (Cu)	+ 40
	Mill scale	+ 45
	Nickel passivated (Ni)	+ 50
	Stainless steel (active)	+ 70
	Silver (Ag)	+ 300
	Stainless steel (passive)	+ 310
	Titanium (passive) (Ti)	+ 370
	Platinum (Pt)	+ 470
Gold (Au)	+ 690	
More cathodic - More noble - Lower Corrosiveness		

2.3.7 Erosion corrosion

Erosion corrosion is usually caused by a movement of sea water, cargo oil and other fluids flow impinge at an existing corrosion cell. This kind of attack is dependent on the degree of liquid turbulence and velocity. Severe erosion corrosion can be developed under the cargo and ballast suction bellmouths. Crude oil washing can also be considered a form of erosion by removing corrosion inhibitor such as greasy or waxy layer and corrosion products on tank surface by keeping the steel clean and corrosion active. The typical effects of sea water velocity on the corrosion of carbon steel, cast iron and copper alloy were introduced by *Chandler* [3]. It was found that the changing of sea water velocity from 0.3 m/s to 1.2 m/s and 8.2 m/s will accelerate corrosion rates of carbon steel to 2.1 and 7.4 times respectively.

2.3.8 Stress corrosion cracking

Stress corrosion cracking is a phenomenon that can occur when steel structures are subjected to quasi-static or dynamic tensile stresses and associated fatigue with

exposure to certain corrosive environments. Cracks are initiated and propagated by the combined effects of stress and the environment. Stress corrosion cracking is particularly insidious in that catastrophic failure can occur even at low applied stress levels and often no warning.

2.4 Causes of accelerated corrosion

OCIMF [8] examined a variety of causes of accelerated corrosion in cargo oil tanks and RINA [21] reviewed factors affecting the corrosion process in both cargo and ballast tanks, which are listed as below:

- *Cargo tanks:*
 - *type of cargo,*
 - *high sulphur content of cargo oil,*
 - *frequency of sediment removal,*
 - *presence of surface coating,*
 - *presence of water,*
 - *design and structural arrangement of the tank,*
 - *inert gas quality,*
 - *high humidity,*
 - *high temperature,*
 - *excessive crude oil washing.*

- *Ballast tanks:*
 - *ballast frequency,*
 - *full or partial filling of the tank,*
 - *cleanliness of ballast water,*
 - *frequency of sediment removal,*
 - *cargo temperature of adjacent tanks,*
 - *design and structural arrangement of the tank,*
 - *coating type, application and related maintenance,*
 - *presence of sacrificial anodes.*

- *Common factors for cargo and ballast tanks:*
 - *inadequate earthing and grounding of electrical equipment,*
 - *material of construction,*
 - *microbial attack,*
 - *sludge/scale accumulation,*
 - *high temperature,*
 - *structural flexing.*

2.5 Various corrosion prevention methods and guidelines

Among the factors which could accelerate corrosion, the effects of tank cleaning washing, temperature changing in cargo oil tanks and ballast tanks due to crude oil tank heating, and inert gas have not been investigated well and should be studied

more in order to define what are the different corrosion effects and behaviours at different tank heating temperatures, working pressure of tank cleaning machines and clean inert gas effect to reduce corrosion rates of marine structures.

2.5.1 Crude oil washing effects on cargo oil tanks

Crude oil washing was made mandatory for new tankers by the *1978 Protocol to the MARPOL Convention* [22]. *MARPOL Annex I Regulation 13 (6)* requires every new crude oil tanker of 20,000 tonnes deadweight and above to be fitted with a cargo tank cleaning system using crude oil washing. *IMO resolution A446(XI)* requires that shadow area should not exceed 10% for horizontal area and 15% for vertical shadow area. The minimum number of tank cleaning machines for each tank is determined by the *IMO resolution A446(XI)* requirement. Normally fixed type tank cleaning machines are provided for the cargo tanks and slop tanks and cleaning is carried out either by crude oil itself or by sea water through these high pressure tank cleaning machines as shown in Fig. 2.6.



Fig. 2.6. Single nozzle type fixed tank cleaning machine [23]

In the past, it was usual that the construction of cargo oil tanks did not apply coating and left the structure completely uncoated, since most ship owners and builders thought that a subsequent natural coating of greasy or waxy crude oil deposit could protect against corrosion as paint does and thus directly reduce the production cost. But actually continuous high pressure crude oil washing is necessary on board and this can remove the protective waxy layer on the steel together with any corrosion products and rust scales. If the protective waxy layer and corrosion products are removed by any fluid impact load and vibration, it potentially originates the new start of the non-linear corrosion growth process.

Normally crude oil washing will be performed by high pressure (5~12 bar) jet nozzles which are driven by cargo oil pumps or by dedicate tank cleaning pump. Apparently high pressure tank cleaning system can cause deformation of any corroded

longitudinal stiffeners under upper deck and eventually will potentially effect on the strength and stiffness of ship structure. It is necessary to investigate that the possible effect of high pressure tank cleaning machines on corroded stiffened plate components and the subsequent behaviour of ultimate strength.

2.5.2 Temperature effects of cargo oil heating in cargo tanks

Most crude oil tankers have a cargo oil heating system for both cargo oil tanks and slop tanks. Steam is usually used as the heating medium at a working pressure 6 ~ 8 bar and Al-brass material is the most prevalent material for the heating coil, however stainless steel or other types of steel material is also used in accordance with ship owner's requirement and shipyard's standard. The purpose of crude oil tank or slop tank heating is to decrease the viscosity of the cargo, so as to facilitate the discharge of crude oil by cargo oil pumps or for the heating up of the tank cleaning medium (crude oil or sea water) for efficient tank cleaning performance.

One set of typical design criteria for crude oil tanker heating system in the market is presented in the following Table 2-3. In the case of VLCC vessels the heating coil is normally installed in slop tanks only.

Table 2-3
Typical design criteria for cargo oil tank heating

Item / Tank name	Cargo oil tanks and starboard slop tank	Port slop tank
Maintain temperature	44°C	44°C
Raising temperature	From 44 to 66°C within 96 hours during voyage	From 15 to 66 °C within 24 hours during voyage
Loading condition	98% full with cargo oil	50% full with sea water
Sea water temperature	5°C	5°C
Ambient air temperature	2°C	2°C

There are no specific design criteria for cargo oil tank heating in Class Rules, and frequently design criteria is different according to type of cargo, route of voyage, and both operator's and builder's standard.

Many seafarers may not be aware of the possible effects of temperature on the life of a ship's structure and heating up of cargoes without consideration of the temperature control in cargo tanks. It is apparent that the maintaining and heating up of cargoes should be based on fluid characteristics and viscosity of the cargo.

Generally chemical corrosion processes occur faster at higher temperature. For iron in a water temperature range from 0°C to 100°C, the rate of corrosion is increasing up to 80°C under the influence of increasing oxygen diffusion rate and then decreasing up to 100°C under the influence of the reduction of oxygen solubility [10].

A temperature increase of 10°C may approximately double the electrolytic reaction rates [4]. This means that the corrosion rate is approximately doubled for every 10°C of temperature increase.

The relative corrosion rates of hull structural steel at various temperatures are identified by the *Registro Italiano Navale* as illustrated in Fig. 2.7.

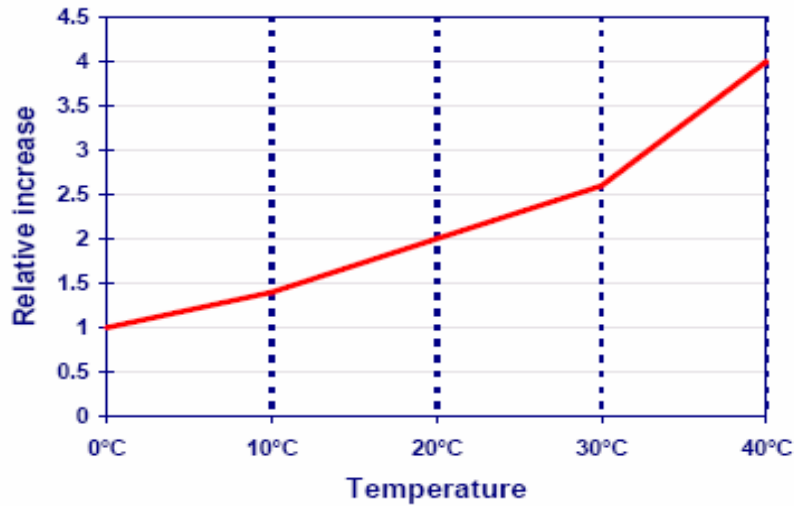


Fig. 2.7. Increase of corrosion rate with increase in temperature [21]

Melchers [24] introduced the corrosion rate r_0 as a function of the carbon content that was based on various relatively short exposure periods (between 10 days and 1.5 years) and the annual mean water temperature based on existing data, [25-31], as following Fig. 2.8.

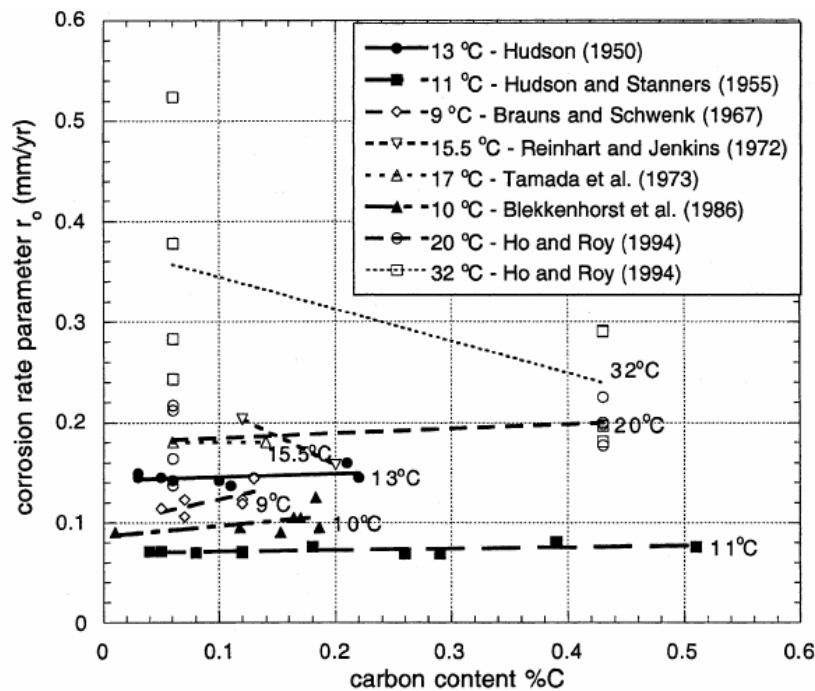


Fig. 2.8. Corrosion rates corresponding to various temperatures [24]

In the case of double hull tankers, the wing and double hull spaces act as a thermal barrier and these spaces insulate the cargo tanks from the sea water. Actually cargo tanks are not significantly affected by normal ambient temperature fluctuations, such as sea water temperature and air temperature, and tend to keep the cargo loading temperature. Sometimes cargo oil heating is not necessary during the summer or for short laden voyage. After cargo discharge has taken place, the cargo tank structure remains at an elevated temperature for certain periods until the ballast tanks are filled by sea water. In a high temperature environment, the bacteria thrive for a longer time and consequently there will be an associated increase in microbial influenced corrosion rates.

It is thus apparent that the higher temperature potentially accelerates the corrosion degradation in the structure. However the effects of cargo tank heating on wing and double bottom ballast tank degradation have not been investigated well. When cargo oil tanks maintain or are heated up to certain temperature, the temperature of the adjacent emptied ballast tank structure tends to similarly increase to some appreciable extents.

As mentioned above, the main purpose of crude oil tank or slop tank heating is to decrease the viscosity of cargo, so as to facilitate discharge the crude oil cargo by cargo oil pumps. According to published data most of crude oil viscosity at 30°C is between 3 cSt and 200 cSt [32].

Fig. 2.9 shows a typical performance curve and viscosity relationship based on a typical cargo oil pump capacity of $2,500\text{ m}^3$ at 130 mwc total head and -5 m suction head.

There is no significant difference in pump performance and power consumption between cargo oil viscosity values of 30 cSt and 200 cSt . Considering the fact that cargo oil pumps normally operate at less than the design condition, the difference of power consumption between 30 cSt and 200 cSt can be ignored.

It is thus clear that excessive heating of cargo is not only a cause of potentially accelerating corrosion but also results in a large amount of operation cost by consuming the steam which is supplied by auxiliary boilers. It is often the case that there is argument between the ship's owner and the shipyard during the design and construction regarding the total length of heating coil which is laid on the cargo oil tank bottom.

Most of ship owners prefer and think that the greater the length of heating coil that is laid on the cargo oil tank bottom, the better it is for operation. But ships owners and shipyard should know the fact that an over-designed cargo heating system leads to a large amount of initial cost for installation, increasing operation cost and reducing ship's life by increasing corrosion rates due to high temperature heating in cargo oil tanks.

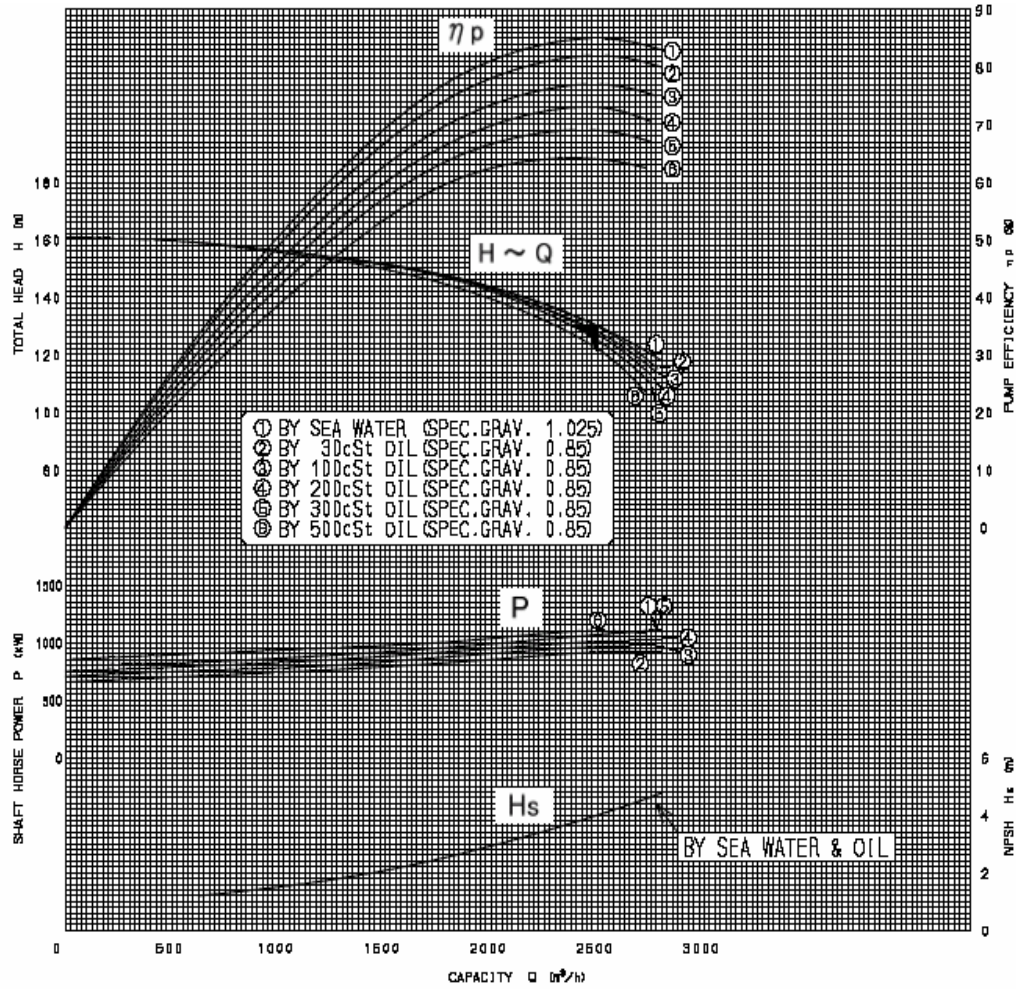


Fig. 2.9. Performance curve of typical cargo oil pump

JSDS [33] proposed that the steam consumption for cargo oil heating, is given by:

$$S_M = \frac{1}{i_1 - i_2} \sum K_i A_i (T_k - T_s) \quad (\text{Eq.2.3})$$

$$S_U = S_M + \frac{1}{(e^{\alpha r} - 1)} \left(\frac{T_a - T_b}{i_1 - i_2} \right) \sum K_i A_i \quad (\text{Eq.2.4})$$

- where
- S_M = required steam consumption to maintain oil temperature (kg/h)
 - S_U = required steam consumption to raise-up oil temperature (kg/h)
 - i_1 = heating coil steam enthalpy at inlet (kcal/kg)
 - i_2 = heating coil condensate enthalpy at outlet (kcal/kg)
 - K_i = heat transfer coefficient (kcal/m²h °C)
 - A_i = area of surface (m²)
 - T_k = oil maintaining temperature (°C)

T_s	= surrounding media temperature	($^{\circ}C$)
T_a	= temperature of cargo oil after heating up	($^{\circ}C$)
T_b	= temperature of cargo oil before heating	($^{\circ}C$)
α	= $\frac{\sum K_i A_i}{\gamma V c}$	
γ	= specific gravity of cargo oil	(kg/m^3)
V	= oil volume	(m^3)
c	= specific heat of cargo oil	($kcal/kg^{\circ}C$)

To estimate the total steam consumption during cargo oil temperature maintaining or raising-up the following design conditions are considered:

- Heating coil steam inlet pressure : $6 kg/cm^2 g$
- Heating coil steam condensate pressure : $3 kg/cm^2 g$
- Heating coil material : *Al-Brass (O.D 44.5mm)*
- Specific gravity of cargo oil : $850 kg/m^3$
- Specific heat of cargo oil : $0.94 kcal/kg^{\circ}C$

The total steam consumption is calculated based on oil maintaining temperatures of alternatively $30^{\circ}C$, $40^{\circ}C$, $50^{\circ}C$ and $60^{\circ}C$ and the design criteria as shown on Table 2-4.

Table 2-4
Illustrative design criteria of cargo oil tank heating temperature

Item / Tank name	Cargo oil tanks	Slop tanks
Maintain temperature	$30^{\circ}C / 40^{\circ}C / 50^{\circ}C / 60^{\circ}C$	Same as cargo tanks
Raising temperature	From 44 to $66^{\circ}C$ within 96 hours during voyage	Same as cargo tanks
Loading condition	98% full with cargo oil	Same as cargo tanks
Sea water temperature	$5^{\circ}C$	$5^{\circ}C$
Ambient air temperature	$2^{\circ}C$	$2^{\circ}C$

Table 2-5, Figs. 2.10 and 2.11 show the differences in the total steam consumption and heating coil length at each of the design conditions and for the *AFRAMAX* tanker model which has been selected in order to calculate steam consumptions.

Table 2-5
Steam consumption and heating coil length

Item	$30^{\circ}C$	$40^{\circ}C$	$50^{\circ}C$	$60^{\circ}C$	Heating-up ($44^{\circ}C$ to $66^{\circ}C$)
Steam consumption (kg/hour)	4,620	6,387	8,153	10,009	26,539
Required heating coil length (m)	920	1,384	1,937	2,632	7,456

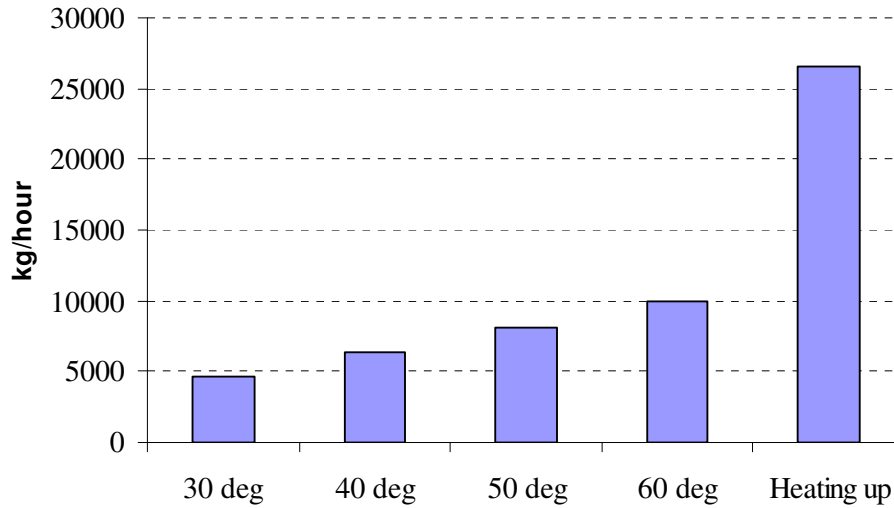


Fig. 2.10. Total steam consumption (kg/hour)

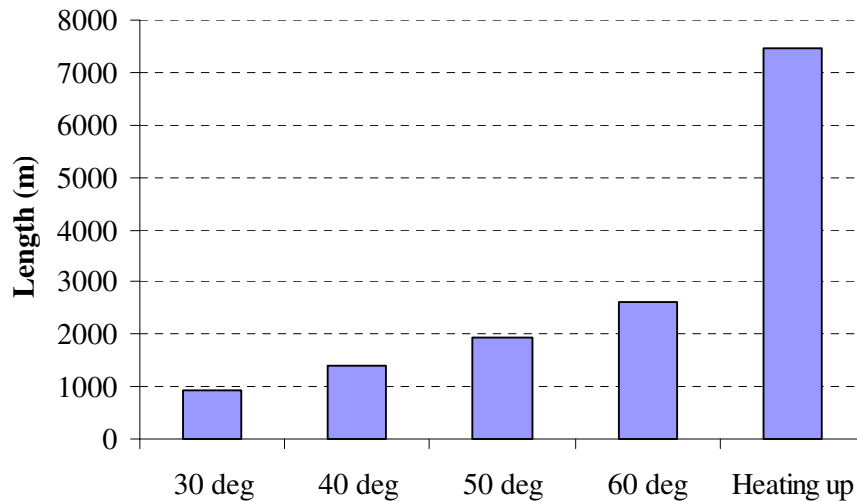


Fig. 2.11. Total required length of heating coil

As shown in the above illustrative examples, the present design provision for cargo heating, which is applied on crude oil tankers, will effect not only the resulting high value of corrosion degradation rate but also the increasing overall construction costs such as increasing heating coil length, piping and fitting size on steam lines and the capacity of auxiliary boiler.

An additional cost evaluation shall not be carried out any further in this research because the final decision to change the design criteria of cargo heating is solely dependent on the ship's owner and the shipyard. However it is apparent that reducing the design criteria of cargo oil tank heating will lead to not only a reduction of the

corrosion degradation of cargo oil tanks and adjacent ballast tanks but also a reduction of large amount of construction and subsequent operating costs.

2.5.3 Inert gas system

In the mid of 1970's there was a series of explosions in crude oil tankers, especially during the tank cleaning operations on-board and where an inert gas system was not installed. As a consequence an inert gas system is now required on new tankers as described by *Regulation 60* and *Regulation 62* of *Chapter II-2* of the *SOLAS Protocol* [34].

With such a system protection against a tank explosion is achieved by the introduction of inert gas into a cargo tank to keep the oxygen content low and to reduce the hydrocarbon gas concentration in the tank atmosphere both of which significantly reduce the chance of accidental ignition.

Generally an inert gas system is used during the following operations of crude oil tankers:

- Cargo oil discharging,
- Hydrocarbon gas purging after tank cleaning for gas freeing,
- Tank cleaning,
- Topping-up at sea,
- Gas freeing of ballast tanks in cargo area.

For a gas carrier, an inert gas system is used for following operations:

- To supply inert gas into the cargo tanks during gas purging,
- To supply inert gas into the cargo tanks during air purging,
- To supply dry air into the cargo tanks during aeration,
- To supply dry air for drying the cargo tanks and cofferdam spaces,
- To supply inert gas for inerting cargo piping, cargo machinery and cargo machinery room via spool piece,
- To supply dry air for drying the duct keel via spool piece.

2.5.3.1 Types of inert gas systems

There are three types of inert gas plant as follows:

- Conventional boiler flue gas uptake based inert gas plant
- Inert gas generator by fuel oil (F.O) or diesel oil (D.O) burning
- Pure N_2 generator

1) Conventional boiler flue gas uptake based inert gas plant

A conventional boiler flue gas uptake based inert gas plant uses flue gas taken from

the exhaust gas duct of the auxiliary boilers. This plant typically consists of a scrubber and demister, two(2) inert gas blowers, a deck water seal unit, a pressure vacuum breaker, ducting and necessary fittings. A typical schematic arrangement of this type of inert gas system for tanker is shown in Fig. 2.12.

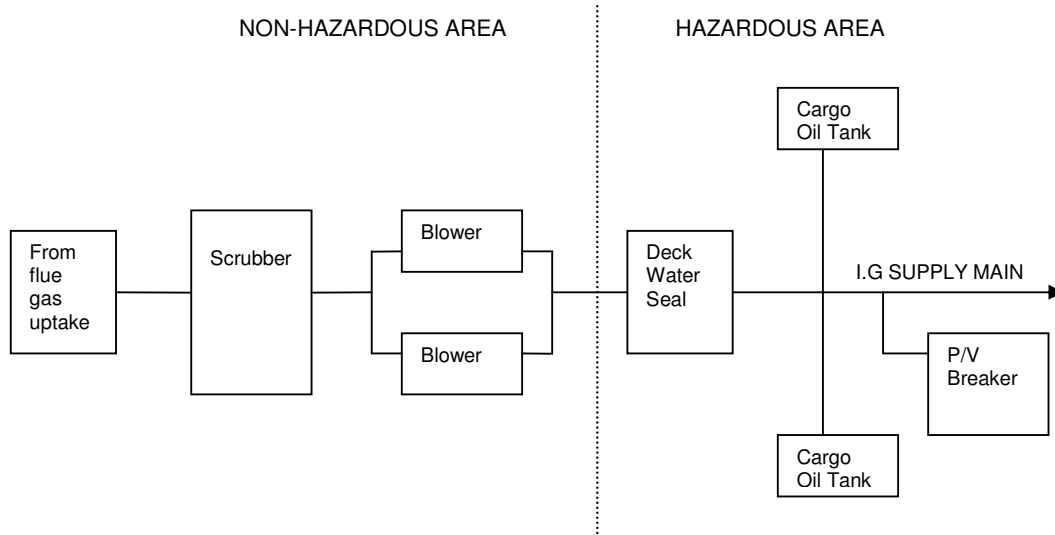


Fig. 2.12. Typical schematic of a boiler flue gas uptake inert gas system

Basic boiler flue gas and final inert gas compositions are typically as in the following Table 2-6 [35].

Table 2-6
Typical boiler flue gas and corresponding inert gas composition [35]

Item	Flue gas composition	Inert gas composition
CO_2	13.5 %	13.5 %
SO_2	0.3 %	less than 0.03 %
O_2	4.2 %	4.3 %
N_2	77.0 %	79.6 %
H_2O	5.0 %	2.0 %

Actually each manufacturer has slightly different standards in inert gas composition. Generally the SO_2 content is not more than 100 ppm in inert gas composition and O_2 content is less than 5.0 % by volume.

Inert gas is to have an oxygen content of less than 8 % by the rule and this will result in a reduced corrosion rate compared with normal atmosphere conditions which has an oxygen content of 20.95 % by volume. The rate of corrosion of steel structure is significantly reduced when the oxygen content is below 1 %. This low oxygen level can be achieved by other types of inert gas plants such as the inert gas generator and N_2 generator systems.

The corrosion rate tends to increase with increasing O_2 and SO_2 levels in inert gas. Sulphur dioxide is of major importance for atmospheric corrosion. Absorption of SO_2 into the surface of a metal depends on the relative humidity and the presence of corrosion products. SO_2 oxidizes to SO_3 in the atmosphere or in the moisture film on the metal surface and this subsequently reacts with the H_2O to form H_2SO_4 and which leads to an acid reaction against a metal surface. The SO_2 content in a tank is more related to the type and origin of crude oil cargoes rather than to the presence of inert gas. Sometimes, for example, the hydrogen sulphide content can be more than 600 ppm depending on the type of crude oil [4].

2) Inert Gas Generator by F.O and D.O burning

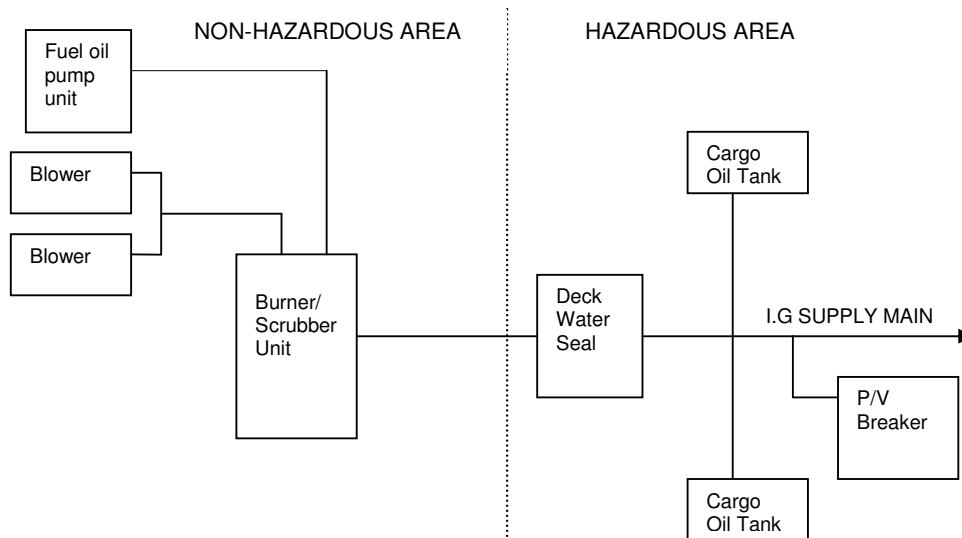


Fig. 2.13. Typical schematic of an inert gas generator based system for tanker

This type of system employs a separate inert generator which is normally located in engine room or engine casing on upper deck level. The separate inert gas generator is provided with two or more fuel oil or diesel oil pumps. This type of inert gas generator is normally used where high quality inert gas is required in such as chemical tankers and gas carriers where it is necessary to protect the quality of cargoes and spaces from any possible contaminations. However the price and operating costs of such system are somewhat more expensive than conventional boiler flue gas uptake based inert gas system. The typical arrangement of inert gas generator is shown in Fig. 2.13.

Table 2-7 shows a general design specification from one of current manufacturer.

- To purge cargo liquid line, vapour lines and vent masts,
- To seal high duty and low duty compressors.

A N_2 generator consists of air compressor, separators, filters, heaters and membrane modules as illustrated in Fig. 2.14.

The gas composition from the N_2 generator depends on the design of the system, normally between 95% and 99.9% N_2 with 5% to 0.01% of other inert gases which can be adjustable by changing the operating conditions.

2.5.3.2 Inert gas system for ballast tank and ship structure

Ship structures are continuously suffering from corrosion related fatigue, strength and integrity problems under the sea water environment. However there have been only a few investigations undertaken regarding the effects of inert gas on the corrosion of ship structures. *Johansson and Vannerberg* [37] studied the atmospheric corrosion of a commercial steel by laboratory tests under relative humidity of 90% at 22°C and with the following conditions:

- Type A : Polished steel samples were exposed to an inert gas consisting of 3.0 % O_2 , 12.0 % CO_2 and 10 ppm (by volume) SO_2
- Type B : Polished steel samples were exposed to a mixture of humid air and 10 ppm (by volume) SO_2
- Type C : Polished steel samples were exposed to an inert gas consisting of 3.0 % O_2 , 12.0 % CO_2 and 100 ppm (by volume) SO_2
- Type D : Polished steel samples were exposed to an inert gas consisting of 3.0 % O_2 , 0 % CO_2 and 100 ppm (by volume) SO_2
- Type E : Pre-corroded samples were exposed to the same atmosphere as in experiment C
- Type F : Pre-corroded samples were exposed to an atmosphere consisting of 3.0 % O_2 , 12.0 % CO_2 and 300 ppm (by volume) SO_2

However, contrary to common expectation and other recent researches, the study revealed that high concentrations of SO_2 in an inert gas may, under certain circumstances, be corrosion-inhibitive by creating the formation of a protective coating consisting of iron sulphide and iron sulphite hydrate on the surface of the steel. This result illustrates that it is difficult to simulate in a laboratory corrosion test environment. A full actual onboard test is considered to be necessary in order to evaluate the effects of inert gas on marine structures.

Miyuki et al. [38] have carried out laboratory simulations of corrosion in a wet inert gas environment (13% CO_2 , 5% O_2 and a small amount of SO_2) and they found that the corrosion rates increased with increasing levels of O_2 and SO_2 contents in the inert gas [4].

Matsuda et al. [39] have introduced a new anticorrosion method that purges oxygen from ballast tanks by providing a continuous supply of nitrogen. The design concept is that liquid nitrogen, that is stored in independent tank, supplies nitrogen gas passing through an evaporator and a reduction valve into the ballast water. The pressure within the ballast tank is controlled by a pressure release device and the ballast tank is monitored by pressure, temperature and oxygen sensors as shown in Figure 2-15.

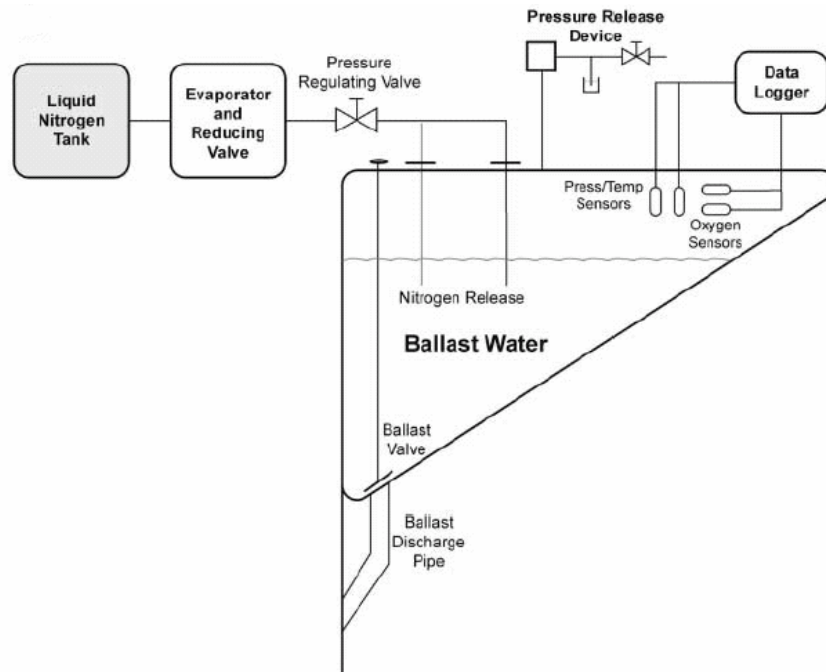


Fig. 2.15. New anticorrosion method by using nitrogen gas [39], [40]

In order to verify the system efficiency in the control of corrosion, an experimental test was carried out in a 150,000 tonnes coal/ore carrier for a period of 18 months (583 days). Steel test plates were used in one tank with the nitrogen gas control and other plates in an untreated standard ballast tank condition. The changing pattern of oxygen content in the nitrogen treated tank during operation is shown in Fig. 2.16.

Subsequently they found that the rate of rusting on shot blasted steel test plates placed at the bottom of the nitrogen treated ballast tank was 0.039 mm/year, compared with 0.382 mm/year for the same type of plates at the bottom of a standard ballast tank with normal operating tank atmosphere condition as shown in Fig. 2.17. This means that the corrosion rate of nitrogen treated environment is approximately 10 % that of normal operating tank atmosphere condition. It also found that painted steel plates with the nitrogen atmosphere treatment the corrosion rate was reduced to 0.001 mm/year.

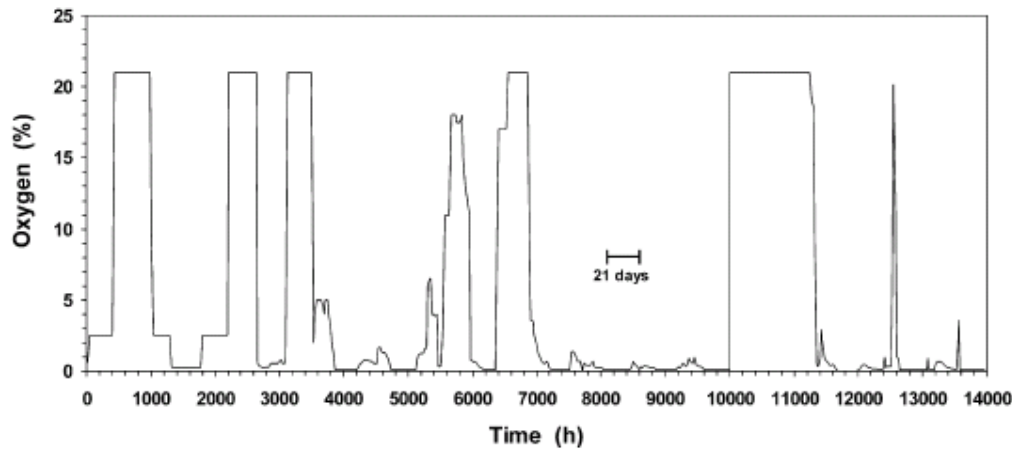


Fig. 2.16. Percent oxygen in the nitrogen treated ballast tanks during 18 months of operations of the coal/ore vessel [39] [40].

Another new solution was introduced by *Tamburri et al.* [41]. This is called the *Ventury Oxygen StrippingTM* system. The system produces inert gas by combusting low-sulphur marine diesel in a special device and then mixing the output gases with the ballast water using a ventury injector that is installed in-line, just down stream of the ballast pump. Both the continuous nitrogen supply system and *Ventury Oxygen StrippingTM* system are used for ballast water treatment in order to reduce both aquatic organism introduction and corrosion control in ballast tanks. But the initial cost for installation and operating costs are still too high to adopt these kinds of system for many ship's owners.

However the company *Hellespont* has adopted full inert gas coverage of its ballast tanks during laden voyages, in both old and new ships. This inert gas is double scrubbed to produce a sulphur dioxide content of less than 2 ppm. There is a separate inert gas injection pipe with holes at each stringer level installed at the aft end of each ballast tank in order to ensure good purging flow and adequate distribution of inert gas pressure within the tank space. This innovative design cuts corrosion of the steelwork and piping considerably in the ballast tank where the coating has begun to break down [42] [43].

Cox [44] briefly introduced and reviewed the advantages and disadvantages of the various inert gas systems to ballast tanks.

In connection to this research, recently *Ok and Pu* [45] presented the economical and innovative solution to control corrosion in marine and offshore structures by using clean inert gas and concluded that clean inert gas can be advantageous, economical and innovative methods to control corrosion for marine and offshore structures. The details and results are introduced in following sections regarding an optimized anti-corrosion design by clean inert gas system, cost evaluation and degradation of section modulus over service life in Chapter 3.

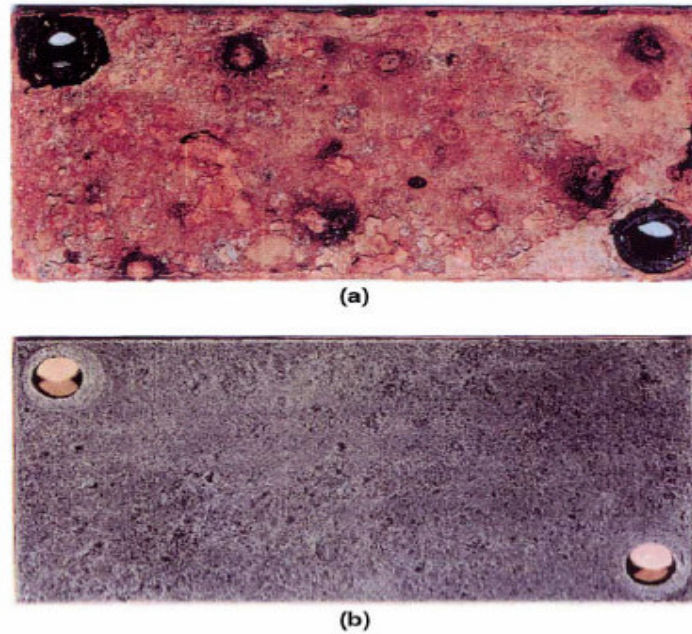


Fig. 2.17. Corrosion levels on steel plates placed in ballast tanks during the 18 months shipboard study: (a) plate from controlled tank under constant air saturation levels with a corrosion rate of 0.382 mm/year, (b) plate from the nitrogen treated ballast tanks under periodic hypoxia with a corrosion rate of 0.039 mm/year [39], [40]

2.5.3.3 Optimized anti-corrosion design by inert gas generator

It is apparent that an oxygen content of below 1% will reduce the rate of corrosion significantly. An inert gas generator or a N_2 generator can thus be used to control corrosion within cargo tanks and ballast tanks. An inert gas generator especially can be installed on board with a relatively small amount of initial cost and this system would reduce the corrosion rate of ship structure.

A N_2 generator could be an economic solution for container vessels and bulk carriers where an inert gas system is not compulsory by the rule requirements. This means that there is no restriction in capacity and the capacity of the N_2 generator could be designed in accordance with the operation concept of the ballast tanks and their tank capacity. An optimised design approach for an oil tanker is proposed in this research and cost based criteria to apply clean inert gas system in ship structures are to be introduced and investigated.

(1) Proposed design

SOLAS [34] Regulation II-2/59.4 requires oil tankers constructed on or after 1 October 1994, to be provided with suitable arrangement for gas freeing and for ventilation of double hull spaces.

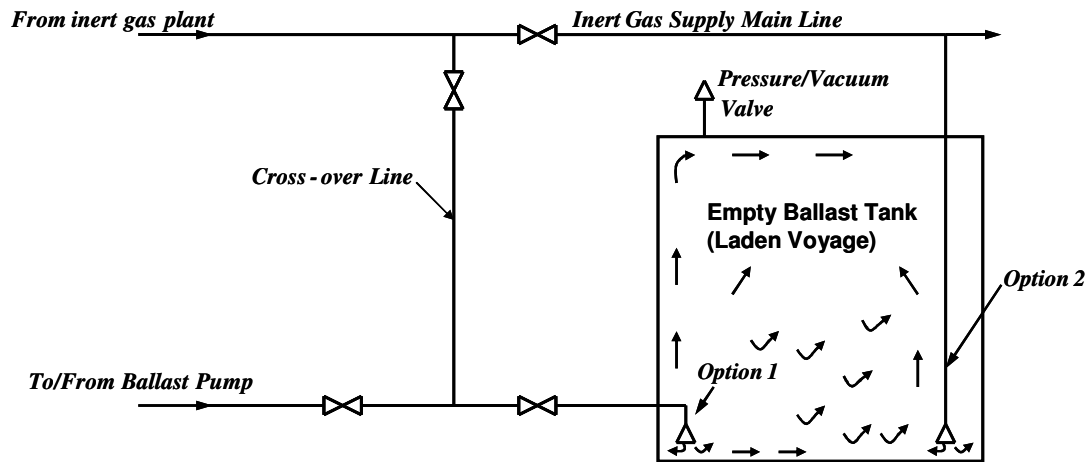


Fig. 2.18. Inert gas supply to double hull space during laden voyage

In addition, oil tankers fitted with inert gas systems are required to have suitable arrangements for inerting double hull spaces, when necessary. The arrangements for the inerting of double hull spaces may be through portable connections to the inert gas system for cargo tanks or by fixed piping connections. Practically, a cross connection with portable spool piece, non return valve and manual isolation valves are to be provided between the inert gas main line and the water ballast main line in the cargo oil pump room so as to supply either inert gas or fresh air into the ballast tanks.

Fig. 2.18 shows a typical schematic of the inert gas supply from an inert gas generator to a double hull ballast tank through an existing inert gas supply main and ballast piping line. There is no additional piping, except for the cross over, necessary for a crude oil tanker and this design allows the system to put the inert gas into the ballast tank during a laden voyage where the ballast tanks are empty.

However there is no actual onboard corrosion measurement data available for tank structures which compare the difference in corrosion rate between a conventional boiler flue gas uptake and an inert gas generator system. However from the past test data obtained by *Matsuda et al.* [39], we can assume that an adequately inerted environment will result in significantly reduced corrosion degradation rates than the normal sea water environment in ballast tanks.

The potential effect of an inert gas generator system on a hull section modulus degradation over service life is introduced and discussed in Chapter 3.

(2) Design consideration for double hull tanker inert gas supply

The above design approach outlines the most economic solution to supply inert gas to double hull spaces. There are many alternative and improved designs that are available, however this research is to focus on introducing the most economic solution that will be required in order to appreciably reduce the corrosion rates for ballast tanks

and cargo tanks and thus have the financial benefit of reducing steel replacement costs in ageing ships.

The provision of inert gas supply to the double hull space through existing ballast piping is carried out after completion of de-ballasting in the tanks. There are no specific rule requirements to supply inert gas to ballast tanks and some classification societies may be more conservative than others in the application and interpretation of this system. However considering the potential reduction of corrosion rates and the resultant increasing reliability of a ship's structure, a more optimistic interpretation is justified in order to apply this system.

Generally the following should be considered during the initial design of inert gas system in double hull spaces.

- Air vent heads for ballast tanks should be blinded during a laden voyage and permanent high velocity pressure vacuum valves are to be provided for each ballast tank.
- The size of high velocity pressure/vacuum valves should allow for the design concept of inert gas supply rate to each double hull tank. However during the operation it is advisable that the ballast tank access hatch should always be opened during inert gas supply to ballast tanks.
- If high velocity pressure/vacuum valves are not of a water tight design, then they should be located such as to avoid any accidental flooding during heavy seas, such as near the ship's centre line. Alternatively the possibility of accidental flooding rate through a pressure/vacuum valve into a water ballast tank should be calculated and considered during design stage.
- Interpretation of each classification society rules and requirement should be checked in order to ensure compliance.

(3) Cost evaluation

In connection to this research, *Ok and Pu* [46] firstly introduced an approximate cost evaluation between a conventional boiler flue gas uptake based inert gas system without inert gas supply to the double hull space and an inert gas generator with inert gas supply to the double hull space based on an *AFRAMAX* tanker. It was found that using clean inert gas to marine structure will reduce overall maintenance costs considerably for replacement of steel structures, and possibly can reduce tank coating thicknesses for both new building ships and ageing ships.

Generally, it is recommended to install a clean inert gas system in crude oil tankers, if the total through-life cost of the boiler flue uptake based inert gas system is expected more than the total through-life cost of clean inert gas system as follows:

$$\sum(C_{F-M} + C_{F-I} + C_{F-O} + C_{F-MT}) > \sum(C_{G-M} + C_{G-I} + C_{G-O} + C_{G-MT}) \quad (\text{Eq.2.5})$$

where C_{F-M} , C_{F-I} , C_{F-O} , C_{F-MT} are the cost of material/equipment, cost of installation, cost of operation and cost of maintenance (hull structure and equipment)

during designed ship's life, respectively for boiler flue gas uptake inert gas system. C_{G-M} , C_{G-I} , C_{G-O} , C_{G-MT} are cost of material/equipment, cost of installation, cost of operation and expected cost of maintenance (hull structure and equipment) during designed ship's life, respectively for clean inert gas system such as inert gas generator or N_2 generator.

If ship and offshore structures are not required to have an inert gas system by rule, it is recommended to install an clean inert gas system when the total cost of maintenance of hull structure is expected being more than the total through-life cost of clean inert gas system given by:

$$\sum(C_{MT}) > \sum(C_{G-M} + C_{G-I} + C_{G-O} + C_{G-MT}) \quad (\text{Eq.2.6})$$

where C_{MT} is total maintenance cost for whole design life.

2.6 Concluding remarks

There are many factors which accelerate corrosion in marine structures. Among these factors, the effects of high pressure tank cleaning washing, temperature changing due to cargo oil tank heating and clean inert gas system have not been investigated well. This chapter generally reviews and investigates the effects of these factors on marine structures.

A temperature increase of 10°C may approximately double the electrolytic reaction rates. This means that the corrosion rate is approximately doubled for every 10°C of temperature increase. It is thus apparent that the higher temperature potentially accelerates the corrosion degradation in a structure. When cargo oil tanks maintain or are heated up to certain temperature, the temperature of the adjacent emptied ballast tank structure tends to similarly increase to some appreciable extents. In this research it is found that current design of tank heating system for cargo tanks slop tanks in crude oil tanker has relatively higher maintained and raising temperature to keep the viscosity of cargo than actually required temperature to facilitate discharge the crude oil cargo by cargo pumps. The effects of different design criteria of tank heating on the steam consumption and required heating coil length have also been investigated. Obviously a well-designed cargo heating system can lead to a large amount of cost reduction for installation, operation and increasing ship's life by decreasing corrosion rates in cargo oil tanks and ballast tanks, thus it is recommended that a design optimization to determine design criteria of cargo heating system for each new building or conversion project has to be carried out by ship's owner or shipyard which consider viscosity of cargo, period and route of voyage etc.

Crude oil washing operation by high pressure (5~12 bar) jet nozzles can cause deformation of any corroded longitudinal stiffeners under upper deck and eventually this will potentially effect on the strength and stiffness of ship structures. It is necessary to investigate the possible effects of high pressure tank cleaning machines

on corroded stiffened plate components and the subsequent structural behaviour in terms of ultimate strength.

The clean inert gas system, either a high quality inert gas generator system or a N_2 generator system, can be used to reduce corrosion degradation in marine structures in areas such as ballast tanks and permanent void spaces. This system can be adopted to not only crude oil tankers but also to bulk carriers and container vessels. The application on bulk carriers, container vessels and other types of vessels has the advantage that there is no capacity restriction to apply to inert gas systems and the operator can adopt a smaller capacity considering individual operation concepts and can reduce equipment cost. In connection to this study, *Ok and Pu* [46] firstly introduced an approximate cost evaluation between a conventional boiler flue gas uptake based inert gas system without inert gas supply to the double hull space and an inert gas generator with inert gas supply to the double hull space based on an *AFRAMAX* tanker. It is found that the clean inert gas can effectively control corrosion of marine and offshore structures, accordingly can minimize hull girder stresses increasing over service life and will reduce overall maintenance costs considerably for replacement of steel structures, and possibly can reduce tank coating thicknesses for both new building and repairing ships.

It is recommended that further research activities with actual onboard tests are required to verify effectiveness of high pressure tank cleaning washing, cargo oil tank heating and clean inert gas system on marine/offshore structures against corrosion for certain type and size of vessels.

References (Chapter 2)

1. Johnson, N., *A protocol to protect the Mediterranean from shipping accidents enters into force*, in *Green Horizon*. 2004.
2. Kawano, H. and M. Hirakata, *Tanker Structure and Hull Failure Strength*. The Petroleum Association of Japan PAJ-2003 Symposium, 2003.
3. Chandler, K.A., *Marine and Offshore Corrosion*. 1984.
4. TSCF, *Corrosion Protection of Cargo Tanks*. Tanker Structure Co-Operative Forum, 2000. **TSCF Working Group #2, Chevron, Shipping Company**.
5. Wang, G., J. Spencer, and H. Sun, *Assessment of corrosion risks to ageing ships using an experience database*. 22nd International Conference on Offshore Mechanics and Arctic Engineering, 2003.
6. Wang, G., J. Spencer, and T. Elsayed, *Estimation of Corrosion Rates of Structural Members in Oil Tankers*. International Conference on Offshore Mechanics and Arctic Engineering, CANCUN, MEXICO, 2003. **22nd**.
7. Paik, J.K., et al., *A Time-Dependent Corrosion Wastage Model for the Structures of Single and Double-Hull Tankers and FSOs and FPSOs*. Marine Technology, 2003. **Vol.40, No.3**: p. 201-217.
8. OCIMF, *Factors Influencing Accelerated Corrosion of Cargo Oil Tanks*. Oil Company International Marine Forum, 1997.
9. Rogers, T.H., *Marine Corrosion*. 1968.
10. Butler, G. and H.C.K. Ison, *Corrosion and its Prevention in Waters*. 1966.
11. Ross, T.K., *Metal Corrosion*. Engineering Design Guides, 1977.
12. West, J.M., *Basic corrosion and oxidation*. 1980.
13. Mattsson, E., *Basic corrosion technology for scientists and engineers*. 1989.
14. Paik, J.K. and A.K. Thayamballi, *Ultimate Limit State Design of Steel Plated Design*. 2003: John Wiley & Sons Ltd.
15. Hutchinson, S.C. and R.G. Bea, *Maintenance of Marine Structures; A State of the Art Summary*. Ship Structure Committee, SSC-372, 1993.
16. Laycock, P.J. and P.A. Scarf, *Exceedances, extremes, extrapolation and order statistics for pits, pitting and other localized corrosion phenomena*. Corrosion Science, 1993. **35**(1-4 SU -): p. 135-145.
17. Daidola, J.C., et al., *Residual strength assessment of pitted plate panels*. Ship Structure Committee, SSC-394, 1997.
18. Paik, J.K., et al., *Time-dependent risk assessment of ageing ships accounting for general/pit corrosion, fatigue cracking and local dent damage*. SNAME, Annual Meeting in San Francisco (World Maritime Technology Conference), 2003.
19. IACS, *Renewal criteria for side shell frames and brackets in single side skin bulk carriers not built in accordance with UR S12 Rev.1 or subsequent revisions*. International Association of Classification Societies, 2003 Rev.1.
20. TSCF, *Condition Evaluation and Maintenance of Tanker Structures*. Tanker Structure Cooperative Forum, May, 1992.
21. RINA, *Guide for the Structural Design of Oil Tankers*. Registro Italiano Navale, 2004.
22. MARPOL, *International Convention for the Prevention of Pollution by Ships (MARPOL 73/78)*. 1978.

23. SCANJET, *Tank Cleaning Machine Brochure*. <http://www.scanjet.se/BROSCHYRER/90T2.pdf>, 2004.
24. Melchers, R.E., *Effect on marine immersion corrosion of carbon content of low alloy steels*. Corrosion Science, 2003. **45**(11): p. 2609-2625.
25. Hudson, J.C., *The corrosion resistance of low alloy steels*. J. Iron Steel Inst.(180), 1955: p. 271-284.
26. Blekkenhorst, F., et al., *Development of high strength low alloy steels for marine applications, Part 1: results of long term exposure tests on commercially available and experimental steels*. 1986: p. 163-176.
27. Hudson, J.C., *Corrosion of bare iron and steel in sea water*. J. Iron Steel Inst.(166), 1950: p. 123-136.
28. Ho, K.H. and S.K. Roy, *Corrosion of steel in tropical sea water*. Brit. Corros. J. 29 (3), 1994: p. 233-236.
29. Tamada, A., M. Tanimura, and G. Tenmyo, *Corrosion behavior of low alloy steels in sea water*. Proceedings of the Fifth International Congress on Metallic Corrosion, Tokyo, Japan, National Association of Corrosion Engineers, Houston, TX, 1972: p. 789-791.
30. Brauns, E. and W. Schwenk, *Korrosion unlegierter Stahle in Seewasser*. Stahl und Eisen 87 (12), 1967: p. 713-718.
31. Reinhart, F.M. and J.F. Jenkins, *Corrosion of materials in surface seawater after 12 and 18 months of exposure*. Technical Note N-1213, Naval Civil Engineering Laboratory, Port Heuneme, CA, 1972.
32. KSA, *Ship Design Standard (Japanese)*. Kansai Shipbuilding Association, 1996(4th Edition).
33. JSDS, *Design standard for deck steam pipe*. Japan Ship Design Standard - 5, 1970.
34. SOLAS, *International Convention for the Safety of Life at Sea, 1974 and amendment*. IMO, 1974.
35. JSDS, *Design standard of inert gas system*. Japan Ship Design Standard - 22 (Japanese), 22.
36. HAMWORTHY, *Inert Gas Generator System Brochure*. <http://www.hamworthykse.com/docGallery/47.PDF>.
37. Johansson, L.-G. and N.-G. Vannerberg, *The corrosion of unprotected steel in an inert-gas atmosphere containing water vapour, oxygen, nitrogen and different amounts of sulphur dioxide and carbon dioxide*. Corrosion Science, 1981. **21**(12 SU -): p. 863-876.
38. Miyuki, H., et al., *Corrosion resistance of TMCP steels for VLCC cargo oil tanks*. Inter-Industry Seminar on Corrosion in Cargo Tanks, London, 8 and 9 October, 1998.
39. Matsuda, M., et al., *An anticorrosion method for ballast tanks using nitrogen gas*. Ship and Ocean Foundation Technical Report, 1999.
40. Tamburri, M.N., K. Wasson, and M. Matsuda, *Ballast water deoxygenation can prevent aquatic introductions while reducing ship corrosion*. Biological Conservation, 2002. **103**(3 SU -): p. 331-341.
41. Tamburri, M.N., et al., *Evaluations of Venturi Oxygen Stripping as a Ballast Water Treatment to Prevent Aquatic Invasions and Ship Corrosion*. 2nd International Ballast Water Treatment R & D Symposium, IMO London, 2003.

42. Woinin, P., *How to build a really sound tanker*. April 26 2001 edition of Lloyds List, 2001.
43. HELLESPONT, *Hellespont Group Web Site*. 2004. <http://www.hellespont.com/index.htm>.
44. Cox, Q., *Restriction of corrosion in double hull ballast spaces*. Design & Operation of Double Hull Tanker, RINA, 2004.
45. Ok, D., Y. Pu, and A. Incecik, *Artificial neural networks and their application to assessment of ultimate strength for plate elements with pitting corrosion*. Ocean Engineering, 2006. **In Processing**.
46. Ok, D. and Y. Pu. *Corrosion control method by using clean inert gas to ballast tanks and permanent void spaces in marine and offshore structures*. in *3rd International Marine Science and Technology for Environmental Sustainability (ENSUS) Conference*. 2005. Newcastle upon Tyne, UK.

Chapter 3

Corrosion Rate Estimation Model

3.1 Introduction

Uniform corrosion is the most common form of corrosion found in the many grades of mild steel that are mainly used for marine structures. Normally uniform corrosion is calculated from weight loss or sampled thickness measurement from test plate coupons and many researches have been carried out and considerable efforts have been made to develop time-based predictive mathematical models. Many data have been obtained from large numbers of thickness measurements made on vessels that have been in-service for some years. Such thickness measurements are typically made using ultrasonic techniques and several point measurements may be made over the surface of a plate in order to arrive at an assumed average value. Comparisons would then be made between as-built scantling thicknesses. Obviously thickness measurements must be made by approved technicians and using approved methods in order to ensure that there is a good degree of confidence in the obtained data. Such measurements would also be made for the web and flange element thicknesses of hull structures.

Many differences are often found in each set of corrosion data, even though corrosion data was sampled in the same type of vessels. This means that any generalised models will have a fairly high level of uncertainty. Most of recent corrosion models are based on actually measured data. Normally we can consider that the most reliable corrosion models are those that are based on actual measurement in hundreds of vessels, this means that a large degree of scattered data is unavoidable in sampled values. The reason is that there are many factors which accelerate individual levels of corrosion such as type of cargoes, frequency of cleaning and sediment removal, type of coating, humidity, temperature, inert gas quality, ballast frequency and presence of sacrificial anodes, etc. It is apparent that slow and progressive corrosion and fatigue are weakening the structure of ageing ships. In the past there have been many casualties of ageing ships. Thus reliability and safety assessment considering corrosion degradation is very important in ageing ships. This is clearly the most significant where the level of corrosion exceeds the corrosion margins that are mandated by the relevant classification society.

Generally, there are three stages of anti-corrosion activities throughout the life of a vessel as follows;

- Corrosion prevention at the initial design and construction stages of the vessel by effectiveness of paint coatings and other anti corrosion methods.
- Regular monitoring and intermediate hull surveys of the hull structure.
- Renew or repair of the excessively corroded and coating breakdown areas.

There are two kinds of methods to predict the corrosion rates of ship structures. The first one is to employ statistical models which collect corrosion data from existing ageing ships and to calculate the mean and standard deviation of corrosion rates for each primary member. The other is to employ probabilistic corrosion prediction models which are formulated in terms of key variables with an understanding of the mechanisms of the processes of corrosion.

Schumacher [1] provided a summary of early experimental data of mild steel exposed to seawater together with a description of the main influencing variables. *Viner and Tozer* [2] described the main types of corrosion, which can occur in ship structures. It was concluded that corrosion in ships is influenced mainly by the following factors: salinity of seawater, temperature, marine fouling, pollution, corrosion films, speed of flow, stray-current, frequency of tank washing, humidity and oxygen availability, type of cargo, cargo residues and mechanical abrasion. A general analysis of ship corrosion and estimation of corrosion rates in various spaces for various types of ships reflecting their operational purpose was also presented by *Yamamoto et al.* [3] and also by *Ohyagi* [4]. Additionally many studies of corrosion in tankers have been presented by *Pollard* [5], *TSCF* [6, 7] and *Loseth et al.*[8], which introduced estimated tanker corrosion rates. The comprehensive historical overviews on corrosion models from *Schumacher* [1] to *TSCF* [7] are presented by *Gardiner and Melchers* [9]. *Hajeesh* [10] investigated the corrosion rate effects on carbon steel from its interaction with different variables both singly and in combination, such as temperature, oxygen, urea, sulphide, inhibitor and chloride. In the case of temperature (30 °C and 45 °C) and oxygen (Deaerated and Aerated) interaction, they found that increasing temperature increases the corrosion rate on average by 1.48 mils (0.03759 mm) per year, and which is significant. The main effect of oxygen is positive and strong. The corrosion rate increases by 2.86 mils (0.07264mm) per year, and a combined two-way interaction produces a sharp rise in the corrosion rate especially at high levels of oxygen.

The most important role of a corrosion model is to enable an operator to be able to estimate when at some time in the future a ship's structures will require some maintenance by replacing corroded plate, renewing coating and anodes etc. If plate thickness or coating condition is below the level required by classification society rules then the replacement or upgrade must be carried out. An economical decision for the next maintenance and replacement period can be planned and facilitated when the rate of future corrosion degradation can be estimated properly.

Ballast tanks are normally considered to have the most corrosive environment. Some guidelines propose the requirement for 10, 15, and 25 year of ballast tank coating systems and associated surface preparations in order to prevent excessive corrosion in ballast tanks [11]. The typical hull strength degradation by ageing up to 25 years service of a conventional tanker was investigated by *Kawano and Hirakata* [12].

This Chapter introduces various published corrosion models and data. A new marine immersed corrosion model based on an average of several existing corrosion models is introduced. Time variant section modulus degradation models are also proposed in this Chapter.

3.2 Existing general corrosion rate estimation models for tanker

General corrosion is the most common and typical pattern of large scale corrosion. Existing corrosion models assume that the corrosion proceeds over the whole surface of the exposed metal at the same nominal rate. The corrosion degradation rate varies according to the operating area, types of cargo, temperature, corrosion location and other factors. It is a question of the reliability of the measurement and sampling processes that were used to collect data from corroded structures and to arrange such data in a valid and accurate manner. There are many corrosion models that have been developed and published, but only a few models can be adequately reliable and be adopted as acceptable corrosion models for application during design of structure and the evaluation of the reliability of an existing ship structure. There is no single unified model to estimate corrosion rates. The measured values from each model are so scattered, therefore it is necessary to develop unified average corrosion model which is based on existing models. Each classification society has its own guidance for minimum corrosion deduction values for plating and structural members for oil tankers [13-15]. Recently IACS published unified new rules and guidelines, so called “Common Structural Rules for Double Hull Oil Tankers”, of corrosion additions for double hull tanker structures. These rules apply to double hull oil tankers of 150m length and upward classed with the society and contacted for construction on or after 1st April 2006 but for double hull tankers of less than 150m in length, the rules of the individual classification society are to be applied [16].

3.2.1 Melchers’s model

Melchers [17] proposed a simple equation for the effect of temperature on corrosion and which was based on long-term immersion corrosion observations that were collected during the 1930~40s, and given by:

$$d_2 = \frac{(t_2 - t_0)}{(t_1 - t_0)} d_1 \quad (\text{Eq.3.1})$$

where t_0 = the annual mean temperature below which there is ‘no’ corrosion throughout the year
 t_1 = the corresponding temperature
 t_2 = the annual mean temperature
 d_1 = the corresponding depth of corrosion penetration at t_1
 d_2 = the depth of corrosion penetration at annual mean temperature t_2

The common observation that is frequently made is that corrosion does not occur below the freezing point of seawater (approximately -2°C at 3.5% salinity) and that the annual variation in temperature for most operational regions is around $15 \sim 20^\circ\text{C}$. In this research, five years of corrosion results for several sites based on ASTM field data [18] were plotted as a function of annual mean water temperature, the results of which are as illustrated in Fig. 3.1. Melchers also proposed both linear and non-linear function models based on all field exposed specimen data, as shown in Fig. 3.2.

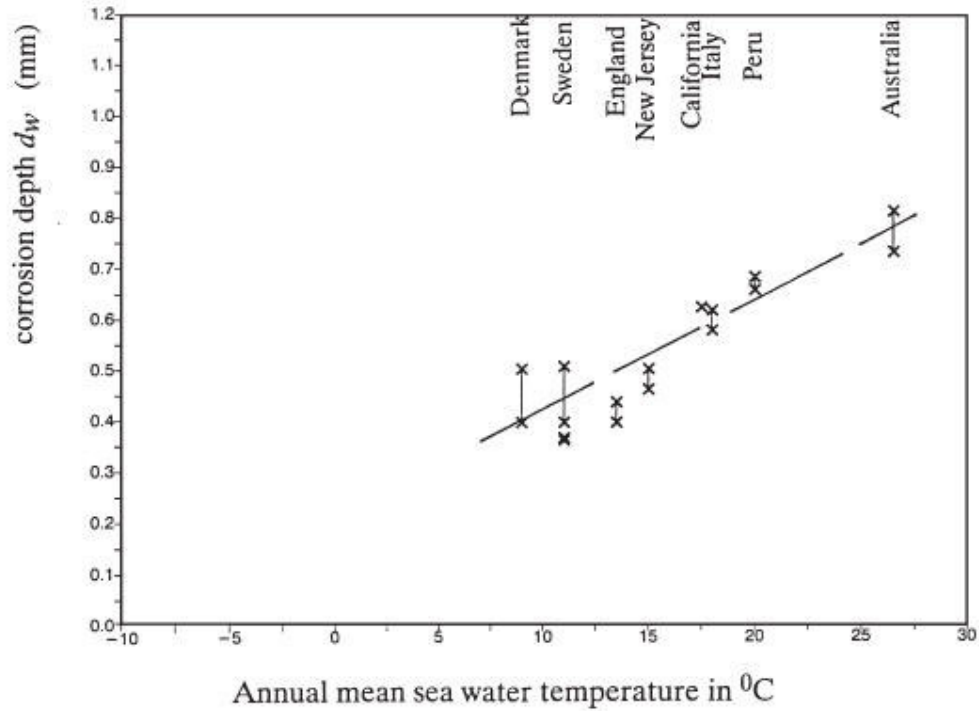


Fig. 3.1. Five years of corrosion as a function of annual mean water temperature [17]

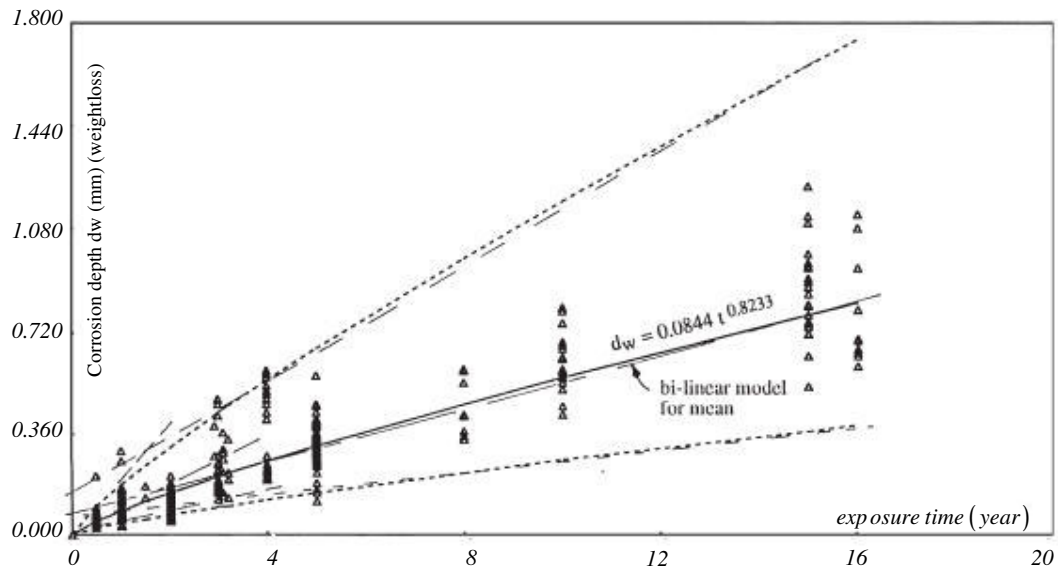


Fig. 3.2. Corrosion data points for field exposed specimens [17]

By adopting a bi-linear model [19], a mean value $\mu_d(t)$ and an associated standard deviation function $\sigma_d(t)$ with expected corrosion depth at any time t , are given by:

$$\mu_d(t) = 0.09t \quad 0 < t < 1.46 \text{ years} \quad (\text{Eq.3.2})$$

$$\mu_d(t) = 0.076 + 0.038t \quad 1.46 < t < 16 \text{ years} \quad (\text{Eq.3.3})$$

$$\sigma_d(t) = 0.062t \quad 0 < t < 1.46 \text{ years} \quad (\text{Eq.3.4})$$

$$\sigma_d(t) = 0.035 + 0.017t \quad 1.46 < t < 16 \text{ years} \quad (\text{Eq.3.5})$$

By using a non-linear model [17, 20], the equation is given by:

$$d_w(t) = \mu_d(t) = 0.084t^{0.823} \quad (\text{Eq.3.6})$$

$$\sigma_d(t) = 0.056t^{0.823} \quad (\text{Eq.3.7})$$

He also introduced a corrosion-time relationship showing various characteristic controlling phases as illustrated in Fig. 3.3 [21-23].

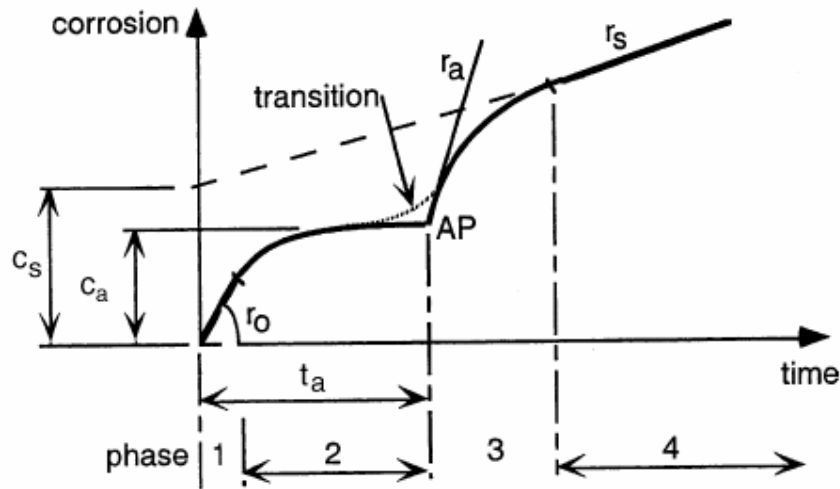


Fig. 3.3. Multiphase corrosion time model [22]

Fig. 3.3 illustrates corrosion modelled as four consecutive controlling phases. The kinetic Phase 1 shows a linear function. As corrosion proceeds the rust layer increases in depth and a nonlinear Phase 2 commences when the rust layer has so impeded the diffusion of oxygen through it to the basic metal such that it controls the subsequent rate of the corrosion process. Consequently, the corrosion rate reduces as the rust layer increases in thickness. This is called “diffusion control”. Eventually the rate of diffusion of oxygen through the rust layer becomes so small that anaerobic conditions begin to set in at the corroding surface. Corrosion controlled by anaerobic conditions is modelled as commencing with Phase 3, which defines an initial period of rapid growth of *sulphate reducing bacteria (SRB)* and a relatively high corrosion rate. Finally Phase 4 shows a more gradual linear function, so called the longer term *SRB* corrosion range. In general the corrosion rate r_s under anaerobic conditions increases both with increasing carbon content, in the range 0.04 ~ 0.5%, and average seawater temperature between 10 and 28°C .

3.3.2 Guedes Soares and Garbatov’s model

Soares and Garbatov [24] proposed a time-dependent model of corrosion degradation. They separated the corrosion process into three phases. Phase 1 assumes that there is no corrosion taking place owing to the applied paint or other similar

protection of metal surfaces and which it is assumed that it works properly. This is illustrated $t \in [O', O]$ in Fig. 3.4.

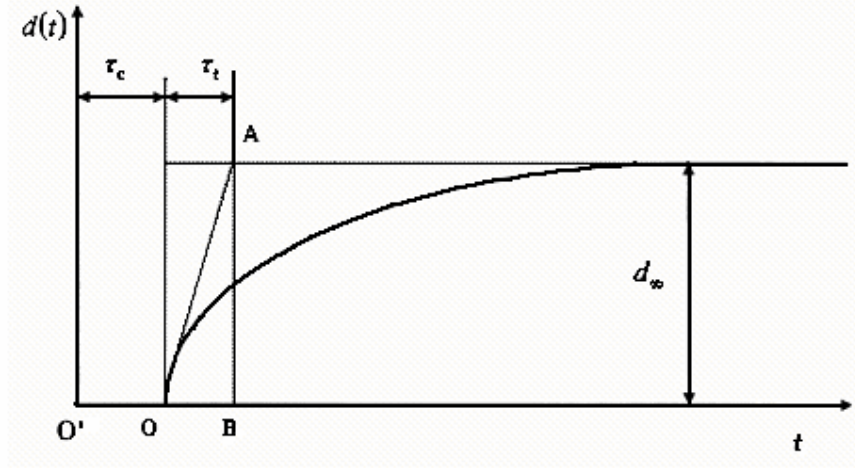


Fig. 3.4. Thickness of corrosion wastage as a function of time [24]

Phase 2 is initiated when the corrosion protection is damaged and metal surface corrosion starts to decrease the thickness of the plate, $t \in [O, B]$. The Phase 3 corresponds to a stop in the corrosion process and the corrosion rate becomes effectively zero caused by heavy corrosion products on the plate surface, ($t > B$) in Fig. 3.4. If the corrosion products are removed, for example by impact load, vibration or tank cleaning, from a surface, it originates the new start of the non-linear corrosion growth process, effectively opening-up a new fresh surface to the corrosive environment. The model was developed by the solution of a differential equation of the corrosion wastage process.

$$d_{\infty} \dot{d}(t) + d(t) = d_{\infty} \quad (\text{Eq.3.8})$$

where d_{∞} denotes long term thickness of the corrosion wastage, $d(t)$ indicates the thickness of the corrosion wastage at time t and $\dot{d}(t)$ is the corrosion rate.

The solution of Eq.3.8 was found to have the general form:

$$d(t) = d_{\infty} (1 - e^{-t/\tau_i}) \quad (\text{Eq.3.9})$$

and the particular solution leads to:

$$d(t) = d_{\infty} (1 - e^{-(t-\tau_c)/\tau_i}), \quad t > \tau_c \quad (\text{Eq.3.10})$$

$$d(t) = 0, \quad t \leq \tau_c \quad (\text{Eq.3.11})$$

where τ_c indicates the coating life and τ_i is the transition time

3.2.3 Paik and Thayamballi's model

Paik et al. [25-28] also assumed that there was no corrosion as long as the protective coating was effective and also that there was a short transition time for the full corrosion process to develop after breakdown of the coating. They categorized corrosion behaviour into three phases as (1) durability of coating, (2) transition to corrosion and (3) progress of corrosion. These phases are shown in Fig. 3.5.

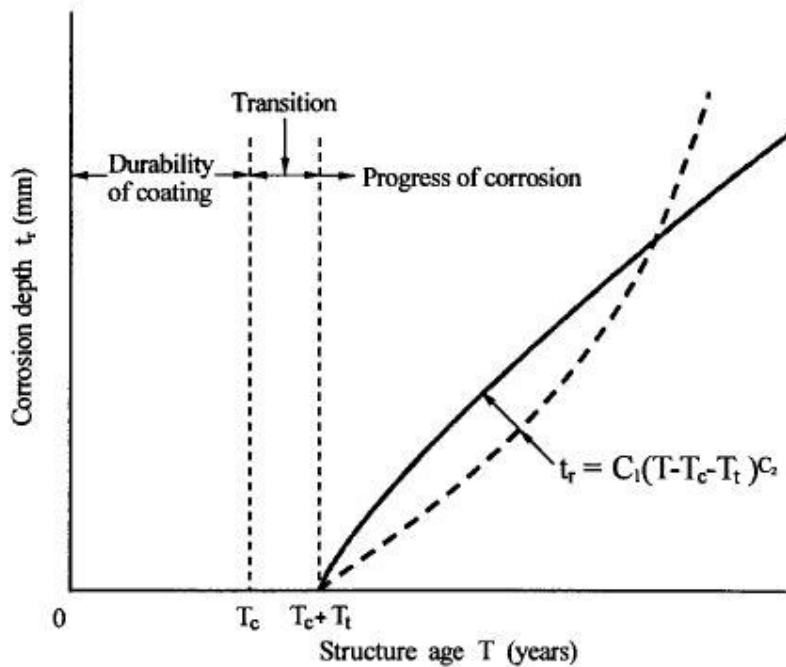


Fig. 3.5. A schematic of the corrosion process for steel structure [27]

The life of a coating depends on the type and quality of the coating system, type of cargoes, temperature, humidity and relevant maintenance and other factors which are described in Chapter 2. The effective life of coating to a predefined state of breakdown at which corrosion initiation can be said to follow the log-normal distribution and is given by [25, 27]:

$$f(T_c) = \frac{1}{\sqrt{2\pi}\sigma_c} \exp\left[-\frac{(\ln T_c - \mu_c)^2}{2\sigma_c^2}\right] \quad (\text{Eq.3.11})$$

where μ_c is mean value of $\ln T_c$ in years, σ_c denotes standard deviation of $\ln T_c$ and T_c represents coating life in years.

The coating life T_c is usually assumed to be either 5 years, 7.5 years or 10 years [26, 29].

The reduction of plate thickness due to corrosion may be generally expressed as a function of the time (years) after corrosion starts [25, 28], can be given by:

$$t_r = C_1 T_e^{C_2} \quad (\text{Eq.3.12})$$

where t_r represents corrosion depth in mm, T_e denotes exposure time in years, after breakdown of coating ($= T - T_c - T_t$), T indicates age of vessel in years, T_c is life of coating in years, T_t means duration of transition in years ($=$ pessimistically 0) and $C_1, C_2 =$ coefficient

Paik et al. [28] proposed a corrosion wastage model for ballast tanks based on a total of 1937 corrosion data sets measured in seawater ballast tanks, as follows:

$$t_r = \begin{aligned} &= \text{corrosion depth in mm} \\ &= 0.0466(T - 5.0) \text{ for } T_c = 5 \text{ years} \end{aligned} \quad (\text{Eq.3.13})$$

$$= 0.0579(T - 7.5) \text{ for } T_c = 7.5 \text{ years} \quad (\text{Eq.3.14})$$

$$= 0.0823(T - 10.0) \text{ for } T_c = 10 \text{ years} \quad (\text{Eq.3.15})$$

When only the corrosion data for the 95% and above band is used, they proposed severe (upper bound) corrosion trends to be given by:

$$t_r = \begin{aligned} &= \text{corrosion depth in mm based on 95\% and above band} \\ &= 0.1469(T - 5.0) \text{ for } T_c = 5 \text{ years} \end{aligned} \quad (\text{Eq.3.16})$$

$$= 0.1938(T - 7.5) \text{ for } T_c = 7.5 \text{ years} \quad (\text{Eq.3.17})$$

$$= 0.2894(T - 10.0) \text{ for } T_c = 10 \text{ years} \quad (\text{Eq.3.18})$$

Fig. 3.6 shows the “95% and above band” wastage model and Fig. 3.7 indicates the comparison of annualized corrosion rate formulations.

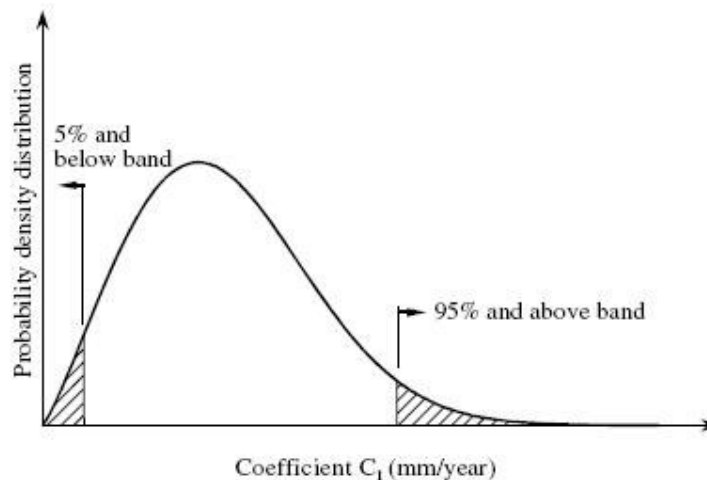


Fig. 3.6. The 95% and above band for corrosion wastage model [28]

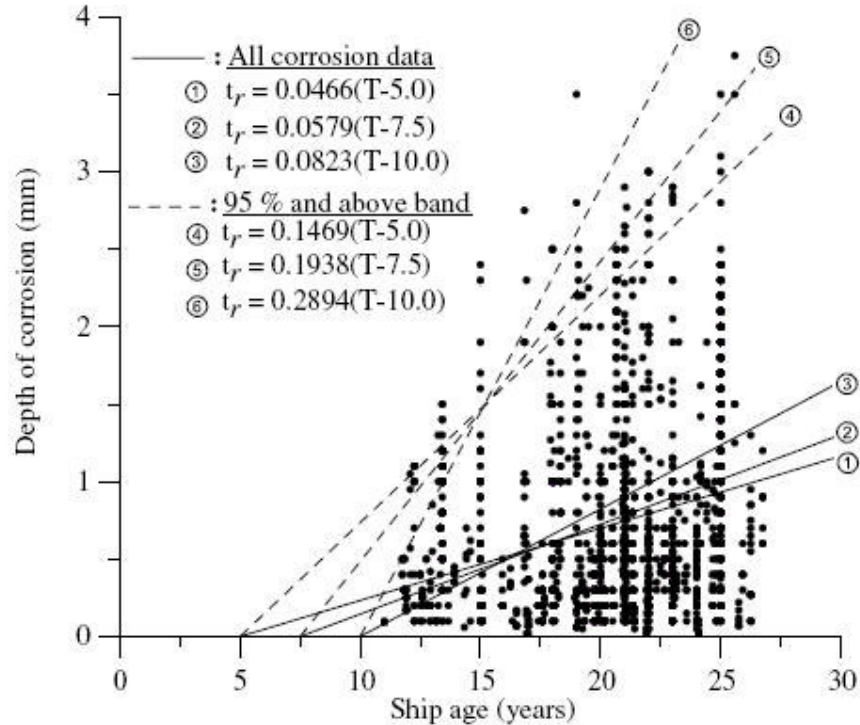


Fig. 3.7. Corrosion rate formulations and data for sea water ballast tanks [28]

3.2.4 Qin and Cui's model

Qin and Cui [30] also introduced similar three stages for the whole corrosion process model. *Phase 1* assumes that there is no corrosion while the corrosion protection system is fully effective; *Phase 2* denotes that corrosion is developing and accelerating when the pitting corrosion generates and progresses; and *Phase 3* indicates the overall corrosion rate is decelerating due to the increasing thickness of the corrosion products inhibiting further formation at the metal surface.

They recommend a combined model which can accommodate other existing corrosion models such as those suggested by *Melchers* [17], *Soares and Garbatov* [24] and *Paik et al.* [25, 31].

3.2.5 Average model for marine immersed general corrosion

Due to there being so much scatter in the pattern of the measured data that forms the basis for each corrosion model, there is no clear and unambiguous answer which to consider as a standard model for marine immersed steel structures. The data, on which each of the existing models has been developed, may not have been collected according to some common well established and agreed-upon process, e.g. type of equipment, skills of the technicians, etc. It is considered that the best way is to evaluate each of existing corrosion models and to adopt an "average" model from the various models in order to reduce uncertainty of data from individual models.

Ok and Pu [32] proposed an “average” model which was developed from the following models:

- Melchers’s model [17, 20]
- Soares and Garbatov’s model [24, 33]
- Wang *et al.*’s model [34]
- Paik *et al.*’s model [28]

Soares and Garbatov [24], Wang *et al.* [34] and Paik *et al.* [28] models introduced a coating effective life, however Melchers [17, 20] model did not consider coating effective life and assumed that the corrosion process started immediately after the construction of the vessel. In this study, every model is considered to have 5 years of effective coating life and Melchers’s [17, 20] model has been modified and corrected to assume an equivalent initial period based upon 5 years of effective coating life. The Soares and Garbatov’s [24] model is assumed to have a transition time(τ_i) of 10 years and that the long term thickness of the corrosion wastage(d_∞) is 1.5mm. In addition, the side shell plate component is selected from Wang *et al.*’s [34] model in order to evaluate marine immersion corrosion model.

Fig.3.8 illustrates combined time dependant corrosion degradation values based on the selected corrosion models.

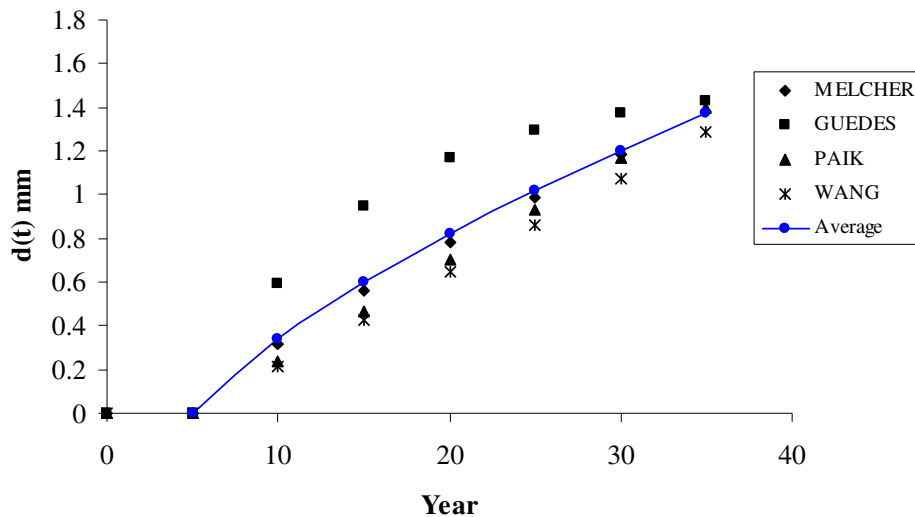


Fig. 3.8. Time dependant average general corrosion degradation model

Finally, the equation of average marine immersion model can be calculated and given by:

$$d(t) = \text{corrosion depth in mm}$$

$$= 0 \quad \text{for } 0 < T \leq 5 \text{ years (Eq.3.19)}$$

$$= -0.319 + 0.0699 T - 0.00063 T^2 \quad \text{for } 5 \text{ years} < T \quad \text{(Eq.3.20)}$$

3.3 Pitting corrosion estimation model

Pitting corrosion is a highly localized form of attack which occurs randomly. Normally it mostly prevails in the aftermost bays of ballast tanks and under bellmouths. Excessively deep pits and a large grouping of pitting corrosion may lead to a loss of local strength, thus degrading hull integrity and may result in serious pollution by eventual perforation of the plate.

TSCF [35] undertook a study to determine the strength of uniformly pitted plate models subjected to bending and with a range of uniform pitting intensities of 14 %, 23.5 % and 35.5 %, and together with uniform variation of pit depths from 5mm to 15.4mm. The results of the tests showed a 25.8 % maximum reduction in bending capacity for the plates analysed in the tests [36].

There are some models to estimate the effects of the occurrence of pitting corrosion in both depth and size. Among others following models can be considered as the most common and recently developed models.

3.3.1 Hutchinson and Bea's model

Hutchinson and Bea [37] proposed a fairly rudimentary model for predicting the equivalent reduced plate thickness with an assumed uniform pitting distribution based on the average volume and distribution density of pits given by:

$$T_{REDUCED} = \left(\frac{T_0 A_{Plate} - \rho_{A_{PIT}} V_{PIT}}{A_{Plate}} \right) \quad (\text{Eq.3.21})$$

where $T_{REDUCED}$ = equivalent reduced plate thickness with uniform pit distribution

T_0 = original plate thickness

A_{Plate} = plate area

$\rho_{A_{PIT}}$ = average area density of pits

V_{PIT} = average volume of pits

3.3.2 Daidola and Parente's model

Daidola et al. [36] developed a mathematical model based upon average, maximum values of pitting data and using the number of deepest pits. A 300 x 300mm square plate was used for their study as illustrated on Fig. 3.9.

They proposed a mathematical model using average and maximum pit data given by:

$$V = \sum_{i=1}^N c_i a_i d_i \quad (\text{Eq.3.22})$$

where V = volume loss of steel due to pitting

a_i = area of pit 'i'

- d_i = depth of pit 'i'
 c_i = cylinder coefficient, defined as the actual pit volume divided by the corresponding cylinder of depth d_i , and top area a_i .
 The parameter c_i has the range ($0 < c_i \leq 1.0$)
 w = pit width
 N = number of pits in the 300 x 300mm sample square

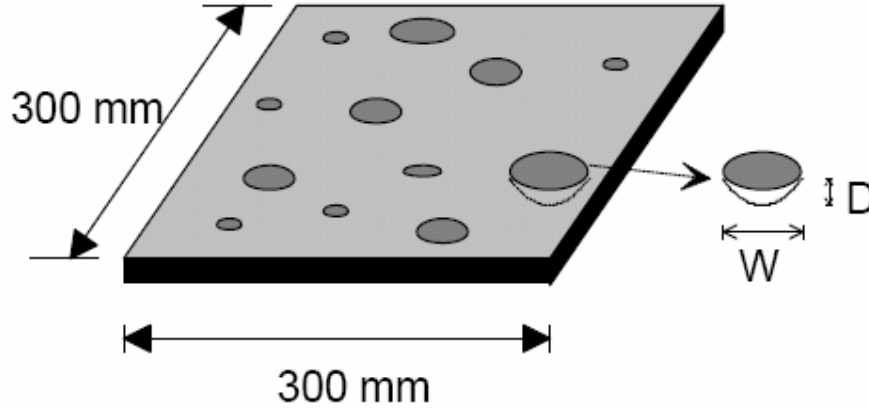


Fig. 3.9. A representative sample square of the typical inspected pitted panel [36]

To simplify Eq.3.22, if a constant cylinder coefficient and a round shape for all pits are assumed. The wasted steel volume, V , can be computed by the following equation:

$$V = c \sum_{i=1}^N \left(\frac{\pi}{4} w_i^2 d_i \right) \quad (\text{Eq.3.23})$$

If all pits are assumed to have a semi-spherical shape, the value of the cylinder coefficient can be obtained as:

$$c = \frac{V_{\text{semisphere}}}{V_{\text{cylinder}}} = \frac{\frac{1}{2} \left(\frac{1}{3} \pi w^2 d \right)}{\frac{1}{4} \pi w^2 d} = 0.667 \quad (\text{Eq.3.24})$$

They proposed and recommended that the total cross sectional area lost in any section of the pitted plate should not be more than 15%.

3.3.3 Paik's model

Paik et al. [38] carried out various experimental and numerical computations and introduced the degree of pit corrosion intensity (DOP), given by:

$$DOP = \alpha = \frac{1}{ab} \sum_{i=1}^n A_{pi} \times 100(\%) \quad (\text{Eq.3.25})$$

where DOP = the ratio percentage of the corroded surface area to the original plate surface area

n = number of pits

A_{pi} = surface area of the i th pit.

d_{ri} = diameter of i th pit

a = plate length

b = plate breadth

They found that the ultimate strength of a plate with pitting corrosion can be estimated using a strength knockdown factor, given by:

For uni-axial compression loading:

$$R_{xr} = \frac{\sigma_{xu}}{\sigma_{xuo}} = \left(\frac{A_o - A_r}{A_o} \right)^{0.73} \quad (\text{Eq.3.26})$$

Paik et al. [39] performed finite element modelling to find out ultimate edge shear strength for a pitted plate, expressed by:

$$\begin{aligned} R_{\tau r} = \frac{\tau_u}{\tau_{uo}} &= 1.0 && \text{for } \alpha \leq 1.0 \\ &= -0.18 \ln \alpha + 1.0 && \text{for } \alpha > 1.0 \end{aligned} \quad (\text{Eq.3.27})$$

where R_{xr} = a factor of ultimate compressive strength reduction due to pitting corrosion

$R_{\tau r}$ = a factor of ultimate shear strength reduction due to pitting corrosion

σ_{xu} = ultimate compressive strength for a member with pitting corrosion

σ_{xuo} = ultimate compressive strength for an intact (uncorroded) member

A_o = original cross sectional area of the intact member

A_r = cross sectional area involved by pit corrosion at the smallest cross section

τ_u = ultimate shear strength for a pitted plate

τ_{uo} = ultimate shear strength for an intact (uncorroded) plate

α = degree of pitting intensity (DOP)

They found out that the ultimate strength of a plate element can be significantly decreased due to pitting corrosion. The ultimate strength of a plate element with pit corrosion and under edge shear is governed by the DOP, whereas a pitted plate under axial compressive loads is governed by the smallest cross-sectional area of the most corroded (pitted) plate section.

3.3.4 TSCF's model

TSCF [7] proposed the following guidance for evaluating the minimum remaining plate thickness in pits for pitting density < 20% as follows:

Table 3-1
Guidance on minimum remaining plate thickness in pits

Structural component	Normally no action is required when the following conditions are fulfilled
Bottom plate	$t_{\min} \geq 2/3 \times t_0$
Webs of horizontal members (Stringers, longitudinals etc.)	$t_{\min} \geq 1/2 \times t_0$

where t_{\min} is minimum acceptable remaining thickness and t_0 denotes original thickness or rule thickness

TSCF [40] also reported based on some single hull tankers of less than 5 years old, the average pit depth was found to be 2 to 3 mm, with a density of around 200 to 400 pits per m^2 and a maximum pit depth of 5 mm. The accelerated pitting corrosion rates that were experienced were as high as 5 times the normally anticipated rates, and these experiences were thought to be due largely to *Microbial Influenced Corrosion (MIC)* attack.

TSCF Working Group 2 [40] carried out a survey involving 111 existing tankers and released the results as following in Table 3-2 and Table 3-3.

Table 3-2
Experience with bottom pitting (maximum depth)

Maximum Depth / Years in Service	Coated Area				Uncoated Area			
	5 year	10	15	20 +	5 year	10	15	20 +
0.5 mm	36%	46%	18%	0%	25%	22%	22%	0%
5 – 10 mm	46%	63%	55%	27%	75%	73%	78%	20%
10 – 15 mm	18%	25%	5%	46%	0%	0	0%	40%
15 – 20 mm	0 %	0%	0%	27%	0%	0	0%	40%

Table 3-3
Experience with bottom pitting (average depth)

Average Depth / Years in Service	Coated Area				Uncoated Area			
	5 year	10	15	20 +	5 year	10	15	20 +
0.3 mm	50%	25%	64%	9%	69%	15%	22%	0%
3 – 5 mm	50%	38%	18%	9%	19%	77%	67%	20%
5 – 7 mm	0%	37%	18%	64%	12%	7	11%	60%
7 – 10 mm	0 %	0%	0%	18%	0%	0	0%	20%

3.3.5 IACS recommendation

IACS [41] recommends that if pitting intensity is higher than 15% in area, thickness measurements should be taken to check pitting corrosion. The minimum acceptable remaining thickness in pits or grooves is equal to:

- 75% of the as-built thickness, for pitting or grooving in frames and in bracket webs and flanges,
- 70% of the as-built thickness, for pitting or grooving in the side shell, hopper tank and top side tank plating attached to the side frame, over a width up to 30 mm from each side of it.

Recently IACS [16] introduced the assessment of local wastage in “Common Structural Rules for Double Hull Oil Tankers”, Section 12, 1.6. It requires steel renewal for pitting, grooving and edge corrosion if the measured thickness is less than the criteria defined in rules.

For plate with pitting intensity less than 20% and the overall corroded height of the edge corrosion of the flange, or web in the case of flat bar stiffeners, is less than 25% of the stiffener flange breadth or web height, the measured thickness, t_m , of any individual measurement is to meet the lesser of the following criteria:

$$t_m \geq 0.7(t_{as-built} - t_{own}) \text{ mm} \quad (\text{Eq.3.28})$$

$$t_m \geq t_{ren} - 1 \text{ mm} \quad (\text{Eq.3.29})$$

where $t_{as-built}$ denotes as built thickness of the member, t_{own} means owner/builder specified additional wastage allowance, t_{ren} is renewal criteria for general corrosion ($= t_{as-built} - t_{was} - t_{own} - t_{corr-2.5}$), t_{was} indicates wastage allowance and $t_{corr-2.5}$ is 0.5mm.

Where the groove breadth is a maximum of 15% of the web height, but not more than 30mm, the measured thickness, t_m , in the grooved area is to meet the lesser of the Eq.3.28 and following criteria, but not less than 6 mm:

$$t_m \geq t_{ren} - 0.5 \text{ mm} \quad (\text{Eq.3.30})$$

3.4 General corrosion estimation models for specific regions

Recently several general corrosion models have been proposed in order to estimate the corrosion degradation rates in various regions within tanker structures. The *Tanker Structure Co-operative Forum* presented various corrosion data based on thickness measurements carried out on 54 oil tankers [6] and issued guidance on corrosion control for tankers [7].

The *Tanker Structure Co-operative Forum Work Group 2* [40], lead by the *Chevron Shipping Company*, undertook further surveys for corrosion rate data among 111 oil

tankers and proposed new corrosion data against *TSCF 1992* [6]. However neither *TSCF 1992* [6] and *TSCF 2000* [40] considered the durability of coating life.

Kawano and Hirakata [12] introduced 5 years, 10 years, 15 years and 20 years corrosion rate predictions for tanker structures based on a *Class NK* database. *Paik et al.* [26] presented corrosion measurement data obtained from 230 aged ocean going single hull tankers with a total of 33,820 individual measurements for 34 different structural member groups. In their paper they introduced corrosion wastage mean values based on 5, 7.5 and 10 years coating breakdown time. *Wang et al.* [29, 34] investigated the corrosion rates of structural members in oil tankers based on a corrosion wastage database of over 110,000 individual thickness measurements from 140 single hull oil tankers and assumed that there was no corrosion during the first five years of service (an assumed coating effective period).

Recently *Ok and Pu* [42] investigated various existing general corrosion models for tanker structures and compared the time variant neutral axis, section modulus at deck and keel based on various years of service. Simplified formulas to estimate time variant vertical/horizontal section modulus degradation and stress changes at both upper deck and keel were developed based on the double hull tanker.

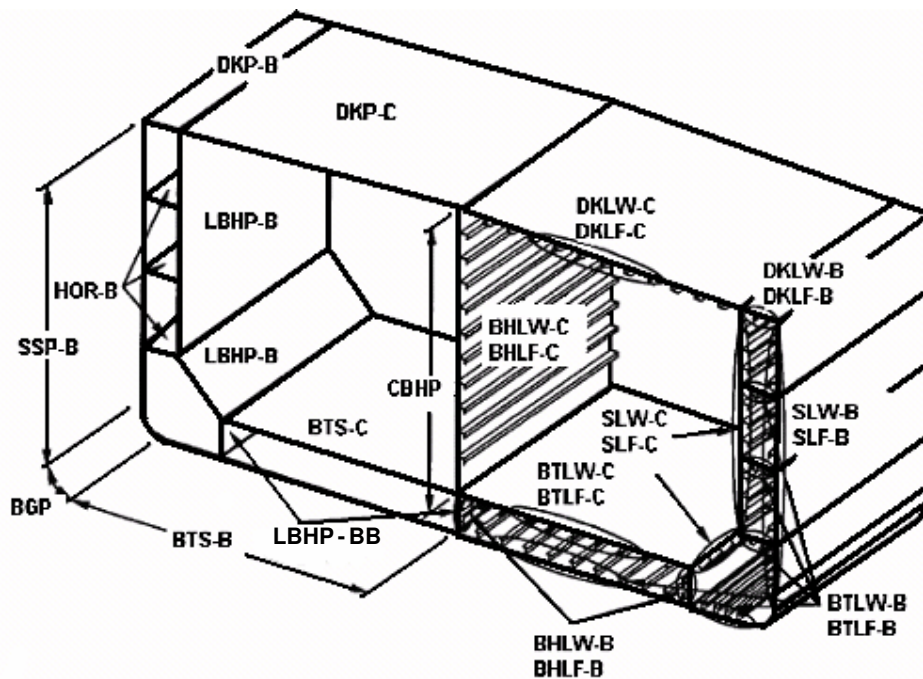


Fig.3.10. The name of individual double hull tanker structural components

Among the various corrosion models that have been published, *TSCF 1992* [6] and *TSCF 2000* [40] did not consider coating effective periods and assumed that corrosion started immediately after construction of the vessel. Whereas the *Paik et al.* [26] and *Wang et al.* [34] models can each be considered to be one of the latest and more

detailed corrosion models which include coating effective periods. However both models do not show similar corrosion rates and there are large differences in values between these two models as shown in Table 3-4. It is also found that Paik et al. model shows higher corrosion rates for upper deck plate and deck longitudinal web in ballast tank than in cargo tank, whereas Wang et al. model indicates higher corrosion rates in cargo tank than in ballast tank.

Table 3-4, which is a compilation of the above data, shows that there is considerable scatter in the data between each corrosion model even though the same area and structure are referred to. This is because there are so many corrosion uncertainties and different corrosion environments in each ship as well as potential variations in actual measurement practices.

In this study, oil tanker structures are sub-divided into 27 individual components as shown in Fig. 3.10 and Table 3-4.

Table 3-4
Comparison of existing general corrosion models

NO	STRUCTURE		TSCF 1992 [6]	TSCF 2000 [40] mean/max	PAIK [26] 5 year/7.5 year mean value	WANG [34] 5 years mean / max
1	DKP-C	Cargo	0.03-0.10	0.057/0.2174	0.0489/0.0581	0.066/0.580
2	DKP-B	Ballast	0.10-0.50	-	0.0824/0.1084	0.055/0.277
3	DKLW-C	Cargo	0.03-0.10	0.018/0.0874	0.0620/0.0716	0.055/0.807
4	DKLW-B	Ballast	0.25-1.00	-	0.2081/0.2403	0.047/0.444
5	DKLF-C	Cargo	-	0.04/0.0404	0.0509/0.0588	0.037/0.243
6	DKLF-B	Ballast	-	-	0.0764/0.0882 *	0.044/0.175
7	SSP-C	Cargo	0.03	0.02/0.0688	0.0444/0.0523	0.044/0.547
8	SSP-B	Ballast	0.06-0.10	-	0.0552/0.0661	0.043/0.573
9	SLW-C	Cargo	0.03	0.011/0.0454	0.1697/0.1960	0.040/0.567
10	SLW-B	Ballast	0.10-0.25	-	0.1224/0.1413	0.042/0.800
11	SLF-C	Cargo	-	0.007/0.0284	0.1543/0.1782	0.033/0.171
12	SLF-B	Ballast	-	-	0.0764/0.0882	0.032/0.482
13	BTS-C	Cargo	0.04-0.10	0.09/0.1264	0.0526/0.0607	0.085/0.690
14	BTS-B	Ballast	0.04-0.10	-	0.0518/0.0597	0.049/0.320
15	BTLW-C	Under Cargo	-	-	0.1697 /0.1960	0.032/0.207 *
16	BTLW-B	Ballast	-	-	0.1184/0.1367	0.027/0.117
17	BTLF-C	Under Cargo	0.20-0.60	-	0.1543/0.1782	0.047/0.730
18	BTLF-B	Ballast	-	-	0.0976/0.1127	0.045/0.700
19	CBHP-C	Cargo	0.03	0.037/0.1272	0.0475/0.0577	0.049/0.654
20	LBHP-B	Ballast	0.10-0.30	-	0.0792/0.1012	0.051/0.470
21	LBHP-BB	Ballast	0.10-0.30	-	0.1111/0.1408	0.051/0.470 *
22	BHLW-C	Cargo	0.03	0.009/0.044	0.0476/0.0550	0.038/0.411
23	BHLW-B	Ballast	0.20-1.20	-	0.1224/0.1413	0.042/0.800 *
24	BHLF-C	Cargo	-	0.019/0.0778	0.0440/0.0508	0.045/0.782
25	BHLF-B	Ballast	0.20-0.60	-	0.0764/0.0882	0.032/0.482 *
26	BGP	Ballast	-	0.02/0.0688 *	0.0539/0.0619	0.043/0.573 *
27	HOR-B	Ballast	-	-	0.1111/0.1408	0.051/0.470 *

Note) The values of * marked structural components are selected from same location with similar structural components.

Abbreviations)

C / COT	: Cargo oil tank
B / WBT	: Water ballast tank
DKP	: Deck plate
DKLW	: Deck longitudinal web
DKLF	: Deck longitudinal flange
SSP	: Side shell plate
SLW	: Side longitudinal web
SLF	: Side longitudinal flange
BTS	: Bottom shell
BTLW	: Bottom longitudinal web
BTLF	: Bottom longitudinal flange
LBHP	: Longitudinal bulkhead
CBHP	: Longitudinal centre bulkhead
BHLW	: Bulkhead longitudinal web
BHLF	: Bulkhead longitudinal flange
BGP	: Side shell bilge plate
HOR-B	: Horizontal stringer, outboard and centre girder in ballast tank

Fig. 3.11 illustrates average corrosion rates for each structural member which is based on Table 3-4. The results indicate that the highest corroded structural components is deck longitudinal web in ballast tank based on Paik et al. model, whereas bottom shell in cargo tank based on TSCF [40] and Wang et al. models. Generally the Paik et al. model shows higher corrosion degradation rates than does the TSCF [40] and Wang et al. models.

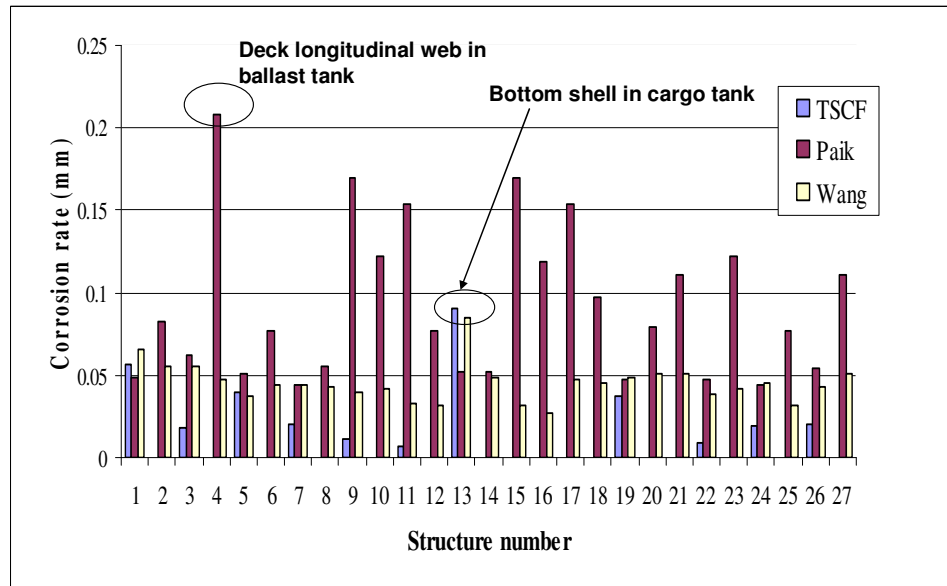


Fig. 3.11. Corrosion rate in each structural component (27 components)

According to some recent studies, it is clear that the corrosion rates of double hull tanker structures are less than those of single hull tankers.

Yoneya *et al.* [43] introduced the following comparison of corrosion levels corresponding to 95% cumulative probability at 20 years operational life and made between *Post-MARPOL* and *Pre-MARPOL* tankers as following Table 3-5:

Table 3-5

Corrosion of structural members in *Post-MARPOL* and *Pre-MARPOL* ships

Member	Post – MARPOL (mm)		Pre-MARPOL (mm)	
	COT	WBT	COT	WBT
Upper Deck	3.14	1.92	3.22	2.78
Side Shell	1.92	2.09	2.66	1.59
Bottom Plate	3.27	2.96	5.62	3.44
Longitudinal BHD plate	1.96	1.95	2.91	3.24
Side longitudinal face	1.8	1.75	2.65	2.69
Bottom longitudinal face	1.94	1.77	2.84	2.79

The *Tanker Structure Co-operative Forum Work Group 3* by Bergesen D.Y. ASA [44] presented corrosion rate data from three double hull VLCCs as following Table 3-6:

Table 3-6

Summary of plate thickness diminution

Structure	Average annual diminution (mm/year)	
	3 years	5 years
Upper deck plate	0.07	0.06
Deck longi.(web) upper	0.12	-
Deck longi.(web) lower	0.10	-
Deck longi.(web) average	0.11	0.07
Deck longi.(face)	0.07	0.04
T. BHD plate	0.04	0.02
Transverse web frame plate	0.04	0.02
Tank top plate	0.02	0.05
Vertical stiffener on T. BHD(web)	0.04	0.03
Vertical stiffener on T. BHD(face)	0.06	0.05
Swash BHD plate	0.00	-
Inner L. BHD plate	0.02	0.02
Outer L. BHD plate	0.02	0.02

3.5 Section Modulus Degradation Model

The ultimate longitudinal bending moment capacity could be calculated by any one of following methods [13]:

- Assessment method using simplified equations
- Assessment method using cross-section moment

- Assessment method by direct calculation using analysis codes
- Assessment of ultimate hull girder strength

If the assessment of ultimate hull girder strength method is considered, the total longitudinal bending moment in extreme conditions should not exceed the moment capacity of hull transverse section, M_u , in the hogging and sagging conditions, expressed by:

$$|M_s + M_w| \leq \frac{M_u}{\eta} \quad (kN-m) \quad (\text{Eq.3.31})$$

where M_s is a longitudinal bending moment in still water, M_w represents a wave-induced longitudinal bending moment in extreme sea conditions and η denotes safety factor.

All longitudinal surfaces must be completed with initial scantlings and steel grade selection. The designer may need to consider if each panel is fully effective for contribution to hull girder strength and undertake full hull girder cross-section area property calculations.

The location of neutral axis of the hull transverse cross section above the base line can be calculated as follows:

$$H_{NA} = \frac{\sum a_i h_i}{\sum a_i} \quad (\text{Eq.3.32})$$

where a_i = cross sectional area of the i th structural member
 h_i = distance of i th structural member from the base line

From the parallel axis theorem, the moment of inertia of the hull cross section is expressed by:

$$I_y = \sum a_i (h_i - H_{NA})^2 + \sum k_i \quad (\text{Eq.3.33})$$

where k_i = local moment of inertia for each member

Finally the section modulus at deck (Z_D) and at keel (Z_K) are given by:

$$Z_D = \frac{I_y}{D - H_{NA}} \quad (\text{Eq.3.34})$$

$$Z_K = \frac{I_y}{H_{NA}} \quad (\text{Eq.3.35})$$

where D = Depth of ship (m)

Hull girder section modulus represents a measurement of the ship's longitudinal strength and the section modulus should be always greater than the rule requirement. The value of hull girder section modulus will be decreasing with time due to corrosion progress in ageing ship structures, consequently stress levels of local members will also be increased over the design life. However it is time consuming and routine work to calculate the section modulus repeatedly, so it is advantageous to develop a model to estimate time dependent section modulus degradation which considers annual corrosion degradation in ageing ships not only for initial corrosion margins in design stage but also for estimating future maintenance period.

3.5.1 Vertical section modulus degradation model

Based on various corrosion models as examined earlier [26, 34, 40], the progressive time related changing of the vertical and horizontal section modulus values are investigated for an existing *AFRAMAX Double Hull Tanker* (L=219.08m, B=42.0m, D=21.3m). For these calculations, an additional average corrosion rate model is also proposed as follows:

- PW model : Average of *Paik et al.* [26] and *Wang et al.* [34] models

where H_{NA0} : Initial distance of the neutral axis above base line (=9.142 m)

H_{NA} : Distance of the neutral axis allowing for corrosion

Z_{DO} : Initial section modulus at deck (=28.86 m³)

Z_{DC} : Reduced section modulus at deck

Z_{KO} : Initial section modulus at keel (=38.379 m³)

Z_{KC} : Reduced section modulus at keel

T : Ship's age

The corrosion data from Paik's et al and Wang's et al. models are all collected from ageing single hull tankers. Fig. 3.11 indicates statistical uncertainty and huge differences in corrosion rates between Paik et al. and Wang et al. models for each structural member. Generally Paik's et al. model shows much higher corrosion degradation rate than other models. However some recent studies have revealed that the corrosion rate of double hull tankers is much lower than that of single hull tankers [43, 44]. This means that Paik's model could be too conservative to be adopted for double hull tankers, thus it is reasonable to propose an average model as an alternative corrosion degradation model for double hull tankers.

3.5.1.1 Section modulus at deck

Fig. 3.12 shows the time related changes in the vertical section modulus for the deck structure according to *Paik et al.* [26], *Wang et al.* [34] and *PW* models. *Paik et al.*'s model results in a smaller section modulus at deck than *Wang et al.*'s model. The *PW* model can be proposed as an average model of section modulus reduction at deck. Figs. 3.12 and 3.13 show that section modulus predicted by all the three degradation models is above the requirement of *IACS* [45] recommendation up to 35 years.

Table 3-7
Comparisons of the section modulus at deck

Corrosion Model / Ship's Age	10 years	15 years	20 years	25 years	30 years	35 years	
PAIK 2003	Z_{DC}	27.68 m^3	27.02 m^3	26.36 m^3	25.69 m^3	25.03 m^3	24.37 m^3
	Z_{DC} / Z_{DO}	0.9590	0.9361	0.9132	0.8903	0.8674	0.8445
WANG 2003	Z_{DC}	27.80 m^3	27.27 m^3	26.73 m^3	26.20 m^3	25.67 m^3	25.13 m^3
	Z_{DC} / Z_{DO}	0.9634	0.9448	0.9263	0.9078	0.8893	0.8708
PW	Z_{DC}	27.75 m^3	27.15 m^3	26.56 m^3	25.97 m^3	25.38 m^3	24.79 m^3
	Z_{DC} / Z_{DO}	0.9614	0.9409	0.9203	0.8998	0.8793	0.8588

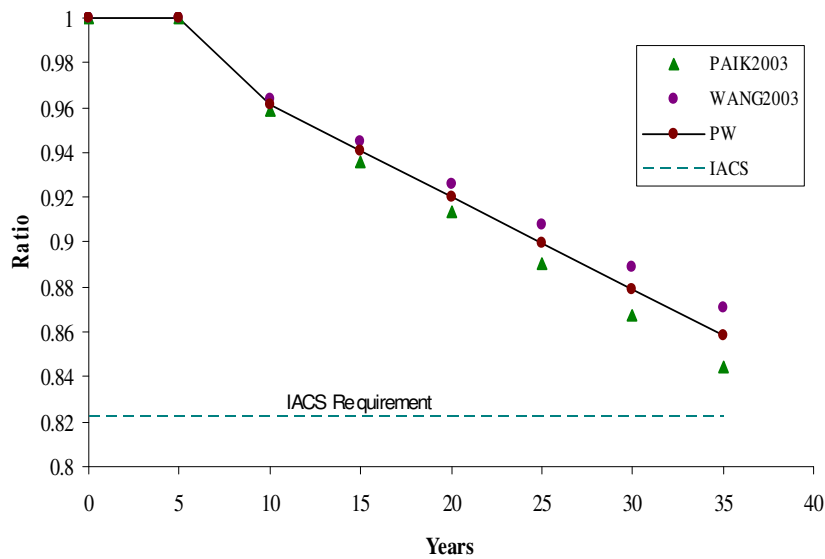


Fig. 3.12. Time variant section modulus changes at deck

The time dependent average section modulus reduction ratio (Z_{DC} / Z_{DO}) based on Paik *et al.*, Wang *et al.* and PW models are derived by curve fitting as in Table 3-8:

Table 3-8
Equations of section modulus degradation models at deck

Model / Year	$\geq 5 \text{ years}$	$5 < T \leq 35 \text{ years}$
Paik 2003d	1	$1.0281 - 0.0067T + 0.00004T^2$
Wang 2003c	1	$1.0237 - 0.0058T + 0.00004T^2$
PW	1	$1.0257 - 0.0062T + 0.00004T^2$

3.5.1.2 Section modulus at keel

As shown in Fig. 3.13, Paik *et al.* model is a more pessimistic model than Wang *et al.* model of section modulus reduction at keel. The PW model can also be proposed as an average model of section modulus reduction at keel.

Table 3-9
Comparison of the section modulus at keel

Corrosion Model / Ship's Age		10 years	15 years	20 years	25 years	30 years	35 years
PAIK 2003	Z_K	36.22 m ³	35.25 m ³	34.28 m ³	33.30 m ³	32.33 m ³	31.35 m ³
	Z_K / Z_{K0}	0.9438	0.9184	0.8931	0.8677	0.8423	0.8169
WANG 2003	Z_K	36.58 m ³	35.96 m ³	35.34 m ³	34.73 m ³	34.11 m ³	33.49 m ³
	Z_K / Z_{K0}	0.9530	0.9370	0.9209	0.9048	0.8887	0.8726
PW	Z_K	36.42 m ³	35.65 m ³	34.88 m ³	34.11 m ³	33.33 m ³	32.56 m ³
	Z_K / Z_{K0}	0.9490	0.9289	0.9088	0.8886	0.8685	0.8484

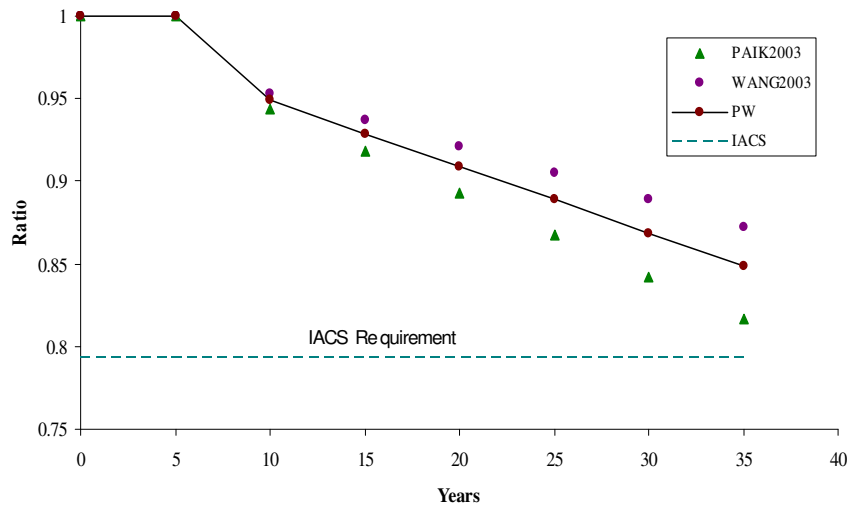


Fig. 3.13. Time variant section modulus changes at keel

The time dependent average section modulus reduction ratio (Z_{DC}/Z_{D0}) based on Paik *et al.* [26], Wang *et al.* [34] and PW models are derived as in Table 3-10:

Table 3-10
Equations of section modulus degradation models at keel

Model / Year	≥ 5 years	$5 < T \leq 35$ years
Paik 2003d	1	$1.0341 - 0.0087T + 0.000073T^2$
Wang 2003c	1	$1.05576 - 0.01385T + 0.00049T^2 - 0.000007T^3$
PW	1	$1.05974 - 0.01464T + 0.00048T^2 - 0.0000068T^3$

3.5.2 Horizontal section modulus degradation model at ship side shell

Based on various corrosion models [26, 34], The horizontal section modulus at ship side shell (starboard) was investigated on *AFRAMAX Double Hull Tanker* model.

Table 3-11 and Fig. 3.14 show the horizontal section modulus degradation pattern at ship side shell based on *Paik et al.* [26], *Wang et al.* [34] and the average (PW) models.

Table 3-11

Comparison of the horizontal section modulus at ship side shell

Corrosion Model / Ship's Age		10 years	15 years	20 years	25 years	30 years	35 years
PAIK 2003	Z_{S2}	46.28 m^3	45.03 m^3	43.79 m^3	42.56 m^3	41.29 m^3	40.04 m^3
	$Z_{S2} / Z_{S0,2}$	0.9460	0.9204	0.8949	0.8694	0.8438	0.8183
WANG 2003	Z_{S2}	46.75 m^3	45.98 m^3	45.20 m^3	44.42 m^3	43.638 m^3	42.86 m^3
	$Z_{S2} / Z_{S0,2}$	0.9556	0.9397	0.9237	0.9078	0.8919	0.8760
PW	Z_{S2}	46.50 m^3	45.47 m^3	44.44 m^3	43.40 m^3	42.37 m^3	41.34 m^3
	$Z_{S2} / Z_{S0,2}$	0.9504	0.9293	0.9082	0.8871	0.8660	0.8449

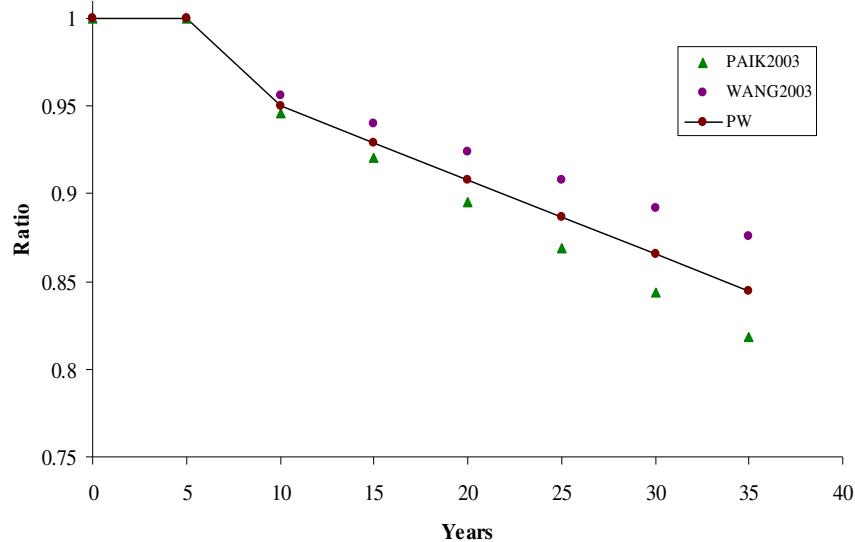


Fig. 3.14. Time variant section modulus changes at ship side shell

The time dependent average section modulus reduction ratio ($Z_{S2} / Z_{S0,2}$) based on Paik et al. [26], Wang et al. [34] and PW models can be expressed as following Table 3-12:

Table 3-12

Equations of section modulus degradation models at ship side shell

Model / Year	≥ 5 years	$5 < T \leq 35$ years
Paik 2003d	I	$1.0622 - 0.01493T + 0.00044T^2 - 0.0000063T^3$
Wang 2003c	I	$1.0525 - 0.01298T + 0.00045T^2 - 0.0000063T^3$
PW	I	$1.0577 - 0.01404T + 0.00044T^2 - 0.0000063T^3$

3.6 Estimated section modulus degradation model with I.G.G System

Chapter 2 provided a general review of high quality inert gas systems such as an inert gas generator and a N₂ generator system. It is apparent that the low oxygen and low SO₂ content provided by an inert gas system can control corrosion and reduce the corrosion rate significantly [46, 47].

In Chapter 2 and Ok et al. [47] found that inert gas generator based clean inert gas could be economical solution to control corrosion in an oil tanker environment and minimize structural maintenance cost in ageing double hull tankers.

As investigated in Chapter 2, some recent study by Matsuda et al. [46] indicates that the rate of rusting on shot blasted steel test plates placed at the bottom of the clean inert gas (nitrogen) treated ballast tank was 0.039 mm/year, compared with 0.382 mm/year for the same type of plates at the bottom of a standard ballast tank with normal operating tank atmosphere condition based on 18 months onboard testing period. This means that the corrosion rate of clean inert gas treated environment is approximately 10% that of normal operating tank atmosphere condition.

It is clear that the ship structures under clean inert gas environment will reduce corrosion rate remarkably than under normal operating condition. However the extent of effectiveness of clean inert gas system for double hull tanker structures is still questionable and actual onboard tests are necessary. In this study, the effects of high quality inert gas on time variant section modulus degradation have been investigated by assuming that the corrosion rate under inert gas is respectively 10%, 30%, 50% and 70% of average corrosion degradation model (PW model) with the assumption that the effective coating life is 5 years.

Table 3-13 shows the corrosion degradation rate based on expected corrosion rates under an inert gas system. Fig. 3.15 and Fig. 3.16 indicate the corresponding time variant section modulus degradation at deck and keel. The results show that the ratios of section modulus degradation at deck over original as-built value at 25 years after construction are 0.899 for average model (PW model) and 0.924, 0.941, 0.957 and 0.974 for corrosion rates under inert gas environment of 70%, 50%, 30% and 10 % of average corrosion degradation model and the ratios of section modulus degradation at keel over original value at 25 years after construction are 0.888 for average model (PW model) and 0.912, 0.929, 0.945 and 0.961 for corrosion rates under inert gas environment of 70%, 50%, 30% and 10 % of average corrosion degradation model.

Table 3-13
Assumed different corrosion rates under high quality inert gas system

STRUCTURE		PM model (mm/year)	70% of PM model (mm/year)	50% of PM model (mm/year)	30% of PM model (mm/year)	10% of PM model (mm/year)
DKP-C	Cargo	0.05745	0.04022	0.02873	0.01724	0.00575
DKP-B	Ballast	0.0687	0.04809	0.03435	0.02061	0.00687
DKLW-C	Cargo	0.05850	0.04095	0.02925	0.01755	0.00585
DKLW-B	Ballast	0.12755	0.08929	0.06378	0.03827	0.01276
DKLF-C	Cargo	0.04395	0.03077	0.02198	0.01319	0.00440
DKLF-B	Ballast	0.06020	0.04214	0.03010	0.01806	0.00602
SSP-C	Cargo	0.04420	0.03094	0.02210	0.01326	0.00442
SSP-B	Ballast	0.04910	0.03437	0.02455	0.01473	0.00491
SLW-C	Cargo	0.10485	0.07340	0.05243	0.03146	0.01049
SLW-B	Ballast	0.08220	0.05754	0.04110	0.02466	0.00822
SLF-C	Cargo	0.09365	0.06556	0.04683	0.02810	0.00937
SLF-B	Ballast	0.05420	0.03794	0.02710	0.01626	0.00542
BTS-C	Cargo	0.06880	0.04816	0.03440	0.02064	0.00688
BTS-B	Ballast	0.05040	0.03528	0.02520	0.01512	0.00504
BTLW-C	Under Cargo	0.10085	0.07060	0.05043	0.03026	0.01009
BTLW-B	Ballast	0.07270	0.05089	0.03635	0.02181	0.00727
BTLF-C	Under Cargo	0.10065	0.07046	0.05033	0.03020	0.01007
BTLF-B	Ballast	0.07130	0.04991	0.03565	0.02139	0.00713
CBHP-C	Cargo	0.04825	0.03378	0.02413	0.01448	0.00483
LBHP-B	Ballast	0.06510	0.04557	0.03255	0.01953	0.00651
LBHP-BB	Ballast	0.08105	0.05674	0.04053	0.02432	0.00811
BHLW-C	Cargo	0.04280	0.02996	0.02140	0.01284	0.00428
BHLW-B	Ballast	0.08220	0.05754	0.04110	0.02466	0.00822
BHLF-C	Cargo	0.04450	0.03115	0.02225	0.01335	0.00445
BHLF-B	Ballast	0.05420	0.03794	0.02710	0.01626	0.00542
BGP	Ballast	0.04845	0.03392	0.02423	0.01454	0.00485
HOR-B	Ballast	0.08105	0.05674	0.04053	0.02432	0.00811

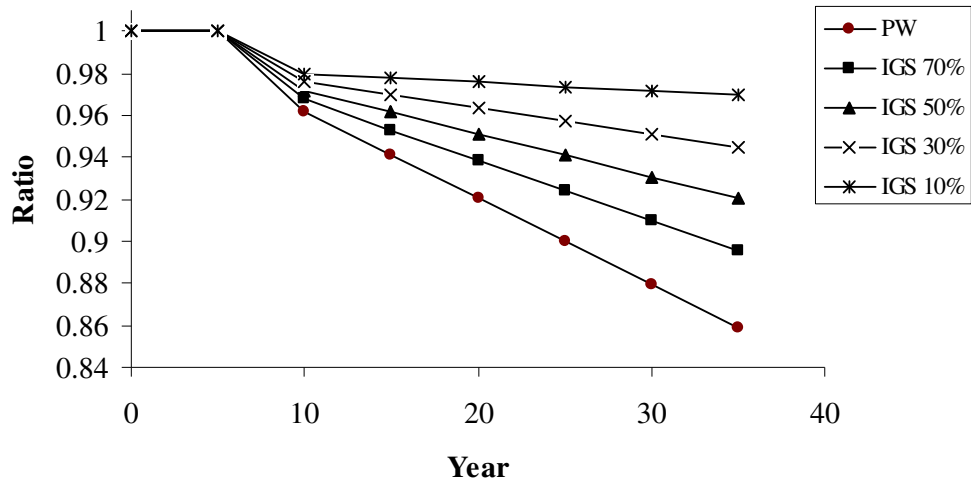


Fig. 3.15. Time variant section modulus changes at deck

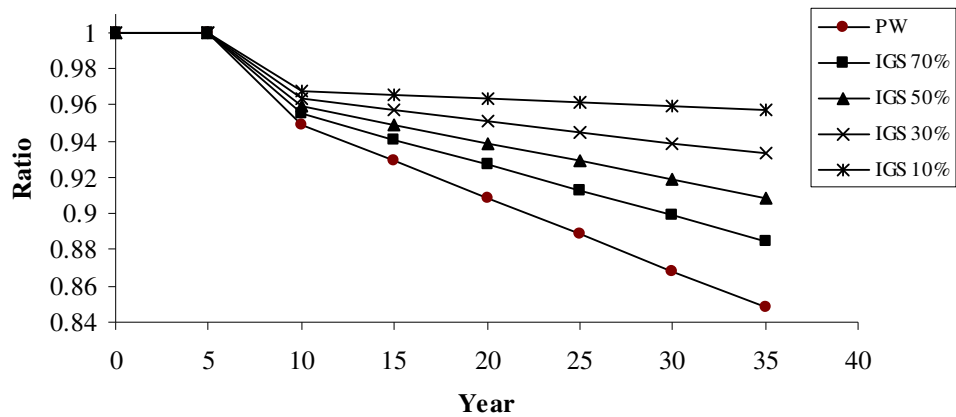


Fig. 3.16. Time variant section modulus changes at keel

The results indicate the effectiveness of clean inert gas on control corrosion of marine and offshore structures, improvement of structural integrity and longitudinal strength in ageing double hull tankers. This means well designed clean inert gas system can minimize corrosion rates of structures and accordingly can minimize section modulus degradation over typical service life. Eventually the maintenance costs for ageing ships will remarkably be reduced compared to the structures which haven't clean inert gas provision as discussed in Chapter 2 and Ok and Pu [47].

3.7 Stress changes based on section modulus degradation model

Based on Paik *et al.* [26], Wang *et al.* [34], and PW models, the changing of hull stresses at keel and upper deck level over original as-built value are investigated on the AFRAMAX Double Hull Tanker as illustrated in Fig. 3.17.

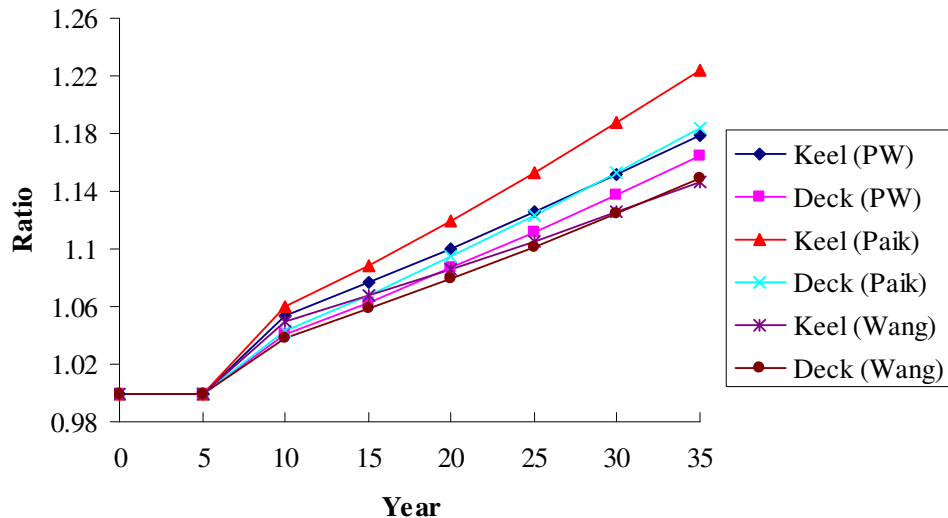


Fig. 3.17. Time variant stress changes pattern based on various models

The results indicate that the stress levels at the deck and keel due to overall hull section corrosion are increasing by time variant manner, thus the margin of structural safety can be reduced substantially and Paik et al.'s model shows the highest values of stress increasing at deck and keel and could consider the most pessimistic values for time variant hull girder longitudinal strength.

By considering Paik et al. model, the changing hull stresses at keel and upper deck levels, which consider the time variant vertical section modulus reduction can be proposed as follows:

For the stress change at upper deck level:

$$\begin{aligned} \left(\frac{\sigma_{DC}}{\sigma_{DO}} \right) &= 1 & 0 < T \leq 5 \text{ years} & \quad (\text{Eq.3.36}) \\ &= 0.9721 + 0.00656 T - 0.000016 T^2 & 5 < T \leq 35 \text{ years} & \end{aligned}$$

For the stress change at the keel:

$$\begin{aligned} \left(\frac{\sigma_{KC}}{\sigma_{KO}} \right) &= 1 & 0 < T \leq 5 \text{ years} & \quad (\text{Eq.3.37}) \\ &= 0.9655 + 0.00864 T - 0.000039 T^2 & 5 < T \leq 35 \text{ years} & \end{aligned}$$

where σ_{DC} , σ_{KC} are the changed stress levels due to overall hull section corrosion at the deck and keel respectively and σ_{DO} , σ_{KO} denotes original stress level in the as-built uncorroded condition at deck and keel respectively.

3.8 Concluding remarks

There are many existing corrosion models to estimate time dependent general corrosion rates. However the estimated corrosion rates from each proposed model are so scattered. This means there is a fairly high level of uncertainty in each corrosion data, such as type and route of vessel, type of equipment, skills of technicians and uncertainty of as-built data etc. In this Chapter various existing general corrosion models have been investigated and new formulae based on *Melchers's* [17, 20], *Soares and Garvatov's* [24, 33], *Paik et al.'s* [28] and *Wang et al.'s* [34] models has been proposed to estimate marine immersed general corrosion rates and to reduce uncertainty of data from individual models. The proposed model shows lesser value than *Soares and Garvatov's*, but indicates more conservative values than other models such as *Melchers's*, *Paik et al.'s* and *Wang et al.'s* models, thus might be consider suitable model to represent marine immersed general corrosion rates.

Excessively deep pits and a large grouping of pitting corrosion may lead to a loss of local strength, thus degrading hull integrity and may result in serious pollution by

eventual perforation of the plates. However the calculation of strength degradation due to localized defects, such as pitting corrosion, are more difficult and complicated than general area-wide corrosion and there have been relatively few research activities and guidelines have been published until now. Accordingly some recent research activities and guidelines to assess localized pitting corrosion have been investigated and studied.

Recently several general corrosion models have been proposed in order to estimate the corrosion degradation rates on various regions within tanker structures. Among the various corrosion models that have been published, *TSCF 1992* [6] and *TSCF 2000* [40] did not consider coating effective periods and assumed that corrosion started immediately after construction of the vessel. Whereas *Paik et al's.* [26] and *Wang et al's.* [34] models can each be considered to be one of the latest and more detailed corrosion models which include coating effective periods. However there are large differences in the predicted corrosion rates between these two models. It is also found that Paik et al's. model shows higher corrosion rates for upper deck plates and deck longitudinal webs in ballast tank than in cargo tanks, whereas Wang et al's. model indicates higher corrosion rates in cargo tanks than in ballast tanks. The comparison of existing corrosion models shows that there is considerable scatter in the data between each corrosion model even though the same structural members are referred to. This is because there are so many corrosion uncertainties and different corrosion environments in each ship as well as potential variations in actual measurement practices. In this study, oil tanker structures are sub-divided into 27 individual components and the existing corrosion models are compared against each structural component. The results indicate that the highest corroded structural components is deck longitudinal web in ballast tank based on Paik et al's. model, whereas bottom shell in cargo tank based on TSCF and Wang et al's models. Generally Paik et al's model shows higher corrosion degradation rates than do the TSCF and Wang's et al. models.

Hull girder section modulus represents a measurement of the ship's longitudinal strength and the section modulus should be always greater than the rule requirement. The hull girder section modulus will be decreasing with time due to corrosion progress in ageing ship structures, consequently stress levels of local structural members will also be increased over the design life. However it is time consuming and routine work to calculate the section modulus degradation which considers annual corrosion degradation in ageing ships not only for initial corrosion margins in design stage but also for estimating future maintenance period. Based on Paik's et al, Wang's et al and the average model (PW model), the progressive time related changing of the vertical and horizontal section modulus values are investigated for an existing AFRAMAX Double Hull Tanker. Paik et al's model shows a more severe decreasing pattern of section modulus at deck than Wang et al's model Finally some simplified formulas to estimate time variant vertical, horizontal section modulus degradation and associated stress change at upper deck and keel are proposed. The proposed formulas are useful to evaluate suitable corrosion margins for marine structures and to assess time variant reliability and hull girder longitudinal strength of ship structures.

It is clear that the ship structures under clean inert gas environment will reduce corrosion rate remarkably than under normal operating condition. However the extent

of effectiveness of clean inert gas for double hull tanker structures is still questionable and actual onboard test are necessary. In this study, the effects of high quality inert gas on time variant section modulus degradation have been investigated by assuming that the corrosion rate under inert gas is respectively 10%, 30%, 50% and 70% of average corrosion degradation model with the assumption that the effective coating life is 5 years. The results indicate the effectiveness of clean inert gas on control corrosion of marine and offshore structures, improvement of structural integrity and longitudinal strength in ageing double hull tankers. This means well designed clean inert gas system can minimize corrosion rates of structures and accordingly can minimize section modulus degradation over typical service life. Eventually the maintenance costs for ageing ships might remarkably be reduced compared to the structures which haven't clean inert gas provision.

It is assumed that different size and structural details might have a different time variant section modulus degradation ratios and associated stress change at upper deck and keel. Accordingly further research activities and investigation are required based on different sizes and types of vessels.

References (Chapter 3)

1. Schumacher, M., *Seawater corrosion handbook*. 1979, NJ: Noyes Data Corporation.
2. Viner, A.C. and D.R. Tozer, *Influence of corrosion on ship structural performance. Hull New Construction Division No.85/29*. Lloyd's Register of Shipping, 1985.
3. Yamamoto, N., A. Kumano, and M. Matoba, *Effect of corrosion and its protection on hull strength (2nd Report)*. Journal of the Society Naval Architects of Japan, 1994. **Vol.176.**: p. 281-289.
4. Ohyagi, M., *Statistical survey on wear of ship's structural members*. NK Techn. Bull., 1987: p. 75-85.
5. Pollard, R.R., *Evaluation of corrosion damage in crude, product carriers*. 1991.
6. TSCF, *Condition Evaluation and Maintenance of Tanker Structures*. Tanker Structure Cooperative Forum, May, 1992.
7. TSCF, *Guidance Manual for Tanker Structures*. Tanker Structure Co-Operative Forum, 1997.
8. Loseth, R., G. Sekkesaeter, and S. Valsgard, *Economics of high-tensile steel in ship hulls*. Marine Structures, 1994. **7(1)**: p. 31-50.
9. Gardiner, C.P. and R.E. Melchers, *Corrosion analysis of bulk carriers, Part I: operational parameters influencing corrosion rates*. Marine Structures, 2003. **Vol.16**: p. 547-566.
10. Hajeeh, M., *Estimating corrosion: a statistical approach*. Materials & Design, 2003. **24(7)**: p. 509-518.
11. Shell, I.T.a.S.C., *An Overview of the TSCF Guidelines for Ballast Tank Coating Systems and Surface Preparation*. Tanker Structure Co-Operative Forum, October, Tokyo, 2000.
12. Kawano, H. and M. Hirakata, *Tanker Structure and Hull Failure Strength*. The Petroleum Association of Japan PAJ-2003 Symposium, 2003.
13. Class NK, *Guidelines for Tanker Structures*. 2001.
14. ABS, *Steel Vessels*. American Bureau of Shipping, 2004. **Pt 5, Ch.1, Sec.2, 3.1**.
15. DNV, *Rules for Ships*. Det Norske Veritas, 2004. **Part 3, Ch.1, Sec.2, D200**.
16. IACS, *Common Structural Rules for Double Hull Oil Tankers*. 2006.
17. Melchers, R.E., *Corrosion uncertainty modelling for steel structures*. Journal of Constructional Steel Research, 1999. **52(1 SU)**: p. 3-19.
18. Phull, B.S., S.J. Pikul, and R.M. Kain, *Seawater corrosivity around world: results from five years of testing In: Kain R.M, Young W.T., editors. Corrosion Testing in natural waters*. ASTM STP 1300, 1997. **2:34-73**.
19. Southwell, C.R., J.D. Bultman, and H.J. CW., *Estimating of service life of steel in seawater*. In: Schumacher M, editor. *Seawater corrosion handbook*. 1979: p. 374-387.
20. Melchers, R.E. *Probabilistic modelling of sea water corrosion of steel structures*. In: *Proceedings of the International Conference on Applications Statistics and Probability in Structural and Geotechnical Engineering (ICASP)*. 1995. Paris.

21. Melchers, R.E., *Mathematical modelling of the diffusion controlled phase in marine immersion corrosion of mild steel*. Corrosion Science, 2003. **45**(5): p. 923-940.
22. Melchers, R.E., *Effect on marine immersion corrosion of carbon content of low alloy steels*. Corrosion Science, 2003. **45**(11): p. 2609-2625.
23. Melchers, R.E., *Probabilistic model for marine corrosion of steel for structural reliability assessment*. Journal of Structural Engineering-ASCE, 2004. **Vol.129, No.11**.
24. Soares, C.G. and Y. Garbatov, *Reliability of maintained, corrosion protected plates subjected to non-linear corrosion and compressive loads*. Marine Structures, 1999. **12**(6): p. 425-445.
25. Paik, J.K. and A.K. Thayamballi, *Ultimate Limit State Design of Steel Plated Design*. 2003: John Wiley & Sons Ltd.
26. Paik, J.K., et al., *A Time-Dependent Corrosion Wastage Model for the Structures of Single and Double-Hull Tankers and FSOs and FPSOs*. Marine Technology, 2003. **Vol.40, No.3**: p. 201-217.
27. Paik, J.K., et al., *Time-variant ultimate longitudinal strength of corroded bulk carriers*. Marine Structures, 2003. **16**(8): p. 567-600.
28. Paik, J.K., et al., *A time-dependent corrosion wastage model for seawater ballast tank structures of ships*. Corrosion Science, 2004. **46**(2 SU -): p. 471-486.
29. Wang, G., J. Spencer, and H. Sun, *Assessment of corrosion risks to ageing ships using an experience database*. 22nd International Conference on Offshore Mechanics and Arctic Engineering, 2003.
30. Qin, S. and W. Cui, *Effect of corrosion models on the time-dependent reliability of steel plated elements*. Marine Structures, 2003. **16**(1): p. 15-34.
31. Paik, J.K., S.K. Kim, and S.K. Lee, *Probabilistic corrosion rate estimation model for longitudinal strength members of bulk carriers*. Ocean Engineering, 1998. **25**(10 SU -): p. 837-860.
32. Ok, D. and Y. Pu, *General and pitting corrosion models*. 2005, MARSTRUCT EU Project (Project No. FP6-PLT-506141) Report MAR-W6-3-UNEW-02(1).
33. Soares, C.G. and Y. Garbatov, *Reliability of maintained ship hulls subjected to corrosion and fatigue under combined loading*. Journal of Constructional Steel Research, 1999. **52**(1): p. 93-115.
34. Wang, G., J. Spencer, and T. Elsayed, *Estimation of Corrosion Rates of Structural Members in Oil Tankers*. International Conference on Offshore Mechanics and Arctic Engineering, CANCUN, MEXICO, 2003. **22nd**.
35. TSCF, *Experimental and theoretical investigation of the strength of corroded hull elements*. Project 300 of "Guidance Manual for the Inspection and Condition Assessment of Tanker Structures", 1986.
36. Daidola, J.C., et al., *Residual strength assessment of pitted plate panels*. Ship Structure Committee, SSC-394, 1997.
37. Hutchinson, S.C. and R.G. Bea, *Maintenance of Marine Structures; A State of the Art Summary*. Ship Structure Committee, SSC-372, 1993.
38. Paik, J.K., et al., *Time-dependent risk assessment of ageing ships accounting for general/pit corrosion, fatigue cracking and local dent damage*. SNAME,

- Annual Meeting in San Francisco (World Maritime Technology Conference), 2003.
39. Paik, J.K., J.M. Lee, and M.J. Ko, *Ultimate shear strength of plate elements with pit corrosion wastage*. *Thin-Walled Structures*, 2004. **vol.42**: p. 1161-1176.
 40. TSCF, *Corrosion Protection of Cargo Tanks*. Tanker Structure Co-Operative Forum, 2000. **TSCF Working Group #2, Chevron, Shipping Company**.
 41. IACS, *Renewal criteria for side shell frames and brackets in single side skin bulk carriers not built in accordance with UR S12 Rev.1 or subsequent revisions*. International Association of Classification Societies, 2003 Rev.1.
 42. Ok, D. and Y. Pu. *Time-variant corrosion degradation, hull girder strength and fatigue assessment for ageing double hull tanker*. in *The 15th International Offshore and Polar Engineering Conference*. 2005. Seoul, Korea.
 43. Yoneya, T., et al., *A Comprehensive Study on the Practical Strength Assessment of Tanker and Bulk Carrier Structures*. Nippon Kaiji Kyokai, Tokyo, 2003.
 44. Bergesen, D.Y.A., *Experience with Double Hull Tankers: an Owner's ViewPoint*. Tank Structure Co-Operative Forum, October 2000, Tokyo, 2000.
 45. IACS, *Requirements Concerning Strength of Ships*. International Association of Classification Societies, 2003.
 46. Matsuda, M., et al., *An anticorrosion method for ballast tanks using nitrogen gas*. Ship and Ocean Foundation Technical Report, 1999.
 47. Ok, D. and Y. Pu. *Corrosion control method by using clean inert gas to ballast tanks and permanent void spaces in marine and offshore structures*. in *3rd International Marine Science and Technology for Environmental Sustainability (ENSUS) Conference*. 2005. Newcastle upon Tyne, UK.

Chapter 4

Fatigue Assessment of Corroded Ship Structures

4.1 Introduction

Ship and offshore structures frequently suffer from the fatigue damage mainly caused by cyclic wave induced loads and both external and internal hydrodynamic pressures. Fatigue thus becomes the cause of various cracks in welded and unwelded ship structure components. Eventually fatigue damage affects not only costly replacement or repair of ship structure but also potential damage to cargo and environment, serviceability and safety of ageing ships. According to recent reports, many cracks have been found in relatively new crude oil tankers which were constructed of higher strength materials. This means that the use of higher strength steel (HTS) leads to higher stresses in ship's structure due to reduced thickness but there is little difference between mild steel and higher strength steel with regard to corrosion and fatigue properties and hence more careful detail design become necessary.

The purpose of the fatigue assessment process is to estimate the fatigue life of individual details of the hull structure and to ensure that the structure is well designed for its intended service, operational and environmental loads over its required lifetime. The estimated length of fatigue life can be basis of initial scantling design and the selection of appropriate design details and shall be used for future developing a maintenance and inspection programme throughout the life of ship. Actually verification of an adequate fatigue life is now becoming a part of the classification society approval process.

Generally, fatigue failure can be prevented by controlling the local cyclic stress amplitude. The designer should ensure that the hull section modulus is large enough considering corrosion degradation of the ageing ships and its ability to continue to withstand wave induced hull girder bending stresses and seek to reduce stress concentrations at local areas by increasing local scantling or suitably modifying the local detail geometry.

The systematic study of fatigue was initiated by *Wöhler* in the period of 1858 ~ 1860, who performed the first systematic experimentation on damage of materials under cyclic loading. He conducted tests on full scale railway axles and also on small scale bending, torsion and axial cyclic loaded specimens of different materials. *Wöhler* introduced the concept of the fatigue curve where a characteristic magnitude of cyclic stress is plotted against the corresponding cycle number that resulted in fatigue failure. This presentation of fatigue life has become very well known as the *S-N* diagram [1].

In 1924 *Palmgren* suggested the damage accumulation concept which is known as

'Linear Rule'. *Miner* [2] first presented the *Palmgren* linear damage concept in mathematical form, expressed by:

$$D = \sum \frac{n_i}{N_i} \quad (\text{Eq.4.1})$$

where D = cumulative damage ratio
 n_i = number of applied cycles
 N_i = number of total cycles to failure

This approach is necessary when a component is subject to complex combination of different stress range cycles and associated frequencies.

U.S. Ship Structure Committee [3-11] have done many comprehensive reviews of ship fatigue and fracture control researches.

Xue et al. [12] investigated the fatigue behaviour of longitudinal stiffeners in oil tankers and container ships by using three different long term marine distributions, namely the *RINA*, *ISSC-88* and *GLIACS* wave environments.

Cramer and Hansen [13] proposed a general procedure for obtaining the long term cyclic wave induced stress range distribution or extreme value distribution to be anticipated over a ship's lifetime. The procedure outlined is built on the specified trading route of the vessel and takes into account ship speeds, heading angle, different loading conditions and effects of manoeuvring. The method was based on a linear frequency domain analysis.

Hansen and Winterstein [14] attempted combining linear frequency domain analysis with realistic wave models to the analysis of the fatigue damage in the side shell region. They found that it is very important to include the water pressure in the fatigue analysis, as this accounts for the majority of the anticipated fatigue damage in the side shell region.

The International Ship and Offshore Structures Congress (ISSC) has reviewed the existing state of the art related to the fatigue and fracture in ship and offshore structures [15, 16]. Comparative fatigue analyses have been performed according to the various Classification Societies rules and guidance promulgated by *ABS*, *BV/RINA*, *DNV*, *GL*, *KR*, *LR*, *NK* and *RS* with an application to a Panamax Container. A welded pad detail on top of a longitudinal hatch coaming bar, and where the hatch covers are supported for vertical loads, had been selected for the analyses. The calculated results showed that large differences existed between the predicted fatigue lives for the same detail as determined by the different *Classification Society* rules and guidance [15].

Additional comparative fatigue FEM-based analyses have been performed on a simple I-beam structure based on the Classification Societies rules and guidance promulgated by *DNV*, *GL*, *ABS* and *LR*. The results showed that fatigue life predictions ranged

from 239,600 to 713,900 cycles [16] that indicates a large variation in calculation results.

A general history and review of fatigue damage can be found in various papers such as *Fatemi and Yang* [17], *Fricke et al.* [18] and *Brennan et al.* [19]. Some recent literature reviews on fatigue analysis of welded joints were introduced by Fricke [20].

Currently the *Classification Societies* fatigue assessment procedures are based on reduced scantling and accordingly the corrosion allowance which is required by each Classification Society should be subtracted from the as-built scantlings before the calculation of the fatigue life. It would be valuable to calculate fatigue life based on expected corrosion rates from existing corrosion models and compare with each Classification Society requirements in order to decide maintenance programme and period in ageing ships.

In this chapter the fatigue life of an existing *AFRAMAX* double hull shuttle tanker considering the effects of corrosion, based on a design target fatigue life of 20 years, has been investigated to evaluate the actual fatigue life of the various ship sideshell longitudinal stiffeners in accordance with the *DNV* method [21].

4.2 Fatigue assessment methods

Normally the assessment of the fatigue strength of welded structural members is carried out in three phases:

- Calculation of stress ranges,
- Selection of the appropriate design S-N curve,
- Calculation of the cumulative damage ratio.

Depending on the characteristics of the stresses used in the calculations, the actual form of the fatigue assessment can be categorized by the so-called “nominal stress approach”, “hot spot stress approach” or by the “notch stress approach”. The three stresses are defined as follows [22]:

■ Nominal stress

A general stress in a structural component calculated by beam theory based on the applied loads and the sectional properties of the component. The sectional properties are determined at the section considered (i.e. the hot spot location) by taking into account the gross geometric changes of the detail (e.g. cutouts, tapers, haunches, brackets, changes of scantlings, misalignments, etc.). The nominal stress can also be calculated using a coarse mesh FE analysis or analytical approach.

■ Hot spot stress

A local stress at the hot spot (a critical point) where cracks may be initiated. The hot-spot stress takes into account the influence of structural discontinuities due to the geometry of the connection detail itself but excludes the effects of welds.

■ Notch stress

A peak stress at the root of a weld or notch taking into account stress concentrations due to the effects of structural geometry as well as the presence of welds.

4.2.1 S-N Curve

The fatigue analysis can be calculated based on a *S-N* curve in conjunction with the *Palmgren-Miner* linear cumulative damage law or by fracture mechanics methods based on crack propagation calculations. The capacity of welded steel joints with respect to fatigue damage is characterized by various *S-N* curves which are obtained from a combination of experience and fatigue tests. The nominal stresses are to be multiplied by relevant stress concentration factors for calculation of local notch stresses.

For ship structural details, *S-N* design curves are given by:

$$S^m N = K \quad (\text{Eq.4.2})$$

which in logarithmic form becomes:

$$\log N = \log K - m \log S \quad (\text{Eq.4.3})$$

where S = stress range
 N = number of cycles to failure
 m = the negative inverse slope of S-N curve
 $\log K$ = the life time intercept of the S-N curve ($=\log a - 2s$)
 a = life intercept of the mean S-N curve
 s = standard deviation of $\log N$

Experimental *S-N* curves are defined by their mean fatigue life and standard deviation. The mean S-N curve means that for a cyclic stress level S the structural detail will fail with a probability level of 50 percent after N loading cycles. The design *S-N* curves represent two standard deviations below the mean lines, which corresponds to a survival probability of 97.5 per cent [22].

Each of the classification societies have their own selected S-N curves for fatigue assessment [21, 23-25] referenced to specific design details and the ship's fatigue life can be evaluated by their own computer program such as *ABS SafeHull*, *LRS ShipRight* and *DNV Nauticus Hull System* that are made available to the shipbuilding industry.

Unless supported by alternative direct measurement, *IACS* [22] recommends the following sets of *S-N* curves:

- U.K. HSE Basic S-N Curves, or
- IIW(The International Institute of Welding) S-N Curves

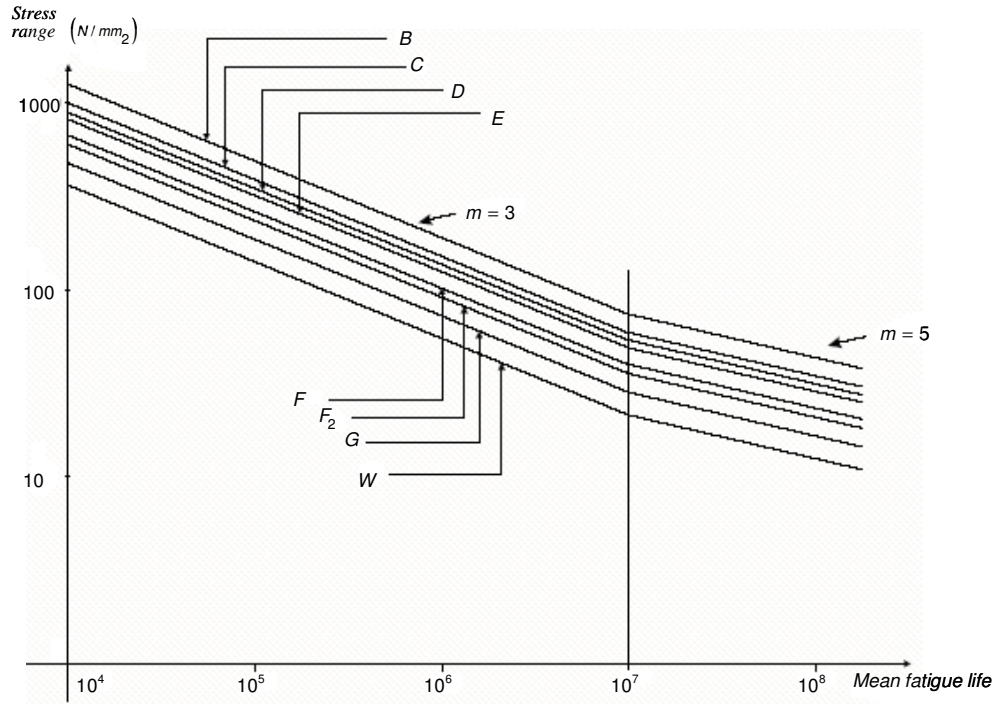


Fig. 4.1. New HSE Basic Design S-N Curves [22]

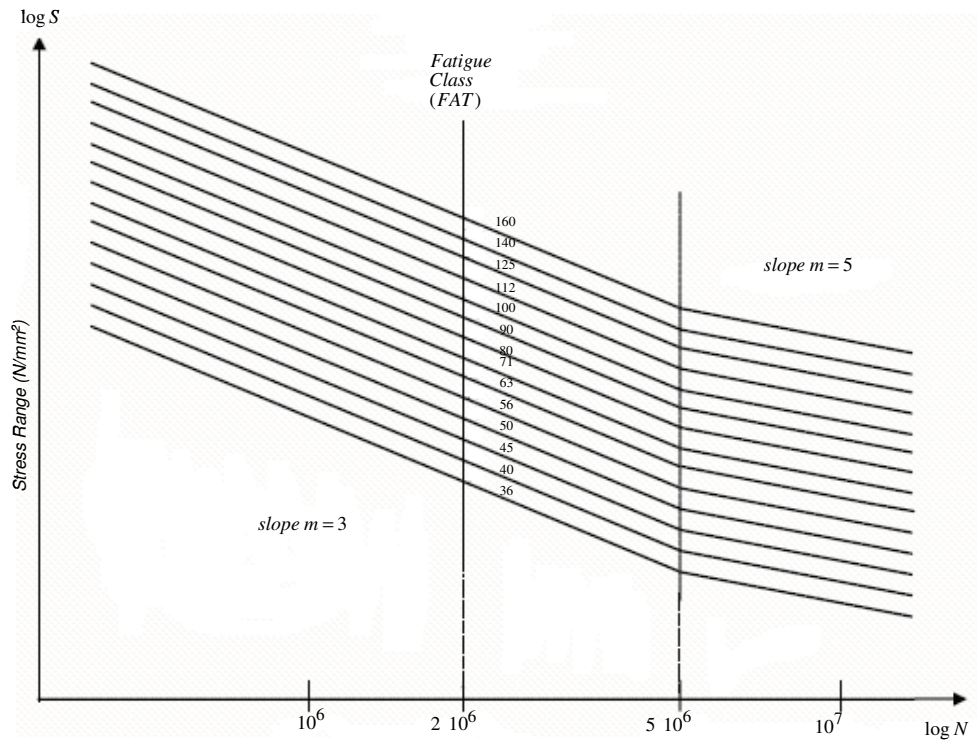


Fig. 4.2. IIW S-N Curve [22]

The *HSE Basic S-N curves* consists of eight curves as shown in Fig. 4.1, These curves give the relationship between the nominal cyclic stress range and the number of constant amplitude load cycles to failure. Each curve represents a class of welded details which are dependent on the geometrical arrangement of the detail. The *Classification Societies* provide guidance regarding the selection of specific curves that are relevant for specific ship structural details.

The *International Institute of Welding (IIW) S-N curves*, as shown in Fig. 4.2, also based on the nominal stress range and correspond to non corrosive conditions are characterized by the fatigue strength at 2×10^6 cycles, The prime slope of all *S-N* curves is $m=3$ and the change in slope ($m=5$) occurs for $N = 5 \times 10^6$ cycles.

4.2.2 Cumulative damage model

The cumulated fatigue damage can be derived from the local stress range responses over the design life of the ship. The target cumulative fatigue damage factor η should be equal to or less than one. If the local long term stress range response is defined through adequately refined histograms, the cumulative damage is given by:

$$D = \sum_{i=1}^p \frac{n_i}{N_i} = \frac{1}{K} \sum_{i=1}^p n_i (\Delta\sigma_i)^m \leq \eta \quad (\text{Eq.4.4})$$

where D = accumulated fatigue damage
 p = number of stress blocks
 m = negative inverse slope of the S-N curve
 K = intercept of the design S-N curve with the log N axis
 n_i = number of stress cycles in stress block i
 N_i = number of cycles to failure at constant amplitude stress range $\Delta\sigma_i$
 η = target cumulative fatigue damage for design.

The difficulty for the designer is the creation of a stress range histogram that adequately represents the applied cyclic stresses experienced by the vessel over its designed lifetime. Such cyclic stresses are generally taken due to the many waves of various amplitudes, periods and frequency of occurrence that the vessel will encounter during its lifetime, allowing for such factors as the vessel loading conditions, heading angles relative to the waves and ship speed, etc.

Various mathematical approaches have been developed to represent the long term wave-induced demands on a vessel. There is also a somewhat more refined approach based upon the availability of more accurately quantified average yearly sea-state statistics. These approaches are reviewed in the following sections.

IACS [22] assumed that the long term distribution of stress ranges fit a two-parameter Weibull probability distribution, by applying the *Palmgren-Miner* rule, the cumulative fatigue damage D_i for each relevant condition is given by:

$$D_i = \frac{\alpha_i N_L}{K} \frac{S_{Ri}^m}{(\ln N_R)^{m/\xi}} \mu_i \Gamma \left(1 + \frac{m}{\xi} \right) \quad (\text{Eq.4.5})$$

where:

- N_L = total number of stress cycles over the design life $\left(= \frac{\alpha_0 T}{4 \log L} \right)$
- α_0 = factor taking into account the time needed for loading / unloading operations, repairs, etc. (=0.85)
- α_1 = part of the ship's life in loaded condition (= 0.5 for tanker)
- α_2 = part of the ship's life in ballast (=0.5 for tanker)
- T = design life, in seconds
- L = ship's length, in m
- m, K = constants
- S_{Ri} = stress range, in MPa, for the basic case considered, at the probability level of $1/N_R$
- N_R = number of cycles corresponding to the probability level of $1/N_R$
- ξ = Weibull shape parameter $\left(= 1.1 - 0.35 \frac{L-100}{300} \right)$
- Γ = Gamma function
- μ_i = coefficient taking into account the change in slope of the S-N curve
- $$= 1 - \frac{\left[\gamma \left(1 + \frac{m}{\xi}, v_i \right) - v^{-\Delta m/\xi} \gamma \left(1 + \frac{m + \Delta m}{\xi}, v_i \right) \right]}{\Gamma \left(1 + \frac{m}{\xi} \right)}$$
- $v_i = \left(\frac{S_q}{S_{Ri}} \right)^\xi \ln N_R$
- S_q = stress range at the intersection of the two segments of the S-N curve
- Δm = slope range at the upper to lower segment of the S-N curve
- $\gamma(a, x)$ = incomplete gamma function, Legendre form

With this proposed method the resultant cumulative damage ratio, given by:

$$D = D_1 + D_2 \quad (\text{Eq.4.6})$$

- where D_1 = cumulative fatigue damage for the loaded condition
- D_2 = cumulative fatigue damage for the ballast condition

The cumulative fatigue damage ratio, D , may be converted to a calculated fatigue life using the relationship expressed by:

$$\text{Predicted Fatigue life} = \frac{\text{Design life}}{D} \quad (\text{Eq.4.7})$$

Finally the calculated fatigue life is to be equal or greater than the design life of the ship.

The total cumulative fatigue damage can also be estimated from the combined accumulated damage within each short term sea state condition. The cumulative damage is then the weighted sum over all the sea states and wave heading directions the ship is encountering over the design life, weighted with the occurrence rate r of the difference sea states and heading directions, given by [21]:

$$D = \frac{N_L}{K} \Gamma\left(1 + \frac{m}{2}\right) \sum_{n=1}^{N_{load}} p_n \times \sum_{\substack{\text{all sea states} \\ \text{all heading}}} r_{i\ jn} \left(2\sqrt{2m_{0i\ jn}}\right)^m \leq \eta \quad (\text{Eq.4.8})$$

where p_n = fraction of design life in load condition n

r_{ij} = the relative number of stress cycles in short-term condition i, j

m_0 = zero spectral moment of stress response.

4.3 Stress and load analysis

There are two general kinds of methods that can be employed in order to estimate long term stress range distribution. One is the stress range based on dynamic loading as specified in the each classification rule. Normally the *Weibull* distribution is adopted for the calculation of long term stress ranges. The nominal stresses are multiplied by the relevant stress concentration factors for calculation of local notch stresses. The other method is that the long term stress ranges are calculated based on wave scatter diagram data of actual or expected routes. This latter method requires considerably more analytical effort than does the former method.

4.3.1 DNV model

Cramer et al. [26] and *DNV* [21] introduced simplified approach for estimating the long term stress range distribution which is based on the assumption of *Weibull* distributed stress ranges, having cumulative probability, expressed by:

$$Q(\Delta\sigma) = 1 - \exp\left[-\left(\frac{\Delta\sigma}{q}\right)^\xi\right] \quad (\text{Eq.4.9})$$

The stress range distribution may also be expressed as:

$$\Delta\sigma = \Delta\sigma_0 \left[\frac{\ln n}{\ln N_R}\right]^{1/\xi} \quad (\text{Eq.4.10})$$

where Q = probability of exceedance of the stress range $\Delta\sigma$
 q = Weibull scale parameter = $\frac{\Delta\sigma_0}{(\ln N_R)^{1/\xi}}$
 $\Delta\sigma_0$ = reference stress range value at the local detail exceeded once out of N_R cycles

The shape parameter ξ depends on the prismatic parameters of the ship, the location of the considered detail and the planned sailing route over the design life as follows:

$$\begin{aligned} \xi &= \xi_0 && \text{for deck longitudinals} \\ \xi &= \xi_0 + \xi_a \frac{D_{Depth} - z}{D_{Depth} - T_{act}} && \text{for ship side above the water line} \\ \xi &= \xi_0 + \xi_a && \text{for ship side at the water line} \\ \xi &= \xi_0 + \frac{\xi_a z}{T_{act}} - 0.005(T_{act} - z) && \text{for ship side below the water line} \\ \xi &= \xi_0 - 0.005T_{act} && \text{for bottom longitudinals} \\ \xi &= \xi_0 + \xi_a && \text{for longitudinal and transverse bulkhead} \end{aligned}$$

where ξ_0 = shape factor as a function of ship's length = $2.21 - 0.54 \times \log_{10}(L)$
 ξ_a = additional factor depending on the motion response period
 = 0.05 in general
 = 0 for plating subjected to forces related to roll motions for vessels with roll period $T_R > 14$ sec
 D_{Depth} = the moulded depth of ship
 T_{act} = the actual draught
 z = the location height above the keel

The combined stress range response from the combined global and local stress range is given by the largest of:

$$\Delta\sigma_0 = f_m \Delta\sigma \quad (\text{Eq.4.11})$$

$$\Delta\sigma = f_e \max \begin{cases} \Delta\sigma_g + 0.6\Delta\sigma_l \\ 0.6\Delta\sigma_g + \Delta\sigma_l \end{cases} \quad (\text{Eq.4.12})$$

where f_e = the operation route reduction factor
 = 0.8 for world wide operation
 = 1.0 for shuttle tankers and vessels that frequently operate in the *North Atlantic*
 f_m = the mean stress reduction factor
 = 1.0 for tension over the whole stress cycle

= 0.85 for mean stress equal to zero
 = 0.7 for compression over the whole stress cycle

The combined global stress range response is estimated by:

$$\Delta\sigma_g = \sqrt{\Delta\sigma_v^2 + \Delta\sigma_{hg}^2 + 2\rho_{vh} \Delta\sigma_v \Delta\sigma_{hg}} \quad (\text{Eq.4.13})$$

where $\Delta\sigma_v$ = wave induced vertical hull girder bending stress ranges
 $\Delta\sigma_{hg}$ = horizontal hull girder bending stress ranges = $2\sigma_h$
 ρ_{vh} = average correlation between vertical and horizontal wave induced bending stress (= 0.10)

The combined local stress response is estimated by:

$$\sigma_l = 2\sqrt{\sigma_e^2 + \sigma_i^2 + 2\rho_p \sigma_e \sigma_i} \quad (\text{Eq.4.14})$$

where σ_e = the external sea pressure induced stress amplitude
 σ_i = the internal inertia pressure induced stress amplitude

The correlation between the external and internal pressure induced stresses is a function of the location of the considered detail, given by:

$$\rho_p = \begin{cases} 0.5 - \frac{z}{10T_{act}} + \frac{|x|}{4L} + \frac{|y|}{4B} - \frac{|x|z}{5LT_{act}} & z \leq T_{act} \\ 0.4 + \frac{|x|}{4L} + \frac{|y|}{4B} - \frac{|x|}{5L} & z > T_{act} \end{cases} \quad (\text{Eq.4.15})$$

where B = the greatest moulded breadth of the ship
 x, y, z = the longitudinal, transverse and vertical distance from the origin at (midship, centreline, baseline) to the load point of the considered structural detail.

The wave induced vertical hull girder bending stress is given by:

$$\sigma_v = 0.5K[M_{w0,h} - M_{w0,s}]10^{-3}|z - n_0|/I_N \quad (\text{Eq.4.16})$$

The wave induced horizontal hull girder bending stress is given by:

$$\sigma_h = K_s M_H 10^{-3} |y|/I_C \quad (\text{Eq.4.17})$$

where $M_{w0,s}$ = vertical wave sagging bending moment amplitude
 $M_{w0,h}$ = vertical wave hogging bending moment amplitude
 $|z - n_0|$ = vertical distance in m from the horizontal neutral axis of hull cross

- section to considered member
- I_N = moment of inertia of hull cross-section in m^4 about transverse axis
- K_{st} = stress concentration factor for considered detail and loading
- M_H = horizontal wave bending moment amplitude
- y = distance in m from vertical neutral axis of hull cross section to member considered
- I_C = the hull section moment of inertia about the vertical neutral axis

The vertical wave induced bending moments and horizontal wave bending moment at 10^{-4} probability level of exceedance, given by:

$$M_{w0,s} = -0.11 f_r k_{wm} C_w L^2 B (C_B + 0.7) \quad (kNm) \quad (\text{Eq.4.18})$$

$$M_{w0,h} = 0.19 f_r k_{wm} C_w L^2 B C_B \quad (kNm) \quad (\text{Eq.4.19})$$

$$M_H = 0.22 f_r L^{9/4} (T_{act} + 0.30B) C_B (1 - \cos(2\pi x / L)) \quad (kNm) \quad (\text{Eq.4.20})$$

- where C_w = wave coefficient
- k_{wm} = moment distribution factor
= 1.0 between 0.40L and 0.65L from A.P
- f_r = factor to transform the load from 10^{-8} to 10^{-4} probability level
= $0.5^{1/\xi_0}$
- ξ_0 = long term Weibull shape parameter = $2.21 - 0.54 \log(L)$
- C_B = Block coefficient

The dynamic external pressure amplitude is given by:

$$p_e = r_p p_d \quad (kN / m^2) \quad (\text{Eq.4.21})$$

where p_d = dynamic pressure amplitude below the waterline

The dynamic pressure amplitude is taken the largest of the combined pressure dominated by pitching motion in head/quartering seas, p_{dp} , or the combined pressure dominated by roll motion in beam/quartering seas, p_{dr} , as:

$$p_d = \max \left\{ \begin{array}{l} p_{dp} = p_l + 135 \frac{|y|}{B + 75} - 1.2(T_{act} - z_w) \\ p_{dr} = 10 \left[|y| \frac{\phi}{2} + C_B \frac{|y| + k_f}{16} \left(0.7 + 2 \frac{z_w}{T_{act}} \right) \right] \end{array} \right\} \quad (kN / m^2) \quad (\text{Eq.4.22})$$

where $p_l = k_s C_w + k_f = (k_s C_w + k_f) \left(0.8 + 0.15 \frac{V}{\sqrt{L}} \right)$ if $\frac{V}{\sqrt{L}} > 1.5$

$k_s = 3 C_B$ between 0.2L and 0.7L from AP.

z_w = vertical distance from the baseline to the loadpoint = maximum T_{act} (m)

y = horizontal distance from the centre line to the loadpoint

$\bar{y} = y$, but minimum B/4 (m)

k_f = the smallest of T_{act} and f

f = vertical distance from the waterline to the top of the ship's side at transverse section considered (m) = maximum $0.8 C_w$ (m)

ϕ = rolling angle, single amplitude (rad) = $50 c / (B + 75)$

$c = (1.25 - 0.025 T_R) k$

$k = 1.2$ for ships without bilge keel

$= 1.0$ for ships with bilge keel

V = vessel's design speed in knots

r_p = reduction of pressure amplitude in the surface zone

$= 1.0$ for $z < T_{act} - z_{wl}$

$= \frac{T_{act} + z_{wl} - z}{2z_{wl}}$ for $T_{act} - z_{wl} < z < T_{act} + z_{wl}$

$= 0.0$ for $T_{act} + z_{wl} < z$

z_{wl} = distance in m measured from actual water line = $\frac{3p_{dT}}{4\rho g}$

$p_{dT} = p_d$ at $z = T_{act}$

T_{ac} = the draught in m of the considered load condition

ρ = density of water = $1.025(t/m^3)$

The dynamic internal pressure amplitude can be taken as the maximum pressure due to acceleration of the internal mass, expressed by:

$$p_i = f_a \max \begin{cases} p_1 = \rho a_v h_s \\ p_2 = \rho a_t |y_s| \\ p_3 = \rho a_l |x_s| \end{cases} \quad (kN/m^2) \quad (\text{Eq.4.23})$$

where p_1 = pressure due to vertical acceleration

p_2 = pressure due to transverse acceleration

p_3 = pressure due to longitudinal acceleration

ρ = density of sea water = $1.025 (ton/m^3)$

x_s = longitudinal distance from centre of free surface of liquid in tank to pressure point considered (m)

y_s = transverse distance from centre of free surface of liquid in tank to the pressure point considered (m)

h_s = vertical distance from point considered to surface inside the tank (m)

- a_v = acceleration in vertical direction (m/s^2)
 a_t = acceleration in transverse direction (m/s^2)
 a_l = acceleration in longitudinal direction (m/s^2)
 f_a = factor to transform the load effect to probability level 10^{-4} , when the accelerations are specified at the 10^{-8} probability level = $0.5^{1/h}$
 $h = h_0 + 0.05 = 2.26 - 0.54 \log_{10}(L)$

4.3.2 ABS Model

ABS [24] defines the determination of total stress range f_R as follows;

$$f_R = c_f (f_{RG} + f_{RL}) \quad N/cm^2 \quad (\text{Eq.4.24})$$

where

- f_{RG} = global dynamic stress range, in $N/cm^2 = \left((f_{d1vi} - f_{d1vj}) + (f_{d1hi} - f_{d1hj}) \right)$
 f_{RL} = local dynamic stress range, in N/cm^2
 $= c_w \left((f_{d2i} + f_{d2i}^* + f_{d3i}) - (f_{d2j} + f_{d2j}^* + f_{d3j}) \right)$
 c_f = adjustment factor to reflect a mean wasted condition = 0.95
 c_w = coefficient for the weighted effects of the two paired loading patterns = 0.75
 f_{d1vi}, f_{d1vj} = wave induced component of the primary stresses produced by hull girder vertical bending moment, in N/cm^2 , for load case i and j of the selected pairs of combined load cases, respectively
 f_{d1hi}, f_{d1hj} = wave induced component of the primary stresses produced by hull girder horizontal bending moment, in N/cm^2 , for load case i and j of the selected pairs of combined load cases, respectively
 f_{d2i}, f_{d2j} = wave induced component of the secondary bending stresses produced by the bending of cross-stiffened panels between transverse bulkheads, in N/cm^2 , for load case i and j of the selected pairs of combined load cases, respectively
 f_{d2i}^*, f_{d2j}^* = wave induced component of the additional secondary stresses produced by the local bending of the longitudinal stiffener between supporting structures (e.g., transverse bulkheads and web frames), in N/cm^2 , for load case i and j of the selected pairs of combined load cases, respectively
 f_{d3i}, f_{d3j} = wave induced component of the tertiary stresses produced by the local bending of plate elements between the longitudinal stiffeners in, N/cm^2 , for load case i and j of the selected pairs of combined load cases, respectively

ABS 2004 Rule 5-1-A1 specifies a listing of the permissible stress ranges, PS , for various categories of structural details based on 20 year minimum design fatigue life.

For vessels designed for a fatigue life in excess of the minimum design fatigue life of 20 years, the permissible stress ranges, PS, calculated above are given by:

$$PY[Y_r] = C(20/Y_r)^{1/m} PS \quad (\text{Eq.4.25})$$

where $PS[Y_r]$ = permissible stress ranges for the target design fatigue life of Y_r
 Y_r = target value in years of “design fatigue life” set by the applicant in five(5) year increments
 m = 3 for Class D through W of S-N curves
= 3.5 for Class C
= 4.0 for Class B
 C = correction factor related to target design fatigue life considering the two-segment S-N curves

4.4 Spectral based fatigue analysis

The purpose of *the Spectral-based Fatigue Analysis* is to accurately determine the dynamic response stresses for each sea state experienced by the structure. Perhaps it should be noted that this approach is only appropriate if there is very good sea state data available for the intended sea area of operation. *The Spectral-based Fatigue Analysis* method for selected structural locations can be categorized into the following components [25].

- Establish fatigue demand
- Determine fatigue strength or capacity
- Calculation fatigue damage or expected life

Through a vessel’s lifetime the irregular ocean waves are considered to be the main source of hull structure fatigue damage. The first steps of a spectral fatigue analysis is the determination of the stress range transfer function, $H(\omega, \beta)$, which expresses the relationship between the stress at a particular structural location with wave frequency and wave heading.

Many references and guidance are available for describing spectral based waves theory [21, 25, 27, 28].

4.4.1 Statistical description of wave

The linear modelling of the ship response to waves is generally used for fatigue assessment of ship structures. The response is described by a superposition of the response to all regular wave components that make up the irregular sea, leading to a frequency domain analysis. The resulting stresses are calculated as a summation of all contributing dynamic loads and load effects.

The wave elevation of a long-crested irregular sea propagating along the positive x-axis can be written as the sum of a large number of wave components.

Considering a long-crested irregular sea described by a sea spectrum $S(\omega)$, whose elevation is given by:

$$\xi(t) = \sum_{j=1}^{\infty} A_j \cos(k_j x - \omega_j t + \theta_j) \quad (\text{Eq.4.26})$$

where A_j = the j -th component of wave amplitude
 k_j = wave number = $2\pi / \lambda$
 λ = wave length
 ω_j = the j -th component of wave frequency = $2\pi / T_{\text{wave}}$
 T_{wave} = wave period
 θ_j = phase angle

For a linear system, the response spectrum $S_R(\omega)$ of stationary structure is given by:

$$S_R(\omega) = H^2(\omega, \beta)S(\omega) \quad (\text{Eq.4.27})$$

where H = response amplitude operator
 ω = wave frequency
 β = angle of wave attack

For ship with a forward speed U , the response spectrum is expressed by:

$$S_R(\omega_e) = H^2(\omega_e, \beta)S(\omega_e) \quad (\text{Eq.4.28})$$

where ω_e = the encountered wave frequency
 $= | \omega - kU \cos \beta |$
 k = wave number = ω^2 / g for deep water
 g = acceleration due to gravity

The wave energy of a random sea is independent of the ship's forward speed, thus

$$S(\omega_e)d\omega_e = S(\omega)d\omega \quad (\text{Eq.4.29})$$

The area m_0 of a response spectrum is expressed by:

$$m_0 = \int_0^{\infty} S_R(\omega_e)d\omega_e = \int_0^{\infty} H^2(\omega_e, \beta)S(\omega_e)d\omega_e \quad (\text{Eq.4.30})$$

or $m_0 = \int_0^{\infty} H^2(\omega_e, \beta)S(\omega)d\omega$

The second moment m_2 of the area of the response spectrum is given by:

$$m_2 = \int_0^{\infty} \omega_e^2 S_R(\omega_e) d\omega_e = \int \omega_e^2 H^2(\omega_e, \beta) S(\omega_e) d\omega_e \quad (\text{Eq.4.31})$$

or
$$m_2 = \int \omega_e^2 H^2(\omega_e, \beta) S(\omega) d\omega$$

The fourth spectral moment m_4 can be calculated as follows:

$$m_4 = \int \omega_e^4 H^2(\omega_e, \beta) S(\omega) d\omega \quad (\text{Eq.4.32})$$

4.4.2 Wave spectrum

The shape of the actual wave spectrum which is observed in the oceans varies depending on the geographical location, duration, wind, stage of growth and decay of a storm and existence of swells. *Bretschneider* [29] was the first to propose that the wave spectrum for a given sea state could be represented in terms of two parameters such as the wave height H and the average wave period T . Since then various other formula have been proposed. Among others, *the International Towing Tank Committee (ITTC)* and *JONSWAP* spectrums are reviewed in the following sections.

4.4.2.1 ITTC Spectrum

The International Towing Tank Conference [30, 31] suggested a modification of the *P-M spectrum* in terms of the significant wave height and zero crossing frequency, ω_z . *The ITTC spectrum* is formulated as:

$$S(\omega) = \alpha g^2 \omega^{-5} \exp\left[-\frac{4 \alpha g^2 \omega^{-4}}{H_s^2}\right] \quad (\text{Eq.4.33})$$

where ω = wave frequency

$$g = 9.81 \text{ m/s}^2$$

H_s = significant wave height

$$\alpha = \frac{0.0081}{k^4}$$

$$k = \frac{\sqrt{g/\sigma}}{3.54 \omega_z}$$

$$\omega_z = \text{zero crossing frequency} = \sqrt{\frac{m_2}{m_0}}$$

$$\sigma = \text{the standard deviation (r.m.s. value) of the water surface} \\ = \sqrt{m_0} = H_s / 4$$

4.4.2.2 JONSWAP spectrum

Hasselmann et al. [32] developed the *JONSWAP spectrum* during a joint North Sea

wave project. The formula for the *JONSWAP spectrum* can be written by modifying the *Pierson-Moskowitz* [33] formulation, given by:

$$S(\omega) = \alpha g^2 \omega^{-5} \exp[-1.25(\omega/\omega_0)^{-4}] \gamma^{\exp\left[-\frac{(\omega-\omega_0)^2}{2\tau^2\omega_0^2}\right]} \quad (\text{Eq.4.34})$$

where ω_0 = the peak wave frequency
 γ = peakedness parameter
 τ = shape parameter (τ_a for $\omega \leq \omega_0$ and τ_b for $\omega > \omega_0$)

Considering a prevailing wind field with a uniform velocity of U_w and a fetch of X , then the average values of these quantities are given by:

$$\begin{aligned} \gamma &= 3.30 && \text{may vary from 1 to 7} \\ \tau_a &= 0.07 \\ \tau_b &= 0.09 \\ \alpha &= 0.076(X_0)^{-0.22} && \text{with } \alpha = 0.0081 \text{ when } X \text{ is unknown} \\ X &= \text{fetch length} \\ X_0 &= \frac{g X}{U_w^2} \\ U_w &= \text{wind velocity} \end{aligned}$$

4.4.3 Short-term statistical analysis

It is clear that the magnitude of the wave induced response will reach a critical value within a few hours of exposure in a severe storm rather than as a normal induced load effect over a long period of time.

Many measurements of wave heights and peak to peak wave induced responses have been found to follow a Rayleigh distribution with a probability density function given by:

$$f(x) = \frac{2x}{R} \exp(-x^2 / R) \quad (\text{Eq.4.35})$$

where R is the mean square value of peak to peak random variable ($= 2m_0$).

The probability of exceeding the response amplitude value X is expressed by:

$$\Pr[x \geq X] = \int_X^\infty f(x) dx \quad (\text{Eq.4.36})$$

In case of the *Rayleigh distribution* the expression is formulated by:

$$\begin{aligned}
\Pr [x \geq X] &= \int_x^{\infty} \frac{2x}{R} \exp(-x^2 / R) dx = \int_x^{\infty} \left[-\frac{d}{dx} \exp(-x^2 / R) \right] dx & \text{(Eq.4.37)} \\
&= \left[-\exp(-x^2 / R) \right]_x^{\infty} \\
&= \exp[-X^2 / 2m_0]
\end{aligned}$$

The most probable extreme value x^{Extr} of response amplitude for a specific sea severity is given by the following formula [34]:

$$x^{Extr} = \sqrt{2m_0 \ln \left(\frac{2\sqrt{1-\varepsilon^2}}{1+\sqrt{1-\varepsilon^2}} N \right)} \quad \text{(Eq.4.38)}$$

where ε = bandwidth parameter = $\sqrt{1 - \frac{m_2^2}{m_0 m_4}}$

N = the number of responses in a given storm = $3600 n^{av} T$

n^{av} = the average number of responses per unit time as given by:

$$= \frac{1}{2\pi} \left(\frac{1 + \sqrt{1 - \varepsilon^2}}{2\sqrt{1 - \varepsilon^2}} \right) \sqrt{\frac{m_2}{m_0}}$$

When the risk of probability P_{risk} is considered, the design extreme value Q_D^{Extr} of response amplitude is expressed by:

$$Q_D^{Extr} = \sqrt{2m_0 \ln \left(\frac{\sqrt{1-\varepsilon^2}}{1+\sqrt{1-\varepsilon^2}} \frac{2N}{P_{risk}} \right)} \quad \text{(Eq.4.39)}$$

4.4.4 Long-term statistical analysis

A long-term analysis is one in which is considered all of the many weather conditions encountered by the structure and integrates all short-term statistical responses on the basis of the long-term joint probabilities of wave parameters and environment directional probabilities such as speed, heading, wave spectrum and sea states.

The probability density function of peak values of responses over the ship's lifetime is a weighted sum of the various short-term probability density functions. The long-term probability of exceeding the value X of dynamic wave induced response in the time of the ship structure can be formulated by:

$$P_r[x > X] = \frac{\sum_{ij} \sum_k \sum_l \sum_m n^{av} p_{ij} p_k p_l p_m \exp[-X^2 / 2m_0]}{\sum_{ij} \sum_k \sum_l \sum_m n^{av} p_{ij} p_k p_l p_m} \quad \text{(Eq.4.40)}$$

where p_{ij} = weighting factor for the joint probabilities of significant wave height and zero crossing period given in the wave scatter diagrams for a specific trade routes
 p_k = weighting factor for wave spectrum
 p_l = weighting factor for heading to waves in a given sea state
 p_m = weighting factor for ship speed in a given sea state and heading

Usually the long-term response probability distribution follows a *Weibull* probability distribution and which is given as:

$$P_r[x > X] = \exp\left[-(X/a_s)^b\right] \quad (\text{Eq.4.41})$$

where a_s = scale parameter
 b = shape parameter

The total number of dynamic wave induced responses expected in the life time of the ship structure can be expressed as:

$$n_L = \left(\sum_{ij} \sum_k \sum_l \sum_m n^{av} p_{ij} p_k p_l p_m \right) \times 3600 T \quad (\text{Eq.4.42})$$

where T = the total exposure time of the structure to seas in hours

The probability of exceeding the extreme amplitude value Q_D^{Extr} of dynamic wave induced response can be obtained from following formula:

$$P_r[x > Q_D^{Extr}] = \frac{P_{risk}}{n_L} \quad (\text{Eq.4.43})$$

4.5 Time variant fatigue assessment of AFRAMAX shuttle tanker

Most of fatigue induced fracture damages in ship structures can be found on the ship side, ship's bottom and tank boundaries where high stresses and cyclic loads are expected. Fig. 4.3 illustrates typical fatigue crack locations in tanker structures, Fig. 4.4 illustrates typical midship section of an existing double hull tanker and Fig. 4.5 shows local geometry details of typical sideshell longitudinal stiffener (No. 38).

The principal dimensions and load conditions for example double hull tanker are as follows:

Length of ship (L.B.P)	L	= 219.08 m
Breadth of ship	B	= 42.0 m
Depth (Moulded)	D_{Depth}	= 21.3 m
Scantling Draft(Moulded)	T_{Load}	= 14.5 m

Ballast Draft	T_{Bal}	= 7.52 m
Block coefficient	C_B	= 0.8063
Design speed	V	= 14.7 knot
Neutral axis above keel	$H_{N.A}$	= 9.142 m
Vertical sectional modulus at deck line	Z_v	= $28.86 m^3$
Horizontal sectional modulus at ship side	Z_h	= $48.93 m^3$
Metacentric height in loaded condition	GM_{Load}	= 5.04 m
Metacentric height in ballast condition	GM_{Bal}	= 13.86 m
Roll radius of gyration in loaded condition	K_{R-Load}	= 16.38 m
Roll radius of gyration in ballast condition	K_{R-Bal}	= 16.38 m
Fraction of time in load condition	P_{Load}	= 0.45
Fraction of time in ballast condition	P_{Load_Bal}	= 0.40

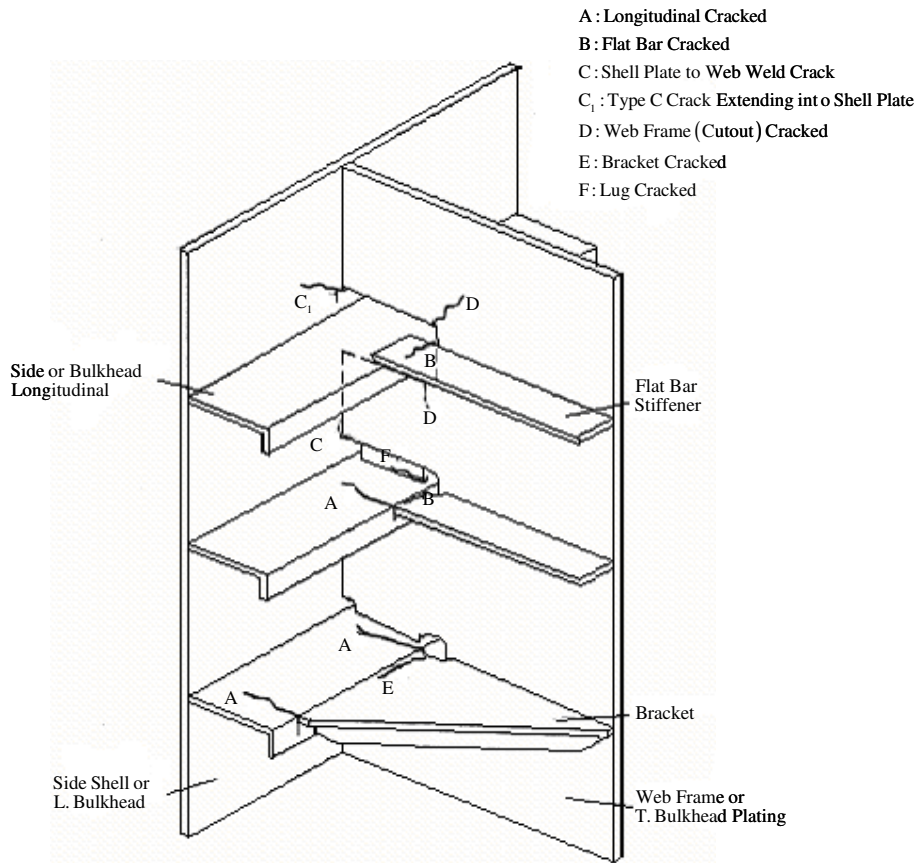


Fig. 4.3. Typical Fatigue Crack Locations in Tanker Structures [8]

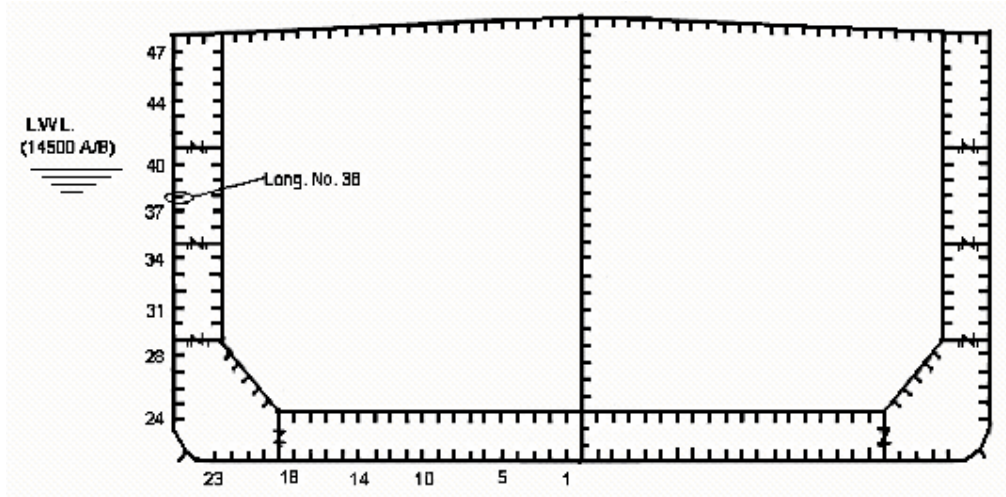


Fig. 4.4. Typical midship section

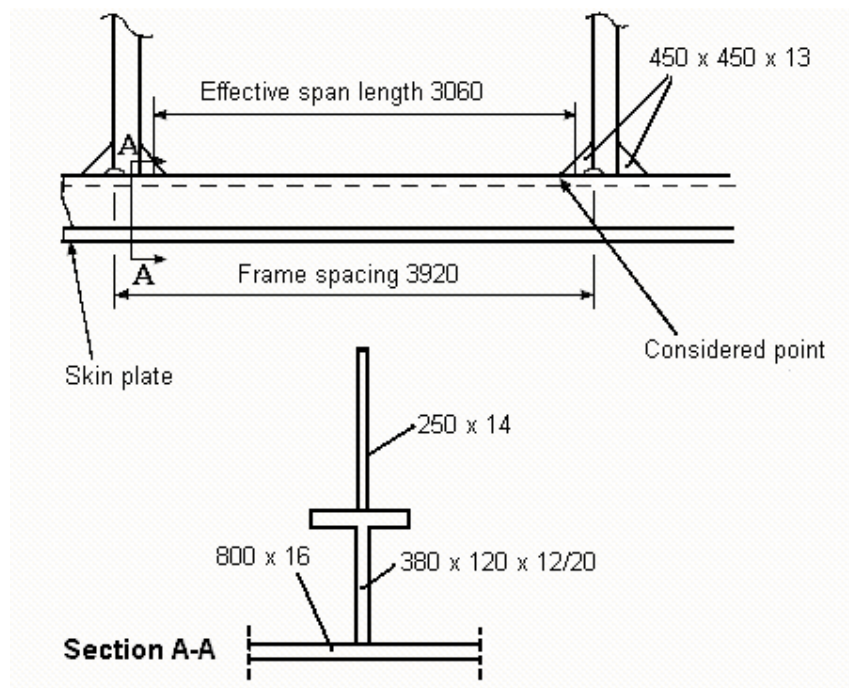


Fig. 4.5. Details of longitudinal stiffener on ship sideshell (stiffener No. 38)

The detail dimensions and geometries of typical sideshell longitudinal stiffener in ballast tanks (No. 38) are as follows and the full geometries of ship sideshell stiffeners are given in Appendix A:

Stiffener sectional modulus at top of flange	Z_s	= 0.001268 m^3
Distance above keel	z	= 13.3 m
Length of bracket side	b_{br}	= 450 mm

Web frame spacing	l_s	= 3920 mm
Stiffener spacing	s_f	= 800mm
Thickness of ship sideshell plate	t_p	= 16.0 mm
Height of stiffener	h	= 380 mm
Thickness of web	t_w	= 12 mm
Width of flange	b_f	= 120 mm
Thickness of flange	t_f	= 20 mm
Thickness of bracket	t_b	= 13 mm
Thickness of transverse frame plating	t_{fr}	= 15 mm
Distance from neutral axis to top flange	z_{01}	= 294 mm

The above geometries of the stiffener are based on the designed values, however *DNV* [21] requires that the stress calculation should be based on the reduced scantling and thus the corrosion allowance should be subtracted from the original as-built values. All stress calculations are thus considered with the deduction of corrosion allowance which is required by *DNV Rules Pt.3, Ch.1, Sec.2, D200* [35].

An existing *AFRAMAX* double hull shuttle tanker, based on a design target fatigue life of 20 years, has been investigated to evaluate the actual fatigue life of the various ship sideshell longitudinal stiffeners in accordance with the *DNV* method [21] as described earlier in section 4.3.1. The detailed procedures of fatigue assessment have been introduced in recent publication by Ok and Pu [36].

The following geometry properties are defined for the sideshell longitudinal stiffeners. The full geometries of ship sideshell stiffeners in the ballast tank are given in Appendix A.

- Stiffener number 45 ~ 46 : 250 x 90 x 11/16 mm (L-type angle)
- Stiffener number 43 ~ 44 : 300 x 90 x 11/16 mm (L-type angle)
- Stiffener number 30 ~ 42 : 380 x 120 x 12/20 mm (T-type angle)
- Stiffener number 25 ~ 28 : 380 x 120 x 12/24 mm (T-type angle)

No.25 to No.46 ship side shell longitudinal stiffeners have been investigated to assess their individual fatigue life based on both as a *North Sea* operating shuttle tanker and as a *World Wide* operating crude oil tanker. Total 57 sets of fatigue assessment have been performed as in Table 4-1.

Fig. 4.6 (DSD) illustrates the predicted cumulative fatigue life based on a shuttle tanker operating in the North Sea in accordance with the *DNV* method. The dynamic pressure amplitude is taken as the largest of the combined pressure dominated by pitch motion in head/quartering seas, or the combined pressure dominated by roll motion in beam/quartering seas. Longitudinal stiffeners no. 43 to 47 show the relatively high cumulative fatigue damage ratio due to the higher vertical global stress range than others and the difference of geometric properties (L-type angle) from

longitudinal stiffeners no.30 to 42 (T-type angle). Fig. 4.7 (DSP) also indicates the predicted cumulative fatigue life based on the vessel operating as a North Sea shuttle tanker. But in this case it is assumed that the dynamic pressure amplitude is dominated by pitch motion in head/quartering seas without considering roll motion in beam/quartering seas. Fig. 4-8 (DWD) shows the predicted fatigue life based on the vessel operating as a World Wide operating crude oil tanker in accordance with the DNV method. The dynamic pressure amplitude is taken as the largest of the combined pressure dominated by pitch motion in head/quartering seas, or the combined pressure dominated by roll motion in beam/quartering seas.

The results show that the fatigue life of longitudinal stiffeners near the upper deck (stiffener no.43 ~ 46) is considerably shorter than for other locations. This is caused by a relatively higher vertical global stress range and small geometry property of stiffeners than at other locations. And also longitudinal stiffener no.32, which is located between the design load water line and the ballast load water line, shows the relatively short fatigue life than other locations.

The details of calculated values of lives are shown in Table 4-1 and Fig. 4-9.

Table 4-1
Fatigue lives of ship side shell longitudinal stiffeners

Stiffener no.	DSD	DSP	DWD
46	28.02 years	28.65 years	45.52 years
45	29.53 years	31.59 years	48.23 years
44	33.52 years	37.25 years	54.56 years
43	33.81 years	39.96 years	54.95 years
42	59.40 years	66.31 years	96.76 years
40	66.89 years	83.51 years	109.11 years
39	69.93 years	94.38 years	113.96 years
38	63.57 years	107.58 years	103.25 years
37	55.74 years	107.58 years	91.05 years
36	49.47 years	100.55 years	80.13 years
34	38.85 years	87.91 years	63.05 years
33	34.57 years	79.71 years	56.35 years
32	31.79 years	73.96 years	51.80 years
31	31.59 years	73.61 years	51.28 years
30	31.53 years	71.56 years	51.45 years
28	41.47 years	81.83 years	67.48 years
27	44.08 years	75.41 years	71.89 years
26	46.76 years	68.38 years	76.16 years
25	48.69 years	61.05 years	79.30 years

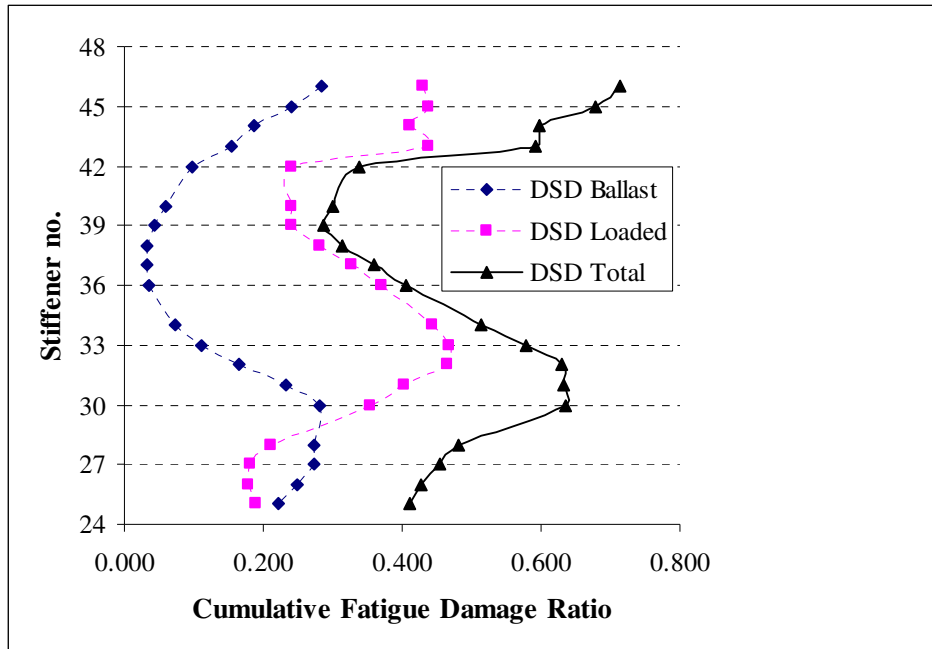


Fig. 4.6. Cumulative fatigue damage ratio of North Sea operating shuttle tanker (DSD)

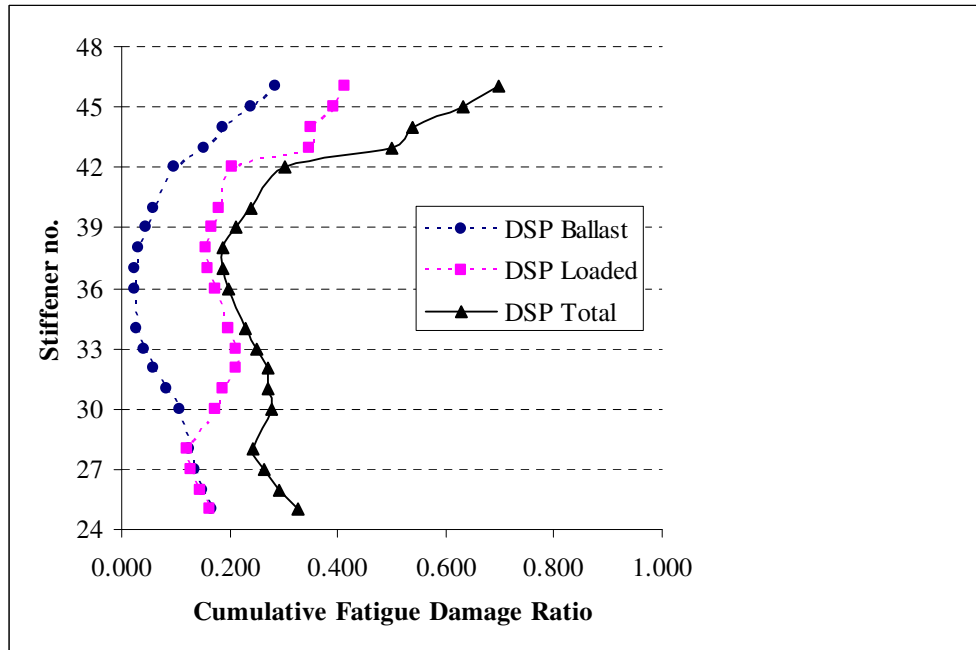


Fig. 4.7. Cumulative fatigue damage ratio of North Sea operating shuttle tanker (DSP)

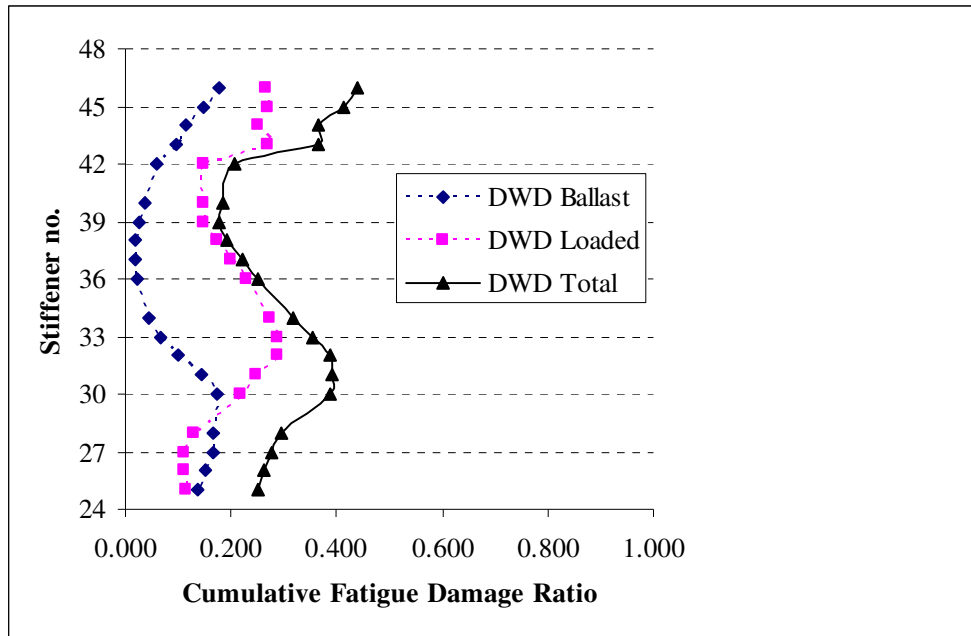


Fig. 4.8 Cumulative fatigue damage ratio of World Wide operating crude oil tanker (DWD)

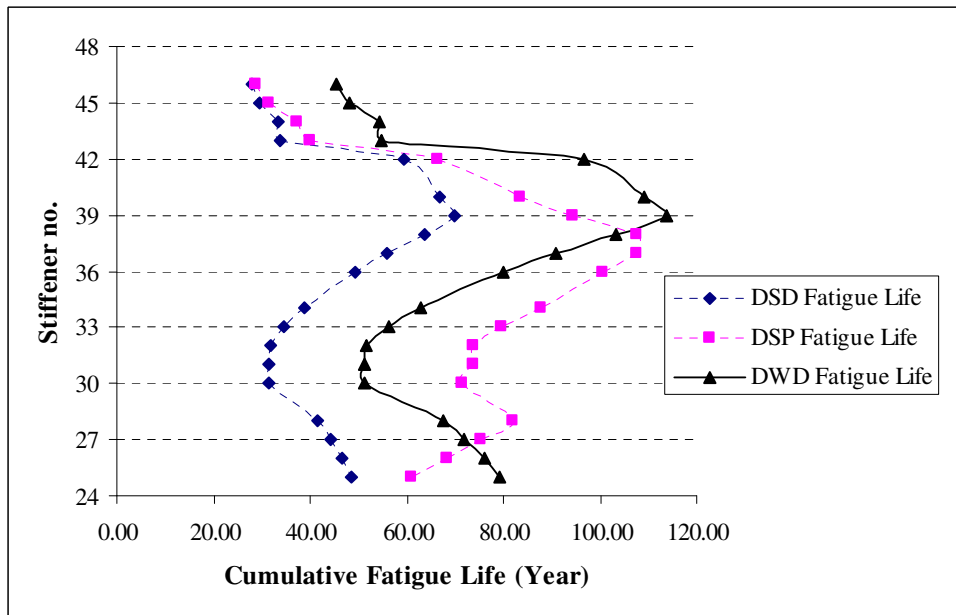


Fig. 4-9. Fatigue Life in Years for various cases

4.6 Fatigue assessment based on corrosion degradation model

Both the *DNV Model* [21] as specified in *section 4.5* and other *Classification Societies* fatigue assessment procedures are based on reduced scantling and accordingly the corrosion allowance which is required by each Classification Society should be subtracted from the as-built scantlings before the calculation of the fatigue life.

Recently IACS [37] published unified new rule, so called “Common Structural Rules of Double Hull Oil Tanker” for double hull oil tanker of 150m length and upward classed with the society and contracted for construction on or after 1st April 2006. IACS specifies that the scantlings and stresses used for the fatigue assessment are to be taken as the representative mean value over the design life. The mean corrosion over the design life is given as half the corrosion assumed for scantling strength assessment. Local stresses are thus calculated based on half the full local corrosion addition and hull girder stresses are calculated based on half the overall global corrosion. Half the global overall corrosion is found by deduction of one quarter of the full local corrosion addition of all structural elements simultaneously.

Another consideration of fatigue damage to account for corrosion protection and degradation of structure exposed to a corrosive environment is proposed by *DNV* [21]. However, for more accuracy, it is necessary to evaluate the consequences of an actual corrosion degradation model on fatigue life assessment. The *WANG’s* model and the average model (*PW* model), which is introduced in *Chapter 3*, are used to investigate the differences between *DNV* guidance on fatigue assessment and more meaningful corrosion degradation models using calculations based on ship sideshell longitudinal stiffener number 32.

The time-variant vertical hull girder section modulus degradation model uses the new equation which is proposed in *section 3.5.1* and the time-variant horizontal section modulus degradation model uses the new equation in *section 3.5.2*. All corrosion degradation data in this chapter is based on *WANG’s* model and *PW’s* model as proposed in *Chapter 3*.

The overall fatigue assessment procedures are followed *DNV* method [21] as described in *section 4.3.1*. Table 4-2 and Table 4-3 show the time-variant design value for fatigue assessment based on the *North Sea* operating shuttle tanker. And Table 4-4, Table 4-5 and Table 4-6 show accumulated fatigue life based on *DNV* model, *WANG’s et al.* model and *PW* model.

Table 4-2
Time variant design values based on *WANG’s et al.* model

Description	Original design value	DNV value	WANG 20 years	WANG 25 years	WANG 30 years
Z_V	28.86 m^3	28.86 m^3	26.74 m^3	26.21 m^3	25.67 m^3
Z_H	48.93 m^3	48.93 m^3	45.18 m^3	44.40 m^3	43.63 m^3
Z_S	0.00140 m^3	0.00127 m^3	0.00135 m^3	0.00134 m^3	0.00132 m^3
t_p	16.0 mm	14.5 mm	15.36 mm	15.14 mm	14.93 mm
t_w	12.0 mm	10.5 mm	11.37 mm	11.16 mm	10.95 mm

t_f	20.0 mm	18.5 mm	19.52 mm	19.36 mm	19.20 mm
t_b	13.0 mm	11.5 mm	12.36 mm	12.14 mm	11.93 mm
t_{fr}	15.0 mm	13.5 mm	14.36 mm	14.14 mm	13.93 mm
z_{01}	293.97 mm	293.54 mm	293.46 mm	293.32 mm	293.00 mm

Table 4-3
Time variant design values based on average (PW) model

Description	Original design value	DNV value	PW 20 years	PW 25 years	PW 30 years
Z_v	28.86 m^3	28.86 m^3	26.56 m^3	25.97 m^3	25.38 m^3
Z_H	48.93 m^3	48.93 m^3	44.46 m^3	43.43 m^3	42.40 m^3
Z_S	0.00140 m^3	0.00127 m^3	0.00131 m^3	0.00129 m^3	0.00126 m^3
t_p	16.0 mm	14.5 mm	15.26 mm	15.02 mm	14.77 mm
t_w	12.0 mm	10.5 mm	10.77 mm	10.36 mm	9.95 mm
t_f	20.0 mm	18.5 mm	19.19 mm	18.92 mm	18.65 mm
t_b	13.0 mm	11.5 mm	12.26 mm	12.02 mm	11.77 mm
t_{fr}	15.0 mm	13.5 mm	14.26 mm	14.02 mm	13.77 mm
z_{01}	293.97 mm	293.54 mm	294.93 mm	295.32 mm	295.68 mm

Table 4-2 and 4-3 indicate that the DNV guideline uses fixed section modulus in their hull girder bending stress calculation whereas applied corrosion models use different section modulus values in each design life. However corrosion rates of local plate and stiffener in DNV guideline shows more conservative values than that of applied corrosion models (Wang's et al. and PW models) which is based on 30 years design life. This reveals that current corrosion margins in DNV guideline have adopted much higher values of corrosion degradation rates than actual statistics based existing corrosion models and data.

Table 4-4
The accumulated fatigue life based on DNV model assuming 5 years effective corrosion protection period

Description	20 years	25 years	30 years
D_{Loaded}	0.704	0.924	1.109
$D_{Ballast}$	0.252	0.332	0.397
D_{Total}	0.956	1.256	1.506
T_{Life}	20.92 years	19.90 years	19.92 years

Table 4-5
The accumulated fatigue life based on WANG's *et al.* model

Description	20 years	25 years	30 years
D_{Loaded}	0.344	0.442	0.540
$D_{Ballast}$	0.125	0.160	0.195
D_{Total}	0.469	0.602	0.735
T_{Life}	42.64 years	41.53 years	40.82 years

Table 4-6
The accumulated fatigue life based on average (PW) model

Description	20 years	25 years	30 years
D_{Loaded}	0.364	0.476	0.599
$D_{Ballast}$	0.131	0.170	0.212
D_{Total}	0.495	0.646	0.811
T_{Life}	40.40 years	38.70 years	36.99 years

The results of Table 4-4, Table 4-5 and Table 4-6 show that the accumulated fatigue life based on DNV model assuming 5 years effective corrosion protection period is noticeably shorter than that of existing corrosion models. This is because that DNV recommendation has very conservative level of corrosion environment factor, D_{corr} , which is to be considered in final calculation of design life.

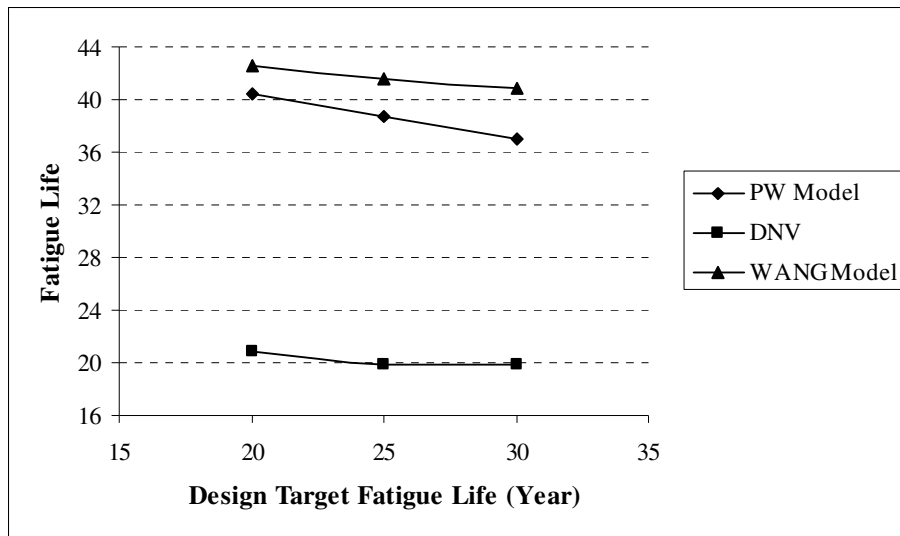


Fig. 4.10. Comparison of fatigue life

Fig. 4.10 illustrates overall comparison of fatigue life for each model. The results indicates that the fatigue life based on *DNV Notes no.30.7* is noticeably shorter than

that of existing corrosion models such as WANG's model and PW model. If the fatigue life is less than design target life, this means that the fatigue failure is to be expected in calculated structural details. Accordingly the design target life of 25 years and 30 years can be considered structurally unsafe condition for ship sideshell longitudinal stiffener number 32 in accordance with DNV guidelines.

4.7 Concluding remarks

Fatigue is the progressive failure under cyclic loading and it is a mode of degradation in which the steel resists until it fails. Fatigue commences as soon as a vessel enters into service and begins to experience wave induced cyclic stresses. Considering the effectiveness of any protective paints or coatings for the first few years of service, the cyclic stresses are a function of the as-manufactured scantlings. As corrosion commences and spreads, resulting in reductions in structural members, then the stress levels in both overall and local levels increase accordingly. As Eq.4.2 shows, if the negative inverse slope of S-N curve, m , is considered 3 and the applied stress range, S , increases by 5%, then the corresponding number of cycles to failures, N , decreases by 13% illustrating that fatigue life decreases at a higher rate as corrosion rates increase. Additionally corrosion may accelerate fatigue damage by creating additional highly localized stress concentration on structural details.

The deduction rate of corrosion allowance from as-built scantling is important factor which affects total fatigue life of ship structures. Currently the *Classification Societies* fatigue assessment procedures are based on reduced scantling and accordingly the corrosion allowance which is required by each Classification Society should be subtracted from the as-built scantlings before the calculation of the fatigue life. Recently IACS [37] specifies that local stresses should be calculated based on half of local corrosion allowance and hull girder stresses should be calculated by deduction of one quarter of the full local corrosion addition of all structural elements simultaneously. However current general recommendations by IACS [37] and each Classification Society show very high level of corrosion margins than actual data from existing corrosion models [38, 39] which were based on hundreds of existing single hull tankers. Some recent studies also found that the corrosion rate of double hull tanker is much less than that of single hull tankers [40, 41]. This means that current IACS [37] and each Classification Society recommendation can be considered somewhat conservative to adopt as an actual corrosion degradation model and actual fatigue assessment model for ageing double hull tankers. It is true that fatigue life is more affected by structural details, location and connection details etc. than the effect of uniform corrosion on the structure. However it would be valuable to calculate fatigue life based on expected corrosion rates from existing corrosion models and compare with IACS [37] and each Classification Society requirements in order to decide maintenance programme and period in ageing ships.

This Chapter has reviewed the general historical background and development of fatigue damage assessment methodologies and the guidance of the Classification Societies (IACS, DNV, ABS).

An existing *AFRAMAX* double hull shuttle tanker, based on a design target fatigue life of 20 years, has been investigated to evaluate the actual fatigue life of the various ship sideshell longitudinal stiffeners in accordance with the *DNV* method [21]. The detailed procedures of fatigue assessment have been introduced in recent publication by Ok and Pu [36]. No.25 to No.46 ship side shell longitudinal stiffeners have been investigated to assess their individual fatigue life based on both as a *North Sea* operating shuttle tanker and as a *World Wide* operating crude oil tanker. Total 57 sets of fatigue assessment have been performed as in Table 4-1. The results show that the fatigue life of longitudinal stiffeners near the upper deck (stiffener no.43 ~ 46) is considerably shorter than for other locations. This is caused by a relatively higher vertical global stress range and small geometry property of stiffeners than at other locations. And also longitudinal stiffener no.32, which is located between the design load water line and the ballast load water line, shows the relatively short fatigue life than other locations.

Another consideration of fatigue damage to account for corrosion protection and degradation of structure exposed to a corrosive environment is proposed by *DNV* [21]. However, for more accuracy, it is necessary to evaluate the consequences of an actual corrosion degradation model on fatigue life assessment. The *WANG's* model and the average model (PW model) are used to investigate the differences between *DNV* guidance on fatigue assessment and more meaningful corrosion degradation models using calculations based on ship sideshell longitudinal stiffener number 32. The time-variant vertical/horizontal hull girder section modulus degradation model uses the new equation which is proposed in *section 3.5.1* and in *section 3.5.2*.

The *DNV* guideline uses fixed section modulus in their hull girder bending stress calculation whereas the applied corrosion models use different section modulus values in each design life. However corrosion rates of local plate and stiffener in *DNV* guideline shows more conservative values than that of applied corrosion models (Wang's et al. and PW models) which is based on 30 years design life. This reveals that current corrosion margins in *DNV* guideline have adopted much higher values of corrosion degradation rates than actual statistics based existing corrosion models and data. The results show that the accumulated fatigue life based on *DNV* model assuming 5 years effective corrosion protection period is noticeably shorter than that of existing corrosion models. This is because that *DNV* recommendation has very conservative level of corrosion environment factor, D_{corr} , which is to be considered in final calculation of design life.

It is recommended that further research works are necessary to develop the first principle based spectral fatigue assessment methodology which considers annual degradation of corrosion on each structural member, time-variant vertical and horizontal section modulus degradation and time-variant stress change.

References (Chapter 4)

1. Bolotin, V.V., *Mechanics of Fatigue*. 1998.
2. Miner, M.A., *Cumulative damage in fatigue*. Journal of Applied Mechanics, 1945(67): p. 159-164.
3. Munse, W.H., et al., *Fatigue Characterization of Fabricated Ship Details for Design*. Ship Structure Committee, SSC-318, 1982.
4. Burnside, O.H., et al., *Long-Term Corrosion Fatigue of Welded Marine Steels*. Ship Structure Committee, SSC-326, 1984.
5. Cramer E.H, Schulte-Strauthaus R., and B. R.G., *Structural Maintenance Project Vol.1 Fatigue Damage Evaluation*. Ship Structure Committee, SSC-386-I, 1995.
6. Capanoglu, C.C., *Fatigue Design Procedures*. Ship Structure Committee, SSC-367, 1992.
7. Bea, R.G. and T. Xu, *SMP Vol. 2 - Study of Fatigue of Proposed Critical Structural Details in Double Hull Tankers*. Ship Structure Committee, SSC-395-II, 1997.
8. Glen, I.F., et al., *Fatigue resistant detail design guide for ship structures*. Ship Structure Committee, SSC-405, 1999.
9. Dexter, R.J. and P.J. Pilarski, *Effect of Welded Stiffeners on Fatigue Crack Growth Rate*. Ship Structure Committee, SSC-413, 2000.
10. Sielski, R.A., J.R. Wilkins, and J.A. Hulst, *Supplemental Commercial Design Guidance for Fatigue*. Ship Structure Committee, SSC-419, 2001.
11. Dexter, R.J., R.J. FitzPatrick, and D.L.S. Peter, *Fatigue Strength and Adequacy of Weld Repairs*. Ship Structure Committee, SSC-425, 2003.
12. Xue, J., A. Pittaluga, and D. Cervetto, *Fatigue damage calculation for oil tanker and container ship structures*. Marine Structures, 1994. 7(6): p. 499-535.
13. Cramer, E.H. and P.F. Hansen, *Stochastic modeling of long term wave induced responses of ship structures*. Marine Structures, 1994. 7(6): p. 537-566.
14. Hansen, P.F. and S.R. Winterstein, *Fatigue damage in the side shells of ships*. Marine Structures, 1995. 8(6): p. 631-655.
15. Fricke, W., et al. *Technical Committee III.2, Fatigue and Fracture*. in *Proceeding of the 14th International Ship and Offshore Structures Congress*. 2000. Nagasaki, Japan: ISSC.
16. Brennan, F., et al. *Technical Committee III.2, Fatigue and Fracture*. in *Proceedings of the 15th International Ship and Offshore Structures Congress*. 2003. San Diego, USA: ISSC.
17. Fatemi, A. and L. Yang, *Cumulative fatigue damage and life prediction theories: a survey of the state of the art for homogeneous materials*. International Journal of Fatigue, 1998. 20(1): p. 9-34.
18. Fricke, W., S. Berge, and F. Brennan, *Technical Committee III.2: Fatigue and fracture*. 14th International Ship and Offshore Structures Congress, October 2000, **Volume 1**: p. 323-392.
19. Brennan, F., W. Cui, and L. Josefson, *Committee III.2: Fatigue and Fracture*. 15th International Ship and Offshore Structures Congress, August 2003. **Volume 1**: p. 329-391.

20. Fricke, W., *Fatigue analysis of welded joints: state of development*. Marine Structures, 2003. **16**(3): p. 185-200.
21. DNV, *Fatigue assessment of ship structures*. Det Norske Veritas, 2003. **Classification Note No 30.7**.
22. IACS, *Fatigue Assessment of Ship Structures*. International Association of Classification Societies, 1999. **Recommendation No.56**.
23. Class NK, *Guidelines for Tanker Structures*. 2001.
24. ABS, *Guide for Fatigue Strength Assessment of Tankers*. ABS Rule 2004, 2004. **part 5, Chapter 1, Appendix 1**.
25. ABS, *Spectral based Fatigue Analysis for Vessels*. ABS Guidance Notes 2004, 2004.
26. Cramer, E.H., R. Loseth, and K. Olaisen, *Fatigue assessment of ship structures*. Marine Structures, 1995. **8**(4): p. 359-383.
27. Faltinsen, O.M., *Sea loads on ships and offshore structures*. 1st ed. 1993: Cambridge University Press.
28. Hughes, O.F., *Ship Structural Design: A Rationally Based, Computer-Aided Optimization Approach*. 1988.
29. Bretschneider, C.L., *Wave variability and wave spectra for wind-generated gravity waves*. Beach Erosion Board, U.S. Army Corps of Engineers, Technical Memorandum No.118, 1959.
30. ITTC. *Recommendations of the 11th International Towing Tank Conference*. in *Proceedings 11th ITTC*. 1966. Tokyo.
31. Mathews, S.T. *A critical review of the 12th ITTC Wave Spectrum Recommendations, Report of Seakeeping Committee, Appendix 9*. in *Proceedings 13th ITTC*. 1972. Berlin.
32. Hasselman et al., K. *Measurement of wind-wave growth and swell decay during the Joint North Sea Wave Project (JONSWAP)*. in *Deutschen Hydrographischen Zeitschrift*. 1973. Ergänzungsheft.
33. Pierson, W.J. and L. Moskowitz, *A proposed spectral form for fully developed wind seas based on the similarity theory of S. A. Kitaigorodskii*. Journal of Geophysical Research, 1964. **69** (24): p. 5181-5203.
34. Ochi, M., *On prediction of extreme values*. Journal of Ship Research, 1973: p. 29-37.
35. DNV, *Rules for Ships*. Det Norske Veritas, 2004b. **Part 3, Ch.1, Sec.2, D200**.
36. Ok, D. and Y. Pu, *Fatigue assessment for ageing double hull tanker*. 2005, MARSTRUCT EU Project (Project No. FP6-PLT-506141) Report MAR-W2-4-UNEW-2(1).
37. IACS, *Common Structural Rules for Double Hull Oil Tankers*. 2006.
38. Wang, G., J. Spencer, and T. Elsayed, *Estimation of Corrosion Rates of Structural Members in Oil Tankers*. International Conference on Offshore Mechanics and Arctic Engineering, CANCUN, MEXICO, 2003. **22nd**.
39. Paik, J.K., et al., *A Time-Dependent Corrosion Wastage Model for the Structures of Single and Double-Hull Tankers and FSOs and FPSOs*. Marine Technology, 2003. **Vol.40, No.3**: p. 201-217.
40. Yoneya, T., et al., *A Comprehensive Study on the Practical Strength Assessment of Tanker and Bulk Carrier Structures*. Nippon Kaiji Kyokai, Tokyo, 2003.

41. Bergesen, D.Y.A., *Experience with Double Hull Tankers: an Owner's ViewPoint*. Tank Structure Co-Operative Forum, October 2000, Tokyo.
42. ABS, *Spectral based Fatigue Analysis for Vessels*. ABS Guidance Notes 2004..

Chapter 5

The Effects of Localized Corrosion on Strength Degradation of Unstiffened Plates

5.1 Introduction

The failure of a ship structure is often caused by overall or local buckling and subsequent plastic collapse of highly stressed structural components such as deck or bottom structures.

Steel plates under predominantly axial tensile loads would fail by gross yielding, whereas the behaviour of steel plates under predominantly compressive loads can be classified into five regimes, namely pre-buckling, buckling, post-buckling, collapse (ultimate strength) and post-collapse [1]. The pattern of collapse in plates is different from columns, typically plate buckled in the elastic regime is still supporting the applied load until it reaches ultimate strength. As the load further increases the maximum stress at the sides of plates increases and the plates finally reach the collapse due to expansion of the yield region. The peak value of applied load is referred to as the ultimate strength of the plate. The principal parameters which can influence plate collapse are: geometric and material properties, type of loading, boundary conditions, initial deflection, residual stresses and local defects caused by corrosion and fatigue cracks etc.

Over the past decades many research activities have been performed to estimate buckling and ultimate strength of unstiffened plates. The structural behaviour of unstiffened plates is well understood. However the knowledge on the strength of plates with defects, such as cracks and corrosion, is quite limited.

Paik et al. [13-16] performed series of mechanical crack propagation tests and FE analyses based on steel plates with pre-existing cracks under monotonically increasing tensile loads and also plates with pitting corrosion under axial compressive loads and edge shear. They suggested that the ultimate strength of a steel plate with pit corrosion under edge shear is governed by the degree of pit corrosion intensity. Whereas the ultimate strength of a pitted plate element under axial compressive loads is governed by the smallest cross section area. They also proposed some empirical simplified formula to estimate the ultimate strength of plate under defects. *Hu et al.* [3, 17] investigated the influence of crack damage on the residual strength of both plates and stiffened panels and the time-variant ultimate strength and reliability of ship hull girder under the degradation of corrosion and fatigue. They used the FE method to find out the effects of fatigue cracks on the tensile and compressive residual ultimate strength of stiffened panels and unstiffened plates and proposed some empirical formulae for effective calculation of the compressive or tensile ultimate strength of cracked or intact unstiffened plates or stiffened panels. They

introduced empirical formula for the ultimate strength of cracked plates based on FE modelling.

British Standard [18] recommends the reference stress concept for failure assessment of the flawed structures or components.

Generally in the case of uniform corrosion, the buckling or ultimate strength of stiffened and unstiffened plates can be easily estimated by simply reducing the plate element thicknesses from their original values. Several empirical formulae are available to obtain the ultimate strength of plates under general corrosion [1, 19-23]. However the calculation of strength degradation due to localized defects, such as pitting corrosion, are more difficult and complicated than general area-wide corrosion and there have been relatively few research activities and guidelines that have been published until now [24-26].

Diadora et al. [27] proposed that an initial determination of the acceptability of a plate panel with pitting can be made on the basis of the pit depths. They proposed that individual pits with a depth less than 50% of the residual thickness can be repaired by filling with epoxy and individual pits with a depth greater than 50% of the residual thickness may be welded if at least 6.5 mm of material remains at bottom of pit, the distance between adjacent pits is at least 76 mm, the maximum diameter of any welded pit does not exceed 305 mm and the total cross sectional area lost in any section through the pitted plate should not be more than 15% of the original cross sectional area. *IACS S31* [28] specifies that if pitting intensity is higher than 15% in surface area, thickness measurement is to be taken to check pitting corrosion and the minimum acceptable remaining thickness in pits or grooves is equal to; 75% of the as-built thickness for pitting or grooving in the frames, brackets, webs and flanges or 70 % of the as built thickness for pitting or grooving in the side shell, hopper tank and topside tank plating attached to the side frame, over a width up to 30 mm from each side of it. *IACS Z10.1* [29] also requires that any bottom plate with a pitting intensity of 20% or more, with wastage in the substantial corrosion range or having an average depth of pitting of 1/3 or more of actual plate thickness is to be noted. Recently *IACS* [30] introduced the assessment of local wastage in “Common Structural Rules for Double Hull Oil Tankers”. The details of new rule requirements are introduced in Chapter 3, Section 3.3.5.

Paik et al. [14, 15, 31] performed a series of experimental and numerical studies on steel plated structure, with pits, under axial compressive loads and under edge shear. A simplified strength knockdown factor for plates with various pitting corrosion was introduced using the formulation of Eq.3.26 and Eq.3.27 in Chapter 3. However in their study, the effects of different pitting locations and pitting lengths, which may contribute significantly to the strength reduction, were not considered.

Dunbar, Pegg et al. [32] investigated the effect of localized corrosion in stiffened plates by finite element analyses. A stiffened plate was divided into four main sections, each of which was further divided into four sub-sections in the longitudinal direction and three sub-sections in the transverse direction. Reductions of 10%, 50% and 75% by volume of the initial plate thickness over individual local sub-sections

were applied and it was found that 10% of corrosion has little effect on the ultimate strength of stiffened plate. Corrosion at higher levels (50% and 75% volume) caused local buckling at the corroded region, which then affected the global collapse mode of the stiffened panel and the ultimate load was further decreased as the corrosion location was closer to the centre of the panel span. However some of the above conclusions contradict with existing knowledge. When a slender plate is under compression, the material near the edges would normally take most of the loading while the material in the central area is less effective than those near the edges. So it would be expected that the damage/corrosion around the central area would have less weakening effects on the strength of a panel. A study of the effects of perforations on the ultimate strength showed that the ultimate compressive strength of plates with edge holes is considerably smaller than that with a central hole [33].

Based on the above discussions it is obvious that there is a need for further research to systematically investigate the effects of plate slenderness, pitting location, length, breadth and depth on the ultimate strength of plate under inplane loading and to develop empirical formulae which include all the important parameters.

5.2 The Parameters which influence the strength

As mentioned earlier, the principal parameters which can influence plate strength are: geometric and material properties, type of loading, boundary conditions, welding induced initial deflection, residual stresses and local defects caused by corrosion and fatigue cracks etc. Among others, the assumed typical value of welding induced initial deflection and residual stresses can be variable in accordance with individual designer or engineer's opinion, experience and the purpose of the each project. In this section, the background and relationship of welding induced initial deflections, residual stress and local defects are reviewed in order to accurately assess corresponding plate strength.

5.2.1 Deflections due to Welding

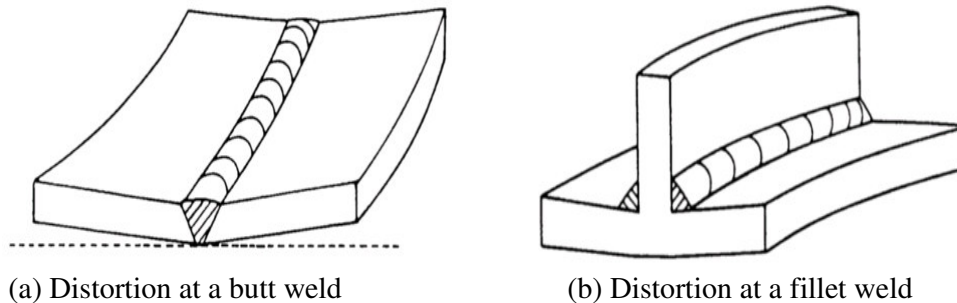


Fig. 5.1. Classification of welding deformation

Generally the shape of welding-induced initial deflections of steel plates between adjacent parallel stiffeners can be expressed as follows [1];

$$\frac{w_0}{w_{0pl}} = \sum \sum B_{0ij} \sin \frac{i\pi x}{a} \sin \frac{j\pi y}{b} \quad (\text{Eq.5.1})$$

where a = plate length
 b = plate breadth
 w_0 = initial deflection function = $\delta_0 \sin \frac{\pi x}{L}$
 δ_0 = initial deflection amplitude
 which is often taken as $0.0015L$ for practical strength calculation
 L = member length between supports
 B_{0ij} = welding-induced initial deflection amplitude
 w_{0pl} = value of maximum initial deflection
 i, j = half wave numbers in the x and y directions

For a long plate with a multi-wave shape in the x (longitudinal) direction and one half wave in the y direction, Eq.5.1 becomes;

$$\frac{w_0}{w_{0pl}} = \sum_{i=1}^M B_{0i} \sin \frac{i\pi x}{a} \sin \frac{\pi y}{b} \quad (\text{Eq.5.2})$$

Paik and Pedersen [34] proposed initial deflection amplitudes for various initial deflection shapes [1].

Through a large number of measurements on frigates, *Faulkner* [19] suggested the mean value of plate central deflection by:

$$\frac{w_{0pl}}{t} = \begin{cases} k\beta^2(t_w/t) & \text{for } t_w < t \\ k\beta^2 & \text{for } t_w \geq t \end{cases} \quad (\text{Eq.5.3})$$

where β is a plate slenderness parameter and k is a coefficient which is 0.12 (for $\beta \leq 3$) and 0.15 (for $\beta > 3$).

Antoniou [35] proposed an empirical formula based on a modified *Carlsen & Czujko's* [36] formula, and given by:

$$\frac{w_{0pl}}{t} = \begin{cases} 0.014 \frac{b}{t} - 0.32 & \text{for } t \geq 14\text{mm} \\ 0.0018 \frac{b}{t} - 0.55 & \text{for } t < 14\text{mm} \end{cases} \quad (\text{Eq.5.4})$$

Based on experimental measurements, *Smith and Davidson et al.* [37] classified the initial imperfection in welded plates as slight, average and severe, given by:

$$\frac{w_{0pl}}{t} = \begin{cases} 0.025\beta^2 & \text{for slight level} \\ 0.1\beta^2 & \text{for average level} \\ 0.3\beta^2 & \text{for severe level} \end{cases} \quad (\text{Eq.5.5})$$

For external shell plates, particularly in thin-walled naval vessels, some permanent deformation may develop in service due to repeated wave impacts.

5.2.2 Welding induced residual stresses

Residual stresses are generally caused by non-uniform plastic deformation in neighbouring regions. These regions can be small, as occurs within weldments, or large, as may occur in curving or straightening a beam or a shell plate during fabrication. The residual stresses are always balanced so that the overall stress field is in static equilibrium. Consequently, wherever tensile residual stress occurs, balancing compressive residual stress exists in neighbouring regions [38].

Residual stress can be induced by thermal, mechanical, or metallurgical processes. Thermal residual stresses are caused by non-uniform permanent deformations that may develop when the plate is locally heated, then cooled under mechanical restraint. Mechanically induced residual stresses are caused by non-uniform permanent deformation when a metal is mechanically stretched under restraint. Therefore, the occurrence of mechanically induced residual stresses requires the presence of both permanent mechanical deformation and restraint that prevents the deformed metal from contracting or expanding to its new unrestrained equilibrium dimension. Fabrication by welding usually results in stresses that are locked into the fabricated assembly. The magnitude of these stresses depends on several factors, including size of the deposited welding beads, weld sequence, total volume of the deposited weld metal, weld geometry, and strength of the deposited weld metal and of the adjoining base metal, as well as other factors.

Actually the compressive residual stresses reduce the compressive strength of plates and increase the tendency to buckle. This is why welded thin plate structures (e.g. superstructures, naval vessels, etc.) tend to have a permanently buckled appearance, even in the absence of any applied forces. Whereas the compressive residual stress may have a beneficial effect on fatigue life and stress corrosion because it delays crack initiation and retards the crack growth, however the tensile residual stress can accelerate the crack growth..

Paik et al. [1] reviewed and introduced welding-induced residual stresses. Fig. 5.2 illustrates the typical idealized welding-induced residual stress distribution inside a rectangular steel plate. Along the welding line, tensile residual stresses are expressed σ_{rx} in the x direction and σ_{ry} in the y direction. Considering the equilibrium of stresses in the plate as a whole, the breadth or length of the related tensile residual stress blocks in the x and y directions can be expressed by:

$$2b_t = \frac{\sigma_{rcx}}{\sigma_{rcx} - \sigma_{rtx}} b, \quad 2a_t = \frac{\sigma_{rcy}}{\sigma_{rcy} - \sigma_{rty}} a \quad (\text{Eq.5.6})$$

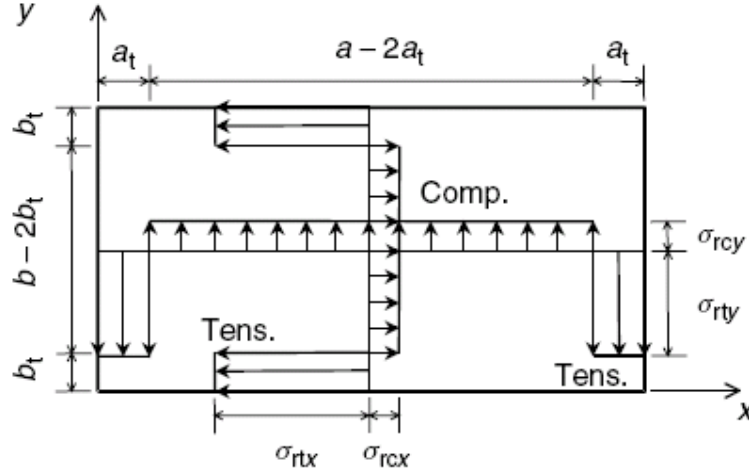


Fig. 5.2. A typical idealized welding-induced residual stress distribution inside a rectangular steel plate element [1]

When the magnitudes of the tensile and compressive residual stresses are measured or defined in some way, the corresponding idealised breadths of the tensile residual stress blocks can be calculated from Eq.5.6. Consequently the residual stress distributions in the x and y directions, given by:

$$\sigma_{rx} = \begin{cases} \sigma_{rtx} & \text{for } 0 \leq y < b_t \\ \sigma_{rcx} & \text{for } b_t \leq y < b - b_t \\ \sigma_{rtx} & \text{for } b - b_t \leq y \leq b \end{cases} \quad (\text{Eq.5.7})$$

$$\sigma_{ry} = \begin{cases} \sigma_{rty} & \text{for } 0 \leq x < a_t \\ \sigma_{rcy} & \text{for } a_t \leq x < a - a_t \\ \sigma_{rty} & \text{for } a - a_t \leq x \leq a \end{cases} \quad (\text{Eq.5.8})$$

Usually the transverse residual stresses of plates are quite small compared to longitudinal direction, thus can be neglected.

Smith *et al.* [37] suggested the following representative values of welding-induced compressive residual stress of steel plates in the longitudinal direction based on the measurement of steel plates of naval ship structures, expressed by:

$$\frac{\sigma_{rcx}}{\sigma_Y} = \begin{cases} -0.05 & \text{for slight level} \\ -0.15 & \text{for average level} \\ -0.3 & \text{for severe level} \end{cases} \quad (\text{Eq.5.9})$$

A redistribution of the initial as-manufactured residual stress field is often found in cyclic loaded structure such as ships and offshore platforms. Residual stresses may gradually diminish or even disappear as a consequence of the long term cyclic stresses; a phenomenon called “shakedown” [39]. There are many factors which affect the residual stress distribution such as the number of load cycles, the amplitude of the cyclic loading, the mechanical properties of the material, the direction, the level and gradient of the residual stresses and the temperature etc.

5.3 Ultimate strength of plates under uni-axial compression

The “effective width” concept is often used to model the strength effectiveness of plate elements that have buckled under predominantly axial compression or have inherently initial deflections subsequent to occurrence of the non-uniform stress distribution in the post-buckling regime or large deflection. The modern era in the effective width concept was started by *von Karman* [41] who developed a general method to solve the problem theoretically, and introduced for the first time the term “effective width”. He idealized the state of stress within the buckled plate by assuming that, due to buckling, the centre portion has no load-carrying capacity, while the edge regions of the plate remain fully effective and carry a uniform stress as illustrated in Fig. 5.3 [42].

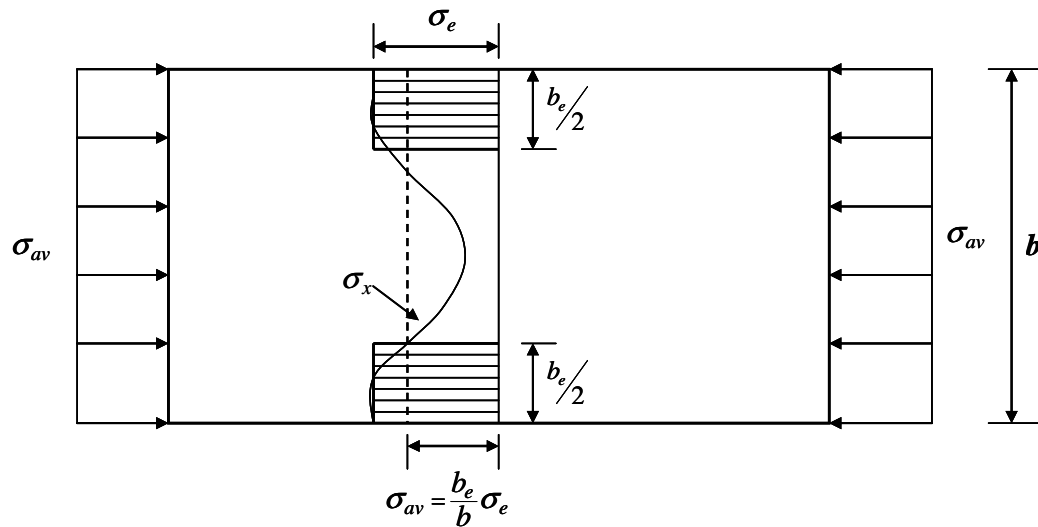


Fig. 5.3. Effective width and stress distribution in plate under uniaxial compression

The effective width is defined as the ratio between the edge stress σ_x and the average stress σ_{av} , given by:

$$b_e = \frac{\int_{-b/2}^{b/2} \sigma_x dy}{\sigma_e} = b \frac{\sigma_{av}}{\sigma_e} \quad (\text{Eq.5.10})$$

where b_e = effective width
 σ_x = non-uniform membrane stress
 σ_{av} = average stress
 σ_e = maximum membrane stress at plate/web junction

The original *von Karman* effective width expression for plates is suitable for relatively thin plates, but it is not accurate for relatively thick plates with initial imperfections. *Winter* [43] proposed the following equation for steel plates stiffened along both longitudinal edges:

$$\frac{\sigma_{Ult}}{\sigma_Y} = \frac{b_e}{b} = \frac{1.9}{\beta} - \frac{0.9}{\beta^2} \quad (\text{Eq.5.11})$$

where σ_{Ult} is ultimate strength or compressive strength of plate.

Some researchers such as *Faulkner* [19], *Murray* [44] and *Soares* [20] have proposed other effective width ratio formulae, among them *Faulkner's* expression is one of the well known expressions. Some graphical comparisons of each theory for effective width ratio, b_e/b , as a function of β were performed by *Hansen* [45].

In the following section, various existing empirical formulae to estimate the ultimate strength of unstiffened plates are investigated:

5.3.1 Faulkner's formula

Ultimate strength of welded plate under compressive load was introduced by *Faulkner* given by [19]:

$$\Gamma_{FK} = \frac{\sigma_{Ult}}{\sigma_Y} = \Gamma_F - \Delta\Gamma_F \quad (\text{Eq.5.12})$$

Γ_F is the strength of an unwelded plate and which is given by:

$$\Gamma_F = \frac{\sigma_U}{\sigma_Y} = \frac{b_e}{b} = \begin{cases} \frac{C_1}{\beta} - \frac{C_2}{\beta^2} & \text{for } \beta > 1 \\ 1.0 & \text{for } \beta \leq 1 \end{cases} \quad (\text{Eq.5.13})$$

where C_1 is 2.0 and C_2 is 1.0 for simply supported condition at all edges, C_1 is 2.25

and C_2 is 1.25 for plates clamped at all edges and where $\Delta\Gamma_F$ is the reduction of strength due to the weld induced residual stress and which can be expressed by:

$$\Delta\Gamma_F = \frac{\sigma_r E_t}{\sigma_y E} \quad (\text{Eq.5.14})$$

where σ_r is the residual stress and E_t is material tangent modulus in compression.

The stress components σ_r / σ_y and E_t / E can be expressed by:

$$\frac{\sigma_r}{\sigma_y} = \frac{2\eta}{(b/t) - 2\eta} \quad (\text{Eq.5.15})$$

$$\frac{E_t}{E} = \begin{cases} \left(\frac{a_3\beta^2}{a_4 + 0.25\beta^4} \right)^2 & \text{for } 0 \leq \beta \leq 1.34 \\ 1.0 & \text{for } \beta > 1.34 \end{cases} \quad (\text{Eq.5.16})$$

where $a_3 = 3.62$ and $a_4 = 13.1$ for simply supported at all edges

$a_3 = 6.31$ and $a_4 = 39.8$ for plates clamped at all edges

η = function of welding

5.3.2 Guedes Soares's method

Guedes Soares [20] proposed an effective width ratio concept derived from *Faulkner's* expression. He included factors for both initial deflection and residual stresses as follows:

$$\Gamma_G = \frac{\sigma_{Ult}}{\sigma_y} = [1.08\Gamma_F] \left[\left(1 - \frac{\Delta\Gamma_F}{1.08\Gamma_F} \right) (1 + 0.0078\eta) \right] \left[1 - (0.626 - 0.121\beta) \frac{\delta_0}{t} \right] \left[0.665 + 0.006\eta + 0.36 \frac{\delta_0}{t} + 0.14\beta \right] \quad \text{for } \beta > 1 \quad (\text{Eq.5.17})$$

where δ_0 is the initial out of plane deflection

The terms in the first bracket express the strength of unwelded perfect plates, the first and second bracket represent the strength of welded plates with residual stress, the first and third bracket propose the strength of unwelded plate with initial deflections. The combined expression which considered initial deflection and residual stress can be found in the fourth term.

Pu [46] evaluated various existing formulae proposed by *Faulkner* [19], *Carlsen* [47], *Guedes Soares* [20], *Vilnay* [48] and *Imperial College's* method and calibrated these against the existing experimental and numerical results. He found that the *Guades*

Soares' method, which had a mean value of 1.031 and a coefficient of variation of 10.1%, was the best among the evaluated methods to predict the ultimate strength of plates.

5.3.3 Fujikubo's formula

Fujikubo *et al.* [21] proposed an ultimate strength formulation for plates under compressive load in shorter side direction based on FEM results and past experience. The ultimate strength estimation formula for a continuous plate under shorter side compression is expressed as :

$$\frac{\sigma_{ult}}{\sigma_Y} = \left(\frac{2.25}{\beta} - \frac{1.25}{\beta^2} \right) \left(\frac{b}{a} \right) + 0.8 \left(\frac{0.06}{\beta - 0.2} + \frac{0.6}{(\beta - 0.2)^2} \right) \left(1 - \frac{b}{a} \right) \quad (\text{Eq.5.18})$$

where β is plate slenderness parameter, a is longer length of plate and b is shorter breadth of plate

5.3.4 NK's formula

Class NK [22] proposed that the ultimate strength under one single stress component is given by :

$$\frac{\sigma_{ult}}{\sigma_Y} = \frac{2.25}{\beta} - \frac{1.25}{\beta^2} \quad \text{for } \beta \geq 1.0 \quad (\text{Eq.5.19})$$

5.3.5 DNV's formula

Class DNV [23] suggested an estimated ultimate stress value based upon a single reference stress and given by:

$$\sigma_{ult} = \frac{\sigma_Y}{\sqrt{1 + \lambda^4}} \quad \text{for } \lambda \leq 1.0 \quad (\text{Eq.5.20})$$

$$\sigma_{ult} = \frac{\sigma_Y}{\lambda\sqrt{2}} \quad \text{for } 1.0 < \lambda \leq 5.0 \quad (\text{Eq.5.21})$$

where $\lambda = \text{reduced slenderness} = \sqrt{\sigma_Y / \sigma_E}$

For states of stress which cannot be defined by one single reference stress, the ultimate capacity of the plate can be determined as the critical value of the equivalent stress according to *von Mises*, which is given by:

$$\sigma_{ult} = \frac{\sigma_Y}{\sqrt{1 + \lambda_e^4}} \quad \text{for } \lambda_e \leq 1.0 \quad (\text{Eq.5.22})$$

$$\sigma_{Ult} = \frac{\sigma_y}{\lambda_e \sqrt{2}} \quad \text{for } 1.0 < \lambda_e \leq 5.0 \quad (\text{Eq.5.23})$$

where λ_e = equivalent reduced slenderness

$$\lambda_e^2 = \frac{\sigma_y}{\sigma_e} \left[\left(\frac{\sigma_x}{\sigma_{Ex}} \right)^c + \left(\frac{\sigma_y}{\sigma_{Ey}} \right)^c + \left(\frac{\tau}{\tau_E} \right)^c \right]^{1/c}$$

σ_e = equivalent stress according to *von Mises*

$$= \sqrt{\sigma_x^2 + \sigma_y^2 - \sigma_x \sigma_y + 3\tau^2}$$

$\sigma_{Ex}, \sigma_{Ey}, \tau_E$ = elastic buckling resistance

$$c = 2 - \frac{b}{a}$$

5.3.6 Paik's methods

Paik et al. [1] classified the behaviour of the response of flat rectangular steel plates under predominantly compressive loads into five regimes, namely pre-buckling, buckling, post-buckling, collapse(ultimate strength) and post-collapse.

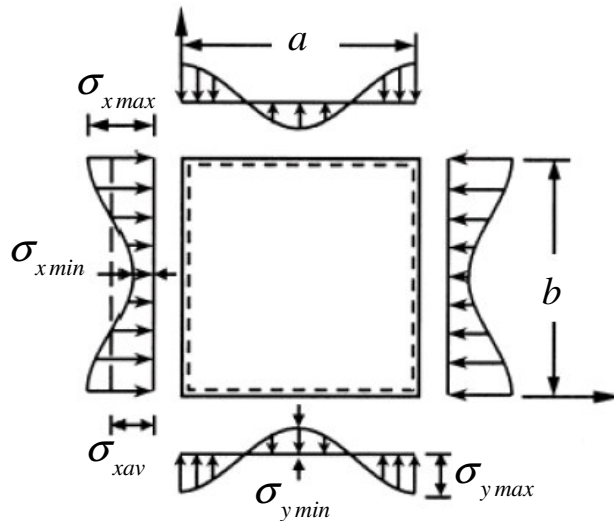


Fig. 5.4. Membrane stress distribution under longitudinal loads

They assumed that the plate edges are simply supported, with zero initial deflection and zero rotational restraints along four edges, and with all edges kept straight.

Based on membrane stress method by solving the non-linear governing differential equations of large-deflection plate theory, the membrane stress distribution at mid thickness of the plate under longitudinal compressive loads can be obtained.

The maximum and minimum membrane stresses in the x and y directions are given by:

$$\sigma_{x \max} = \sigma_{xav} - \rho_x \frac{m^2 \pi^2 EA_m (A_m + 2A_{0m})}{8a^2} \cos \frac{2\pi b_l}{b} \quad (\text{Eq.5.24})$$

$$\sigma_{x \min} = \sigma_{xav} + \rho_x \frac{m^2 \pi^2 EA_m (A_m + 2A_{0m})}{8a^2} \quad (\text{Eq.5.25})$$

$$\sigma_{y \max} = -\rho_x \frac{\pi^2 EA_m (A_m + 2A_{0m})}{8b^2} \cos \frac{2m\pi a_l}{a} \quad (\text{Eq.5.26})$$

$$\sigma_{y \min} = \rho_x \frac{\pi^2 EA_m (A_m + 2A_{0m})}{8b^2} \quad (\text{Eq.5.27})$$

where ρ_x = correction factor
 A_{0m} = amplitude of the response buckling mode initial deflection for axial compressive loading
 A_m = amplitude of the added deflection function

By using the *Mises-Hencky* yield criterion, the ultimate longitudinal axial strength, σ_{xult} , is obtained as the solution of the following equation with regard to σ_{xav} , given by:

$$\left(\frac{\sigma_{x \max}}{\sigma_Y} \right)^2 - \left(\frac{\sigma_{x \max}}{\sigma_Y} \right) \left(\frac{\sigma_{y \min}}{\sigma_Y} \right) + \left(\frac{\sigma_{y \min}}{\sigma_Y} \right)^2 = 1 \quad (\text{Eq.5.28})$$

They developed a computer program, called *ULSAP*, to predict the ultimate strength of plate based on their formulation and which is presented in *Paik et al.* [1].

5.4 Ultimate strength of plates with cracks

Considering the required long term service life of vessels, there is a possibility of fatigue cracks developing due to the cyclic loading on ship structures by waves, currents and sloshing of cargo liquid and ballast water etc. In consideration of the ultimate strength of plates obviously cracks will reduce the strength significantly dependent upon their location and relative size. It is very important to evaluate the residual strength of pre-cracked plating accurately in order to determine the maintenance and repair schedule for the damaged ship structures

Recently some numerical buckling analyses have been carried out for cracked plates under tension, compression and in-plane shear loads, such as by *Kumar et al.*[49] and *Brighenti* [50]. Some other studies have been made to propose the ultimate strength of plates with cracks have been published. Among others *Paik and Thayamballi* [13] performed a series of mechanical crack propagation tests based on steel plates with pre-existing cracks and under monotonically increasing tensile loads. They proposed the ultimate strength of the plate and stiffened panel with crack expressed by:

$$\sigma_{Ult} = \frac{B - a_p}{B} \sigma_{uo} \quad \text{for a plate with a crack} \quad (\text{Eq.5.29})$$

for a stiffened panel with a crack:

$$\sigma_{Ult} = \frac{(B - a_p) / \sigma_{yp} + (h_w - a_s) t_w \sigma_{ys}}{Bt + h_w t_w} \quad (\text{Eq.5.30})$$

where B is the plate width, a_p, a_s are crack length for the plating and the stiffener, respectively and σ_{uo} denotes ultimate strength of perfect plate, and σ_{yp}, σ_{ys} are yield strength of the plating and the stiffener, respectively.

Similar research activities and equations have also been proposed by Paik et al. [14, 16].

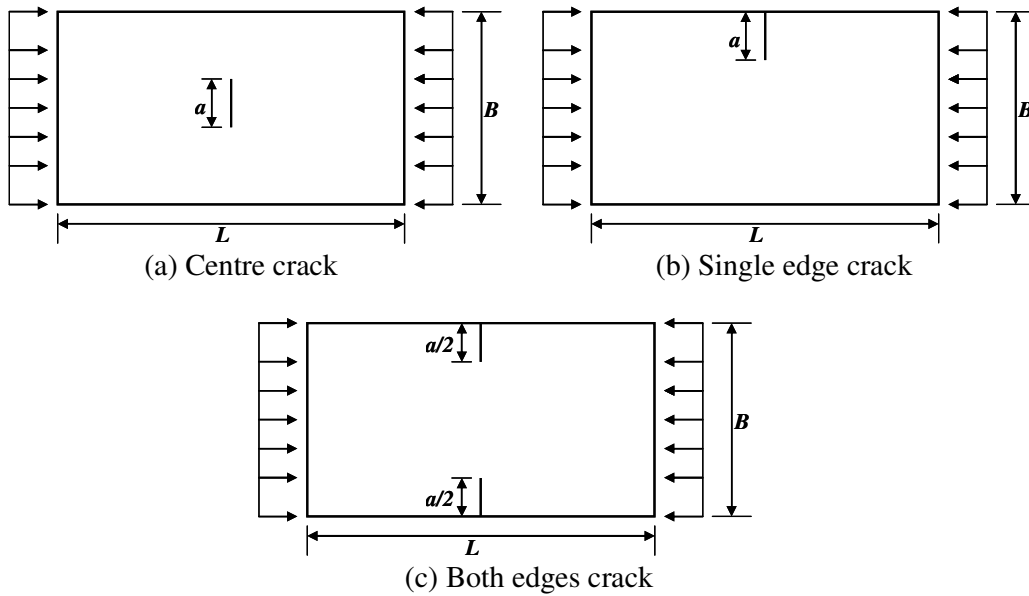


Fig. 5.5. Various types of typical cracks in plates

Hu et al. [3, 17] also investigated the influence of crack damage on the residual strength of both plates and stiffened panels. They used the FE method to find out the effects of fatigue cracks on the tensile and compressive residual ultimate strength of stiffened panels and unstiffened plates and proposed some empirical formula for effective calculation of the compressive or tensile ultimate strength of cracked or intact unstiffened plates or stiffened panels.

For the residual ultimate tensile strength of the cracked unstiffened plate, the empirical formula can be expressed by:

$$\begin{aligned}\phi_{cux}(t) &= \sigma_u(t) / \sigma_Y \\ &= 1.279 - 3.50 [a(t) / B] + 8.974 [a(t) / B]^2 - 11.975 [a(t) / B]^3 \\ &\quad + 5.231 [a(t) / B]^4\end{aligned}\quad (\text{Eq.5.31})$$

$$\begin{aligned}\phi_{eux}(t) &= \sigma_u(t) / \sigma_Y \\ &= 1.281 - 4.045 [a(t) / B] + 6.616 [a(t) / B]^2 - 5.194 [a(t) / B]^3 \\ &\quad + 1.355 [a(t) / B]^4\end{aligned}\quad (\text{Eq.5.32})$$

where $a(t)$ is the crack length at given time t , $\phi_{cux}(t)$ and $\phi_{eux}(t)$ are nominal ultimate strength of plate under tensile load at given time t with centre crack and edge crack, respectively.

When the unstiffened plate is subjected to uniaxial compressive stress, the empirical formula can be given by:

$$\phi_{u-x}(t) = 0.104287 + \phi_{\beta}(t) \phi_{C/B}(t) \quad (\text{Eq.5.33})$$

where

$\phi_{u-x}(t) = \sigma_u(t) / \sigma_Y$ is the nominal ultimate strength of the cracked plate under compressive load

$$\phi_{\beta}(t) = 1.31071 - 0.35075 \beta(t) + 0.03006 \beta(t)^2 - 0.0000277779 \beta(t)^3$$

$$\phi_{C/B}(t) = 0.830528 - 0.23082 [a(t) / B] - 0.67362 [a(t) / B]^2 - 0.0829 [a(t) / B]^3$$

$$\beta(t) = \frac{B}{T(t)} \sqrt{\frac{\sigma_Y}{E}}, \quad T(t) \text{ is the thickness of the plate at given time } t$$

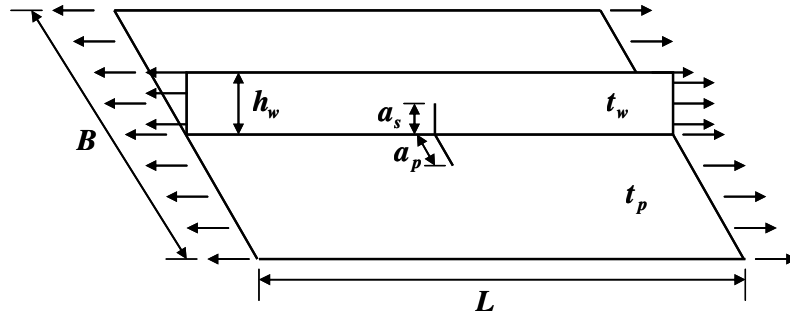


Fig. 5.6. A stiffened plate with a crack

When a stiffened panel is subjected to tensile stress as illustrated in Fig. 5.6, the web has an edge crack damage and the plating has a centre crack damage, the equivalent tensile residual ultimate strength, can be expressed by:

$$\sigma_{usp}(t) = \phi_{us}(t) \sigma_{ys} t_w(t) h_w + \phi_{up}(t) \sigma_{yp} t_p(t) B \quad (\text{Eq.5.34})$$

where $\sigma_{usp}(t)$ is the ultimate strength of the stiffened panel under tensile load, σ_{ys} is the stiffener's yield stress, $\phi_{up}(t)$ can be obtained through Eq.5.31, $\phi_{us}(t)$ can be obtained through Eq.5.32.

Another attempt has been performed by Wang et al. [51] to assess the effect of the crack eccentricity ratio on the ultimate tensile strength of cracked ductile rectangle plates.

5.5 Computation of ultimate strength of plates with localized corrosion

The finite element method based process has now become the most common, powerful and flexible tool in structural analysis and makes it possible to predict the response to applied forces and the strength of complex structure much more accurately than existing classical theoretical formulae based calculations. However the results from the same structural details which are individually performed by each different engineer or institute might have significantly different results due to different assumption in boundary conditions, in geometrical parameters and in modelling procedures, etc.

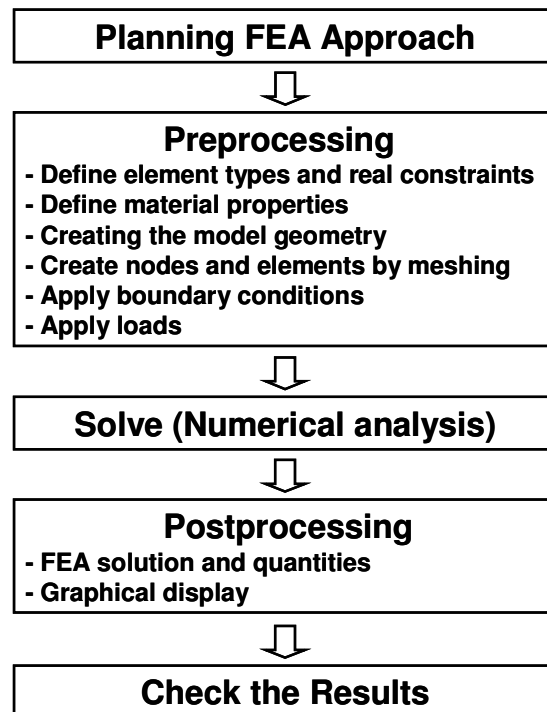


Fig. 5.7. Typical procedure of finite element analysis (FEA)

It is not a straight forward procedure to control non-linear behaviour of structure properly and to obtain a correct determination of the ultimate strength value by finite element analysis. Generally the FEA modelling method and procedure is based appreciably on a user's experience and preference. In this section, the finite element analyses are carried out by using the popular *ANSYS* program [52]. The general procedure of FEA is shown in Fig.5.7.

Many researchers find that designing and building a finite element model requires more time than any other part of the analysis process. The easiest way to communicate with the FEA program is by using the menu system, called the *Graphical User Interface (GUI)*. However *GUI* based modelling is a time consuming and expensive method when we create repeated and similar FEA models. In this study, some useful macro programs have been developed within *ANSYS* program environment. With these programs one can record a frequently used sequence of *ANSYS* commands in a macro program. Creating a macro and using *ANSYS Parametric Design Language (APDL)* enables us to create our own custom *ANSYS* command, automate common tasks or even build our model in terms of parameters (variables) and more importantly reduce the time for building a model dramatically. Generally the input parameters are material yield stress, plate length, plate breadth, plate thickness, plate initial deflection and applied load. The following Fig. 5.8 illustrates the sequence of the macro program. A sample of a *ANSYS* macro file which was created by the author has been introduced in **Appendix B**.

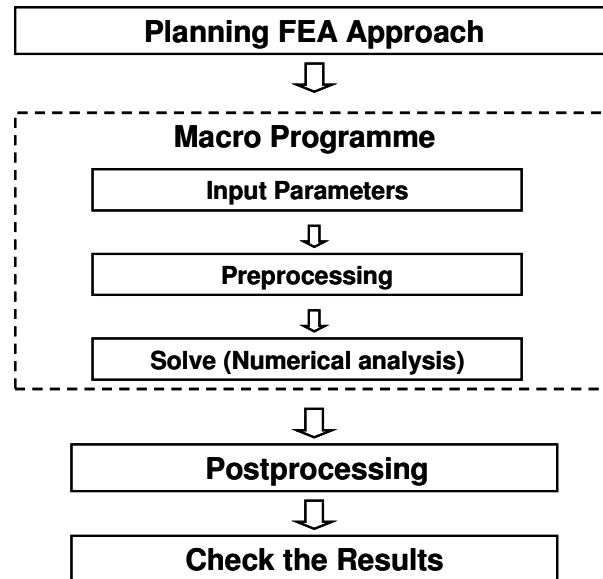


Fig. 5.8. Typical procedure of macro programs for FEA

In this section, the ultimate strength of simple unstiffened rectangular plates with initial geometric imperfection, welding induced residual stress and pitting corrosion is investigated based on both a mild steel and a higher tensile steel which are commonly used in ship's structure.

5.5.1 Modelling details for finite element analysis

5.5.1.1 Material properties

Currently the most frequently used grades of steel for ship structures are mild steel with a yield stress, σ_y , of 235 N/mm^2 and higher strength steels with $\sigma_y = 315 \text{ N/mm}^2$ (LRS AH32, ABS HT32, DNV NV-32) and $\sigma_y = 355 \text{ N/mm}^2$ (LRS AH36, ABS HT36, DNV NV-36). In this research, both mild steel and a higher strength steel with yield stress $\sigma_y = 355 \text{ N/mm}^2$, a Young's modulus, E , of 209000 N/mm^2 and Poisson's ratio of 0.3, were used in the finite element analyses, which were undertaken by using ANSYS software [52].

There are many proposals available for assessing the typical value of welding induced initial deflection [19, 35-37]. An average value ($= 0.1 \beta^2 t$), where $\beta = \frac{B}{t} \sqrt{\frac{\sigma_y}{E}}$, B and t are width and thickness of the plate respectively, of welding induced initial deflection as suggested by Smith et al. [37] is adopted in this study.

5.5.1.2 Boundary conditions

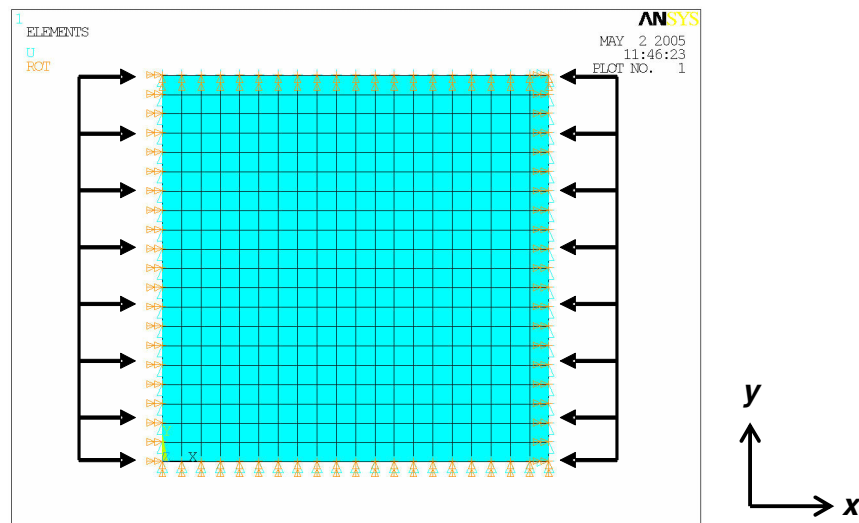


Fig. 5.9. Meshes and constraint details

Ship structures are generally composed of plates supported by various types of framing / stiffening members along the edges and the effective boundary conditions to such plate elements can be defined by the torsional rigidity of support members such as stiffened or transverse frame. For design purposes, the boundary condition can be classified into either simply supported if the edge condition of rotational restraints are zero or clamped when the rotational restraint are infinite. Generally the simply supported boundary condition shows more critical and pessimistic values of buckling and ultimate strength than clamped boundary conditions, thus all finite element analyses in this section are based on simply supported boundary condition. There are

slightly different opinions to define simply supported boundary condition on each boundary edge. In this research following boundary conditions, as shown on Table 5-1, are applied where “F” denotes free and “C” denotes constraint.

Table 5-1
Boundary conditions for unstiffened plate

Description	Ux	Uy	Uz	Rot-x	Rot-y	Rot-z
Left	F	C	C	C	F	C
Right	C	C	C	C	F	C
Top	F	C	C	F	C	C
Bottom	F	C	C	F	C	C

5.5.1.3 Element type

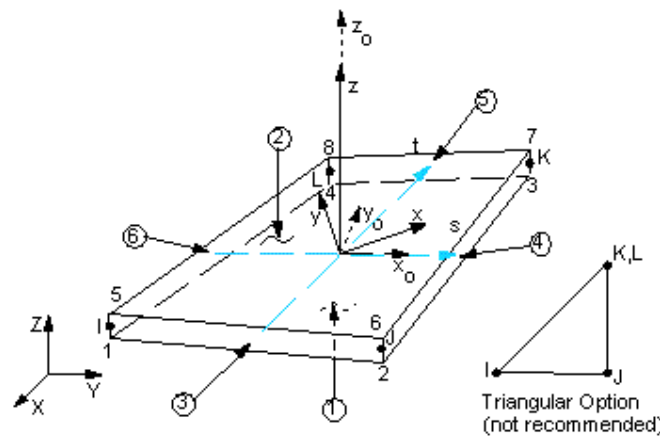


Fig.5.10. Shell181 Geometry [52]

The ANSYS SHELL181 element model is used to assess the ultimate strength of unstiffened and stiffened plates. SHELL181 is suitable for analyzing thin to moderately-thick shell structures. It is a 4-node element with six degrees of freedom at each node: translations in the x, y, and z directions, and rotations about the x, y, and z-axes. SHELL181 is well-suited for linear, large rotation, and/or large strain nonlinear applications. Change in shell thickness is accounted for in nonlinear analyses. In the element domain, both full and reduced integration schemes are supported. In this study, the element matrices and load vectors are derived using an updated Lagrangian formulation. SHELL181 can be used for layered applications for modelling laminated composite shells or sandwich construction.

The geometry, node locations, and the coordinate system for this element are shown in Fig. 5.10 "SHELL181 Geometry". The element is defined by four nodes: I, J, K, and L. The element formulation is based on logarithmic strain and true stress measures. The thickness of the shell may be defined at each of its nodes. The thickness is assumed to vary smoothly over the area of the element. If the element has a constant thickness, only TK(I) needs to be input. If the thickness is not constant, all

four thicknesses must be input. Alternatively the shell thickness and more general properties may be specified using section commands. SHELL181 may be associated with a shell section. Shell section is a more general method to define shell construction than the real constants option. Shell section commands allow for layered composite shell definition, and provide the input options for specifying the thickness, material, orientation and number of integration points through the thickness of the layers. The number of integration points (1, 3, 5, 7, or 9) can be designated through the thickness of each layer when using section input. When only 1, the point is always located midway between the top and bottom surfaces. If 3 or more points, 2 points are located on the top and bottom surfaces respectively and the remaining points are distributed equal distance between the 2 points. In this research *SHELL181* layer element model based on 4 layers through the thickness of plate is used and three integration points are adopted at each layer in order to evaluate ultimate strength of plates with pitting corrosion. The general overview of SHELL181 element model is referred to ANSYS Manual [52].

5.5.1.4 Material plasticity model

In this study, material plasticity model adopts bilinear isotropic hardening model. This option uses the von Mises yield criteria coupled with an isotropic work hardening assumption. The material behavior is described by a bilinear stress-strain curve starting at the origin with positive stress and strain values. The initial slope of the curve is taken as the elastic modulus of the material. At the specified yield stress, the curve continues along the second slope defined by the tangent modulus (having the same units as the elastic modulus). The tangent modulus cannot be less than zero nor greater than the elastic modulus.

5.5.1.5 Non-linear control

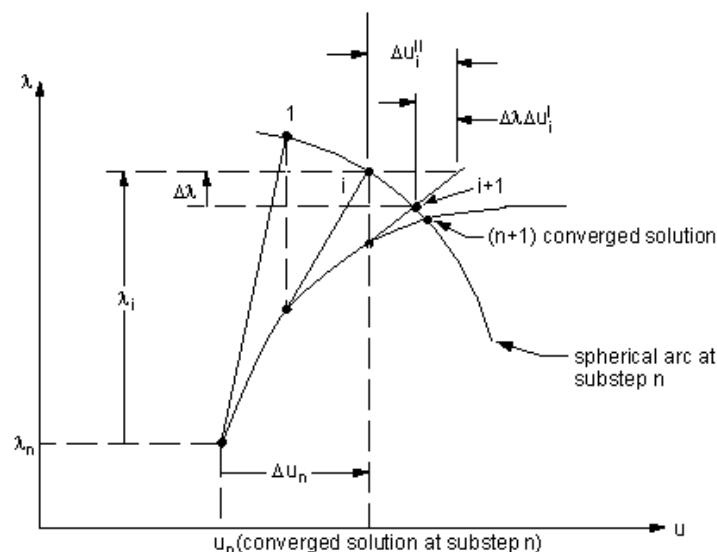


Fig.5.11. Arc-length Approach with Full Newton-Rapson Method [52]

The Arc-length approach with full *Newton-Raphson* method is adopted for non-linear control. The *Arc-length* method is suitable for nonlinear static equilibrium solutions of unstable problems. Applications of the arc-length method involves the tracing of a complex path in the load-displacement response into the buckling/post-buckling regimes. The arc-length method uses explicit spherical iterations to maintain the orthogonality between the arc-length radius and orthogonal directions. It is assumed that all load magnitudes are controlled by a single scalar parameter (i.e., the total load factor). Unsmooth or discontinuous load-displacement response in the cases often seen in contact analyses and elastic-perfectly plastic analyses cannot be traced effectively by the arc-length solution method. Mathematically, the *Arc-length* method can be viewed as the trace of a single equilibrium curve in a space spanned by the nodal displacement variables and the total load factor. Therefore, all options of the *Newton-Raphson* method are the basic method for the arc-length solution. As the displacement vectors and the scalar load factor are treated as unknowns, the arc-length method itself is an automatic load step method. For problems with sharp turns in the load-displacement curve or path dependent materials, it is necessary to limit the arc-length radius (arc-length load step size) using the initial arc-length radius. During the solution, the arc-length method will vary the arc-length radius at each arc-length substep according to the degree of nonlinearities that is involved. The range of variation of the arc-length radius is limited by the maximum and minimum multipliers.

For most nonlinear analyses, the Newton-Raphson method is used to converge the solution at each time step along the force deflection curve. The Newton-Raphson method works by iterating the equation, given by:

$$\left[K_i^T \right] \{ \Delta u_i \} = \{ F_a \} - \{ F_i^{nr} \} \quad (\text{Eq.5.35})$$

where i is subscript representing the current equilibrium iteration, $\left[K^T \right]$ is the tangent stiffness matrix, $\{ \Delta u \}$ is the incremental displacement, $\{ F_a \}$ is the applied load vector and $\{ F_i^{nr} \}$ is the internal load vector calculated from element stress, until the residual, $\{ F_a \} - \{ F_i^{nr} \}$, falls within a certain convergence criterion.

The Newton-Raphson method increments the load a finite amount at each substep and keeps that load fixed throughout the equilibrium iterations. Because of this, it cannot converge if the tangent stiffness (the slope of the force-deflection curve at any point) is zero. To avoid this problem, one should use the arc-length method for solving nonlinear post-buckling. To handle zero and negative tangent stiffnesses, the arc-length multiplies the incremental load by a load factor, λ , where λ is between -1 and 1. This addition introduces an extra unknown, altering the equilibrium equation to:

$$\left[K_i^T \right] \{ \Delta u_i \} = \lambda \{ F_a \} - \{ F_i^{nr} \} \quad (\text{Eq.5.36})$$

The incremental displacement $\{ \Delta u_i \}$ can be expressed by:

$$\{\Delta u_i\} = \Delta\lambda \{\Delta u_i^I\} + \{\Delta u_i^{II}\} \quad (\text{Eq.5.37})$$

where $\{\Delta u_i^I\}$ = displacement due to a unit load factor = $\{K_i^T\}^{-1} \{F_a\}$
 $\{\Delta u_i^{II}\}$ = displacement increment from the Newton-Raphson method
 $= \{K_i^T\}^{-1} \{R_i\}$
 $\{R_i\}$ = residual vector

In each arc-length iteration, the incremental load factor $\{\Delta\lambda\}$ in Eq.5.37 is determined by the arc-length equation which can be written as, at iteration i :

$$\ell_i^2 = \lambda_i^2 + \beta^2 \{\Delta u_n\}^T \{\Delta u_n\} \quad (\text{Eq.5.38})$$

where β is scaling factor used to ensure the correct scale in the equation and Δu_n is the sum of all the displacement increments Δu_i of this iteration. Fig. 5.11 illustrates this process. The general overview of Arc-length method is referred to ANSYS Manual [52].

5.5.2 Evaluation of results from F.E. analysis

It is very important to evaluate the results from an FEA and compare such with existing formulae or programs because the non-linear control of structure behaviour is not easy and may have some mistakes by user during the analysis. Without evaluation of FEA results we cannot rely on and believe the result which is produced by an FEA program. In order to confirm the correctness of FEA control and the results, some existing empirical formulae and programs are compared with some ANSYS output as shown in Table 5-2. The details of these existing formulae are introduced in Section 5.3. Basically the comparison has been carried out based on 1000mm(L) x 1000mm(B) x 20mm(t), $\sigma_y = 235 \text{ N/mm}^2$ with initial deflection = $0.1 \beta^2 t$ of unstiffened plate.

Table 5-2
Comparison of existing methods versus ANSYS FEA results

Model	Ultimate strength
Faulkner	196.73 N/mm^2
Fujikobo	210.87 N/mm^2
NK	210.87 N/mm^2
Johnson-Ostenfeld	189.40 N/mm^2
Paik(ULSAP)	189.79 N/mm^2
LUSAS (FEA)	191.58 N/mm^2
ANSYS (FEA) Shell 181	188.30 N/mm^2

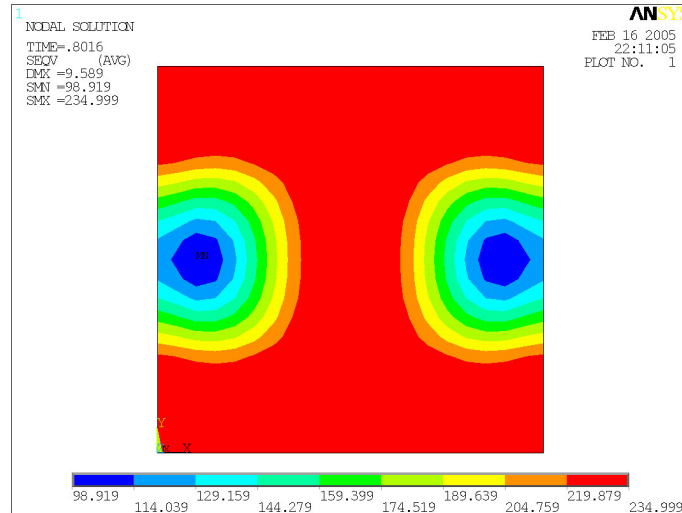


Fig. 5.12. The *Von Mises* stress distribution at the ultimate limit state

As shown in Table 5-2, It can be concluded that FEA based programs such as *LUSAS* [53], *ANSYS* [52] and *Paik's programs* [1] predict ultimate strength more or less same but somewhat more pessimistic than some of the other existing empirical formulae. Fig. 5.12 illustrates the *Von Mises* stress distribution of the unstiffened square plate at the ultimate limit state.

5.5.3 F.E. analysis of plates under uniaxial compression

Based on the commonly used three yield grades of steel as specified in 5.5.1.1, finite element analyses have been performed in order to get the ultimate strength of plates. Two different groups of analyses have been done, one without welding induced residual stress (Table 5-3) and the other with welding induced residual stress (Table 5-4) as follows:

5.5.3.1 Unstiffened plates without residual stresses

Total 25 non-linear modelling analyses have been carried out to determine the ultimate strength of unstiffened flat square plate without considering the possible effects of welding induced residual stress and based on each having different yield stress, thickness and initial deflection values as shown in Table 5-3. Fig. 5.13 indicates typical average stress-strain curve of a simply supported steel plate (mild steel) of various thickness under uni-axial compressive load. Fig. 5.14 shows the effect of plate slenderness parameter on strength reduction under uni-axial compressive loads without consideration of residual stresses.

Table 5-3

Ultimate strength of unstiffened plates without residual stresses

Dimension (L x B) mm	Thick. (mm)	B/t	β	Initial deflection ($=0.1\beta^2t$)	σ_Y N/mm^2	σ_{ult} N/mm^2	$\frac{\sigma_{ult}}{\sigma_Y}$
1000x1000	25.00	40	1.34	4.50	235	214.58	0.913
1000x1000	22.22	45	1.51	5.06	235	200.35	0.853

1000x1000	20.00	50	1.68	5.62	235	188.30	0.801
1000x1000	18.18	55	1.84	6.18	235	178.48	0.759
1000x1000	16.67	60	2.01	6.73	235	170.59	0.726
1000x1000	15.38	65	2.18	7.31	235	164.05	0.698
1000x1000	14.29	70	2.34	7.86	235	157.73	0.671
1000x1000	25.00	40	1.55	6.03	315	264.13	0.839
1000x1000	22.22	45	1.75	6.78	315	246.71	0.783
1000x1000	20.00	50	1.94	7.54	315	233.01	0.740
1000x1000	18.18	55	2.14	8.29	315	222.23	0.706
1000x1000	16.67	60	2.33	9.04	315	213.85	0.679
1000x1000	15.38	65	2.52	9.80	315	207.11	0.658
1000x1000	14.29	70	2.72	10.55	315	201.92	0.641
1000x1000	25.00	40	1.65	6.79	355	287.48	0.810
1000x1000	24.00	41.7	1.72	7.08	355	280.76	0.791
1000x1000	22.22	45	1.85	7.64	355	269.02	0.758
1000x1000	22.00	45.5	1.87	7.72	355	267.57	0.754
1000x1000	20.00	50	2.06	8.49	355	254.82	0.718
1000x1000	18.18	55	2.27	9.34	355	243.81	0.687
1000x1000	18.00	55.6	2.29	9.44	355	242.77	0.684
1000x1000	16.67	60	2.47	10.19	355	235.33	0.663
1000x1000	16.00	62.5	2.58	10.62	355	231.67	0.653
1000x1000	15.38	65	2.68	11.04	355	228.62	0.644
1000x1000	14.29	70	2.88	11.89	355	223.26	0.629

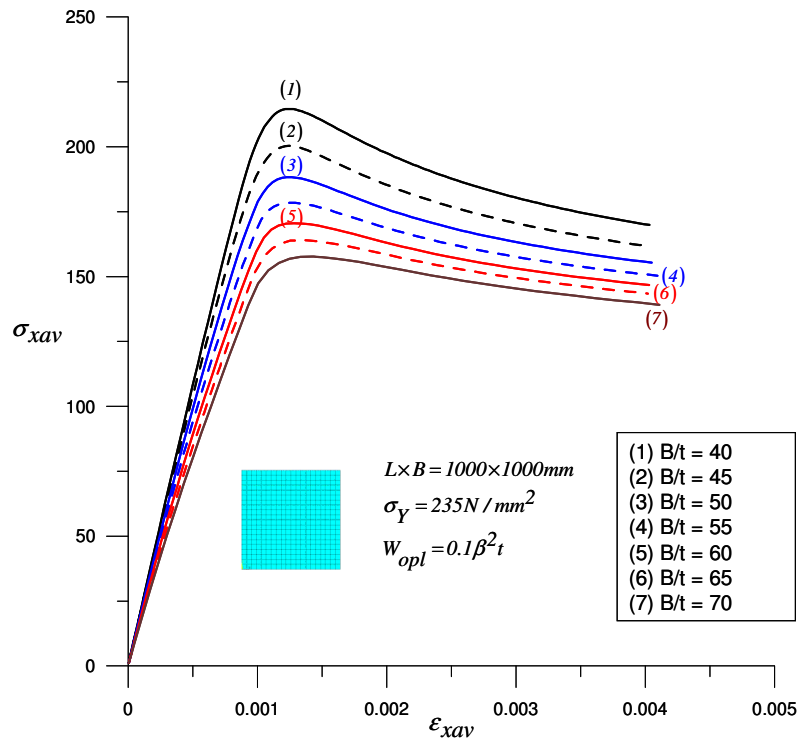


Fig. 5.13. The average stress-strain curves under uni-axial compressive load

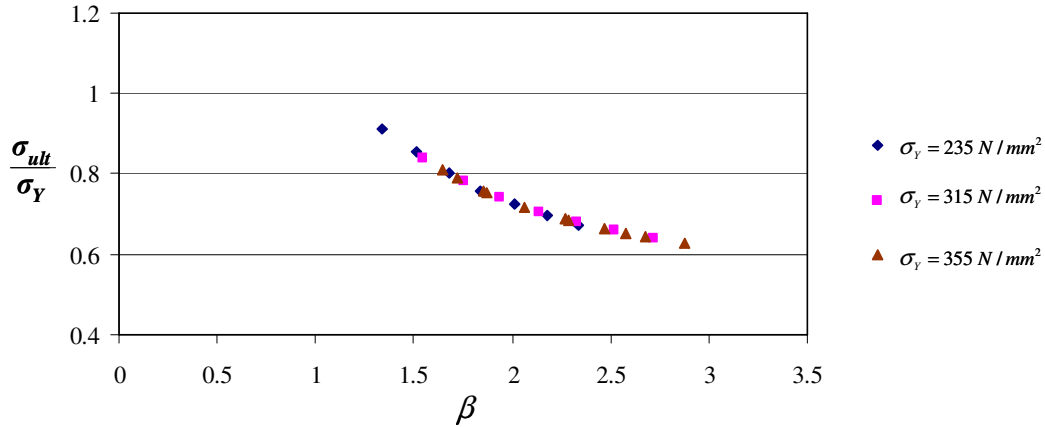


Fig. 5.14. The effect of plate slenderness parameter on strength reduction under uni-axial compressive loads without consideration of residual stresses

5.5.3.2 Unstiffened plates with residual stresses

As described in Section 5.2.2, welding induced residual stresses will reduce the buckling and ultimate strength of plates. In order to verify the effect of residual stresses on the ultimate strength of plates, finite element analyses have been performed based on a total of 21 models.

The transverse residual stresses of plates are quite small compared with those in the longitudinal direction, thus only longitudinal residual stresses are considered and are based on following assumptions:

$$b_t = \frac{\sigma_{rcx}}{2(\sigma_{rcx} - \sigma_{rx})} b = 0.065b \quad (\text{Eq.5.39})$$

where σ_{rx} is σ_Y , σ_{rcx} is $-0.15 \sigma_Y$ as defined in Section 5.2.2.

Fig. 5.15 illustrates the initial residual stress distribution that was imposed on the FEA model and which indicates $\sigma_Y = 355 \text{ N/mm}^2$ in tension block and $\sigma_{rcx} = 53.32 \text{ N/mm}^2$ in compression block. Table 5-4 gives the resulting ultimate strength of the plates analysed with welding induced residual stress. σ_R and σ_{ult} represent ultimate strength of plate with and without welding induced residual stress, respectively.

The results show that the ultimate strength reduction due to the effect of residual stress in these FEA is smaller by between 1.2 % to 2.5 % compare to the ultimate strength of plates without residual stress which are indicated in Table 5-3. Fig.5.16 shows the longitudinal stress distribution (σ_x) of a selected unstiffened plate with residual stresses when it reaches at the ultimate limit state. Fig. 5.17 shows the effect of plate slenderness parameter on streng reduction under uni-axial compressive loads considering residual stresses.

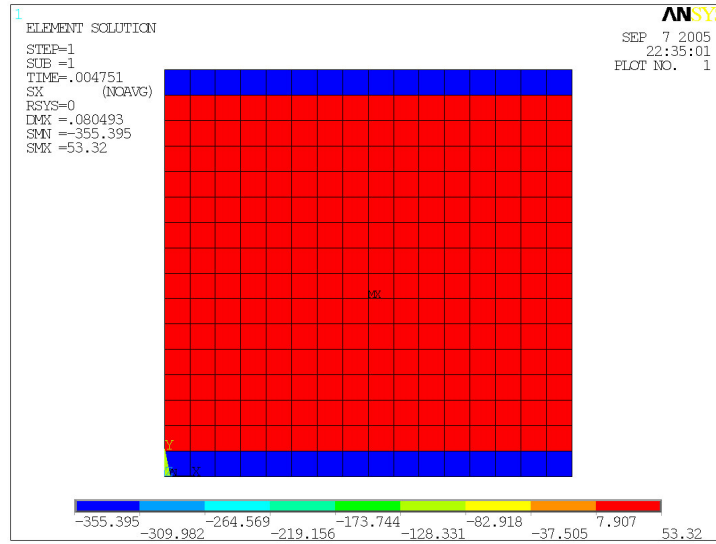


Fig. 5.15. The welding induced residual stress distribution

Table 5-4

Ultimate strength of unstiffened plates with residual stresses

Dimension (L x B) mm	Thick (mm)	B/t	β	Initial deflection ($=0.1\beta^2t$)	σ_Y N/mm^2	σ_R N/mm^2	$\frac{\sigma_R}{\sigma_Y}$	$\frac{\sigma_R}{\sigma_{ult}}$
1000x1000	25.00	40	1.34	4.50	235	211.27	0.899	0.985
1000x1000	22.22	45	1.51	5.06	235	196.70	0.837	0.982
1000x1000	20.00	50	1.68	5.62	235	184.48	0.785	0.980
1000x1000	18.18	55	1.84	6.18	235	174.61	0.743	0.978
1000x1000	16.67	60	2.01	6.73	235	166.62	0.709	0.977
1000x1000	15.38	65	2.18	7.31	235	160.04	0.681	0.976
1000x1000	14.29	70	2.34	7.86	235	155.10	0.660	0.983
1000x1000	25.00	40	1.55	6.03	315	258.93	0.822	0.980
1000x1000	22.22	45	1.75	6.78	315	241.29	0.680	0.978
1000x1000	20.00	50	1.94	7.54	315	227.43	0.722	0.976
1000x1000	18.18	55	2.14	8.29	315	216.72	0.688	0.975
1000x1000	16.67	60	2.33	9.04	315	208.53	0.662	0.975
1000x1000	15.38	65	2.52	9.80	315	201.92	0.641	0.975
1000x1000	14.29	70	2.72	10.55	315	196.88	0.625	0.975
1000x1000	25.00	40	1.65	6.79	355	281.52	0.793	0.979
1000x1000	22.22	45	1.85	7.64	355	263.06	0.741	0.978
1000x1000	20.00	50	2.06	8.49	355	248.86	0.701	0.977
1000x1000	18.18	55	2.27	9.34	355	237.85	0.670	0.976
1000x1000	16.67	60	2.47	10.19	355	229.33	0.646	0.975
1000x1000	15.38	65	2.68	11.04	355	222.94	0.628	0.975
1000x1000	14.29	70	2.88	11.89	355	217.62	0.613	0.975

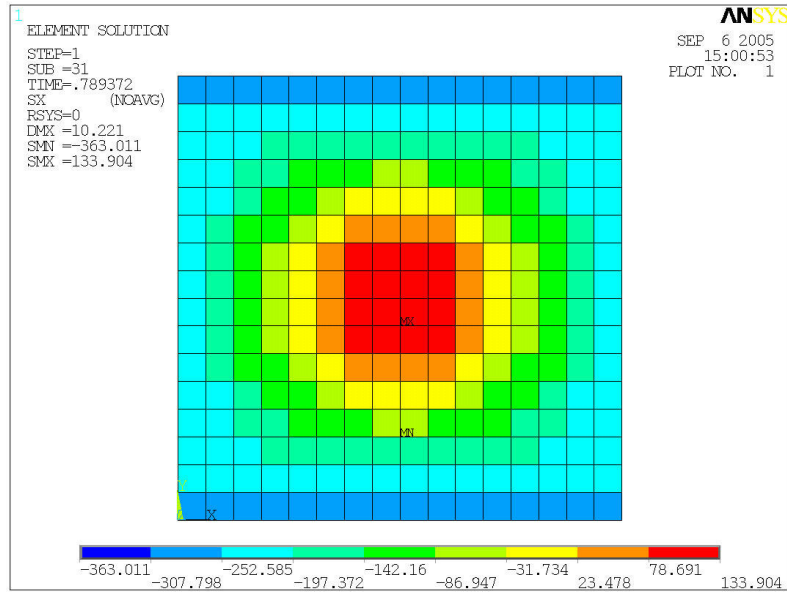


Fig. 5.16. The stress distribution (σ_x) of an unstiffened plate with residual stresses at the ultimate limit state

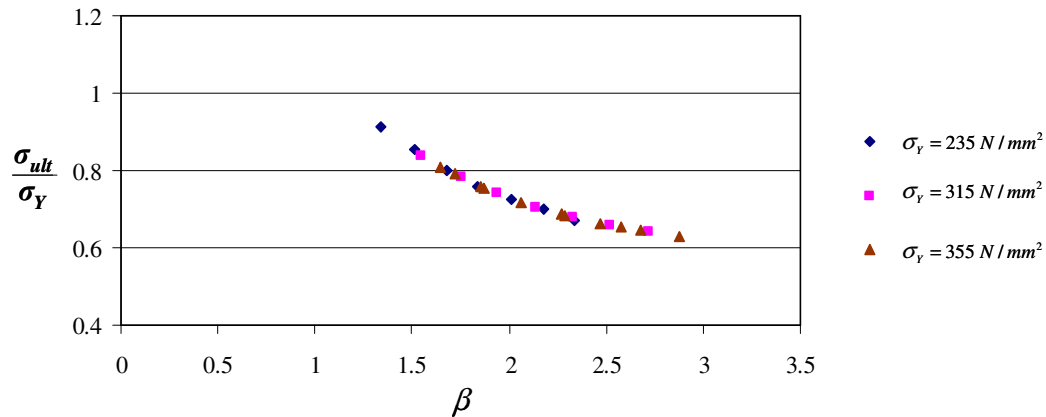


Fig. 5.17. The effect of plate slenderness parameter on strength reduction under uni-axial compressive loads considering residual stresses

5.5.4 Modelling strategy for rectangular plate with pitting corrosion

Localized corrosion often starts from the areas where the highest stresses occur, which can lead to coating break-down and stress corrosion cracking, or in areas where water flows and drains, places of water and sediment accumulation, such as along longitudinal stiffeners and transverse bulkhead. Fig. 5.18 shows a typical localized corrosion pattern in a ballast tank. The localized pitting corrosion can be concentrated at one or several possibly large areas as shown in Fig. 5.18. Another type of localized corrosion is of a regularly pitted form and caused by microbiologically influenced corrosion (MIC), such as sulphate-reducing bacteria (SRB).



Fig. 5.18. Typical localized corrosion in ballast tank [54].

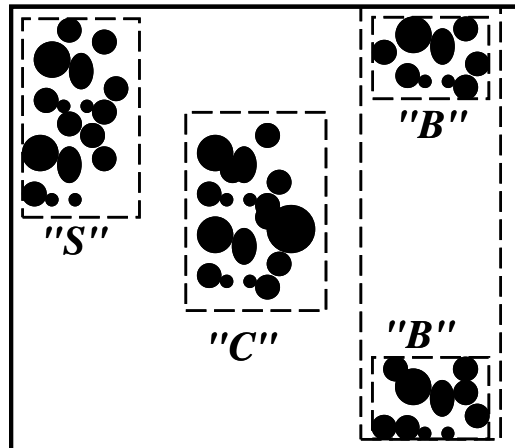


Fig. 5.19. Patterns of pitting corrosion (S: Single edge, C: Centre, B: Both edges).

Generally the most common shape of individual pitting corrosion is a semi-spherical shape. However due to the complexity of finite element modelling in a three dimensional manner of the semi-spherical shape, and as it is usually impractical because of the huge amount of computational costs involved, a local region of pitting corrosion is considered to be acceptably simplified as a rectangular shape [14, 15, 32]. The patterns of pitting corrosion can be thus simplified by making nearest individual pits into one group and classified into pits on a single edge, pits on centre and pits on both edges as illustrated in Fig. 5.19.

There are several finite element techniques available to model pitting corrosion. The easiest way is to reduce the thickness of the plate in a pitted area, carry out buckling analysis to get the buckled shape of plate with pitting corrosion and finally to perform

non-linear finite element control to determine the ultimate strength of the plate by using stress versus strain relationship. Paik *et al.* [1] have assumed in their approach that the plate thickness is subdivided into several layers and the material properties of the pitting corrosion region are taken to be zero. The former method cannot represent proper modelling of pitting corrosion because if the thickness of plate in the pitted area is simply reduced then the node on pitted area will be located on midplane as illustrated in Fig. 5.20. The latter method also cannot represent the real situation and easily tends to fail to converge during non-linear control based on the author's experience.

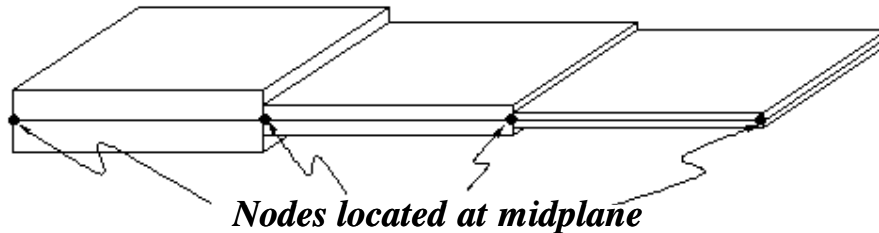


Fig. 5.20. Shell layers with nodes at midplane

In order to represent the real structure with a pitted area, the ANSYS Shell Layer model was adopted and the midplane nodes in the pitted areas were artificially moved to the bottom surfaces and aligned with intact area as illustrated in Fig. 5.21 and Fig. 5.22. This approach thus creates an eccentricity of the inplane load path through the pitted region.

5.5.5 Finite element analyses of typical square plates with pitting corrosion

The patterns and locations of localized corrosion observed in service are various so it is impossible to predict exactly when and where the corrosion will start, how it will progress and at what general rate. Localized corrosion can also start at the places where with high fatigue stresses, welds of seams and crack initiation areas. Sometimes bacteria induced corrosion can be the cause of pitting corrosion. It is clearly very important to assess the remaining structural integrity under localized corrosion correctly not only to determine the schedule for repair but also to decide proper future inspection and maintenance periods for structures with defects.

In this study, over 256 nonlinear finite element analyses model have been carried out to investigate the effects of different material and geometry parameters such as plate slenderness, pit location, size and depth of pits on the ultimate strength of square plates. Higher strength steel of 1m x 1m plate with a yield stress of 355 N/mm^2 was used for this study. Five different B/t ratios (41.7, 45.5, 50.0, 55.6, 62.5) have been chosen by changing plate thickness. The location of pitting corrosion was assumed to start at aft bay (aft end) and the sizes of pitting corrosion have four different length values (0.25L, 0.5L, 0.75L, 1.0L), in which L is the total length of the plate.

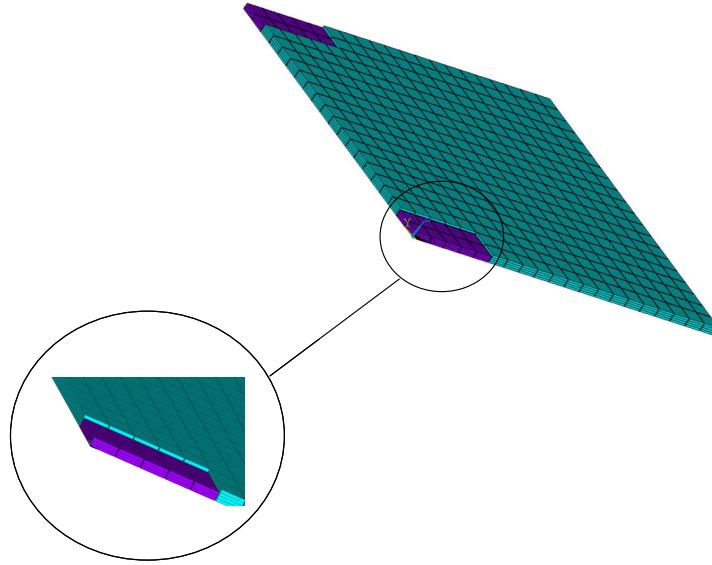


Fig. 5.21. Finite element analysis modelling detail for pitting corrosion

The depths of pits are classified into two cases ($0.25t$ and $0.5t$). For the purpose of simplifying the finite element analyses, the area of pitting corrosion is assumed to have rectangular shape with single edge or both edges corroded pattern as illustrated in Fig. 5.21 in order to reduce the modelling complexity and cost. The initial deflection is assumed being equal to $0.1 \beta^2 t$. However the effect of welding-induced residual stresses was not considered in this specific study.

Fig. 5.22 illustrates the mesh details of the square plate with pitting corrosion at the centre and Table 5-5 summarizes some of the results of finite element analyses. σ_c and σ_0 represent the ultimate strength of plate with localized corrosion and uncorroded condition respectively, x_1 is plate slenderness parameter (β), x_2 denotes the ratio of pit breadth to plate width, x_3 indicates the ratio of pit length to plate length and x_4 is the ratio of pit depth to plate thickness. Fig. 5.23 compares the average stress-strain curves for a rectangular plate with various pitting corrosion sizes and locations. It is shown that the simultaneous pitting corrosion at both edges causes the most strength reduction while corrosion at the centre results in the least strength reduction. The strength of pitting corrosion at both edges is only 90.4 % of that of pitting corrosion at centre location.

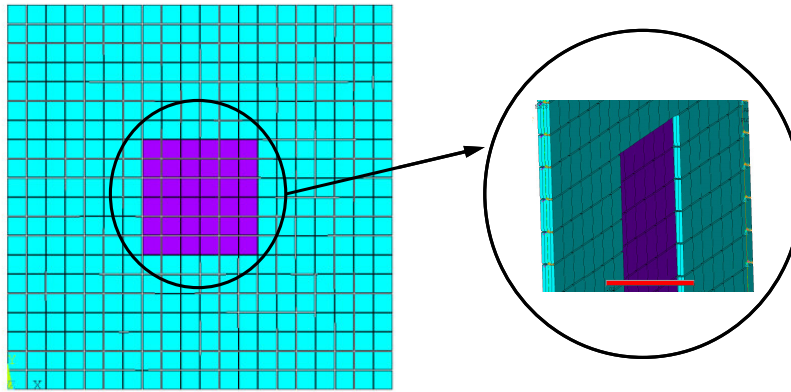


Fig. 5.22. Mesh details of the plate with typical pitting corrosion at central region

Table 5-5

Effects of transverse location of pitting corrosion on ultimate strength

No	Pit location	FEM Input Variables					$\frac{A_0 - A_r}{A_0}$	σ_C N/mm ²	$\frac{\sigma_C}{\sigma_0}$
		B/t	x_1	x_2	x_3	x_4			
1	Centre	50.0	1.68	0.0	0.0	0.00	1.000	188.30	1.000
2	Centre	50.0	1.68	0.3	0.3	0.50	0.888	165.41	0.878
3	Single edge	50.0	1.68	0.3	0.3	0.50	0.888	155.59	0.826
4	Both edges	50.0	1.68	0.3	0.3	0.50	0.888	149.53	0.794

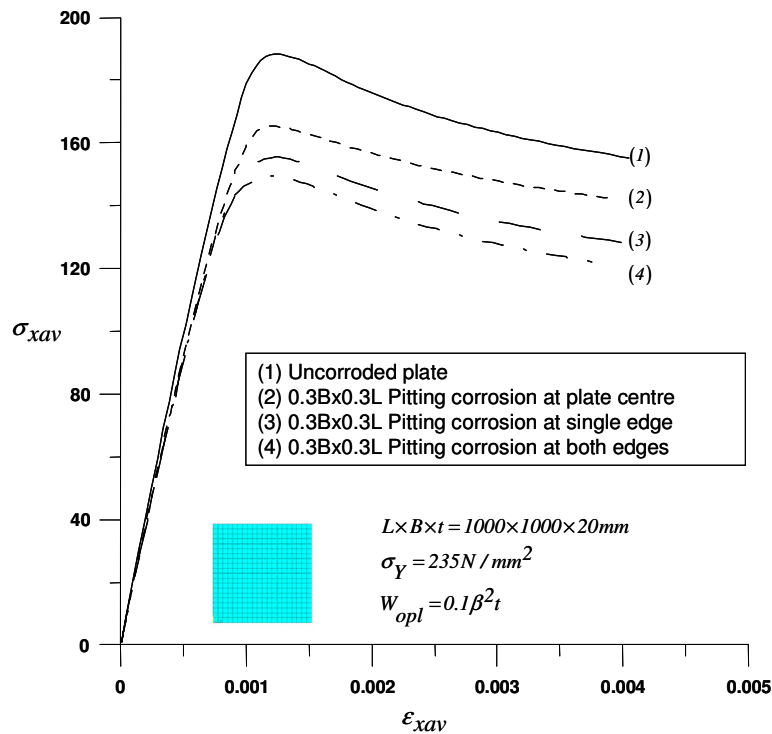


Fig. 5.23. A comparison of the average stress-strain curves

In addition, the effects of corrosion length along plate edges in the longitudinal direction on the ultimate strength of mild steel plate have been investigated based on a pitting width of 20% of plate breadth and a pitting depth of 0.5t.

Table 5-6
Effects of pitting corrosion length on ultimate strength

No	Pit location	FEM Input Variables					$\frac{A_0 - A_r}{A_0}$	σ_c N/mm ²	$\frac{\sigma_c}{\sigma_0}$
		B/t	x_1	x_2	x_3	x_4			
1	Both sides	50.0	1.68	0.0	0.0	0.00	1.00	188.30	1.000
2	Both sides	50.0	1.68	0.2	0.25	0.50	0.90	168.85	0.897
3	Both sides	50.0	1.68	0.2	0.50	0.50	0.90	157.01	0.834
4	Both sides	50.0	1.68	0.2	0.75	0.50	0.90	150.76	0.800
5	Both sides	50.0	1.68	0.2	1.00	0.50	0.90	147.49	0.783

The results are presented in Table 5-6 and Fig. 5.24. It is shown that the both sides pitting corrosion up to 50% of length (see cases 2 and 3) can reduce the strength of the plate significantly, whereas the differences between 50% and 75% or between 75% and 100% of pitting length (cases 4 and 5) are relatively smaller than the former. Fig.5.24 shows the effects of corrosion length on the strength. With the increase of corrosion length, the strength reduction is increased. However their individual post-buckling strengths are fairly close to each other.

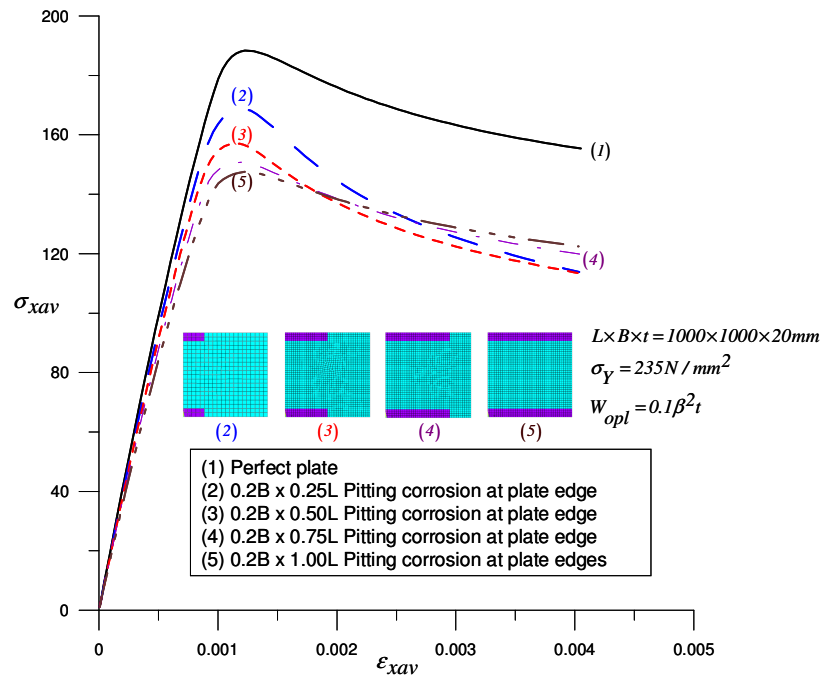


Fig. 5.24. Effects of pitting corrosion length

The above results clearly show that the strength reduction due to pitting corrosion depends on the width, length, depth and location of the corrosion. To further demonstrate this, a comparison between the results of these finite element analyses based on both sides pitting corrosion and using the formulation of Eq.3.26 in Chapter 3, which is proposed by Paik *et al.* [14, 15, 31], is shown in Fig. 5.25. It indicates that increasing pitting length leads to decreasing the ultimate strength of the plate based on the present finite element analyses results. However the formulation of Eq.3.26 cannot reflect this effect. In addition, the current results are more conservative than those of Eq.3.26. This large difference might be attributed to the fact that both sides pitting corrosion, where the plate element is actually being supported, has the most weakening effect on strength.

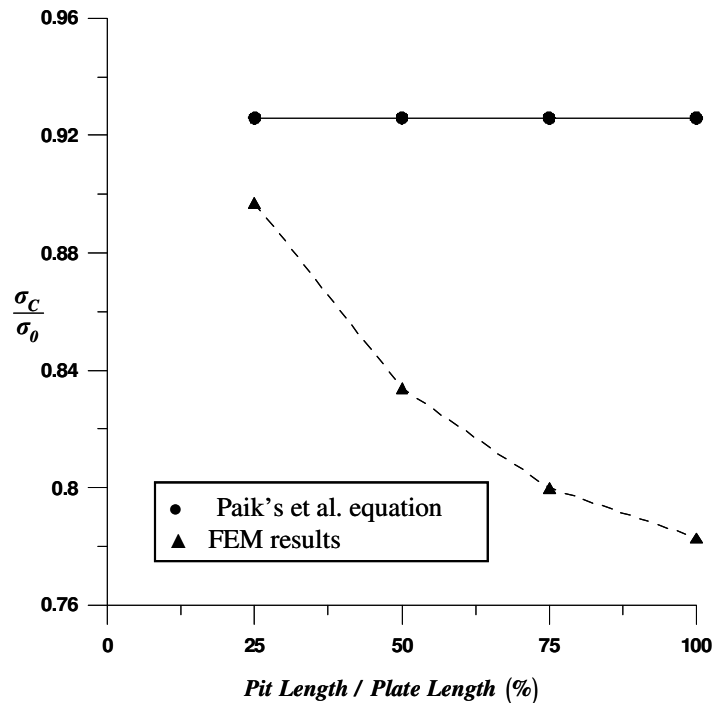


Fig. 5.25. A comparison of the FEA results with those of Eq.3.26

Fig. 5.26 further illustrates the effects of pit corrosion length, breadth and depth on the ultimate strength. It further demonstrates the importance of these three parameters.

Appendix C summarizes the results of 256 nonlinear finite element analyses based on higher tensile steel of 1m x 1m plate with a yield stress of 355 N/mm^2 with different geometry parameters such as plate slenderness, location, size and depth of pits on the ultimate strength of square plates.

Table 5-7 shows the effects of plate slenderness parameter (β), x_1 , on the ultimate strength based on pitting corrosion at both edges which has a pitting width of 20% of plate breadth, a pitting length of 100% of plate length and a pitting depth of 0.25t. The results indicate that the length, breadth and depth of pit corrosion have weakening

effects on the ultimate strength of the plates while plate slenderness has only marginal effect on strength reduction.

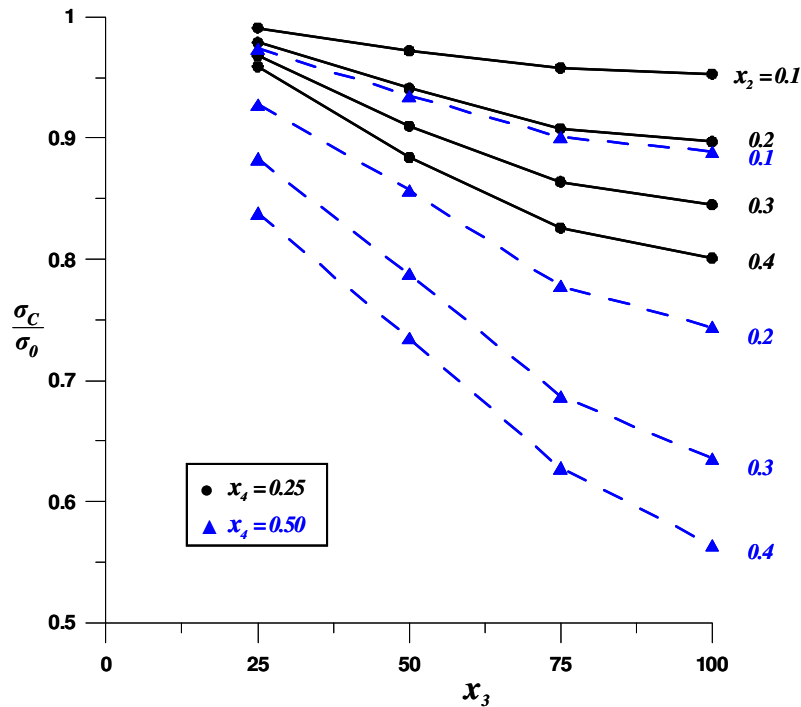


Fig. 5.26. Effects of pit length, breadth and depth on the ultimate strength

Table 5-7
Effects of plate slenderness parameter on ultimate strength

No	Pit location	FEM Input Variables					$\frac{A_0 - A_r}{A_0}$	σ_c N/mm ²	$\frac{\sigma_c}{\sigma_0}$
		B/t	x_1	x_2	x_3	x_4			
1	Both edges	41.7	1.72	0.2	1.0	0.25	0.95	251.87	0.897
2	Both edges	50.0	2.06	0.2	1.0	0.25	0.95	226.03	0.887
3	Both edges	62.5	2.58	0.2	1.0	0.25	0.95	203.66	0.879

Table 5-8 indicates the comparison of ultimate strength of plate (1m x 1m x 20t) with/without pitting corrosion based on existing formulae which are introduced in Section 5.3. Both edges pitting corrosion case is selected for this evaluation, where plate slenderness parameter (β), x_1 , is 2.06 which means that B/t ratio is 50 and $\sigma_y = 355 \text{ N/mm}^2$, x_2 is 0.3, x_3 is as indicated in Table 5-8 and x_4 is 0.5. Case No.1 indicates an uncorroded plate and No.2 to No.5 show corroded plates under different pit lengths. t_{eq} denotes equivalent average plate thickness which considers pitting corrosion, $FEM_{ave-cor}$ means the results of finite element analyses based on equivalent average plate thickness (t_{eq}) values and FEM_{BE} is the results of finite element analyses based on both edges type pitting corrosion.

Table 5-8

Comparison of ultimate strength of plates based on different pit length

No	x_3	t_{eq} (mm)	Faulkner (N/mm ²)	Fujikobo (N/mm ²)	NK (N/mm ²)	DNV (N/mm ²)	FEM _{ave-cor} (N/mm ²)	FEM _{BE} (N/mm ²)
1	0	20.00	260.95	283.11	283.11	231.50	254.82	254.82
2	0.25	19.25	254.18	276.27	276.27	222.82	250.20	227.61
3	0.50	18.50	247.17	269.13	269.13	214.14	245.67	189.39
4	0.75	17.75	239.94	261.70	261.70	205.46	240.83	155.82
5	1.00	17.00	232.46	253.97	253.97	196.77	237.13	149.37

The results show that the ultimate strengths from current finite element analyses based on both edges pitting corrosion concept indicate the most critical and conservative values than any other existing formulae in Section 5.3.

5.6 Proposed formulae for predicting ultimate strength reduction

As part of this overall study, new formulae for predicting the strength reduction due to pitting corrosion are derived by using a *multi-variable regression model*. The general form of a multi-variable regression is given by:

$$Y = \beta_0 + \beta_1 x_1 + \beta_2 x_2 + \dots + \beta_m x_m + \varepsilon \quad (\text{Eq.5.40})$$

The dependent variable Y can be calculated as a function of m independent variables x_1, x_2, \dots, x_m . A random error term (ε) can be added to allow for deviation between the right hand sides of equation, $\beta_0 + \beta_1 x_1 + \beta_2 x_2 + \dots + \beta_m x_m$, and the value of the dependent variable Y . The value of the coefficient β_i determines the contribution of the independent variable x_i and β_0 is the Y -intercept. The primary difference between fitting the single variable model and fitting the *multiple-variable regression model* is in computation difficulty. Recently a number of different statistical program packages have been developed to fit a multiple regression model and based on using the method of least squares. Some of the more popular are *BMD*, *Minitab*, *SAS* and *SPSS*. In this study, the *Minitab* program was used to develop a multiple regression model.

The multiple coefficient of determination R^2 can represent how well a multiple regression model fits a given set of data. $R^2 = 0$ means a complete lack of fit of the model to the data, and $R^2 = 1$ implies a perfect fit and which can be expressed by:

$$R^2 = 1 - \frac{\sum_{i=1}^n (y_i - \hat{y}_i)^2}{\sum_{i=1}^n (y_i - \bar{y})^2} \quad (\text{Eq.5.41})$$

where y_i is arbitrary data point, \bar{y} denotes the mean of the data points and \hat{y}_i

represents the predicted value of Y_i for the model. R^2 represents the fraction of the sample variation of the y values and which is explained by the least-squares prediction equation.

In this study, using data obtained from finite element analyses in *Appendix C*, two formulae were derived for predicting the ultimate strengths of square plates with pitting corrosion under uniaxial compression. One of them is for the plates with pitting corrosion on one side (edge) of the plates, the other is for the plates with symmetrical pitting corrosion on two sides (edges). Four variables, x_1 , x_2 , x_3 and x_4 , have been chosen as independent variables, where the valid ranges of x_1 is 1.719 to 2.576, which corresponds to $B/t = 40$ to 65, x_2 is 0 to 0.4, x_3 is 0 to 1.0 and x_4 is 0 or 0.5. 128 sets of finite element analyses results for single edge type pitting corrosion on the plate and another 128 sets with both edges type pitting corrosion are used to derive the formulae. *Appendix D* indicates all data which include the independent four(4) variables x_1 , x_2 , x_3 , x_4 based on finite element modelling results in *Appendix C*.

The ultimate strength reduction of plates with *single edge* (SS) corrosion can be formulated by:

$$\left(\frac{\sigma_c}{\sigma_0} \right)_{SS} = \begin{cases} 1 & x_2 \cdot x_3 \cdot x_4 = 0 \\ 1.25 - 0.0144x_1 - 0.336x_2 - 0.166x_3 - 0.434x_4 & x_2 \cdot x_3 \cdot x_4 \neq 0 \end{cases} \quad (\text{Eq.5.42})$$

The ultimate strength reduction of plates with *both edges* (BS) corrosion can be expressed by:

$$\left(\frac{\sigma_c}{\sigma_0} \right)_{BS} = \begin{cases} 1 & x_2 \cdot x_3 \cdot x_4 = 0 \\ 1.43 - 0.0414x_1 - 0.603x_2 - 0.220x_3 - 0.576x_4 & x_2 \cdot x_3 \cdot x_4 \neq 0 \end{cases} \quad (\text{Eq.5.43})$$

Fig. 5.27 and 5.28 illustrate the correlation between the finite element results and the derived formulae. The formula for plates with single edge type pitting corrosion has a coefficient of variation (*C.O.V*) of 0.030 and a mean of 1.001, and the multiple coefficient of determination (R^2) is 0.907. In the case of plates with both edges type pitting corrosion, the coefficient of variation (*C.O.V*) is 0.0595, the mean is 0.998, and the multiple coefficient of determination (R^2) is 0.863. So the proposed formulae are quite accurate.

It should be pointed out that the ultimate strength reduction predicted by Eq.5.42 and Eq.5.43 should be always less or equal to 1. However when x_2 , x_3 , and x_4 are very small, Eq.5.42 and 5.43 could possibly produce a value, which is slightly greater than 1. In this case, the ultimate strength reduction should be set as one.

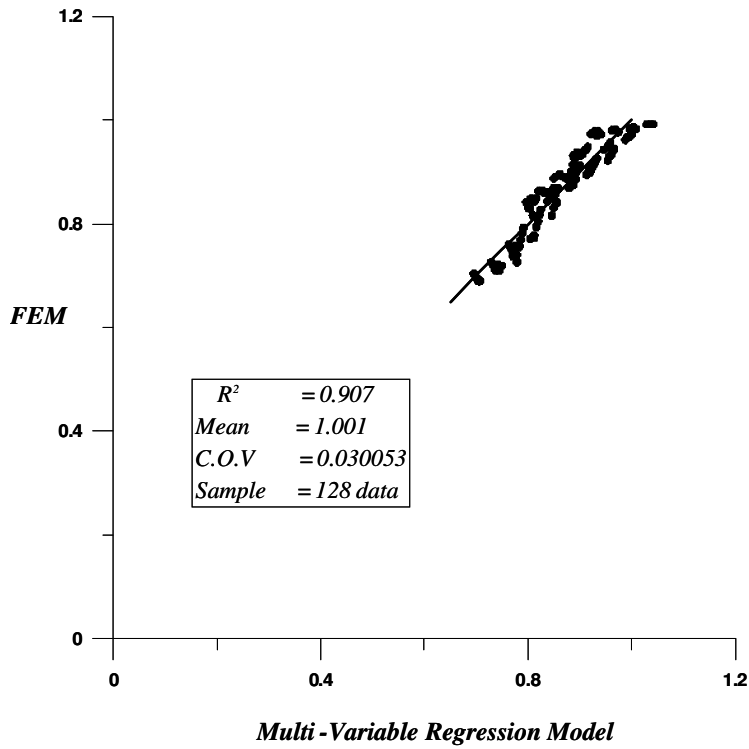


Fig. 5.27. Correlation of FEM results and Multi-Variable Regression based outputs for single edge pitting corrosion

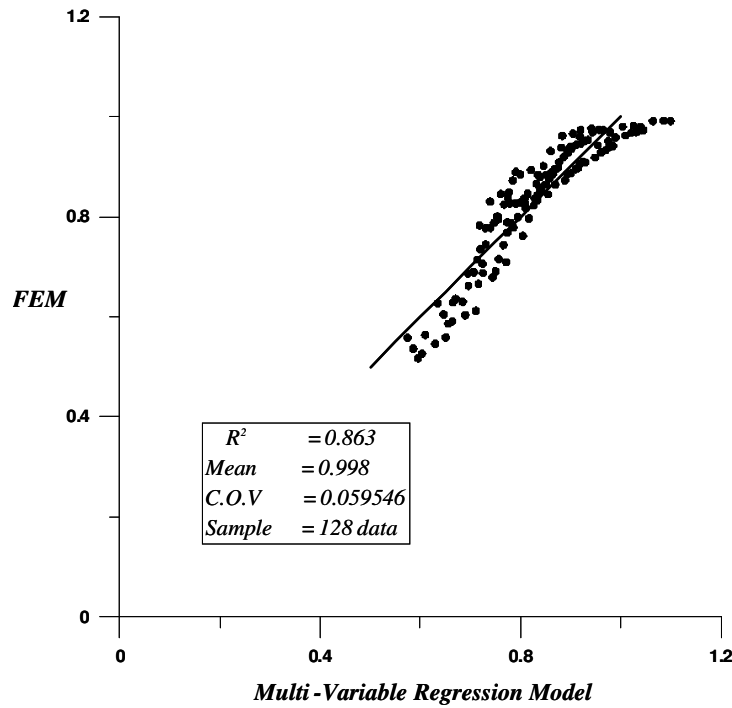


Fig. 5.28. Correlation of FEM results and Multi-Variable Regression based outputs for both edges pitting corrosion

From Eq.5.42 and Eq.5.43 it is observed that corrosion depth has the most weakening effects on strength reduction among the four parameters when the corrosion is on one side of the edge of the plates. Corrosion width is the second most important parameter, while plate slenderness has only marginal effect on the strength reduction. However when corrosion is on both sides of the edges the corrosion width is the most important parameter, which is followed by corrosion depth, and then corrosion length.

Again plate slenderness has very little effect on the strength reduction. This is because currently proposed equations are not based on ultimate strength value itself but based on strength reduction ratio and the valid slenderness ratios are restricted from 1,719 to 2.576, which corresponds to $B/t = 40$ to 65. However if the range of plate slenderness parameter is increased then the effect on ultimate strength of plate might be becoming noticeable.

5.7 Application of Artificial Neural Networks (ANN) to ultimate strength of plates with pitting corrosion

Utilising the results of a considerable number of finite element analyses as described in previous sections, the Artificial Neural Networks (ANN) method can be applied to develop a method to predict the ultimate strength of unstiffened plate with localized corrosion more accurately than by any other existing simplified empirical formulae including the ones developed and proposed in Section 5.6.

The first step toward the development of artificial neural networks was introduced by *Warren McCulloch and Pitts* [55]. They modelled a simple neural network with electrical circuits. In 1959, *Bernard Widrow and Marcian Hoff* [56, 57] developed models which were called “*Adaline*” and “*Madaline*”. These models were named for their use of so-called Multiple Adaptive Linear Elements. “*Madaline*” was the first neural network to be applied to a real world problem [58].

Since the late 1980’s the technology and the application of ANN have been developed considerably and employed remarkably in many fields of science and engineering.

Recently *Artificial Neural Networks* (ANN) methods have been introduced to structural engineering problems. *Hajela et al.* [59] used a back-propagation neural network to represent the force-displacement relationship in static structural analysis. Such models provide computationally efficient capability for rapid reanalysis and appear to be well suited for application in numerical optimum design. *Shao et al.* [60] have applied ANN to predict the reliability of structures. In their paper, a ANN model was used to approximate the limit state function. Then the reliability of the structure was evaluated by a *First Order Second Moment Method (FORM)*. This methodology was applied to a couple of simple examples and to a portal frame. The results obtained from ANN models are considered to be reasonably accurate [61]. *Jenkins* [62] considered a method of structural re-analysis based on use of a neural network on a cable-stayed structure and on a truss structure. *Wei* [63] investigated a two-layered back-propagation neural network to predict the local and distortional buckling behaviour of cold formed steel compression members.

Some recent developments in the application of ANN methodology in marine and offshore structural field have been carried out and which include structural reliability analysis by *Papadrakakis et al.* [64, 65], *Shao et al.* [60], *Hurtado et al.* [66], *Gomes et al.* [67] and *Deng, Gu et al.* [68]. *El-hewy et al.* [69] and *Pu et al.* [61] found out that an ANN-based response surface method (RSM) is much more accurate and efficient than conventional polynomial-based RSM in structural reliability analysis. The ANN method also has been used to estimate the ultimate strength of stiffened and unstiffened plates by *Wei et al.* [70] and *Pu et al.* [61]. They found that ANN-based predictions generally produce better results than those from empirical formulae obtained from conventional regression analysis. Other attempts to use ANN in naval architecture and marine engineering are introduced by *Ray et al.* [71], *Mesbahi and Bertram* [72], *Zubaydi et al.* [73] and *Alkan et al.* [74], and in wave and motion analysis by *Xu and Haddara* [75], *Londhe and Deo* [76], *Agrawal and Deo* [77] and *Mazaheri and Downie* [78].

5.7.1 Biological neurons

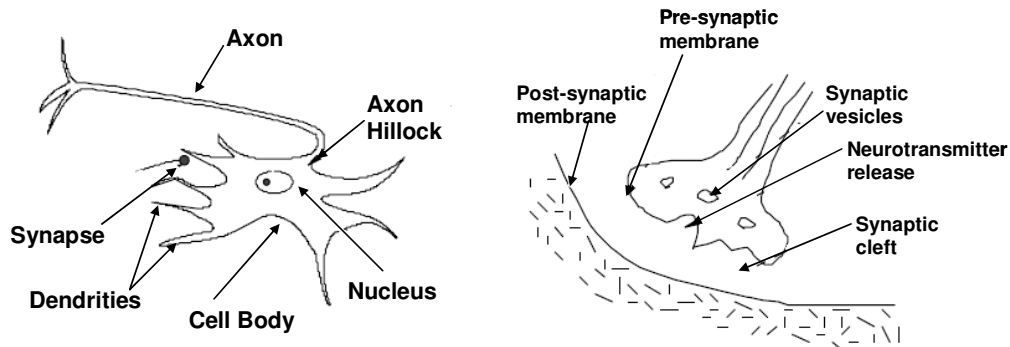


Fig. 5.29. The basic features of a biological neuron and chemical signal at synapse

The human brain contains approximately ten thousand million basic units of a form called neurons. The neuron is the basic unit of the brain, and consists of dendrites, synapses, cell body and axon. A conceptual representation of the basic feature of a neuron is shown in Fig. 5.29. Each of these neurons is connected to about ten thousand others, thus constituting a very complex network.

The soma is the body of the neuron. Dendrites are extension of the soma which act as the connections through which all the inputs to the neuron arrive. Another type of nerve process attached to the soma is called an axon which serves as the output channel of the neuron. The axon terminates in a specialised contact called a synapse that couples the axon with the dendrite of another cell. The synapse releases chemicals called neurotransmitters when its potential is raised sufficiently by the action potential. Generally the process can be described as one that the input channels receive their input through the synapses of other neurons. The soma then turns that further processed value into an output which is sent out to other neurons through the axon and synapses. Thus input to the overall networks is subject to progressive “processing” as it flows further through the network until it reaches some conclusive form deemed to be an acceptable output from the overall network.

Learning in biological systems is thought to occur when modification is made to the effective coupling between one cell and another, at the synaptic junction. The mechanism for achieving this seems to be to facilitate the release of more neurotransmitters. This has the effect of opening more gates on the dendrite on the post-synaptic side of the junction, and so increasing the coupling effect of the two cells. The adjustment of coupling so as to reinforce good connections is an important feature of artificial neural network models, as is the effective coupling, or weighting, that occurs on each of the connections into a neuronal cell.

General overviews of biological neurons are provided in *Robert* [79], *Beale and Jackson* [80] and *Anderson and McNeill* [58], etc.

5.7.2 Artificial neural network

The characteristics and ability of the human brain can be described, such as the ability to adopt or learn, to process information on the basis of knowledge and to modify and accumulate the knowledge in an information processing manner, massive parallelism, a significant amount of redundancy, high processing speed and sophisticated order, the ability to self repair and recognition etc.

An **artificial neural network** (ANN), also called a *simulated neural network* (SNN) or just a *neural network* (NN), is an interconnected group of artificial neurons that uses a mathematical or computational model for information processing based on a connectionist approach to computation [81]. The motivation for the development of a simulated neural network technology stemmed from the desire to develop an artificial system that could perform "intelligent" tasks similar to those performed by the human brain. Artificial neural networks resemble the human brain in the following two ways: a neural network acquires knowledge through learning and a neural network's knowledge is then stored within inter-neuron connection strengths known as synaptic weights.

The true power and advantage of neural networks lies in their ability to represent both linear and non-linear relationships and in their ability to learn these relationships directly from the data being modelled. Traditional linear models are simply inadequate when it comes to modelling data that contains non-linear characteristics.

Artificial neural networks (ANN) have several advantages, because they resemble the principles of the real human neural system structure [81].

- **Learning** : ANN have the ability to learn based on data provided in the so called learning stage. ANN creates its own representation of the data given in the learning process.
- **Tolerance to faults** : because ANN store redundant information, partial destruction of the neural network do not result in damaging completely the network response.
- **Flexibility** : ANN can handle input data without important changes like noisy signals or other changes in the given input data

- **Real Time** : ANN are parallel structures; if they are implemented in this way using computers or special hardware then results response in almost real time can be achieved.

5.7.2.1 ANN fundamentals

The typical artificial neuron is a processing element as depicted in Fig. 5.30 with n inputs, where x_1, x_2, x_3 and x_n are input parameters. Those inputs are each multiplied by individual weight vectors, these weights are represented by w_n , and after summing the results, are fed through an activation transfer function, f , to generate a result, and then the output (Y).

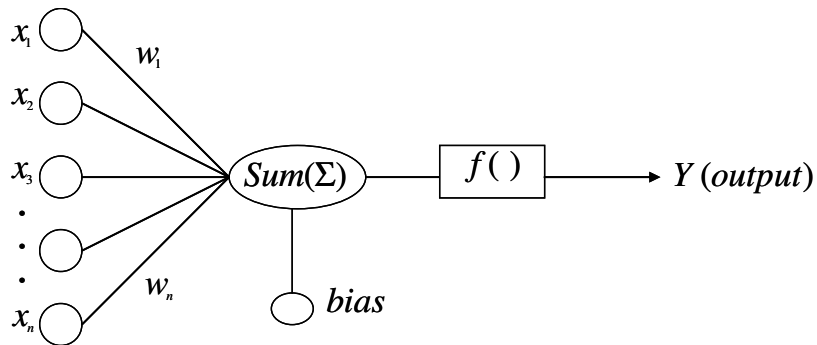


Fig. 5.30. Outline of the basic model of artificial neuron

This can be written as:

$$Y = f \left[\sum_{k=1}^n x_k w_k + b_k \right] \quad (\text{Eq.5.44})$$

where b is a scalar bias or is named as a threshold. This bias is much like a weight except that it has a constant input of 1.

As described above, the result of the summation function is then transformed to a working output through the associated relevant transfer function. There are several types of activation function available as follows:

- A linear activation function

$$f(x) = x$$

- Non-linear activation functions

The Logistic function :
$$f(x) = \frac{1}{1 + \exp(-\beta x)}$$

The Tanh function :
$$f(x) = \frac{e^x - e^{-x}}{e^x + e^{-x}}$$

where β is the slope parameter of the logistic function

- Threshold function :
$$f(x) = \begin{cases} 1 & \text{if } x > 0 \\ -1 & \text{if } x < 0 \end{cases}$$

The most commonly used types are the logistic function and the hyperbolic tangent function because they introduce non-linearity into the network's calculations by "squashing" the neuron's activation level into the range [0,1] for the logistic function and [-1,1] for the hyperbolic tangent function.

Typically the weights in a neural network are initially set to small random values. This represents the network knowing nothing; its resulting output is essentially a random function of its input. As the training process proceeds, the connection weights are gradually modified according to computation rules specific to the particular learning algorithm being used. Ideally the weights eventually converge to values allowing them to perform a useful computation where the overall output meets the required value.

5.7.3 Types of artificial neural networks

There are various kinds of network architectures available, among others the ones following are considered the most common and popular types: The definitions of neural network the reader are referred to existing publications by *Beale and Jackson*, *Wikipedia* and *Principe et al.* [58, 80-82].

5.7.3.1 Single layer feed-forward network

The earliest type of neural network is a *single-layer perception* network, which consists of a single layer of output nodes; and in which the inputs are fed directly to the corresponding output via a series of weights. In this way it can be considered the simplest kind of feed-forward network. The sum of the products of the weights and the inputs is calculated in each node, and if the value is above some threshold (typically 0) the neuron fires and takes the activated value (typically 1); otherwise it takes the deactivated value (typically -1). Neurons with this kind of activation function are also called *McCulloch-Pitts neurons* or *threshold neurons*.

5.7.3.2 Multi-layer feed-forward network

When the neural networks have one or more hidden layers these are called multi-layer neural networks or *multi-layer perceptions (MLP)* and this is the most commonly employed neural network model. This type of neural network is also known as a supervised network because it requires a desired output together with associated input

in order to learn. The goal of this type of network is to create a model that correctly maps the input to the output using historical data so that the model can then be used to produce output from new input when the desired output is unknown. A graphical representation of an MLP is illustrated in Fig. 5.31.

Multi-layer networks are trained by using a variety of learning techniques, the most popular being back-propagation. Here the output values are compared with the correct answer corresponding to a given set of input data in order to compute the value of some predefined error-function. By various techniques the error is then fed back through the network. Using this information, the algorithm adjusts the weights of each connection in order to reduce the value of the error function by some small amount.

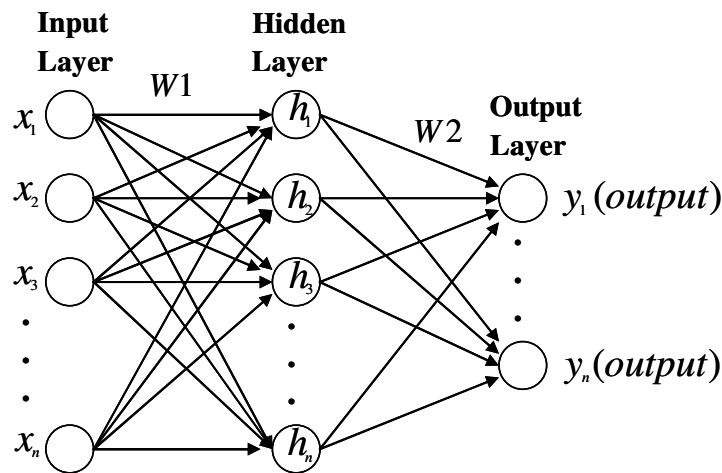


Fig. 5.31. Multi-layer feed-forward neural network

After repeating this process for a sufficiently large number of training cycles the network will usually converge to some state where the error of the calculations is acceptably small. In this case one says that the network has learned to achieve a certain target function. To adjust weights properly one applies a general method for non-linear optimization task that is called gradient descent. For this, the derivation of the error function with respect to the network weights is calculated and the weights are then changed such that the error decreases, thus going downhill on the surface of the error function.

5.7.3.3 Recurrent network

As specified above, the feed-forward network propagates data linearly from input to output. However in a recurrent or feedback neural network, the processing units are allowed bi-directional data flow and also propagate data from later processing stages to earlier stages. The typical examples of this type of networks are a simple recurrent network, so called “*Elman network*”, and a fully recurrent network.

5.7.4 Learning Algorithm

The general learning rule for multilayer perceptions is called the “*backpropagation rule*” which was proposed by *Rumelhard et al.* [83] is the most popular rule due to its well-studied theory. The backpropagation algorithm is an optimization technique designed to minimize the value of an objective function. The most commonly used objective function is a squared error given by:

$$\varepsilon^2 = [t_q - f_{qk}]^2 \quad (\text{Eq.5.45})$$

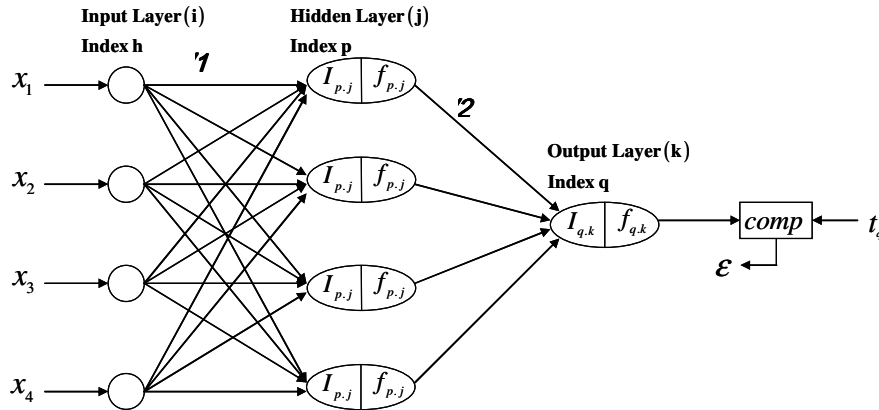


Fig. 5.32. Multi-layer back-propagation neural network

This is the approach that is adopted for this study. The formulation for ultimate strength estimation for plates with pitting corrosion is developed by using the artificial neural network approach trained with the results of detailed numeric analyses. The target output of ANN is strength reduction ratio which represents the ultimate strength of plate with pitting corrosion (σ_c) over the ultimate strength of uncorroded plate (σ_o) as shown in Appendix E. The overall network of back-propagation algorithm is illustrated in Fig. 5.32.

The layers are labeled i, j, k , which represents input, hidden and output respectively and the neurons in each input, hidden and output layers are indexed as h, p, q respectively. x denotes input value, t is target output value, W is weight value, I is internal activation, f is neuron output and ε represents the error term.

The outputs using a logistic activation function can be expressed by:

$$f = \text{logistic}\{W2 \times [\text{logistic}(W1 \times x + b1)] + b2\} \quad (\text{Eq.5.46})$$

where $W1$ denotes first layer weight matrix, $W2$ represents second layer weight matrix, $b1$ is first layer bias vector and $b2$ is second layer bias vector.

The input vector can be augmented with a dummy node representing the bias input. This dummy input of 1 is multiplied by a weight corresponding to the bias value. Thus we can get a more compact matrix representation as follows:

$$f = \text{logistic} \left(\mathbf{W2} \times \begin{bmatrix} 1 \\ \text{logistic}(\mathbf{W1} \times \mathbf{X}) \end{bmatrix} \right) \quad (\text{Eq.5.47})$$

where $\mathbf{X} = [1 \ x_{f1} \ x_{f2} \ x_{f3} \ x_{f4}]^T$

$$\mathbf{W1} = \begin{bmatrix} b_{h_1 \cdot p_1} & w_{h_1 \cdot p_1} & w_{h_2 \cdot p_1} & w_{h_3 \cdot p_1} & w_{h_4 \cdot p_1} \\ b_{h_1 \cdot p_2} & w_{h_1 \cdot p_2} & w_{h_2 \cdot p_2} & w_{h_3 \cdot p_2} & w_{h_4 \cdot p_2} \\ b_{h_1 \cdot p_3} & w_{h_1 \cdot p_3} & w_{h_2 \cdot p_3} & w_{h_3 \cdot p_3} & w_{h_4 \cdot p_3} \\ b_{h_1 \cdot p_4} & w_{h_1 \cdot p_4} & w_{h_2 \cdot p_4} & w_{h_3 \cdot p_4} & w_{h_4 \cdot p_4} \end{bmatrix}$$

$$\mathbf{W2} = [b_2 \ w_{p_1 \cdot q} \ w_{p_2 \cdot q} \ w_{p_3 \cdot q} \ w_{p_4 \cdot q}]$$

5.7.4.1 Output layer weight update

The output layer weights are changed in proportion to the negative gradient of the squared error with respect to the weights. These changes can be calculated using the chain rule expressed by:

$$\begin{aligned} \Delta w_{pq,k} &= -\eta_{p,q} \cdot \frac{\partial \varepsilon^2}{\partial w_{pq,k}} = -\eta_{p,q} \cdot \frac{\partial \varepsilon^2}{\partial f_{q,k}} \cdot \frac{\partial f_{q,k}}{\partial I_{q,k}} \cdot \frac{\partial I_{q,k}}{\partial w_{pq,k}} \\ &= -\eta_{p,q} \cdot (-2) [t_q - f_{q,k}] \cdot f_{q,k} [1 - f_{q,k}] \cdot f_{p,j} \\ &= -\eta_{p,q} \cdot \delta_{pq,k} \cdot f_{p,j} \end{aligned} \quad (\text{Eq.5.48})$$

where η is the step size of the minimization, which is known as *learning rate* and

$$-2 [t_q - f_{q,k}] \cdot f_{q,k} [1 - f_{q,k}] = \delta_{pq,k}$$

Accordingly, the weight update equation for the output neuron can be expressed by:

$$w_{pq,k}(N+1) = w_{pq,k}(N) - \eta_{p,q} \cdot \delta_{pq,k} \cdot f_{p,j} \quad (\text{Eq.5.49})$$

5.7.4.2 Hidden layer weight update

The hidden layer outputs have no target values. Therefore, a procedure is used to back-propagate the output layer errors to the hidden layer neurons in order to modify

their weights to minimize the error. The equation of hidden layer weight updates can be given by:

$$\Delta w_{hp,j} = -\eta_{h,p} \frac{\partial \mathcal{E}^2}{\partial w_{hp,j}} = -\eta_{h,p} \sum_{q=1}^n \frac{\partial \mathcal{E}^2}{\partial w_{hp,j}} \quad (\text{Eq.5.50})$$

$$= -\eta_{h,p} \sum_{q=1}^n \frac{\partial \mathcal{E}_q^2}{\partial f_{q,k}} \cdot \frac{\partial f_{q,k}}{\partial I_{q,k}} \cdot \frac{\partial I_{q,k}}{\partial f_{p,j}} \cdot \frac{\partial f_{p,j}}{\partial I_{p,j}} \cdot \frac{\partial I_{p,j}}{\partial w_{hp,j}}$$

where $\frac{\partial \mathcal{E}_q^2}{\partial f_{q,k}} = (-2)[t_q - f_{q,k}]$, $\frac{\partial f_{q,k}}{\partial I_{q,k}} = \alpha f_{q,k} [1 - f_{q,k}]$, $\frac{\partial I_{q,k}}{\partial f_{p,j}} = w_{pq,k}$,

$$\frac{\partial f_{p,j}}{\partial I_{p,j}} = \alpha f_{p,j} [1 - f_{p,j}], \quad \frac{\partial I_{p,j}}{\partial w_{hp,j}} = x_h$$

$$\begin{aligned} \frac{\partial \mathcal{E}^2}{\partial w_{hp,j}} &= \sum_{q=1}^n (-2)[t_q - f_{q,k}] \cdot \alpha f_{q,k} [1 - f_{q,k}] \cdot w_{pq,k} \cdot \alpha f_{p,j} [1 - f_{p,j}] \cdot x_h \\ &= \sum_{q=1}^n \delta_{pq,k} \cdot w_{pq,k} \cdot \alpha f_{p,j} [1 - f_{p,j}] \cdot x_h \end{aligned} \quad (\text{Eq.5.51})$$

where $\delta_{pq,k} w_{pq,k} \frac{\partial f_{p,j}}{\partial I_{p,j}} = \delta_{hp,j}$

Accordingly, the weight update equation for the hidden neuron can be expressed by:

$$w_{hp,j}(N+1) = w_{hp,j}(N) - \eta_{hp} \cdot x_h \cdot \delta_{hp,j} \quad (\text{Eq.5.52})$$

Momentum learning is an improvement to the straight gradient-decent search in the sense that the past increment to the weight is used to speed up and stabilize convergence. In momentum learning the equation to update the weights can be expressed by:

$$w_{i,j}(N+1) = w_{i,j}(N) - \eta \cdot \delta_i(N) \cdot x_j(N) + \alpha (w_{i,j}(N) - w_{i,j}(N-1)) \quad (\text{Eq.5.53})$$

where α is the momentum constant.

5.7.5 Design of ANN model

There are no well defined rules for building up a ANN structure for a particular purposed data. Generally we can find and recommend the most suitable ANN

structure by trial and error and by comparing the results with existing available data. The general procedure to establish an ANN model is illustrated in Fig. 5.33.

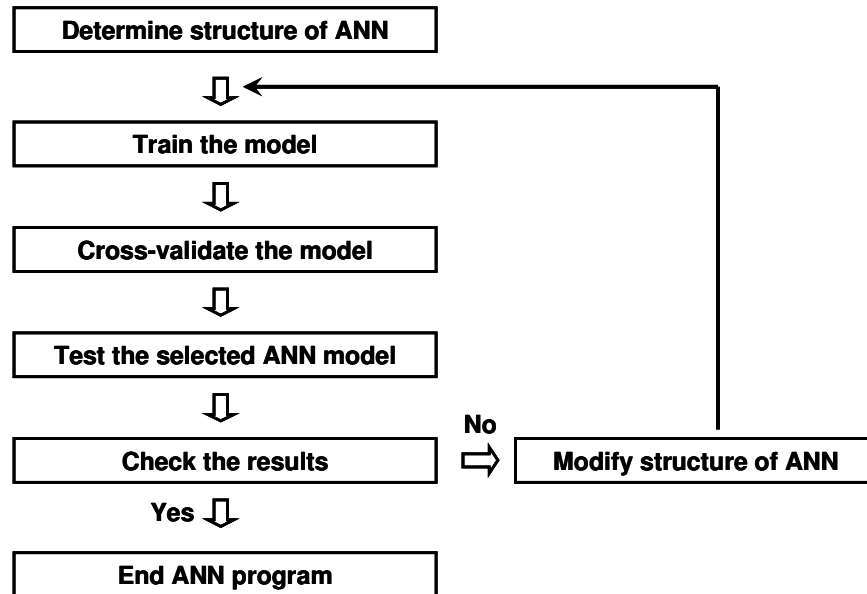


Fig. 5.33. Procedure to establish ANN models

5.7.5.1 Determine structure of ANN

The processing elements in the input layer and output layer are generally selected by the nature of the data and structural models. In this research, four(4) independent input parameters (x_1, x_2, x_3 and x_4) are selected as input vectors. x_1 is plate slenderness parameter (β), x_2 denotes the ratio of pit breadth to plate width, x_3 indicates the ratio of pit length to plate length and x_4 is the ratio of pit depth to plate thickness. The target output vector of the ANN is the ratio of the ultimate strength of plate with pitting corrosion (σ_c) over the ultimate strength of uncorroded plate (σ_o) as illustrated in Fig. 5.32. The overall input and output vectors for ANN networks based on previous 265 cases of finite element analyses of higher strength steel plate with pitting corrosion are listed in *Appendix E*.

There are no rules available to determine the optimum number of hidden layers and the number of processing elements (PE) in each hidden layer. In this study, all network models have one hidden layer because this kind of model has been found to have sufficient accuracy and less demand on the amount of training data. Some evaluation procedures have been performed within this study to determine the most suitable number of PEs in a hidden layer. Both the hidden layer and the output layer used a logistic (sigmoid) activation function. Among the 265 sets of finite element analysis results, nine models are based on perfect plate (no pitting corrosion) with different B/t ratios (40.0, 41.7, 45.0, 45.5, 50.0, 55.0, 55.6, 60.0, 62.5) and with corresponding plate slenderness parameters. 127 sets are finite element analyses for pitting corrosion on single edge location (SE). 96 sets were selected for training data

and 20 sets were taken for cross validation data. One of the popular commercial artificial neural network program, so called *NeuroSolutions* [84] has been used for this study.

The effects of the number of PEs in the hidden layer have been evaluated by changing it from 2 to 9. The number of epochs (the complete mapping out procedure of input data onto output neurons through the Artificial Neural Network Model) used for this testing has been initially set to 5000 and cross validation termination criteria is to terminate after 100 epochs without further improvement. As the network is trained, the weights of the system are continuously adjusted to incrementally reduce the difference between the output of the system and the desired response. This difference can be measured by the mean squared error (MSE). The MSE is the average of the differences between each output PE and the desired output. The formula for the average MSE is given by:

$$MSE = \frac{\sum_{j=0}^P \sum_{i=0}^N (d_{ij} - y_{ij})}{N P} \quad (\text{Eq.5.54})$$

where P = number of output processing elements
 N = number of exemplars in the data set
 d_{ij} = desired output for exemplar i at processing element j
 y_{ij} = network output for exemplars i at processing element j

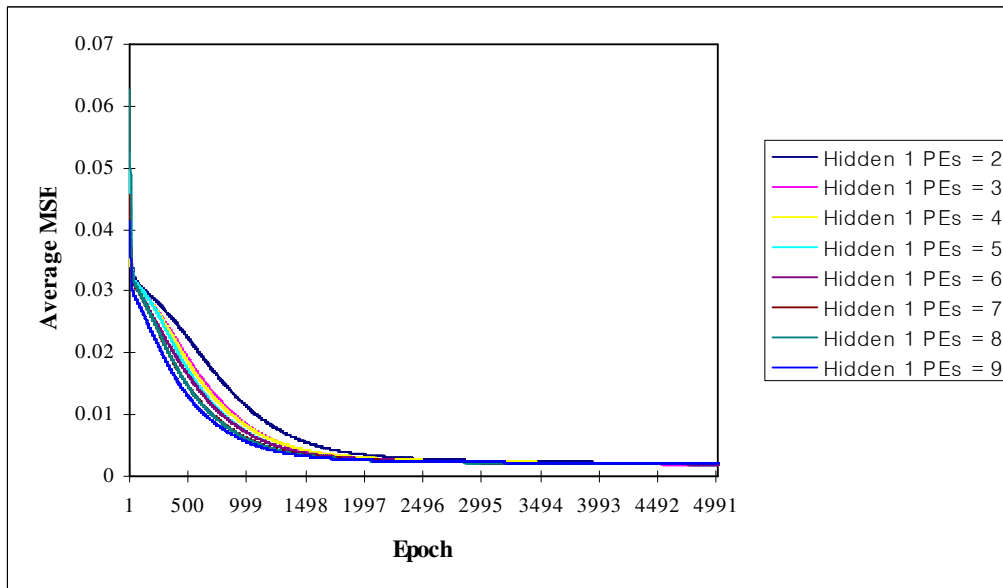


Fig. 5.34. Average MSE versus epoch for trained data based on various numbers of hidden layer processing elements

The results indicate that the number of PEs in hidden layer will not effect on the accuracy of ANN based estimation as long as there is an adequate number of epochs.

This means that after a certain number (3000) of epochs, the average MSE is almost same at all different PE numbers (2 to 9) as shown in Fig. 5.34. In this study, the same number of processing elements (4 PEs) in hidden layer has been selected as illustrated in Fig. 5.32.

5.7.5.2 Training and cross validation

Most of artificial neural network solutions have been trained with so-called supervised training. In this study, data from Appendix E are used for input and corresponding output values. In supervised training, the actual output of a neural network is compared to the desired output. The initial weights are chosen randomly, then adjusted by the network so that the next iteration, or cycle, will produce a closer match between the desired and the actual output. The learning method tries to minimize the current errors of all processing elements. Errors are then propagated back through the system, causing the system to modify the input weights until an acceptable network accuracy is reached.

As far as applicable, training data need to be fairly large to contain all the needed information if the network is to learn the features and relationships that are important. Generally the training data should have both the large value range of data and also include all the characteristics of the problem class of data. After training data, if the network accuracy is not considered to be good enough, then the inputs and outputs, the number of layers, the number of elements per layer and transfer functions should be reviewed.

During the training procedure, the input and desired data will be repeatedly presented to the network. As the network learns more and more, the error tends to drop toward zero. However a lower error does not always mean a better network. It is possible to over-train a network. Cross validation is a highly recommended criteria for stopping the training of a network. In this research, a total 116 training data sets (include cross validation) have been used for pitting corrosion at a single edge location (SE) from *Appendix E*. The number of epoch used for this testing has been set to 5000 and cross validation termination criteria is to automatically terminate after 100 epochs without improvement.

5.7.5.3 Testing ANN models

Once the trained ANN model has been validated, a comparison between the desired output and actual network output have been evaluated based on randomly selected 20 sets of new data for pitting corrosion on a single edge location (SE). Table 5-9 shows two sets of results of ANN tests, one based on the logistic (sigmoid) activation function and another based on the hyperbolic tangent (Tanh) activation function. It indicates that the ANN results based on the hyperbolic tangent (Tanh) activation function shows more accurate than the logistic based ANN results.

Table 5-9
Comparison of ANN outputs and desired output for single edge pitting corrosion

No	ANN Input Variables				$\frac{\sigma_c}{\sigma_o}$	ANN Output (Sigmoid)	ANN Output (Tanh)	
	Type	x1	x2	x3				x4
1	SE	1.719	0.1	0.50	0.25	0.972	0.973	0.969
2	SE	1.875	0.4	0.50	0.50	0.782	0.778	0.783
3	SE	2.576	0.4	1.00	0.50	0.704	0.718	0.693
4	SE	2.576	0.3	1.00	0.50	0.726	0.730	0.713
5	SE	1.719	0.4	0.50	0.25	0.913	0.917	0.923
6	SE	1.719	0.1	0.25	0.50	0.969	0.955	0.984
7	SE	2.291	0.1	0.50	0.25	0.967	0.969	0.960
8	SE	2.060	0.0	0.00	0.00	1.000	1.000	1.000
9	SE	2.576	0.3	0.25	0.25	0.980	0.959	0.964
10	SE	1.719	0.2	0.25	0.50	0.930	0.928	0.946
11	SE	2.061	0.1	0.75	0.25	0.948	0.949	0.946
12	SE	2.291	0.1	0.50	0.50	0.901	0.901	0.907
13	SE	2.291	0.2	0.50	0.50	0.831	0.856	0.834
14	SE	1.875	0.4	1.00	0.25	0.846	0.818	0.846
15	SE	2.061	0.3	0.75	0.50	0.740	0.766	0.735
16	SE	1.875	0.3	0.50	0.25	0.922	0.940	0.920
17	SE	2.291	0.3	0.50	0.50	0.793	0.807	0.789
18	SE	2.576	0.1	0.75	0.50	0.843	0.836	0.851
19	SE	2.576	0.4	0.25	0.50	0.863	0.809	0.841
20	SE	2.291	0.4	1.00	0.25	0.845	0.807	0.843

Fig. 5.35 and Fig. 5.36 indicate that the hyperbolic tangent (Tanh) activation function is more accurate and can converge at less number of testing procedure (epoch) than logistic activation function for this ANN model for pitting corrosion.

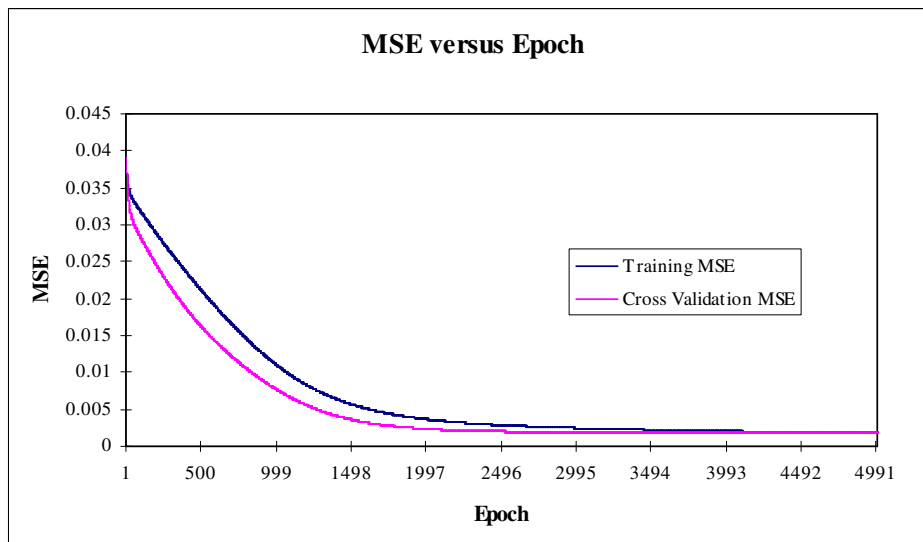


Fig. 5.35. Mean square error versus epoch for pitting corrosion on single edge location by using a logistic activation function

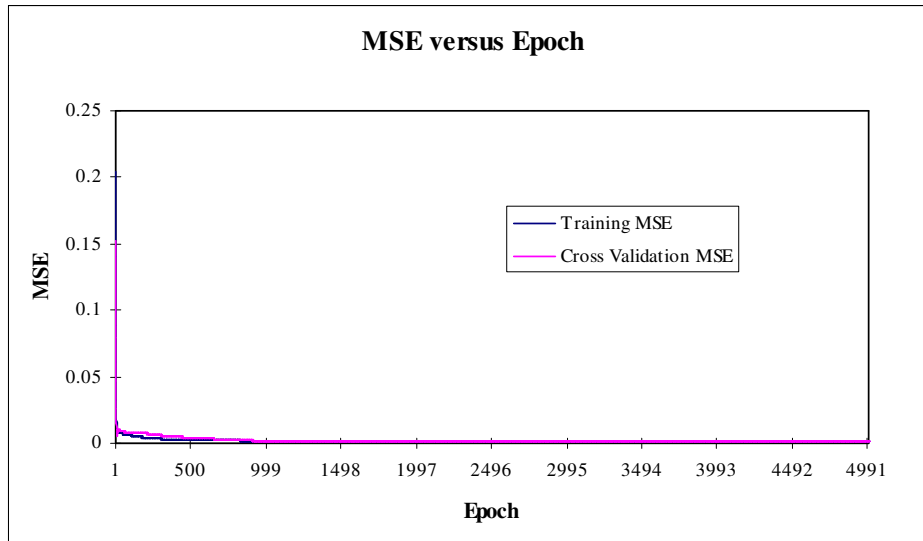


Fig. 5.36. Mean square error versus epoch for pitting corrosion on single edge location by using a hyperbolic tangent (Tanh) activation function

Fig. 5.37 and 5.38 illustrate a comparison of desired output obtained from finite element modelling and the corresponding ANN based output. Generally the size of the mean square error (MSE) can be used to determine how well the network output conforms to the desired output, but it doesn't necessarily reflect whether the two sets of data move in the same direction. The correlation coefficient (r) solves this problem. The correlation coefficient between a network output y and a desire output d can be expressed by:

$$r = \frac{\sum_i (y_i - \bar{y})(d_i - \bar{d})}{\sqrt{\frac{\sum_i (d_i - \bar{d})^2}{N}} \sqrt{\frac{\sum_i (y_i - \bar{y})^2}{N}}} \quad (\text{Eq.5.55})$$

The correlation coefficient is confined to the range $[-1,1]$. When $r=1$ there is a perfect positive correlation between y and d which mean that they vary by the same amount. When $r=-1$, there is a perfectly linear negative correlation between y and d which means they vary in opposite ways.

Table 5-10 summarizes comparison results of the selected 20 sets of examples for a logistic (sigmoid) and a hyperbolic tangent (Tanh) activation functions.

Table 5-10

Comparison of the performance of sigmoid and hyperbolic tangent activation function

ANN Network	Sigmoid	Tanh
MSE (mean square error)	0.0003932	0.0000882
r (correlation coefficient)	0.9751	0.9954

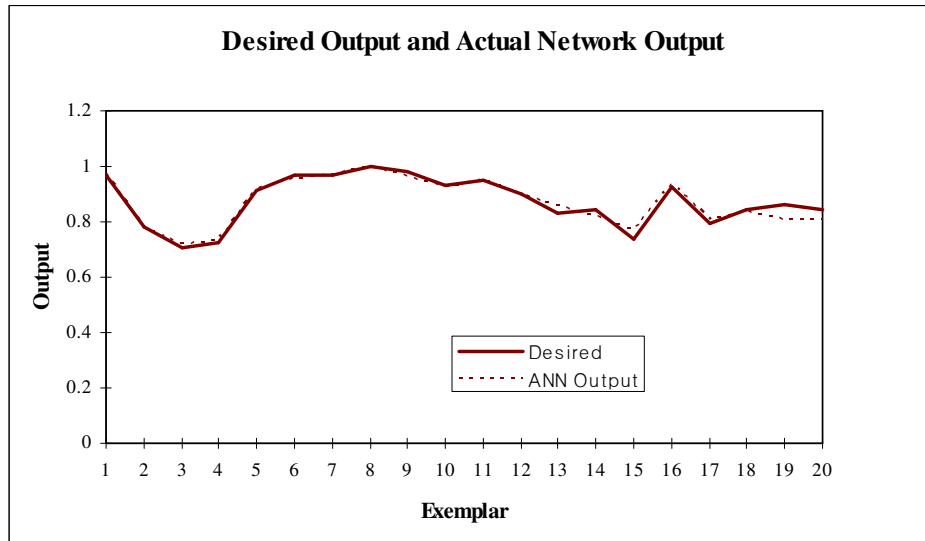


Fig. 5.37. Comparison of desired output and ANN output for pitting corrosion on single edge location as obtained using logistic (sigmoid) activation function

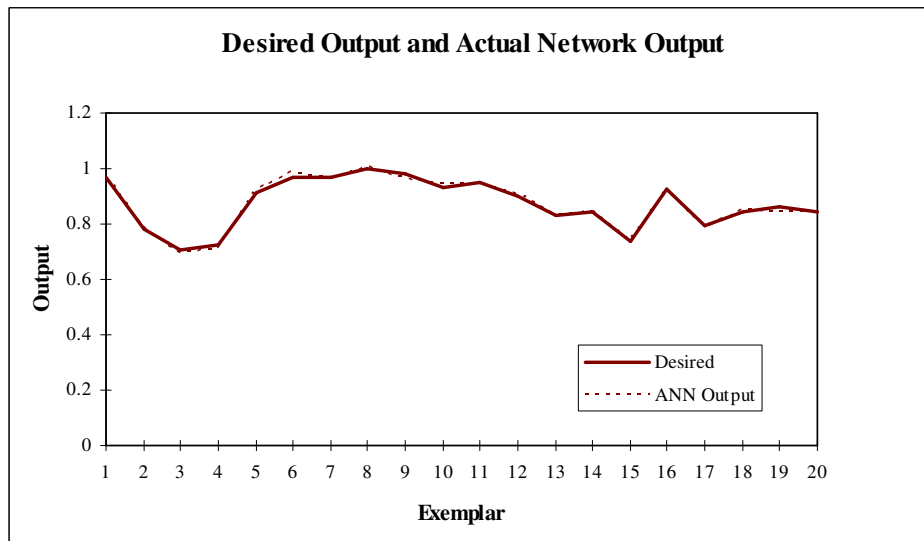


Fig. 5.38. Comparison of desired output and ANN output for pitting corrosion on single edge location as obtained using hyperbolic tangent (Tanh) activation function

5.7.6 ANN based formulae for ultimate strength of plate with pitting corrosion

Once an ANN model has been trained and validated, it must be tested with new data as investigated above. Finally we can conclude that the hyperbolic tangent (Tanh) activation function based network is more suitable and accurate than the logistic activation function to predict the ultimate strength of plate with pitting corrosion either at one edge or at both edges for new problems that were not studied within the

previous finite element analyses. As far as applicable, the number of training data needs to be fairly large to contain all the needed information if the network is to learn the features and relationships that are important. Generally the training data should cover large range of data and also include all the characteristics of the problem class of data. In this study, the results of 265 nonlinear finite element analyses have been used to develop ANN models. In these analyses, 1m x 1m plates with a yield stress of 355 N/mm^2 were used. 9 models are based on plates without pitting corrosion with different B/t ratios (40.0, 41.7, 45.0, 45.5, 50.0, 55.0, 55.6, 60.0, 62.5). For each corrosion scenario including single edge corrosion and both edges corrosion, x_1 has four values ranging from 1.650 to 2.576; x_2 has four values (0.1, 0.2, 0.3 and 0.4); The longitudinal location of pitting corrosion was assumed to start at aft bay (aft end) and x_3 has four different values (0.25, 0.5, 0.75, 1.0); x_4 has two cases (0.25 and 0.5). So the dataset has quite good coverage of the input and output space.

5.7.6.1 ANN (Tanh) based output for single end pitting corrosion

Overall comparisons between finite element results and ANN based outputs (σ_c / σ_o) for the ultimate strength of plate with single edge type pitting corrosion have been carried out to evaluate the accuracy of ANN based outputs. *Appendix E* indicates all trained and cross validated data with the ANN output values based on hyperbolic tangent (Tanh) activation functions. As illustrated in Fig. 5.39 which shows correlation of both FEM results and ANN based outputs, the results is very accurate with MSE is 0.000068, r is 0.995643, mean value is 0.999926 and coefficient of variation (C.O.V) is 0.009572.

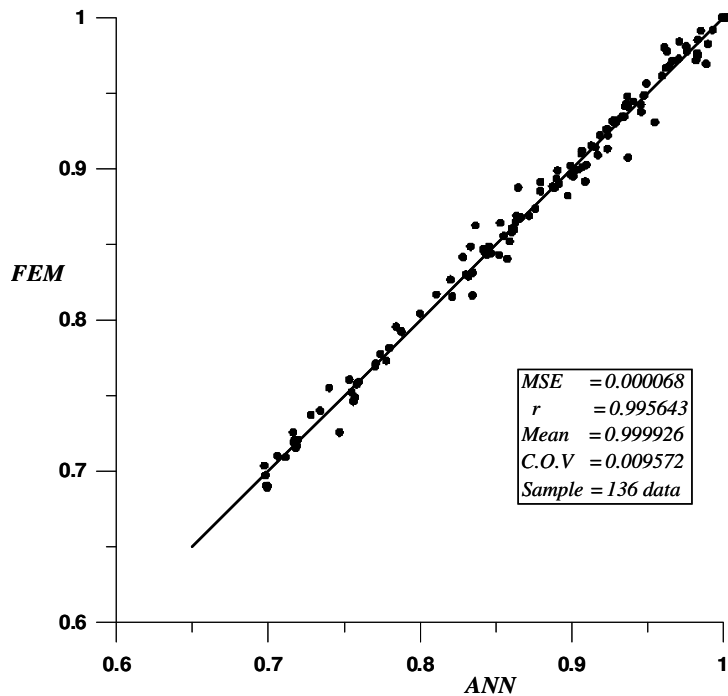


Fig. 5.39. Correlation of FEM results and ANN (Tanh) based outputs for single edge pitting corrosion

Based on this current study it is considered to be advantageous to derive empirical formula to estimate the ultimate strength of rectangular plate with pitting corrosion. Generally many of conventional empirical formulae are polynomial equations based on regression analysis. In this research matrix based equations, so called ANN based empirical formula, have been developed as Eq.5.56. This equation is based on the assumption that the boundary condition of rectangular plate is a simply supported condition, the initial plate deformation follows half wave numbers which are same as plate aspect ratio or to the nearest whole number and only the most severely corroded square area in total plate length should be considered to determine input parameters x_1, x_2, x_3, x_4 .

$$\sigma_c = \frac{Y + 4.8860}{5.7860} \times \sigma_o \quad (\text{Eq.5.56})$$

where σ_c = ultimate strength of plate with pitting corrosion (N/mm^2)

σ_o = ultimate strength of uncorroded plate (N/mm^2)

Y = value of matrix based equation

$$= \left| \text{Tanh} \left(\mathbf{W2} \times \left[\begin{array}{c} 1 \\ \text{Tanh}(\mathbf{W1} \times \mathbf{X}) \end{array} \right] \right) \right|$$

x_1 = plate slenderness parameter (β)

x_2 = the ratio of pit breadth over plate width

x_3 = the ratio of pit length over plate length

x_4 = the ratio of pit depth over plate thickness

$$\mathbf{X} = [1 \ x_{f1} \ x_{f2} \ x_{f3} \ x_{f4}]^T$$

$$x_{f1} = (1.9441 * x_1) - 4.1078$$

$$x_{f2} = (4.5000 * x_2) - 0.8999$$

$$x_{f3} = (1.7999 * x_3) - 0.8999$$

$$x_{f4} = (3.5999 * x_4) - 0.8999$$

$$\mathbf{W1} = \begin{bmatrix} -0.2751 & 0.0282 & 0.0496 & 0.3851 & 0.7093 \\ 1.8543 & -0.0115 & -0.6978 & -0.1098 & -1.6504 \\ -0.4064 & -0.0183 & -2.0535 & -0.3542 & -0.3978 \\ -1.0153 & -0.2708 & 0.5036 & -2.1643 & 0.6909 \end{bmatrix}$$

$$\mathbf{W2} = [0.1681 \ -0.1755 \ 1.0057 \ 0.3621 \ 0.6168]$$

5.7.6.2 ANN (Tanh) based output for both ends pitting corrosion

Another comparison between finite element results and ANN based outputs (σ_c / σ_o) for the ultimate strength of plate with both end type pitting corrosion have been investigated. Appendix E indicates all trained and cross validated data with the ANN output values based on hyperbolic tangent (Tanh) activation functions. Fig. 5.40 illustrates correlation of both FEM results and ANN based outputs, the results is very accurate with the results is very accurate with MSE is 0.000199, r is 0.994084, mean value is 0.998067 and coefficient of variation (C.O.V) is 0.020693.

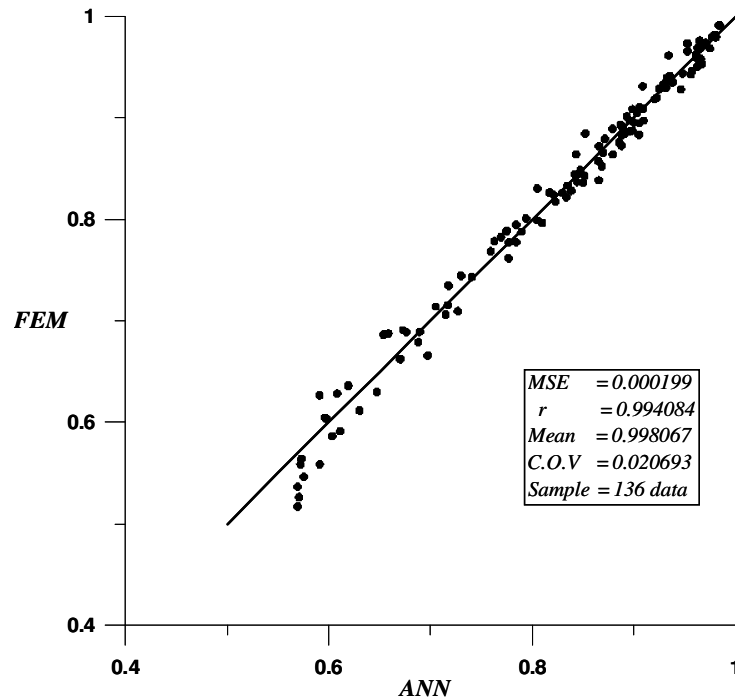


Fig. 5.40 Correlation of FEM results and ANN (Tanh) based outputs for both edges pitting corrosion

The matrix based formula for the ultimate strength of plate with both end type pitting corrosion can be expressed by:

$$\sigma_c = \frac{Y + 3.0658}{3.9658} \times \sigma_o \quad (\text{Eq. 5.57})$$

where σ_c = ultimate strength of plate with pitting corrosion (N / mm^2)
 σ_o = ultimate strength of uncorroded plate (N / mm^2)
 Y = value of matrix based equation

$$= \left| \text{Tanh} \left(\mathbf{W2} \times \left[\begin{array}{c} 1 \\ \text{Tanh}(\mathbf{W1} \times \mathbf{X}) \end{array} \right] \right) \right|$$

- x_1 = plate slenderness parameter (β)
- x_2 = the ratio of pit breadth over plate width
- x_3 = the ratio of pit length over plate length
- x_4 = the ratio of pit depth over plate thickness

$$\mathbf{X} = [1 \ x_{f1} \ x_{f2} \ x_{f3} \ x_{f4}]^T$$

$$x_{f1} = (2.0896 * x_1) - 4.4912$$

$$x_{f2} = (4.5000 * x_2) - 0.8999$$

$$x_{f3} = (1.7999 * x_3) - 0.8999$$

$$x_{f4} = (3.5999 * x_4) - 0.8999$$

$$\mathbf{W1} = \begin{bmatrix} 1.5899 & -0.3056 & -0.7707 & -1.0947 & -0.6146 \\ 1.1090 & -0.1769 & 0.5681 & -1.9262 & 0.5216 \\ -0.0856 & -0.1755 & -0.9780 & -1.0876 & -0.0798 \\ -0.4588 & 0.2109 & 1.1998 & -0.4158 & -0.8671 \end{bmatrix}$$

$$\mathbf{W2} = [0.7260 \ 0.9123 \ -0.6682 \ 0.8597 \ 0.5669]$$

The hand calculation of above equations are somewhat complicated, thus a useful MATLAB program has been developed as shown in *Appendix F* in order to calculate the ultimate strength of plate with localized corrosion. Total five(5) input parameters are required that is the ultimate strength of uncorroded plate and x_1, x_2, x_3, x_4 . Readers can also create their own program by using a simple spread sheet program (MS excel, etc.) based on above formulae and concept. Table 5-11 indicates six randomly selected data to evaluate the accuracy of the MATLAB based program. The results demonstrate that the developed MATLAB based program can predict the ultimate strength of plate with single edge and both edges pitting corrosion quite accurately.

Table 5-11
Comparison of ANN outputs and desired output for single edge pitting corrosion

No	ANN Input Variables					σ_c (FEM) (N/mm ²)	ANN Output (N/mm ²)	MATLAB Output (N/mm ²)
	Type	x1	x2	x3	x4			
1	SE	1.719	0.3	0.25	0.50	250.30	255.24	255.23
2	SE	2.060	0.2	1.00	0.25	226.23	226.61	226.63
3	SE	2.576	0.1	1.00	0.25	216.42	216.50	216.51
4	BE	1.719	0.2	0.25	0.25	274.90	275.29	275.30
5	BE	2.060	0.2	0.50	0.25	237.77	236.68	236.69
6	BE	2.576	0.3	0.50	0.50	157.28	159.31	159.33

5.8 Concluding remarks

In this Chapter, general review of existing formulae and recommendation to estimate elastic buckling strength and ultimate strength of unstiffened and stiffened plate have been carried out. Some recent research activities and guideline for the strength degradation due to localized corrosion have also been reviewed.

Obviously localized corrosion on a plate could reduce the strength of the plate. In this research, the ultimate strength of square plates with pitting corrosion has been investigated by using nonlinear finite element analyses. The effects of pitting corrosion width, depth, length and its transverse location on ultimate strength have been systematically studied. Over 256 nonlinear finite element analyses have been carried out which is the full combination of two cases of transverse pitting locations, four cases of plate slenderness, four cases of pitting breadths, four cases of pitting lengths and two cases of pitting depths. The results can be summarized as follows:

- The length, breadth and depth of pit corrosion have weakening effects on the ultimate strength of the plates while plate slenderness has only marginal effect on strength reduction.
- The depth and width of the corrosion are the two dominant parameters. So this finding, to some extent, justifies the formula proposed by Paik, *et al.* [13-15], in which the corroded cross sectional area was chosen as the only parameter related to corrosion.
- Transverse location of pit corrosion is also an important factor determining the amount of strength reduction. When corrosion spreads transversely on both edges, it has the most deteriorating effect on strength.

The *Multi-Variable Regression Method* has been applied to derive empirical formulae to predict strength reduction due to pitting corrosion. The derived formulae are quite accurate. The formula for single side type pitting corrosion is slightly more accurate than that for both sides type pitting corrosion.

In addition, the *Artificial Neural Network (ANN) Method* is applied and some matrix based new formulae are derived to predict ultimate strength reduction of locally corroded plates. It is found out that the proposed formulae can accurately predict the ultimate strength reduction of locally corroded plates under uni-axial compression. The results can be summarized as follows:

- The number of *processing elements (PE)* in the hidden layer will not effect on the accuracy of ANN based output as long as there is an adequate number of epochs (more than 3000 epochs).
- The hyperbolic tangent (Tanh) activation function produces more accurate results than the logistic activation function.
- The ANN based empirical formulae show excellent accuracy to predict the ultimate strength reduction of unstiffened plates with localized corrosion under uniaxial compression. The formula for single side type pitting corrosion is slightly more accurate than that for both sides type pitting corrosion.

The formulae, which are derived by the *Multi-Variable Regression Method* and the *Artificial Neural Network (ANN) Method*, could be useful to determine structural integrity and residual strength of plates with localized corrosion during the initial design and on-site inspection and maintenance programme and could save considerable amount of time and efforts comparing with finite element analyses.

In Chapter 5, finite element analyses have been carried out to investigate the effects of different material and geometry parameters such as plate slenderness, location, size and depth of pits on the ultimate strength of square plates under uni-axial compression. It is recommended further investigation of the effect of localized corrosion on plate with consideration of residual stresses and the effects of different locations, sizes and depths of pits on the ultimate strength of plate under lateral load, multi-loads and under shear have to be investigated.

References (Chapter 5)

1. Paik, J.K. and A.K. Thayamballi, *Ultimate Limit State Design of Steel Plated Design*. 2003: John Wiley & Sons Ltd.
2. Vasta, J., *Lessons learned from full-scale structural tests*. Trans. SNAME, 1958. **66**: p. 165-243.
3. Hu, Y., W. Cui, and P. Terndrup Pedersen, *Maintained ship hull xcgirxcder ultimate strength reliability considering corrosion and fatigue*. Marine Structures, 2004. **17**(2): p. 91-123.
4. Caldwell, J.B., *Ultimate longitudinal strength*. Trans. RINA, 1965. **107**: p. 411-430.
5. Mansour, A.E., *Assessment of reliability of ship structures*. Ship Structural Committee, 1997. **SSC-398**.
6. Bai Y., E. Bendiksen, and P. Terndrup Pedersen, *Collapse analysis of ship hulls*. Marine Structures, 1993. **6**(5-6 SU -): p. 485-507.
7. Ueda, Y., S.M.H. Rashed, and J.K. Paik, *Buckling and ultimate strength interaction in plates and stiffened panels under combined inplane biaxial and shearing forces*. Marine Structures, 1995. **8**(1 SU -): p. 1-36.
8. Hu, S.Z., et al., *Ultimate collapse tests of stiffened-plate ship structural units*. Marine Structures, 1997. **10**(8-10 SU -): p. 587-610.
9. Fujikubo, M. and T. Yao, *Elastic local buckling strength of stiffened plate considering plate/stiffener interaction and welding residual stress*. Marine Structures, 1999. **12**(9-10): p. 543-564.
10. Sadosky, Z., A.P. Teixeira, and C. Guedes Soares, *Degradation of the compressive strength of rectangular plates due to initial deflection*. Thin-Walled Structures, 2005. **43**(1): p. 65-82.
11. Simonsen, B.C., et al. *Committee III.1 Ultimate Strength*. in *15th International Ship and Offshore Structures Congress* 2003. San Diego, USA.
12. Yao, T., *Hull girder strength*. Marine Structures, 2003. **16**(1 SU -): p. 1-13.
13. Paik, J.K. and A.K. Thayamballi. *Ultimate strength of ageing ship*. in *Proceedings of the I MECH E Part M*. 2002.
14. Paik, J.K., et al., *Time-dependent risk assessment of ageing ships accounting for general/pit corrosion, fatigue cracking and local dent damage*. SNAME, Annual Meeting in San Francisco (World Maritime Technology Conference), 2003.
15. Paik, J.K., J.M. Lee, and M.J. Ko, *Ultimate shear strength of plate elements with pit corrosion wastage*. Thin-Walled Structures, 2004. **vol.42**: p. 1161-1176.
16. Paik, J.K., Y.V. Satish Kumar, and J.M. Lee, *Ultimate strength of cracked plate elements under axial compression or tension*. Thin-Walled Structures, 2005. **43**(2): p. 237-272.
17. Hu, Y. and W.C. Cui, *Residual ultimate strength of cracked plates and stiffened panels under combined loading*. Journal of Ship mechanics, Chinese, 2003. **Vol.7 No.1**: p.63-78.
18. British Standard, *Guidance on methods for assessing the acceptability of flaws in fusion welded structures*. BS7910, 1999.

19. Faulkner, D., *A review of effective plating for use in the analysis of stiffened plating in bending and compression*. Journal of Ship Research, 1975. **19(1)**: p. 1-17.
20. Soares, C.G., *Design equation for the compressive strength of unstiffened plate elements with initial imperfections*. Journal of Constructional Steel Research, 9, 1988: p. 287-310.
21. Fujikubo, M., T. Yao, and M.R. Khedmati, *Estimation of Ultimate Strength of Ship Bottom Plating under Combined Transverse Thrust and Lateral Pressure*. Journal of the Society Naval Architects of Japan, Vol.186., 1999.
22. Class NK, *Guidelines for Tanker Structures*. 2001.
23. DNV, *Buckling strength analysis*. Det Norske Veritas, Classification Notes No.30.1, 1995.
24. Chapkis, D.T., *Simulation of pitting corrosion of hull plating under static loading*. Trudy TSNIIMF, 1967. **No.82**: p. 34-50.
25. Flaks, V.Y., *Correlation of pitting corrosion of aluminium plates and reduction of load-bearing capacity under tension*. Fiziko-Khimicheskaya Mekhanika Materialov, 1978. **14(1)**: p. 89-93.
26. TSCF, *Experimental and theoretical investigation of the strength of corroded hull elements*. 1984, Tanker Structure Co-operative Forum, Project 300, Report No. 84-3438.
27. Daidola, J.C., et al., *Residual strength assessment of pitted plate panels*. Ship Structure Committee, SSC-394, 1997.
28. IACS, *Requirements Concerning Strength of Ships*. International Association of Classification Societies, 2003.
29. IACS, *Requirements Concerning Survey and Certification*. International Association of Classification Societies, 2003. **Z10.1**.
30. IACS, *Common Structural Rules for Double Hull Oil Tankers*. 2006.
31. Paik, J.K., J.M. Lee, and M.J. Ko, *Ultimate compressive strength of plate elements with pit corrosion wastage*. Journal of Engineering for the Maritime Environment, 2003. **217(M4)**: p. 185-200.
32. Dunbar, T.E., et al., *A computational investigation of the effects of localized corrosion on plates and stiffened panels*. Marine Structures, 2004. **17(5)**: p. 385-402.
33. Pu, Y., et al., *Prediction of ultimate capacity of perforated lipped channels*. Journal of Structural Engineering, 1999. **Vol.125, No.5**: p. 510-514.
34. Paik, J.K. and P.T. Pedersen. *A simplified method for predicting the ultimate compressive strength of ship panels*. in *International Shipbuilding Progress*. 1996.
35. Antoniou, A.C., *On the Maximum Deflection of Plating in Newly Built Ships*. Journal of Ship Research, 24(1), 1980: p. 31-39.
36. Carlsen, C.A. and J. Czujko, *The specification of post welding distortion tolerance for stiffened plates in compression*. The Structural Engineer, 1978. **56A(5)**: p. 133-141.
37. Smith, C.S., P.C. Davidson, and J.C.D. Chapman, P.J., *Strength and stiffness of ships' plating under in-plane compression and tension*. RINA Transactions, 130, 1988: p. 277-296.
38. Barsom, J.M. and S.T. Rolfe, *Fracture and Fatigue Control in Structures: Applications of Fracture Mechanics*. Third Edition ed. 1999: ASTM.

39. Broek, D., *The practical use of fracture mechanics*. 2nd ed. 1988, AA Dordrecht, The Netherlands: Kluwer Academic Publishers.
40. Dexter, R.J. and P.J. Pilarski, *Crack propagation in welded stiffened panels*. Journal of Constructional Steel Research, 2002. **58**(5-8): p. 1081-1102.
41. von Karman, T., *Die mittragende Breite*. Beitrage zur Technischen Mechanik und Technischen Physik, August Foppl Festschrift, 1924; p. 114-127.
42. Hughes, O.F., *Ship Structural Design: A Rationally Based, Computer-Aided Optimization Approach*. 1988.
43. Winter, G., *Strength of thin steel compression flanges*. Reprint No.32, 1947.
44. Murray, N.W., *Introduction to the Theory of Thin-Walled Structures*. 1986: Clarendon Press, Oxford.
45. Hansen, A.M., *Reliability Methods for the Longitudinal Strength of Ships*. Ph.D thesis, 1995.
46. Pu, Y., *Reliability analysis and reliability-based optimisation design of swash ships*, in *Department of Naval Architecture and Ocean Engineering*. 1995, University of Glasgow: PhD thesis, Glasgow, U.K.
47. Carlsen, C.A., *A parametric study of collapse of stiffened plates in compression*. The Structural Engineer, 1980. **vol. 58B, No.2**.
48. Vilnay, O. and K.C. Rockley, *A Generalised effective width methods for plates loaded in compression*. Journal of Constructional Steel Research, 1981. **vol.1, no.3**: p. 3-12.
49. Kumar, Y.V.S. and J.K. Paik, *Buckling analysis of cracked plates using hierarchical trigonometric functions*. Thin-Walled Structures, 2004. **42**(5): p. 687-700.
50. Brighenti, R., *Buckling of cracked thin-plates under tension or compression*. Thin-Walled Structures, 2005. **43**(2): p. 209-224.
51. Wang, F., X.P. Huang, and W.C. Cui, *Stress intensity factor and ultimate tensile strength analysis of eccentrically cracked plates*. Journal of ship mechanics, 2005. **vol.9, no.3**: p. 97-110.
52. ANSYS, *User's Manual (version 7.0)*. ANSYS Inc., 2003.
53. LUSAS, *Worked Examples, Version 13.3*. 2003.
54. Anderson, C., *Protection against corrosion*. University of Newcastle upon Tyne, Lecture Notes 2003, http://www.ncl.ac.uk/marine/assets/docs/NclUni_Lect1_1103.pdf, 2003.
55. McCulloch, W.S. and W.H. Pitts, *A logical calculus of the ideas immanent in nervous activity*. Bulletin of Mathematical Biophysics, 1943. **vol.5**: p. 115-133.
56. Widrow, B. and M. Hoff, *Adaptive Switching Circuits*. IRE WESCON Convention Record, 1960. **Part 4**.
57. Widrow, B., *An Adaptive 'Adaline' Neuron Using Chemical 'Memistors'*, *Technical Report Number 1553-2*. 1960b, Stanford Electronics Laboratories.
58. Anderson, D. and G. McNeill, *Artificial Neural Networks Technology, Report No. F30602-89-C-0082*. 1992, Kaman Sciences Corporation.
59. Hajela, P. and L. Berke, *Neurobiological computational models in structural analysis and design*. Computers & Structures, 1991. **41**(4): p. 657-667.
60. Shao, S. and Y. Murotsu, *Structural reliability analysis using a neural network*. JSME International Journal, Series A; Mechanics and Material Engineering, 1997. **Vol 40, No.3**: p. 242-246.

61. Pu, Y., E. Mesbahi, and A.H. El-hewy. *ANN-based response surface method and its application to ultimate strength of plates*. in *The Fifteenth International Offshore and Polar Engineering Conference*. 2005. Seoul, Korea.
62. Jenkins, W.M., *A neural network for structural re-analysis*. *Computers & Structures*, 1999. **72**(6): p. 687-698.
63. Wei, L., *Neural network model for distributional buckling behaviour of cold-formed steel compression members*. 2000: Helsinki University of Technology Laboratory of Steel Structures Publications 16.
64. Papadrakakis, M., V. Papadopoulos, and N.D. Lagaros, *Structural reliability analysis of elastic-plastic structures using neural networks and Monte Carlo simulation*. *Computer Methods in Applied Mechanics and Engineering*, 1996. **136**(1-2): p. 145-163.
65. Papadrakakis, M. and N.D. Lagaros, *Reliability-based structural optimization using neural networks and Monte Carlo simulation*. *Computer Methods in Applied Mechanics and Engineering*, 2002. **191**(32): p. 3491-3507.
66. Hurtado, J.E. and D.A. Alvarez, *Neural-network-based reliability analysis: a comparative study*. *Computer Methods in Applied Mechanics and Engineering*, 2001. **191**(1-2): p. 113-132.
67. Gomes, H.M. and A.M. Awruch, *Comparison of response surface and neural network with other methods for structural reliability analysis*. *Structural Safety*, 2004. **26**(1): p. 49-67.
68. Deng, J., et al., *Structural reliability analysis for implicit performance functions using artificial neural network*. *Structural Safety*, 2005. **27**(1): p. 25-48.
69. El-hewy, A.H., E. Mesbahi, and Y. Pu. *Artificial neural networks and their application to composite plate reliability analysis*. in *2nd International ASRANet Colloquium*. 2004. Barcelona, Spain.
70. Wei, D. and S. Zhang. *Ultimate compressive strength prediction of stiffened panels by counterpropagation neural networks (CPN)*. in *The Ninth International Offshore and Polar Engineering*. 1999. Brest, France.
71. Ray, T., R.P. Gokarn, and O.P. Sha, *Neural network applications in naval architecture and marine engineering*. *Artificial Intelligence in Engineering*, 1996. **10**(3): p. 213-226.
72. Mesbahi, E. and V. Bertram. *Empirical design formula using Artificial Neural Networks*. in *1st International Conference on Computer Applications and Information Technology in the Maritime Studies, COMPIT 2000*. Berlin, Germany.
73. Zubaydi, A., M.R. Haddara, and A.S.J. Swamidias, *Damage identification in a ship's structure using neural networks*. *Ocean Engineering*, 2002. **29**(10): p. 1187-1200.
74. Alkan, A.D., K. Gulez, and H. Yilmaz, *Design of a robust neural network structure for determining initial stability particulars of fishing vessels*. *Ocean Engineering*, 2004. **31**(5-6): p. 761-777.
75. Xu, J. and M.R. Haddara, *Estimation of wave-induced ship hull bending moment from ship motion measurements*. *Marine Structures*, 2001. **14**(6): p. 593-610.

76. Londhe, S.N. and M.C. Deo, *Wave tranquility studies using neural networks*. Marine Structures, 2003. **16**(6): p. 419-436.
77. Agrawal, J.D. and M.C. Deo, *Wave parameter estimation using neural networks*. Marine Structures, 2004. **17**(7): p. 536-550.
78. Mazaheri, S. and M.J. Downie, *Response-based method for determining the extreme behaviour of floating offshore platforms*. Ocean Engineering, 2005. **32**(3-4): p. 363-393.
79. Robert, H.N., *Neurocomputing*. 1989: Addison-Wesley Publishing Company, Inc.
80. Beale, R. and T. Jackson, *Neural computing: an introduction*. 1990, Bristol and Philadelphia: Institute of Physics Publishing.
81. Wikipedia, *Wikipedia Web Site*. 2005: http://en.wikipedia.org/wiki/Artificial_neural_network.
82. Principe, J.C., N.R. Euliano, and W.C. Lefebvre, *Neural and Adaptive Systems: Fundamentals through Simulation*. 1999: John Wiley & Sons. Inc.
83. Rumelhard, R.E., E. Hinton, and J. Williams, "Learning internal representation by error backpropagation," *Parallel Distributed Processing: Explorations Microstructure of Cognition Cambridge, MA*. MIT Press, 1986. **vol. 1, ch. 8**.
84. NeuroSolutions, "Getting Started Manual" Version 3, ed. NeuroDimension: NeuroDimension.

Chapter 6

The Effects of Localized Corrosion on Strength Degradation of Stiffened Plates

6.1 Introduction

Stiffened plates are assemblage of plating and stiffeners and main structural members in ships and offshore structures. The characteristic of stiffened panels are that even if there is initial plate buckling phenomena in the elastic and inelastic regime the overall stiffened panels are usually sufficiently strong enough to sustain further applied loading until they reach ultimate strength due to excessive plasticity or actual stiffener failure.

The potential failure modes of a stiffened panel are generally classified into four main categories [1]:

- plate failure
- stiffener-plate column failure which can be divided into two modes
 - plate induced failure
 - stiffener induced failure
- torsional failure of the stiffener
- overall grillage buckling

There can be modes of actual failure that are a combination of two or more of these basic modes.

Due to the rapid development of computers with high memory capacity and fast computational speed, numerical calculations have become an increasingly important tool in calculating both linear and non-linear strength calculation of structures, thus now-a-days the behaviour of a stiffened panel can be closely estimated by numerical computational methods.

The design parameters which influence the strength of stiffened panels are generally classified into two main categories, such as geometrical and imperfection parameters. The geometrical parameters are stiffener slenderness, plate slenderness, ratio of top flange to web area and cross-sectional slenderness of the stiffener. The imperfection parameters are initial stiffener deflection, relative stiffener deflection, initial plate deflection, compressive plate welding stresses, axial welding stresses in the stiffeners and plates and material properties, such as yield stress.

In the analyses reported in Chapter 5, the effects of localized corrosion on the ultimate strength of unstiffened square plates have been investigated. The results show that the pitting locations at both edges near the four corners are generally found to be the most critical location.

Localized corrosion often starts from the areas where the highest stresses occurs which leads to coating break-down and stress corrosion cracking or where water flows and drains and places of water and sediment accumulation, such as along longitudinal stiffeners and transverse bulkhead. The localized pitting corrosion can be concentrated at one or at several large areas as shown on Fig. 5.18 in Chapter 5. Another type of localized corrosion is of a regularly pitted form and caused by microbiologically influenced corrosion (MIC), such as sulphate-reducing bacteria (SRB) as illustrated in Fig. 6.1.



Fig. 6.1. Bacteria influenced corrosion in ballast tank [2]

In this Chapter, the ultimate strength of longitudinally stiffened plates with general corrosion and pitting corrosion have been investigated. The effects of corrosion location and size on ultimate strength are studied.

6.2 Ultimate strength of stiffened panels

Many researchers have investigated the ultimate strength of stiffened panels and have proposed some empirical formulae for design purposes; among others the following methods have been reviewed to assess the ultimate strength of stiffened panels.

6.2.1 LRS methods

Lloyd's Register developed a program, so-called *LRPASS 20202*, to assess the ultimate strength of stiffened panels by using a simple beam-column approach in

which the panel behaviour is typified by that of a single stiffener together with an effective width of plating. Full details of the theories are given in *Rutherford* [3] and *Rutherford and Caldwell* [4].

The failure modes of stiffened panels are classified into the plate induced failure mode and the stiffener induced failure mode.

The following expression can be used to determine the ultimate strength of a stiffened panel simply supported on all four sides with initial deflection under plate failure mode, expressed by:

$$\sigma_{Ult} = \frac{K P_c}{A_e} + \frac{K y_p \left[\frac{P_c P_e \Delta}{(P_e - P_c)} + M_q \right]}{I_e} \quad (\text{Eq.6.1})$$

where K = the secant stiffness of the plate panel
 P_c = maximum compressive force
 P_e = Euler load ($= \pi^2 EI_e / L^2$)
 A_e = effective sectional area
 y_p = the distance between its centroid and the middle plane of the plate
 I_e = effective second moment of area of section
 Δ = the eccentric of load at mid-span
 M_q = The moment resulting from lateral pressure at mid span

A similar expression can be used to calculate the maximum compressive force which can be carried by the stiffened panel before the stiffener fails in compression at mid-span. In this case, the section properties I and A together with the Euler load P_e are calculated using the full width of plate since this was found to improve correlation with both test and numerical results, given by:

$$\sigma_{Ult} = \frac{P_c}{A} + \frac{y_s \left[\frac{P_c P_e \Delta}{(P_e - P_c)} + M_q \right]}{I} \quad (\text{Eq.6.2})$$

where A = total sectional area
 y_s = the distance between the centroid of the cross-section and the extreme stiffener fibre
 I = total second moment of area of section

6.2.2 Pu and Das's method

Pu and Das [1, 5] evaluated various existing formulae proposed by *Faulkner* [6], *Carlsen* [7], and Imperial College's method and calibrated these against the existing

experimental and numerical results. They proposed a modified Faulkner's formulae, so-called the *Pu and Das Method*, to predict the ultimate strength of stiffened plates which is given by:

$$\Gamma = \frac{\sigma_{Ult}}{\sigma_Y} = \frac{\sigma_e}{\sigma_Y} \left[\frac{A_s + (b_e \times t)}{A_s + (b \times t)} \right] \quad (\text{Eq.6.3})$$

where $\frac{\sigma_e}{\sigma_Y} = 1 - \frac{1}{4} \frac{\sigma_Y}{\sigma_E}$ if $\sigma_E \geq 0.5\sigma_Y$

$\frac{\sigma_e}{\sigma_Y} = \frac{\sigma_E}{\sigma_Y}$ if $\sigma_E \leq 0.5\sigma_Y$

where $\sigma_E = \frac{\pi^2 \times E \times r_{ce}^2}{a^2}$ and $r_{ce}^2 = \frac{I_e'}{A_s + (b_e \times t)}$

EI_e' is the buckling flexural rigidity of the stiffener. The tangent effective width of the plate (b_e') is given by:

$$\frac{b_e'}{b} = \begin{cases} \frac{1}{\beta_e} \times R_\eta \times R_\delta \times R_{\eta\delta} & \beta_e \geq 1 \\ R_\eta \times R_\delta \times R_{\eta\delta} & 0 \leq \beta_e \leq 1 \end{cases} \quad (\text{Eq.6.4})$$

The effective width of the plate is related to the slenderness as follows:

$$\frac{b_e}{b} = \begin{cases} 1.08 \times \Gamma_F \times R_\eta \times R_\delta \times R_{\eta\delta} & \beta_e \geq 1 \\ 1.08 \times R_\eta \times R_\delta \times R_{\eta\delta} & 0 \leq \beta_e \leq 1 \end{cases} \quad (\text{Eq.6.5})$$

where $\beta_e = \frac{b}{t} \sqrt{\frac{\sigma_e}{E}}$, $\Gamma_F = \frac{2}{\beta_e} - \frac{1}{\beta_e^2}$

$$R_\eta = \left(1 - \frac{\Delta\Gamma_F}{1.08 \times \Gamma_F} \right) (1 + 0.0078\eta)$$

$$R_\delta = 1 - (0.626 - 0.121\beta_e) \frac{\delta_0}{t}$$

$$R_{\eta\delta} = 0.665 + 0.006\eta + 0.36 \frac{\delta_0}{t} + 0.14\beta_e$$

η = welding residual stress factor

δ_0 = initial plate deflection

6.2.3 Paik & Thayamballi's methods

If the stiffened panel is subjected to axial tension, it will fail by gross yielding.

However if the stiffened panel is under predominantly uni-axial compressive loads, there will be several potential failure modes until it reaches to the ultimate strength.

Paik & Thayamballi [8] categorized the primary modes of overall failure for the stiffened panel subject to compressive loads into the following six types:

- Mode I : overall collapse of plating and stiffeners as a unit
- Mode II : biaxial compressive collapse
- Mode III : beam-column type collapse
- Mode IV : local buckling of stiffener web
- Mode V : tripping of stiffener
- Mode VI : gross yielding

They proposed that the *Mode I* strength of a panel might be reasonably modelled as an orthotropic plate for buckling and ultimate strength estimation based on the large-deflection orthotropic plate theory and additionally considered for the effects of welding-induced initial deflections. However the influence of residual stresses and the effect of in-plane bending moment on the ultimate strength of the orthotropic plate are ignored.

In the biaxial compressive collapse case (*Mode II*), they proposed the large-deflection isotropic plate theory by solving the nonlinear governing differential equations to obtain the maximum and minimum membrane stress components.

With increasing panel deflection under loading, the upper and/or lower fibers in the mid-region of the panel will initially yield by the action of out-of-plane bending. By applying the *Mises-Hencky* yield criterion, the first yield condition of the outer surface of the orthotropic plate can be given by:

$$\left(\frac{\sigma_{xb}}{\sigma_{Yeq}}\right)^2 - \left(\frac{\sigma_{xb}}{\sigma_{Yeq}}\right)\left(\frac{\sigma_{yb}}{\sigma_{Yeq}}\right) + \left(\frac{\sigma_{yb}}{\sigma_{Yeq}}\right)^2 = 1 \quad (\text{Eq.6.6})$$

where σ_{Yeq} = equivalent yield stress = $\left(= \frac{Bt\sigma_{Yp} + n_{sx}A_{sx}\sigma_{Ys}}{Bt + n_{sx}A_{sx}} \right)$

$A_{sx} = h_{wx}t_{wx} + b_{fx}t_{fx}$,

σ_{Yp} , σ_{Ys} = the material yield stress for plate and stiffener, respectively

n_{sx} = the number of x stiffeners

h_{wx} , t_{wx} = the height and thickness of web, respectively

b_{fx} , t_{fx} = the breadth and thickness of flange, respectively

where

$$\sigma_{xb} = \sigma_{xav} - \rho_x \frac{m^2 \pi^2 E_x A_m (A_m + 2A_{0m})}{8L^2} - E_x \frac{t_{eq}}{2} \frac{A_m}{1 - \nu_x \nu_y} \left[\left(\frac{m\pi}{L} \right)^2 + \nu_y \left(\frac{\pi}{B} \right)^2 \right]$$

$$\sigma_{yb} = -\rho_x \frac{\pi^2 E_y A_m (A_m + 2A_{0m})}{8B^2} - E_y \frac{t_{eq}}{2} \frac{A_m}{1 - \nu_x \nu_y} \left[\nu_x \left(\frac{m\pi}{L} \right)^2 + \left(\frac{\pi}{B} \right)^2 \right]$$

t_{eq} = equivalent plate thickness

The criterion based on the initial plastic yield at the panel longitudinal edges is given by:

$$\left(\frac{\sigma_{xmax}}{\sigma_{Yeq}} \right)^2 - \left(\frac{\sigma_{xmax}}{\sigma_{Yeq}} \right) \left(\frac{\sigma_{ymin}}{\sigma_{Yeq}} \right) + \left(\frac{\sigma_{ymin}}{\sigma_{Yeq}} \right)^2 = 1 \quad (\text{Eq.6.7})$$

where $\sigma_{xmax} = \sigma_{xav} - \rho_x \frac{m^2 \pi^2 E_x A_m (A_m + 2A_{0m})}{8L^2}$

$$\sigma_{xmin} = \sigma_{xav} + \rho_x \frac{m^2 \pi^2 E_x A_m (A_m + 2A_{0m})}{8L^2}$$

$$\sigma_{ymax} = -\rho_x \frac{\pi^2 E_y A_m (A_m + 2A_{0m})}{8B^2}$$

$$\sigma_{ymin} = \rho_x \frac{\pi^2 E_y A_m (A_m + 2A_{0m})}{8B^2}$$

The ultimate longitudinal axial strength, σ_{xu}^I in *Mode I*, is obtained as the solution of Eq.6.6 and Eq.6.7 with regard to σ_{xav} . The details of the ultimate strength equations for stiffened panels which includes other failure modes are described in *Paik and Thaymballi* [8] and can be calculated by *ULSAP* (Ultimate Strength Analysis of Panels) program.

6.3 F.E. model of stiffened plates without pitting corrosion

In order to evaluate the reliability of the selected finite element analysis program (ANSYS) and its nonlinear control, as well as to provide some baseline response data, some verification procedures are conducted based on the following material properties, geometries, mesh sizes and boundary conditions.

6.3.1 Material properties

To evaluate the ultimate strength of stiffened plates, the material properties that are used are as follows:

- Yield strength (σ_Y) = Higher strength steel (315 N/mm^2)
- Young's modulus (E) = 209000 N/mm^2
- Poisson's ratio (ν) = 0.3

6.3.2 Dimension and details of F.E models

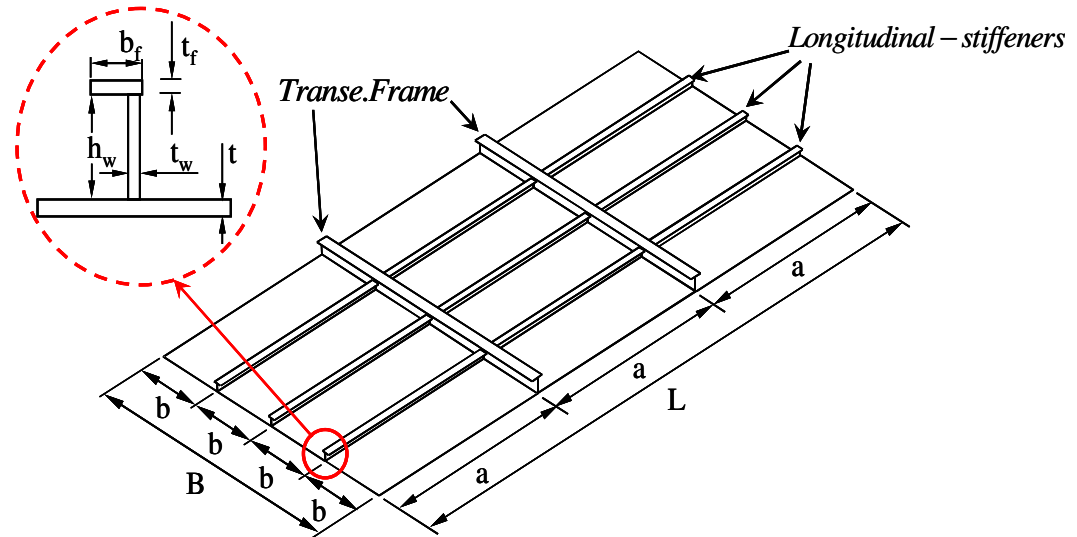


Fig. 6.2. Typical three(3) bay panel model with L-type stiffeners

A representative ship's structure is selected from an existing *AFRAMAX* shuttle tanker design as a basis for the F.E models. The dimensions and sizes of stiffened plates on the deck and ship's bottom structures vary as follows:

- Distance between each longitudinal stiffener : $740 \sim 820 \text{ mm}$
- Distance between each transverse frame space : 3920 mm
- Plate thickness at deck : $15.0 \sim 15.5 \text{ mm}$ (high tensile steel)
- Plate thickness at bottom : $17.0 \sim 19.5 \text{ mm}$ (mild steel)
- Web height : $250 \sim 400 \text{ mm}$
- Web thickness : $11.0 \sim 13.0 \text{ mm}$
- Flange width : $90 \text{ or } 100 \text{ mm}$
- Flange thickness : $16.0 \text{ or } 18.0 \text{ mm}$

Based on these existing structural details, the standard dimensions of a representative stiffened plate for finite element modelling is selected as follows:

- Plate breadth (b) : 800 mm
- Plate length (a) : 4000 mm
- Plate thickness : $15.0 \text{ or } 16.0 \text{ mm}$
- Web height : 300 mm
- Web thickness : $11.0 \text{ or } 12.0 \text{ mm}$
- Flange width : 90.0 mm

- Flange thickness : 16.0 mm

Fig. 6.2 illustrates a typical three(3) bay panel model with L-type longitudinal stiffeners.

6.3.3 Mesh size

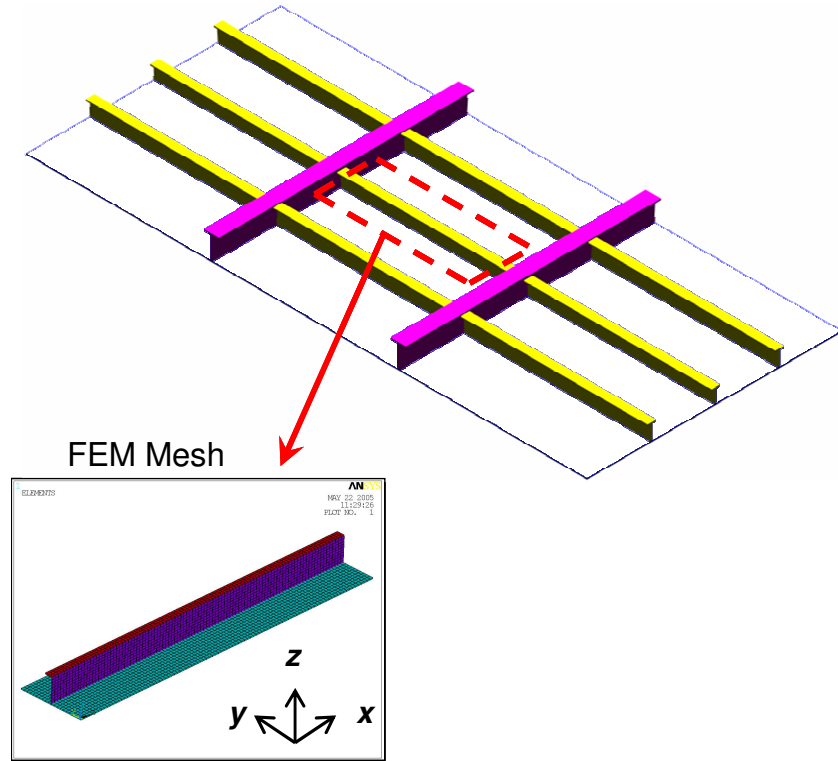


Fig. 6.3. Typical of one stiffened plate component with mesh details

The number of elements (mesh size) for one stiffened plate component is selected as follows:

- No. of elements in plate : 20 x 100 elements
- No. of elements in web : 5 x 100 elements
- No. of elements in flange : 3 x 100 elements

Fig. 6.3 illustrates the selected stiffened plate model with developed mesh details.

6.3.4 Boundary condition

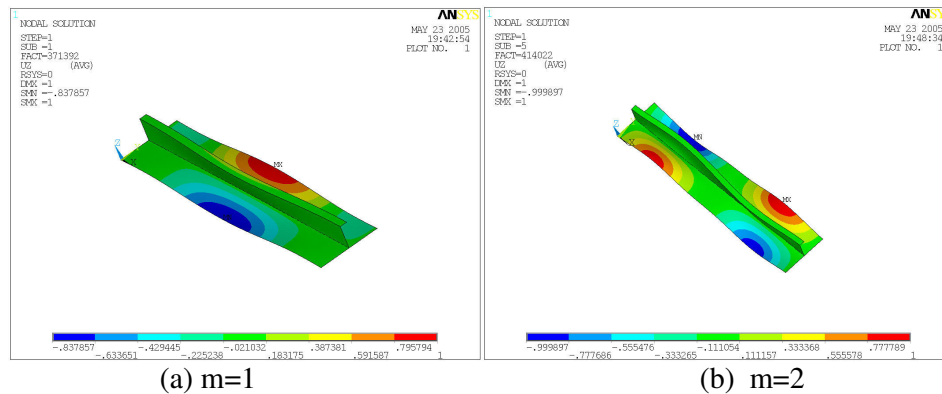
Generally simply supported boundary condition with symmetric boundary condition on upper and bottom line to represent the original full three (3) longitudinally stiffened plate. The details of boundary restrictions are adopted as shown in Table 6-1 for finite element modelling of stiffened plate component, where F means free, C denotes constraint and Sym indicates symmetric.

Table 6-1
Boundary conditions for stiffened plate component

	Ux	Uy	Uz	Rot-x	Rot-y	Rot-z
Plate Left	F	C	C	C	F	C
Plate Right	C	C	C	C	F	C
Plate Top	Sym	Sym	Sym	Sym	Sym	Sym
Plate Bottom	Sym	Sym	Sym	Sym	Sym	Sym
Web Left	F	C	C	C	C	F
Web Right	C	C	C	C	C	F
Flange Left	F	C	C	C	F	C
Flange Right	C	C	C	C	F	C
Stiffener & Plate boundary	F	C	F	F	C	C

6.4 Results of finite element analysis for stiffened plates

The geometry input which considers a welding induced initial imperfection is an important parameter influencing the ultimate strength of stiffened plate. In this Chapter, *Smith et al.*'s average value ($w_{0pl} = 0.1 \beta^2 t$) as specified in Chapter 5.2.1 is used for the initial imperfection of plate and stiffener flange. However the initial imperfection of the web doesn't need to be considered in this research. Two approaches have been used to define initial imperfection of the plate and flange. One approach, which is called $\sigma_{ULT-FEM1}$, uses the eigen buckling analysis to create the initial buckling shape and the desired buckling shape is obtained by multiplying the initial buckling shape with a scaling factor so that the maximum central deflection matches the required central deflection. The other approach, which is called $\sigma_{ULT-FEM2}$, is to create a program which reads the existing coordinate of each node and update the coordinate of nodes to represent perfect half wave shape based on equation Eq.5.2 in Chapter 5.2.1.



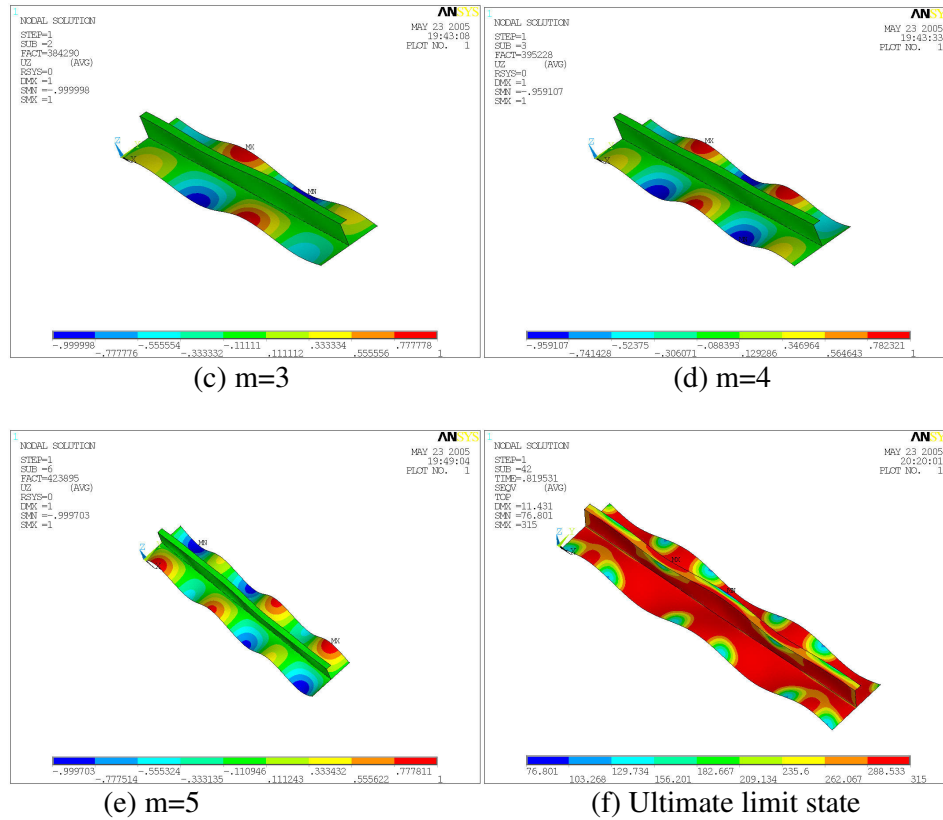


Fig. 6.4. Various buckling modes and *Von-Mises* stress distribution

Fig. 6.4 illustrates different buckling modes based on different half wave numbers (a ~e) and *Von-Mises* stress distribution (f) of the stiffened plate at the ultimate limit state.

Series of comparison of the ultimate strength of the stiffened plates have been carried out based on geometry dimensions of stiffener plate as follows:

- Plate length : 4000mm
- Plate breadth : 800mm
- Plate thickness : 16mm
- Web height : 300mm
- Web thickness : 12mm
- Stiffener flange width : 90mm (L-type)
- Stiffener flange thickness : 16mm

Table 6-2
Comparison of ultimate strength of stiffened plates

Number of half wave (m)	LRPASS N/mm ²	ULSAP N/mm ²	$\sigma_{ULT-FEM1}$ N/mm ²	$\sigma_{ULT-FEM2}$ N/mm ²
1	248.60	258.05	279.89	296.10
2	248.60	258.05	287.37	290.92
4	248.60	258.05	270.00	269.19
5	248.60	258.05	258.05	254.71

Table 6-2 shows the comparison of the ultimate strength of stiffened plates based on *LRPASS* [9], *ULSAP* [8] programs and finite element analyses; where $\sigma_{ULT-FEM1}$ indicates that the geometry update is based on eigen buckling results and $\sigma_{ULT-FEM2}$ means that the geometry update is based on *FORTTRAN* program by using equation Eq.5.2 in Chapter 5.2.1. The results can be summarized as follows:

- *LRPASS* and *ULSAP* programs produce the same ultimate strength regardless of the number of half wave. These programs could not consider the effect of the number of half wave. Of course they intend to produce the smallest value (the most critical one).
- Of these methods, *LRPASS* program proposes the most conservative ultimate strength.
- If the plate aspect ratio is same as the half wave number, the ultimate strength predicted by *ULSAP* is very close to those predicted by the finite element analyses ($\sigma_{ULT-FEM1}$ & $\sigma_{ULT-FEM2}$).
- In higher half wave numbers (4 and 5), which is closer to the plate aspect ratio, *FORTTRAN* program controlled initial imperfection shape (perfect half sine wave) leads to a smaller ultimate strength than eigen buckling based initial imperfection shape.

6.5 Ultimate strength of stiffened plates with general overall corrosion

As investigated in Chapter 3, there are many corrosion degradation models for cargo oil tank and ballast tank structures available, such as *TSCF* [10, 11], *Paik et al.* [12] and *Wang et al.* [13] models. It is necessary to evaluate the effect of general corrosion on the ultimate strength of stiffened plates in order to determine strength degradation at certain ship's ages in order to decide proper maintenance schedules of ship structures.

In this section, structural details of the upper deck in a cargo oil tank are selected to investigate the strength degradation at each design life which is based on *Paik et al.*'s [12] general corrosion model as described in Chapter 3.4.

Table 6-3 indicates the time variant corrosion degradation rates of upper deck structure in cargo oil tanks. *Paik 10 years (20 years, 30 years) model* means that the ship's age is 10 years (20 years, 30 years) old after delivery and which is based on the mean value of observed corrosion rates allowing for five(5) years of effective coating life. Whereas *Paik Max.10 years (20 years, 30 years) model* indicates that the ship's age is 10 years (20 years, 30 years) old after delivery which is based on mean value of 95% and above band corrosion rates considering five(5) years of effective coating life. Thus the latter considers higher rates of corrosion than the observed average trends.

A series of finite element analysis have been carried using the *ANSYS* program [14]. As illustrated in Table 6-3 and Fig. 6.5, *Paik Max. 30 years model* indicates 10% strength reduction compared with uncorroded condition, this means that the ultimate strength of stiffened plates under uniform corrosion on plate, web and flange is not

remarkably reduced. This is because that the existing design is strong enough to withstand against long period of general corrosion. However if the initial design and thickness of stiffened plate is thinner or the assumption of initial plate imperfection is larger, then the structure degradation pattern might be noticeably larger than present results. If there is comprehensive overall corrosion then the combined results should also be considered that overall bending induced stresses are increased and local stiffened panel capacity is decreased, hence the overall margin of safety should consider both of global corrosion effect and local corrosion effect.

Table 6-3
Time variant corrosion degradation rates

No	Description	Plate thickness (mm)	Web thickness (mm)	Flange thickness (mm)	σ_{ULT} / σ_0
1	Paik 0 year (design value)	15.000	11.00	16.000	1.000
2	Paik 10 years of service	14.511	10.38	15.491	0.987
3	Paik 20 years of service	14.022	9.76	14.982	0.971
4	Paik 30 years of service	13.533	9.14	14.473	0.956
5	Paik Max. 10 years of service	13.566	9.918	15.084	0.962
6	Paik Max. 20 years of service	12.132	8.836	14.168	0.930
7	Paik Max. 30 years of service	10.698	7.754	13.252	0.905

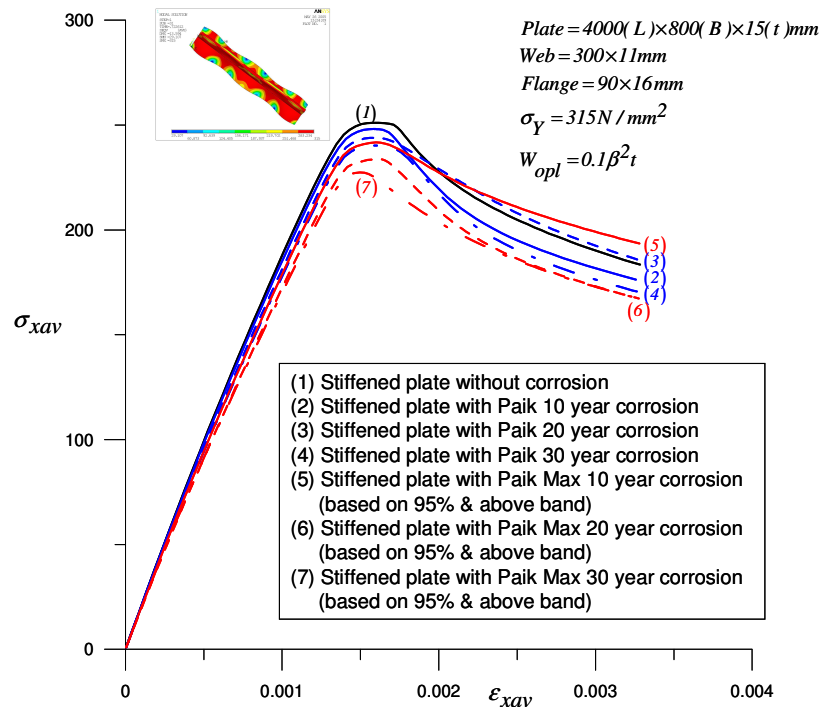


Fig. 6.5. A comparison of the average stress-strain curves for stiffened plates

6.6 Ultimate strength of stiffened plates with pitting corrosion

As shown on Fig. 5.18 in Chapter 5, concentrated patterns of localized corrosion can be frequently found in ageing ship structures. To evaluate proper inspection and maintenance periods and develop rational repair decisions it is important to estimate the ultimate strength of corroded stiffened plate allowing for different location and size of pitting corrosion on plate and stiffener web elements. The material properties are the same as previous modelling as defined by Section 6.3 and modelling geometry details have been selected as follows:

6.6.1 Dimension and details of F.E models

Based on existing structural details, the design dimensions of a one bay length stiffened plate with two longitudinal stiffeners are selected as follows:

- Plate breadth	: 1600 mm (800mm between stiffeners)
- Plate length	: 4000 mm
- Plate thickness	: 16.0 mm
- Web height	: 300 mm
- Web thickness	: 12.0 mm
- Flange width	: 90.0 mm
- Flange thickness	: 16.0 mm

6.6.2 Mesh size

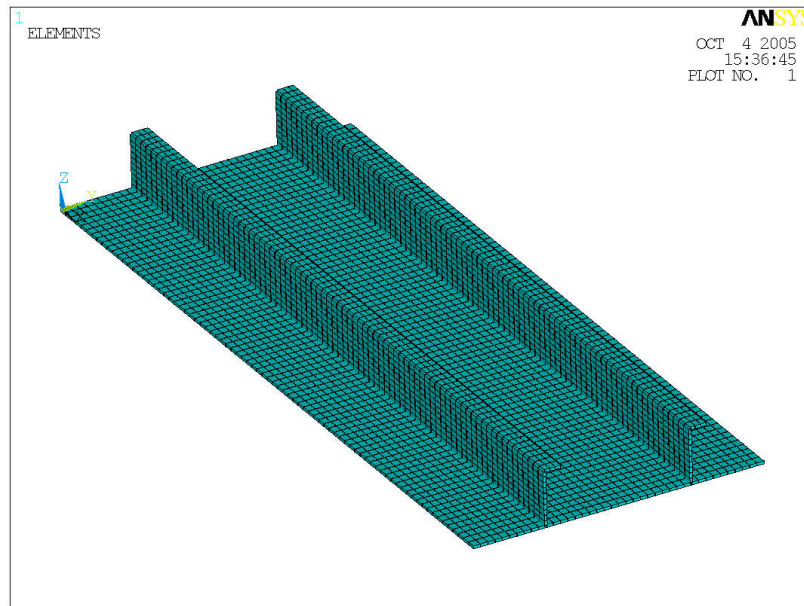


Fig. 6.6. Mesh details for stiffened plate with pitting corrosion model

The number of element (mesh size) for the basic FE stiffened plate model are selected as follows and the resulting mesh arrangement is as illustrated in Fig.6.6.

- No. of elements in plate : 40 x 80 elements
- No. of elements in each web : 10 x 80 elements
- No. of elements in each flange : 3 x 80 elements

6.6.3 Locations of pits and FEA results

In order to evaluate the relationship between the location of pits and strength reduction, seven different locations, each of which are to be analysed with the same size and pit depth pattern, were selected as shown in Fig. 6.7. From number 1 to number 4, the modelled pits are located on both sides of the plate along the longitudinal stiffeners, whereas for number 5 to number 7, the modelled pits are located at the centre of the plate, and, the modelled pits of number 4 and number 7 are located longitudinally at the central position. The total pit breadth of the cases 1, 2, 3, 4 at both sides is the same as the pit breadth of the cases 5, 6, 7, which is 20% of plate breadth, thus the total area of corrosion is the same in each patterns.

For the finite element analysis the dimensions of idealised groups of pits are selected as follows:

- Pit width : 20% of plate breadth (160 mm)
- Pit length : 500 mm
- Pit depth : 50% of plate thickness (8 mm)

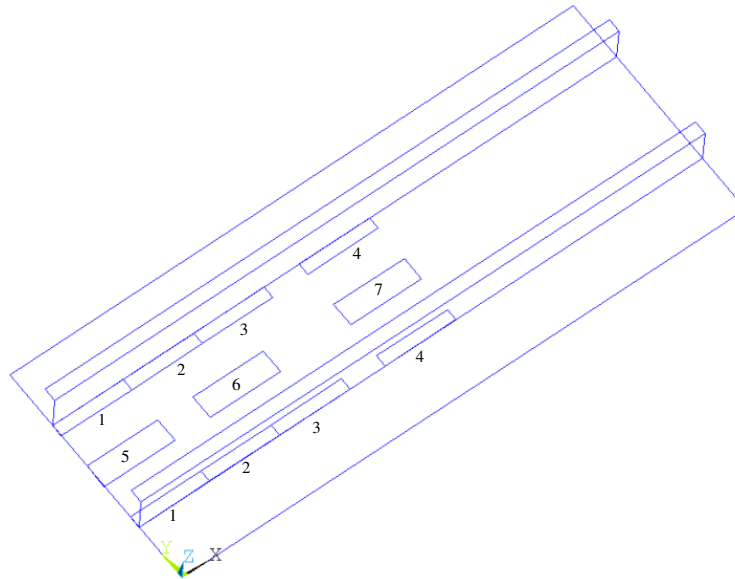


Fig. 6.7. The alternative location of pits on stiffened plate

As described in Chapter 5.5, *ANSYS Shell layer element model* has been used to represent the corroded stiffened plates and the mid-plane nodes in the pitted areas are artificially moved to the bottom surfaces and are aligned with intact areas as shown in Fig.6.8.

Table 6-4 and Fig. 6.10 show the results of the finite element analyses which indicate the ultimate strength of the stiffened plates with different patterns of pitting corrosion.

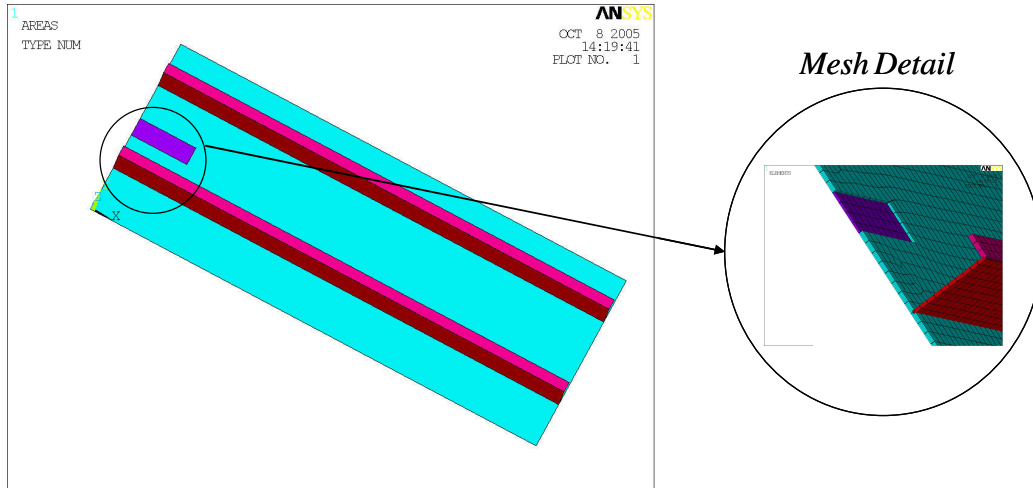


Fig. 6.8. Mesh detail of a stiffened plate with pitted area

Fig. 6.9 illustrates the various finite element results of stiffened plates with pitting corrosion.

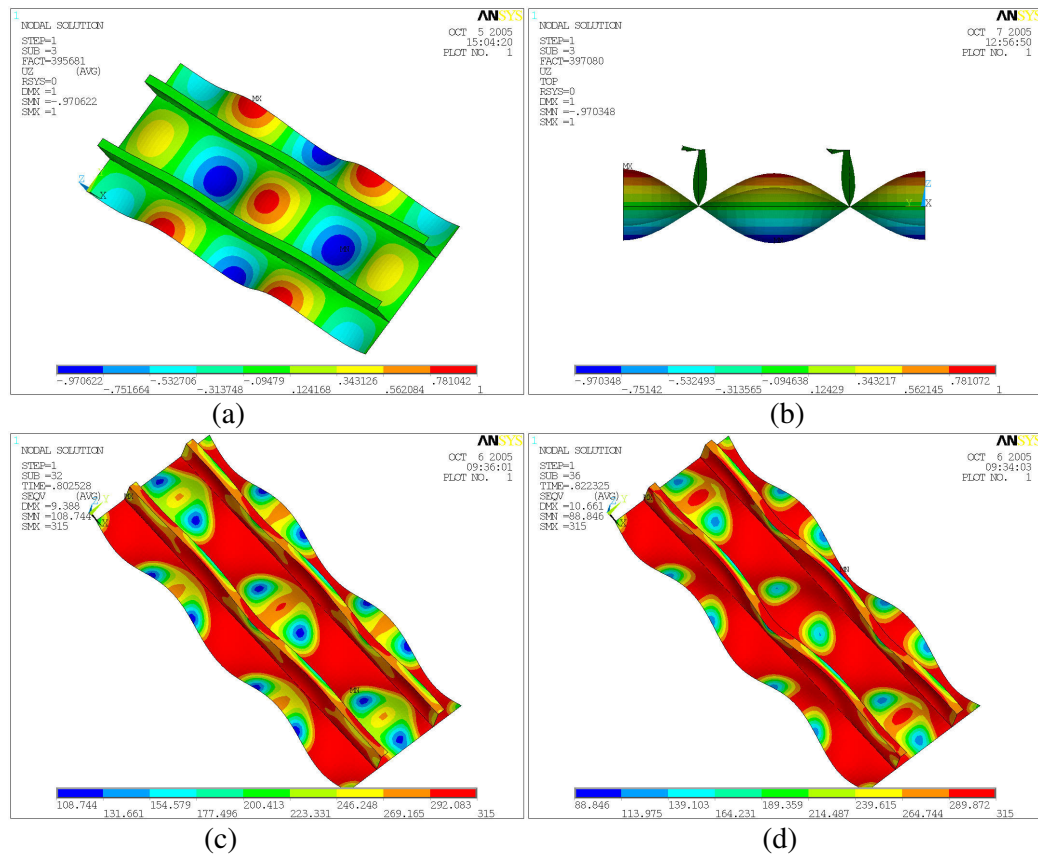


Fig. 6.9. Various finite element results of stiffened plates with pitting corrosion: (a) eigen buckling shape, (b) geometry deformation at ultimate limit state, (c) *Von Mises* stress distribution just before ultimate limit state, (d) *Von Mises* stress distribution at ultimate limit state

The results show that the pitting corrosion on both edges at the longitudinally central location (number 4) has reduced the ultimate strength the most. This is probably due to the fact that stiffeners are served as support to the plate between them. The pitting corrosion along the stiffeners would effectively weaken the support of the stiffeners, so the strength is reduced much. On the other hand, the central area of a plate under uni-axial compression is usually less effective than those close to edges (stiffeners), so pitting corrosion in the central area would weaken the strength less than those close to edges. The strength reduction is only about 5% in the most critical case. Of course, the degree of corrosion in this example is fairly modest and is limited to only one plate. If the degree of corrosion is increased, the strength reduction would be expected to increase as well.

Table 6-4

The results of finite element analysis for stiffened plate with pitting corrosion

Pitting Location	$\sigma_{ULT} (N/mm^2)$	$\sigma_{ULT} / \sigma_Y (N/mm^2)$	σ_{ULT} / σ_0
0 (No pit)	259.03	0.822	1.000
1	248.85	0.790	0.960
2	254.21	0.807	0.981
3	247.28	0.785	0.954
4	245.70	0.780	0.948
5	253.89	0.806	0.980
6	252.32	0.801	0.974
7	251.06	0.797	0.969

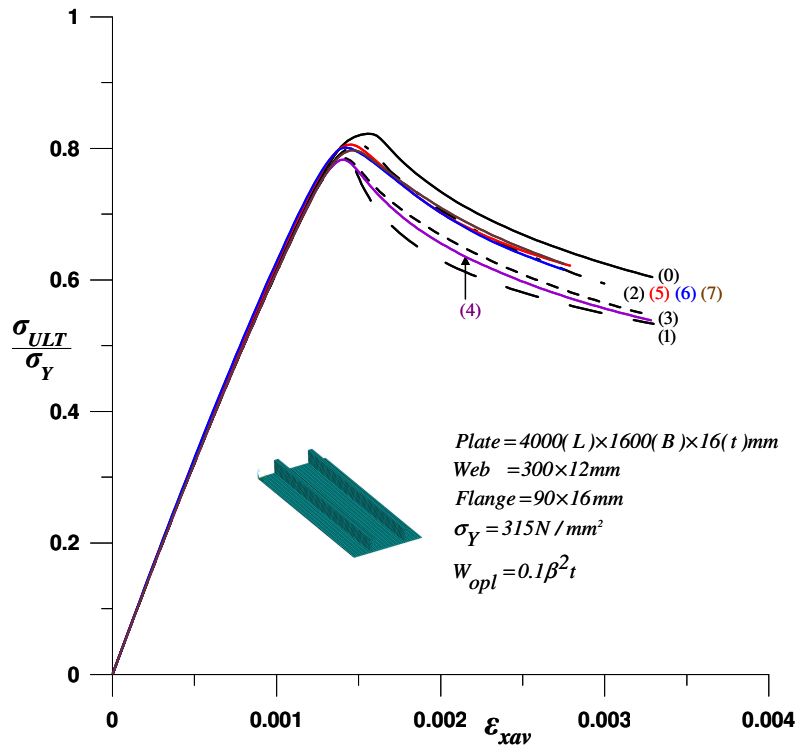


Fig. 6.10. Average stress-strain curves for stiffened plates under various pitting locations

6.7 Ultimate strength of stiffened plate with simultaneous pitting corrosion on both plate and stiffener web

In the previous finite element analyses, the localized pitting corrosion is limited on the plate only. However in the reality the localized corrosion could occur on both the plate and the web of the stiffeners simultaneously as shown in Fig. 5.18 in Chapter 5. The effects of localized defects or pitting corrosion could be changing the overall structural failure mode from plate or stiffened induced failure to other types of failure modes. If the localized corrosion is found on both plate and the web of the longitudinal stiffeners it could be the cause of local buckling of the stiffeners' web or of flexural-torsional buckling (tripping) of the stiffeners. Only a few research activities have been carried out to investigate the effects of the pitting corrosion on both plate and stiffeners simultaneously, which includes a recent publication by Dunbar et al. [15]. Thus, it is necessary to investigate the effects of combined pitting corrosion on both plate and web on the ultimate strength of stiffened plates.

In this section, the ultimate strength of stiffened plates with combined pitting corrosion on plate and web has been investigated. The longitudinally central location was selected as the pitted area and pitting corrosion on both edges are adopted. The pitting corrosion is assumed to be around each longitudinal stiffener as illustrated in Fig. 6.11.

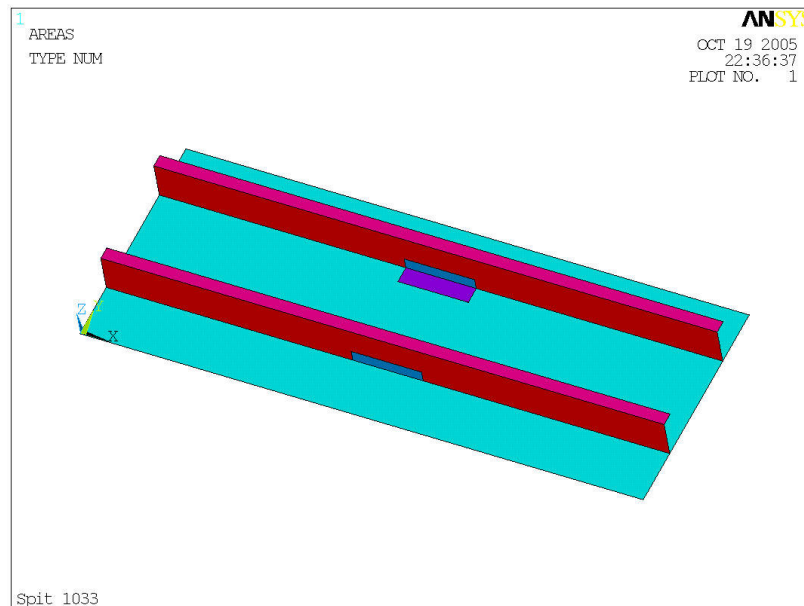


Fig. 6.11. Detail location of pitting corrosion on plate and web

Table 6-5 and Fig. 6.12 provide the results of the finite element analyses, which show the ultimate strength of stiffened plates with combined pitting corrosion on the web and plate. Fig. 6.13 illustrates *Von Mises* stress distribution at both the ultimate limit state and the post ultimate state conditions. The results show that the additional pitting

corrosion on web will reduce ultimate strength further by 4 ~ 6 % compared to without pitting corrosion on the web. This is relatively small amount of reduction in ultimate strength of stiffened plates. However if a relatively weaker stiffened plate was chosen in the analysis, the impact of the corrosion on the ultimate strength might be more significant than what is shown by the current results.

Table 6-5

The results of finite element analysis for stiffened plate with combined pitting corrosion on the web and plate

Case number	Pit breadth on plate	Pit height on web	σ_{ULT} N/mm ²	σ_{ULT} / σ_Y N/mm ²	σ_{ULT} / σ_0
0	0 %	0 %	259.03	0.822	1.000
1	10 %	0 %	253.84	0.806	0.979
2	20 %	0 %	245.70	0.780	0.948
3	30 %	0 %	237.64	0.754	0.917
4	10 %	30 %	242.06	0.769	0.934
5	20 %	30 %	233.62	0.742	0.901
6	30 %	30 %	223.61	0.710	0.863

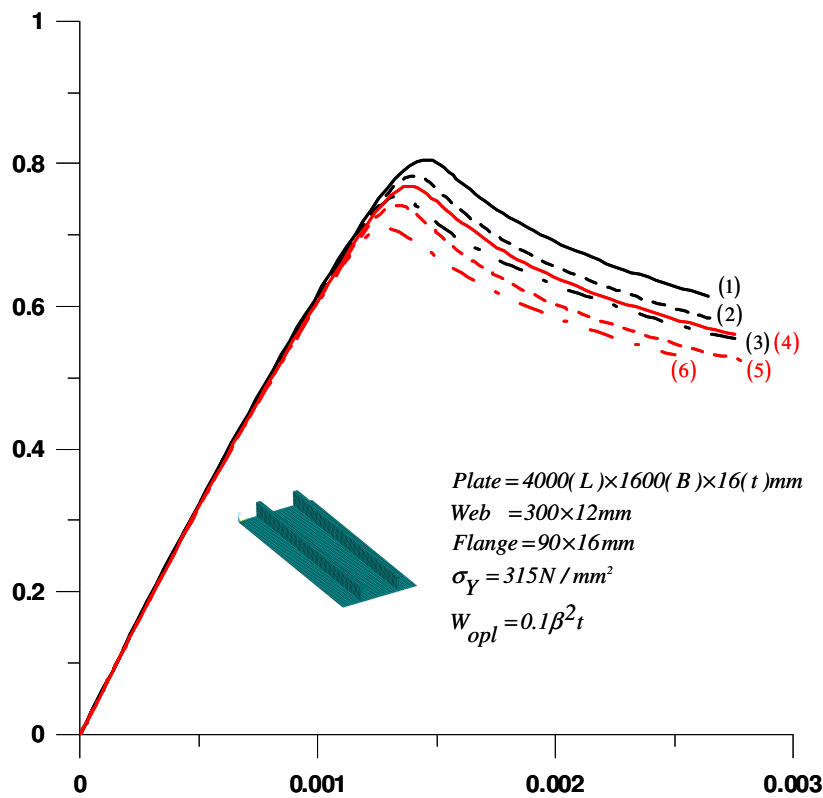


Fig. 6.12. Average stress-strain curves for stiffened plates with combined pitting corrosion on both stiffener the web and plate

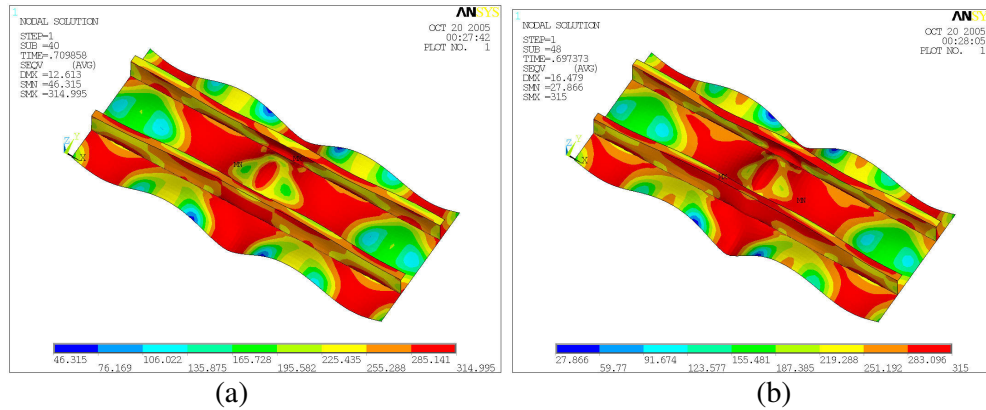


Fig. 6.13. Von Mises stress distribution : (a) at ultimate limit state (b) at post ultimate state

6.8 Concluding remarks

In this Chapter, the effects of pitting corrosion on the ultimate strength of stiffened plates have been investigated by using nonlinear finite element analyses. The effects of different buckling modes based on half wave number, pitting corrosion width, transverse location and combined pitting corrosion on plate and web on ultimate strength have been studied. The results can be summarized as follows:

- The ultimate strength of stiffened plates shows remarkable decrease as the number of half sine waves of initial deflection increases.
- LRPASS and ULSAP programs produce the same ultimate strength regardless of the number of half wave. These programs could not consider the effect of the number of half wave. Of course they intend to produce the smallest value (the most critical one).
- Of these methods, LRPASS program proposes the most conservative ultimate strength.
- If the plate aspect ratio is same as the half wave number, the ultimate strength predicted by ULSAP is very close to those predicted by the finite element analyses ($\sigma_{ULT-FEM1}$ & $\sigma_{ULT-FEM2}$).
- In higher half wave numbers (3 and 4), which is closer to the plate aspect ratio, FORTRAN program controlled initial imperfection shape (perfect half sine wave) leads to a smaller ultimate strength than eigen buckling based initial imperfection shape.
- The ultimate strength of stiffened plates under the existing uniform corrosion models and IACS [9] corrosion allowance on the plate, web and flange is not remarkably reduced.
- The results show that the pitting corrosion on both edges at the longitudinally central location (number 4) has reduced the ultimate strength the most. This is probably due to the fact that stiffeners are served as support to the plate between them. The pitting corrosion along the stiffeners would effectively weaken the support of the stiffeners, so the strength is reduced much. On the

other hand, the central area of a plate under uni-axial compression is usually less effective than those close to edges (stiffeners), so pitting corrosion in the central area would weaken the strength less than those close to edges. The strength reduction is only about 5% in the most critical case. Of course, the degree of corrosion in this example is fairly modest and is limited to only one plate. If the degree of corrosion is increased, the strength reduction would be expected to increase as well.

- In case of combined pitting corrosion on web and plate, the results show that the additional pitting corrosion on web will reduce ultimate strength further by 4 ~ 6 % compared to without pitting corrosion on the web. This is relatively small amount of reduction in ultimate strength of stiffened plates.

References (Chapter 6)

1. Pu, Y., *Reliability analysis and reliability-based optimisation design of swash ships*, in *Department of Naval Architecture and Ocean Engineering*. 1995, University of Glasgow: PhD thesis, Glasgow, U.K.
2. DNV, *Bacterial corrosion, brochure*, http://www.dnv.com/binaries/Bacterial%20corrosion%20brochure_tcm4-10613.pdf. 2005.
3. Rutherford, S.E., *Stiffened compression panels: The Analytical Approach*. 1982, Lloyds Register International Report No.82/26/R2.
4. Rutherford, S.E. and J.B. Caldwell, *Ultimate longitudinal strength of ships: A Case Study*. SNAME Transactions, 1990. **vo.98**: p. 441 – 471.
5. Pu, Y. and P.K. Das, *Ultimate strength and reliability analysis of stiffened plate*. 1994, Department of Naval Architecture and Ocean Engineering Report NAOE-94-37, University of Glasgow.
6. Faulkner, D., *Compression strength of welded grillages*, in *Ship Structural Concept*, J.M. Evans, Editor. 1975, Cornell Maritime Press. Chapter 21.
7. Carlsen, C.A., *A parametric study of collapse of stiffened plates in compression*. The Structural Engineer, 1980. **vol. 58B, No.2**.
8. Paik, J.K. and A.K. Thayamballi, *Ultimate Limit State Design of Steel Plated Design*. 2003: John Wiley & Sons Ltd.
9. LRS, *User's Manual "LR.PASS Personal Computer Programs"*. 1997.
10. TSCF, *Condition Evaluation and Maintenance of Tanker Structures*. Tanker Structure Cooperative Forum, May, 1992.
11. TSCF, *Corrosion Protection of Cargo Tanks*. Tanker Structure Co-Operative Forum, 2000. **TSCF Working Group #2, Chevron, Shipping Company**.
12. Paik, J.K., et al., *A Time-Dependent Corrosion Wastage Model for the Structures of Single and Double-Hull Tankers and FSOs and FPSOs*. Marine Technology, 2003. **Vol.40, No.3**: p. 201-217.
13. Wang, G., J. Spencer, and T. Elsayed, *Estimation of Corrosion Rates of Structural Members in Oil Tankers*. International Conference on Offshore Mechanics and Arctic Engineering, CANCUN, MEXICO, 2003. **22nd**.
14. ANSYS, *User's Manual (version 7.0)*. ANSYS Inc., 2003.
15. Dunbar, T.E., et al., *A computational investigation of the effects of localized corrosion on plates and stiffened panels*. Marine Structures, 2004. **In Press, Corrected Proof**.
16. IACS, *Common Structural Rules for Double Hull Oil Tankers*. 2006.

Chapter 7

Crack and Crack Propagation on Marine Structures

7.1 Introduction

General fatigue assessment methods and actual fatigue assessments of both a North Sea operating shuttle tanker and a world wide operating tanker were investigated in Chapter 4 and by *Ok et al.* [1, 2]. Eventually fatigue failure probably leads to the majority of structural failures in marine structures. It is a very rare case that a fracture occurs due to a singular excessive environmental load on undamaged and unflawed marine structures. Normally it is caused by repeated applications of relatively normal service loads, such as external wave loads and internal sloshing effects, which often develops cracks and progressively increases the size of cracks during the continued operation.

It is certain that undetected defects and developing cracks may lead to leakage and possibly to catastrophic fracture failure. Fracture control is necessary to ensure that the ship's structure safety will not fall down to below a certain safety limit. It is very important to calculate how the local structural strength is affected by cracks and to calculate the time in which a crack growth to the unacceptable limits. Fatigue analysis can estimate the elapsed time and locations where cracks could develop, whereas fracture mechanic approach can estimate crack growth times and response of structural strength as a function of crack size. It is essential that periodical inspections should be carried out in order to detect any developing and undesirable crack sizes and the inspection intervals should be determined to ensure the operational safety and reliability based on the crack growth time calculation by a damage tolerance analysis which should consider the possibility that a crack may not have been detected at an inspection period. *Garbatov and Ok et al.* [3, 4] have investigated various inspection procedures and techniques for crack and damage detection for ship structures.

Fig. 7.1 illustrates critical fatigue crack length of 24 meters across an upper deck in a tanker. Normally cracks may propagate in the transverse direction in the longitudinally stiffened panels. Although most of fatigue cracks in ships are not detected during the periodical survey, ship hull generally can tolerate relatively large transverse cracks without unstable fracture as long as a unduly severe wave loads are not experienced because of the good material properties, ductility and redundancy of ship structure etc.

Corrosion is also an important factor which affects crack initiation and the propagation of short cracks. In the initiation stage the localized corrosion can produce defects of the required size to trigger crack initiation. Whereas in the propagation stage, localized corrosion tends to weaken the resistance of micro-structural barrier such as grain boundaries and enables the crack to reinitiate in adjacent grains, thus potentially increasing the rate of growth.



Fig. 7.1. Cracked deck in tanker 'Castor' [5]

The first attempt to analysis fracture behaviour of brittle materials was done by *Griffith* in 1920 [6]. The analysis was based on the assumption that incipient fracture in ideally brittle materials takes place when the magnitude of the elastic energy supplied at the crack tip during an incremental increase in crack length is equal to or greater than the energy required to create a new crack tip surface.

Irwin [7] and *Orowan* [8] subsequently suggested that the *Griffith* fracture criterion for ideally brittle materials could be modified and applied to brittle materials and to metals that exhibit plastic deformation. *Irwin* [9] developed the energy release rate concept of *Griffith's* theory using the theory of *Westergaard* [10]. He also introduced the concept that the stress and displacements near the crack tip could be described by a single parameter, so called stress intensity factor (K), which was related to the energy release rate [11].

Since last decades there have been many attempts and investigations in fracture toughness of ship structures. *Poe* [12] developed a solution for crack propagating in a stiffened plate where the stiffeners were attached to the plate by means of rivets, and noticed that the K solution decreases as the crack approaches a stiffener, indicating that the stiffener aided in restraining the crack or slowing down the propagation. He also realized that the riveted stiffeners continue to limit crack growth after the crack propagates past the stiffener since a crack cannot propagate directly up into the stiffener. However for a welded stiffener, he assumed that once a crack reaches a stiffener, the stiffener is completely and suddenly severed and the load previously carried by the stiffener is shed to the remaining net section. *Thayamballi* [13] studied the effect of residual stresses on crack propagation in welded stiffened panels, and outlined an analytical approach to calculate the fatigue crack growth. The contribution of the residual stresses to K was based on Green's function, integrating the solution for a pair of forces acting on the crack faces. *Petershagen and Fricke* [14] conducted several fatigue crack growth experiments on welded stiffened panels with cutouts.

They reported that the influence of welded stiffeners on propagation of the crack was rather small, and that at least for the test condition in their experiments, residual stresses did not seem to effect the propagation of crack. For an elaborate summary of early researches undertaken by *Poe, Thayamballi and Petershagen et al.* are referred to Dexter et al. [5].

Anderson [15] reviewed the history and state of the art in elastic-plastic fracture mechanics. He also carried out experimental and analytical studies of fracture toughness tests for two ship steels ASTM A131 EH36 and HSLA 80 over a various range of temperatures. *Sumpter and Bird et al.* [16] and *Sumpter and Caudrey et al.* [17] suggested the minimum toughness of $125 \text{ MPa m}^{1/2}$ at a temperature of 0°C and a loading rate of $10^4 \text{ MPa m}^{1/2} / \text{s}$ based on dynamic fracture mechanics testing. Consequently they considered *Grade A* plate as being unsuitable for use in the outer hulls of ships. *Clarke* [18] investigated various fatigue crack problems in warships. He found that many cracks are associated with unsuitable and/or poor structural details.

Boukerrou and Cottis et al. [19] tested the growth of short cracks immersed in salt water 3.5% NaCl using smooth bending structural steel specimen. They found that the corrosion effect on the initial stage is to produce defects of the required size to trigger crack initiation through pitting from the electrochemically active sulphide containing inclusions, whereas in the growth stage, corrosion tends to weaken the resistance of microstructural barriers such as grain boundaries and enables the crack to reinitiate in adjacent grains. *Tomita et al.* [20] tested a welded I beam joint simulating the side longitudinal of ship structural member in order to examine fatigue crack growth behaviour under various storm loading models and proposed material constants as $C = 3.07 \times 10^{-12}$ and $m = 3.42$ in *MPa* to calculate fatigue crack growth behaviour.

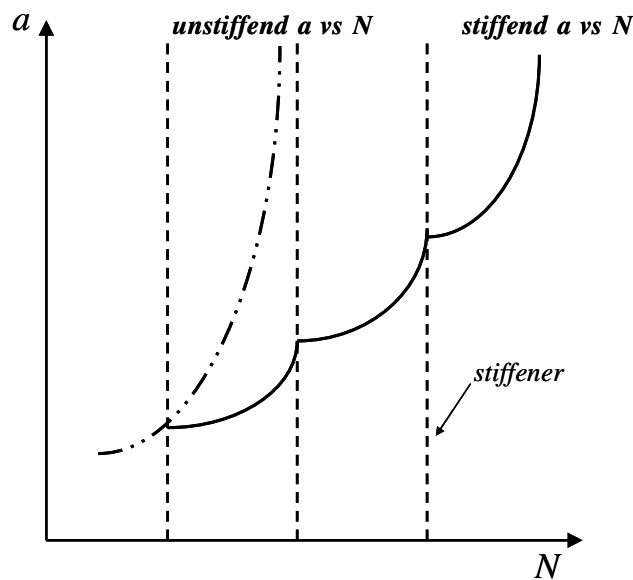


Fig. 7.2. Typical crack growth for stiffened and unstiffened panel [21]

Xu and Bea [21] investigated the load shedding behaviour in the stiffener panels of typical ship structure based on multiple load path effects, boundary effects and redistribution of residual stress. The stiffener may retard the crack growth rate and reduce the stress intensity factor as well as arresting the crack growth rate when the crack tip approaches a stiffener. Fig. 7.2 illustrates the typical pattern of the crack growth rate for both stiffened and unstiffened plate, where a is half the crack length and N indicates number of cycles.

Rokhlin and Kim *et al.* [22] presented a literature review on the pitting corrosion effect on fatigue crack growth. They also studied fatigue crack initiation and growth from artificial pits of different depths based on Al 2024-T3 aluminium alloy specimen. Wistance and Pumpherey *et al.* [23] carried out charpy impact and dynamic fracture toughness tests on Grade A and AH36 ship plates. A total of 39 Grade A plates of 12 mm to 16 mm thickness and 22 Grade AH36 plates of 15mm to 22mm thickness were tested and compared with LRS requirements of an impact energy of 27J at +20°C for Grade A and 34J at 0°C for Grade AH36 ship plates. They found that the toughness of modern Grade A and higher strength grade AH36 steel ship plates from various steel makers were sufficient to exceed the LRS requirements and thus to ensure the structural integrity of ship structure. Akpan and Koko *et al.* [24] developed time-dependent random function models for corrosion growth, fatigue cracks and corrosion enhanced fatigue cracks that potentially weaken the capacity of ship hulls. They also recommended threshold values of stress intensity factor $\Delta K_{th} = 5 \sim 6 \text{ ksi} / \sqrt{\text{in}}$, $C = 2.54 \times 10^{-9}$ and $m=2.53$ for carbon steel in accordance with Dobson and Brodrick *et al.* [25].

Dexter and Pilarski *et al.* [26, 27] carried out experimental tests of the large scale redundant box girder to show the effects of welding residual stress, the presence of transverse butt welds and stiffener details such as drain holes on the growth rate of these cracks. They found the results as follows:

- Welded stiffeners substantially reduce the crack propagation rate relative to a plate with no stiffeners.
- The number of cycles to propagate between a pair of stiffeners is approximately double the number of cycles to propagate this same distance in the unstiffened plate.
- The crack growth rate up the stiffener web is about the same as the crack growth rate past the stiffener in the shell plate.
- Stiffeners with cutouts such as drain holes perform about the same solid stiffeners.
- Specimens fabricated with tee stiffeners and ship steel did not perform significantly different than specimens fabricated with angle stiffeners and ordinary structural steel.

Dexter, Pilarski *et al.* [27] presented an analytical model to predict the growth rate of long fatigue cracks in stiffened panels and estimated the stress intensity factor based on superposition of linear elastic fracture mechanics solutions. They recommended a

threshold value of stress intensity factor $\Delta K_{th} = 2 \text{ MPa m}^{1/2}$, $C = 1.65 \times 10^{-11}$ and $m=3.0$ in accordance with *BS 7910* [28].

Garbatov and Guedes Soares [29] investigated the differences in crack propagation rate based on four different steels consists of low carbon steel and high tensile steels. They found that the high tensile steels develop higher rates of crack propagation and required less time for achieving certain crack size due to reduction of thickness which will lead to high costs and more frequent repair work.

Among others, *Ship Structure Committee* has carried out many researches in fracture, fatigue behaviour and damage tolerance criteria of ship structures [5, 25, 30-46].

General historical overviews of brittle failure in ships are provided in *Barsom et al.* [47] and *Stambaugh et al.* [44]. Elaborate summaries of fracture mechanics methods and researches are given in *Broek* [48], *Anderson* [15], *Barsom and Rolfe* [47], *Fricke and Berge et al.* [47, 49], *Dexter and Pilarski* [50] and *Brennan, and Cui et al.* [51] etc.

The Objectives of this chapter are to review classical theory of the *linear elastic fracture mechanics (LEFM)* approach and the *elastic plastic fracture mechanics (EPFM)* approaches, which is based on *crack tip displacement method* and *J-integral method*. In addition, the general concept of crack propagation, prediction of crack propagation and fracture control and inspection have also been investigated. Finally the effects of crack size, loads and material properties on stress intensity factors, *J-Integral* and *crack tip opening displacement (CTOD)* values have been investigated through 100 cases of finite element analyses for *LEFM* approach and another 300 cases of finite element analyses for *EPFM* approach.

7.2 Concept of fracture mechanics design

7.2.1 General

Frequently fracture is initiated by structural flaws or cracks subject to appropriately high local stress levels. These flaws and cracks sizes are typically increased slowly with repeated service loads. Fracture control is intended to prevent fracture due to previously undetected manufacturing defects and cracks at the loads anticipated to be experienced during operational service. To determine the permissible crack size and the safe operation life, it is necessary to know the effect of crack on the structural strength and to calculate the operational time in which a crack grows to a permissible size. Based on damage tolerance analysis, periodic inspections should be scheduled so that cracks can be repaired or components replaced when critical cracks are detected. Fracture control is a combination of measurements and analyses. It may include damage tolerance analysis, material selection, design improvement, determination of maintenance and inspection schedule etc. The mathematical tool for damage tolerance analysis is called fracture mechanics. It provides the concepts and equations to determine how cracks grow and how cracks affect the local strength of a structure.

Fig. 7.3 shows typical internal load or stress path lines, the load from the cracked side

will be transferred to the uncracked side which will carry the total load. Eventually higher stresses occur close to the crack. For uniform load the flow lines are straight lines and equally spaced. But if there is a crack the flow lines go around crack tip within a short distance. This means that more loads are flowing and concentrated through a small area. In the vicinity of the crack the stress has a vertical as well as horizontal component. Generally a blunt crack tip produces lower local stress than a sharp crack tip. The presence of cracks also affects the strength of structure. Apparently the buckling or ultimate strength of cracked structure is much smaller than those of uncracked structures.

The fundamental design approach to prevent fracture in structural materials is to keep the calculated stress intensity factor (K_I) below the critical stress intensity factor (K_C).

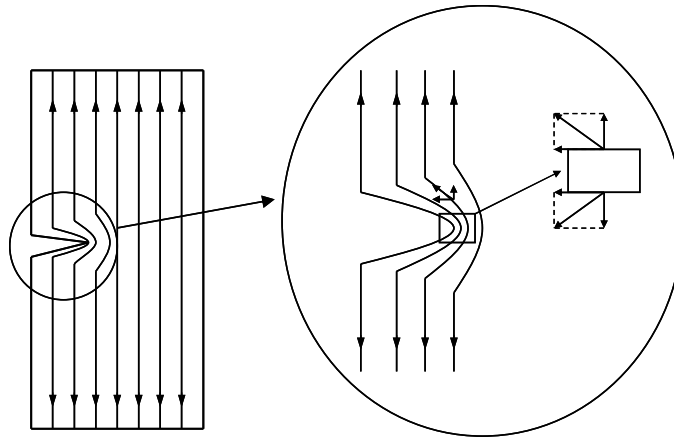


Fig. 7.3. Typical load path lines with crack

Generally the following procedure should be followed in order to prevent fracture in structural members [52]:

- Calculate the maximum nominal stress σ .
- Estimate the most likely flaw geometry and initial crack size a_0 . Estimate the maximum probable crack size during the expected lifetime.
- Calculate K_I for the stress, σ , and flaw size, a , using the appropriate K_I relation.
- Determine or estimate the critical stress-intensity factor K_C by testing the material from which the member is to be built.
- Compare K_I with K_C . To insure that K_I will be less than the critical stress-intensity factor K_C , throughout the entire life of the structure.

7.2.2 Modes of crack extension

“Linear-elastic fracture mechanics” approach is based on an analytical procedure that relates the stress-field magnitude and distribution in the vicinity of a crack-tip to the normal stress applied to the structure, to the size, to the shape and the orientation of

crack or crack-like discontinuity and to the basic material properties. The surfaces of a crack are the dominating influence on the distribution of stresses near and around the crack-tip. Other remote boundaries and loading forces affect only the intensity of the local stress field at the crack tip. There are basically three different types of crack extension as illustrated in Fig. 7.4. These displacement modes represent the local deformation in an infinitesimal element containing a crack front.

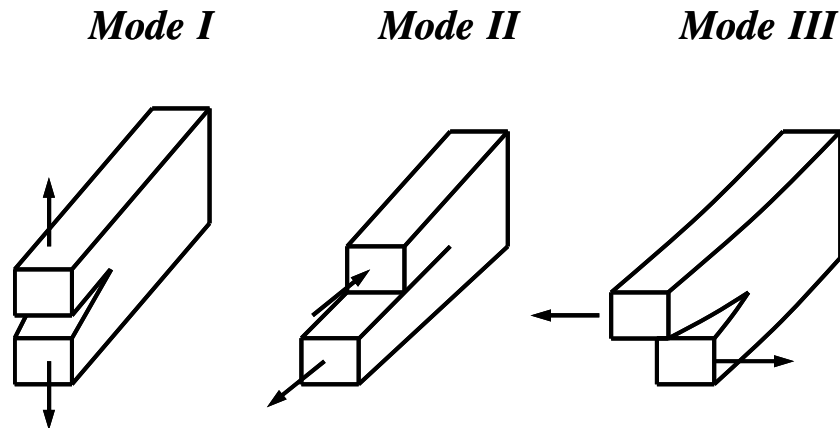


Fig. 7.4. The three basic modes of crack surface extensions

Mode I (The opening crack propagation mode)

This mode is characterized by local displacements that are symmetric with respect to the x - y and x - z planes. The two opposing fracture surfaces are displaced perpendicular away from each other in opposite directions.

Mode II (Local displacements in the sliding or shear mode)

This mode is symmetric with respect to the x - y plane and skew symmetric with respect to the x - z plane. The two fracture surfaces slide over each other in a direction perpendicular to the line of the crack tip.

Mode III (tearing mode)

This mode is associated with local displacements that are skew symmetric with respect to both x - y and x - z planes. The two fracture surfaces slide laterally over each other in a direction that is parallel to the line of the crack front.

In practice, most cracks occur and propagate at *Mode I* loading. Whereas the other modes may often occur in combination with *Mode I* crack.

7.3 Linear elastic fracture mechanics design

Materials which have the characteristic of relatively low fracture resistance and generally fail below their collapse strength can be analysed on the basis of elastic

concepts through the use of the *Linear Elastic Fracture Mechanics (LEFM)* approach.

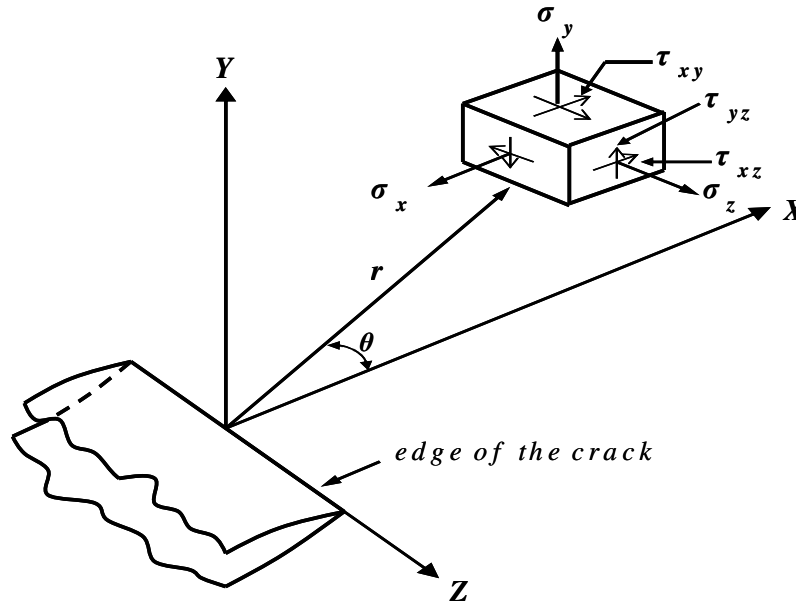


Fig. 7.5. Local coordinate system and stress components ahead of a crack

Westergaard [10] performed an elastic analysis of a continuum with a sharp crack. *Irwin* [53] determined the stress and displacement fields in the vicinity of crack tips subjected to the three modes of deformation, as noted earlier, on the basis of *Westergaard's* theory. For a cracked body of arbitrary shape and size with a linear elastic material as illustrated in Fig. 7.5, the stress components near the crack tip in the xy plane can be described by:

Mode I:

$$\begin{aligned}
 \sigma_x &= \frac{K_I}{\sqrt{2\pi r}} \cos \frac{\theta}{2} \left[1 - \sin \frac{\theta}{2} \sin \frac{3\theta}{2} \right] \\
 \sigma_y &= \frac{K_I}{\sqrt{2\pi r}} \cos \frac{\theta}{2} \left[1 + \sin \frac{\theta}{2} \sin \frac{3\theta}{2} \right] \\
 \tau_{xy} &= \frac{K_I}{\sqrt{2\pi r}} \sin \frac{\theta}{2} \cos \frac{\theta}{2} \cos \frac{3\theta}{2} \\
 \sigma_z &= \nu(\sigma_x + \sigma_y), \quad \tau_{xz} = \tau_{yz} = 0
 \end{aligned} \tag{Eq.7.1}$$

$$\begin{aligned}
 u &= \frac{K_I}{\mu} \sqrt{\frac{r}{2\pi}} \cos \frac{\theta}{2} \left[1 - 2\nu + \sin^2 \frac{\theta}{2} \right] \\
 v &= \frac{K_I}{\mu} \sqrt{\frac{r}{2\pi}} \sin \frac{\theta}{2} \left[2 - 2\nu - \cos^2 \frac{\theta}{2} \right] \\
 w &= 0
 \end{aligned}$$

where r, θ = the stress components and the coordinates as illustrated in Fig. 7.5
 u, v, w = the displacements in the x, y and z directions, respectively
 ν = Poisson's ratio
 μ = the shear modulus of elasticity = $\frac{E}{2(1+\nu)}$

Similarly the equation for stress components near the crack tip for Model II and Mode III can be found in many text books [47, 48].

For combined modes, the stress or displacement components may be given as a direct sum of those for each mode as follows [54, 55]:

$$\sigma_{ij}(r, \theta) = \frac{1}{\sqrt{2\pi r}} [K_I f_{ij}^I + K_{II} f_{ij}^{II} + K_{III} f_{ij}^{III}] \quad (\text{Eq.7.2})$$

$$u_i(r, \theta) = \frac{1}{2\mu} \sqrt{\frac{r}{2\pi}} [K_I g_i^I + K_{II} g_i^{II} + 4K_{III} g_i^{III}]$$

where $f_{ij}^I, f_{ij}^{II}, f_{ij}^{III}$ = stress functions of θ for *Mode I, II and III*.
 $g_i^I, g_i^{II}, g_i^{III}$ = displacement functions of θ for *Mode I, II and III*.
 K_I, K_{II}, K_{III} = stress intensity factors for *Mode I, II and III*.

It is apparent that the applied stress, the crack shape and size, and the structural configuration associated with structural components subjected to a given mode of deformation affect the value of the stress-intensity factor (K). Dimension analyses of Eq.7.1 indicates that the stress-intensity factor must be linearly related to stress and must be directly related to the square root of a distance from crack tip.

7.4 Stress intensity factor (K)

The stress intensity factor K characterizes the intensity of the stress immediately surrounding a sharp crack tip in a linear elastic and isotropic material. From the Eq.7.1, the stress intensity factor, K_I at crack tip can be written as [5]:

$$K = F_C F_S F_W F_G \sigma \sqrt{\pi a} \quad (\text{Eq.7.3})$$

where σ is applied load (tensile stress), a represents a half the crack length, F_C is a crack shape factor, F_S denotes a crack surface factor, F_W implies a finite width factor and F_G is a non-uniform stress factor.

Extensive stress-intensity factor equations for various geometries and loading conditions are described in *Paris and Sih* [56], *Tada et al.* [57], *Murakami* [58] and *Broek* [48].

Fracture will occur when the K factor reaches the critical value at which rapid unstable growth could commence:

$$K \geq K_C \text{ or } K_{IC} \quad (\text{Eq.7.4})$$

where K_C and K_{IC} denote a fracture toughness under plane stress and plane strain condition respectively.

Broek [48] strongly proposed to use the plane strain model, regardless of the state of stress.

The fracture toughness for *Mode I*, K_C , is a function of many factors such as thickness, temperature, strain-rate and microstructure. Fig.7.6 shows the relationship between fracture toughness and thickness, whereas Fig. 7.7 illustrates the relationship between fracture toughness and temperature. As the plate thickness increases the fracture toughness decreases and as the temperature increases the fracture toughness also tends to increase.

As the load increases in a structural member the critical crack size is decreased significantly and the different fracture toughness values lead to different values of critical flaw sizes as illustrated in Fig. 7.8.

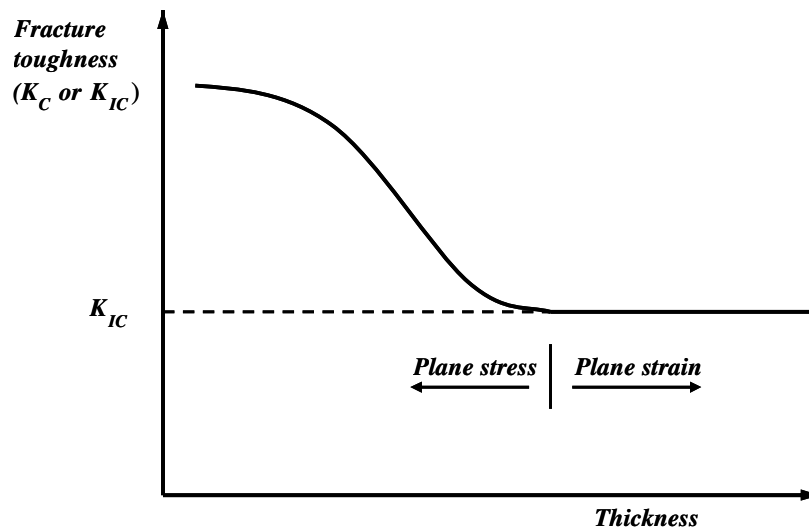


Fig. 7.6. The effect of plate thickness on fracture toughness

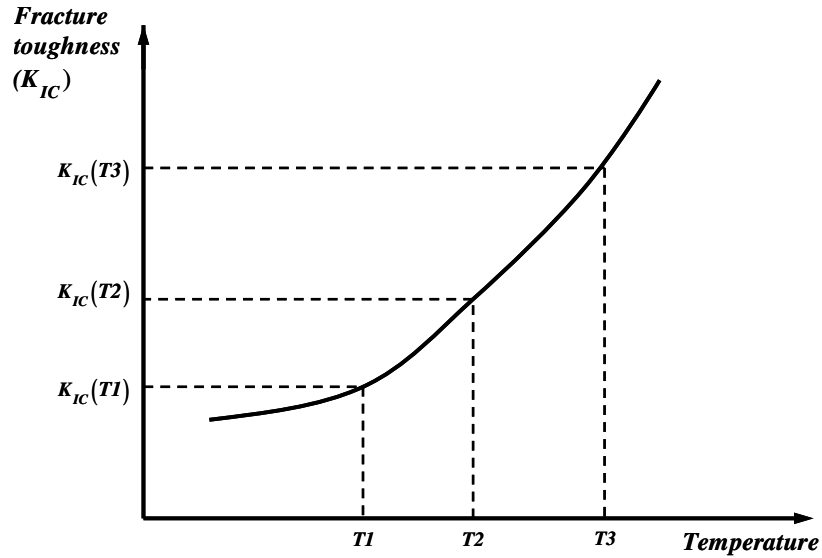


Fig. 7.7. Effect of temperature on fracture toughness

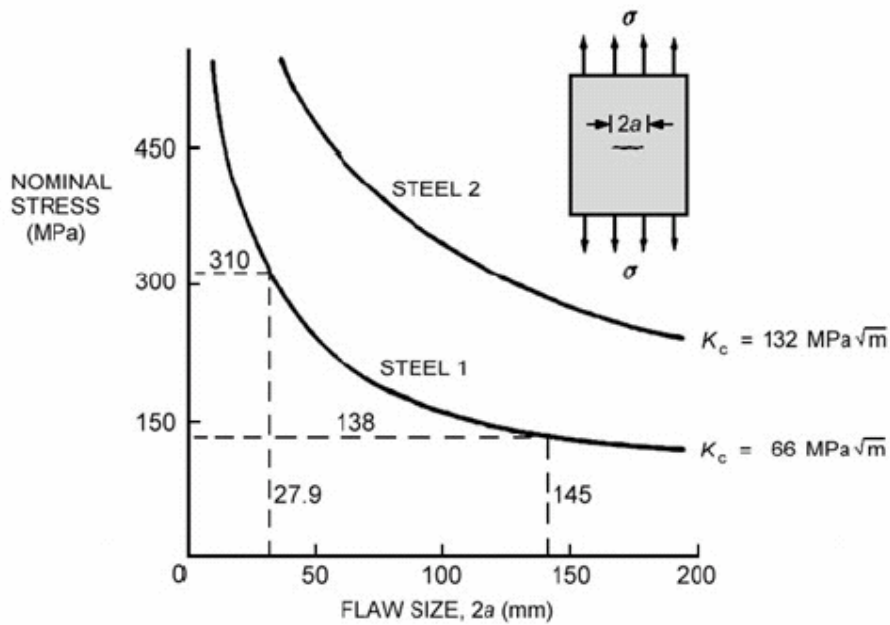


Fig. 7.8. Residual strength curves for two steel [59]

Typical idealised crack locations in a plate under tensile stress are shown in Fig.7.9 and various formulas for stress intensity factor based on each crack locations and size are introduced as follows:

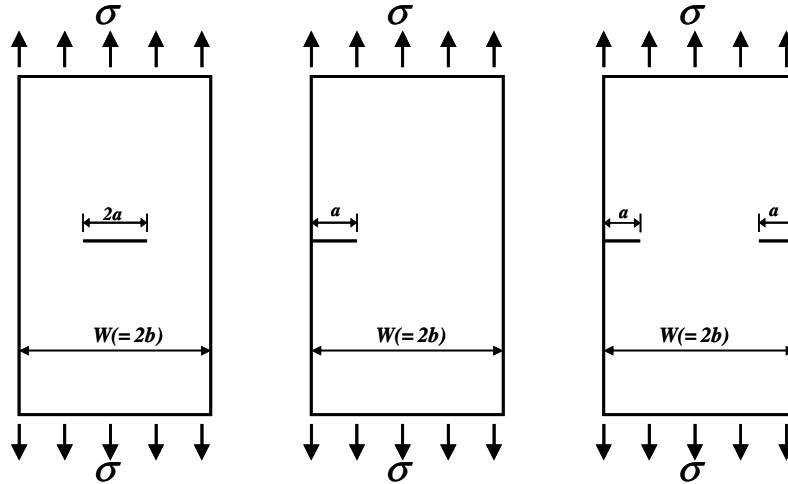


Fig. 7.9. Typical crack geometries under tensile load (a) centre crack; (b) single edge crack; (c) double edge crack

The stress intensity factor for an infinite plate with through thickness centre crack of length $2a$ is defined by following equation:

$$K_I = \sigma\sqrt{\pi a} \quad (\text{Eq.7.5})$$

A tangent-correction factor as given in Eq.7.6 is used to approximate the stress intensity factor for a plate of finite width, $2b$.

$$F = \sqrt{\frac{2b}{\pi a} \tan \frac{\pi a}{2b}} \quad (\text{Eq.7.6})$$

Consequently, the stress-intensity factor for a plate of finite width $2b$ with a through thickness centre crack subjected to uniform tensile stress (σ) is given by [56]:

$$K_I = 1.12 \cdot \sigma\sqrt{\pi a} \cdot F(a/b) \quad (\text{Eq.7.7})$$

The tangent correction factors which were proposed by Paris et al. [56] could not represent all correction values of a/b ratio between 0 and 1, thus alternative correlation factor by using curve fitting method can be proposed as follows:

For centre crack:

$$F(a/b) = 0.9925 - 0.1061\left(\frac{a}{b}\right) - 0.090\left(\frac{a}{b}\right)^2 + 0.8448\left(\frac{a}{b}\right)^3 \quad (\text{Eq.7.8a})$$

For single edge crack:

$$F(a/b) = 0.9350 - 0.4728\left(\frac{a}{b}\right) - 1.5338\left(\frac{a}{b}\right)^2 + 2.0338\left(\frac{a}{b}\right)^3 \quad (\text{Eq.7.8b})$$

Similar approaches have been done and introduced by *Tada and Paris et al.* [60, 61] and *Broek* [48].

Isida [62] proposed stress intensity factor based on each different boundary correction factors, $F_I(\alpha, \beta)$, which is introduced in *Murakami* [58].

Similar approaches as through thickness centre crack have been investigated and introduced for both single edge crack and double edge crack in *Paris and Sih* [56], *Tada and Paris* [60, 61] and *Broek* [48], for single edge crack in *Brown and Srawley* [63], for double edge crack in *Irwin* [53] and *Nisitani* [64].

Kitagawa and Yuuki [65] introduced correlation factors for centre slant crack under uniform uni-axial tensile stress.

The stress intensity factor for a part through (surface) crack in a plate subjected to uniform tensile stress also introduced by *Barsom and Rolfe* [47] which is expressed by:

$$K_I = 1.12 \sigma \sqrt{\pi \frac{a}{Q}} M_k \quad (\text{Eq.7.9})$$

where M_k = free-surface correction factor

$$= 1.0 + 1.2 \left(\frac{a}{t} - 0.5 \right) \quad \text{for values of } a/t \geq 0.5$$

t = thickness of plate

a = depth of surface crack

Q = flaw-shape parameter

Tada and Paris et al. [61] and *Isida et al.* [66] proposed another empirical formula for correlation factor for semi-elliptical surface crack in a finite thickness plate. And stress-intensity factors for cracks emanating from circular holes in infinite plates were also introduced by *Paris and Sih* [56] and *Newman* [67].

7.5 Elastic plastic fracture mechanics design

When the fracture is accompanied by considerable plastic deformation at the crack tip due to the ductile behaviour of structure, a simple correction to the *LEFM* method may not be valid and fracture parameters which allow for nonlinear material behaviour, so called *Elastic-Plastic Fracture Mechanics (EPFM)* method, should be applied.

7.5.1 Crack tip opening displacement (CTOD)

The crack propagation will take place when the plastic strain at the crack tip exceeds a critical value. *Irwin* [68] proposed a simple plastic correction to the stress intensity factor. An alternative plastic zone correction was developed by *Dugdale* [69], *Wells* [70, 71] and *Barenblatt* [72]. The first attempt to find out the elastic-plastic fracture parameters, the *crack tip opening displacement (CTOD)* was proposed by *Wells* [70]. He found that the fracture would initiate when the strains in the crack-tip region reach a critical value, which can be characterized by a critical crack-tip opening displacement.

Rolfe and Henn *et al.* [73] undertook studies on the prediction of critical crack sizes and fracture control based on actual *crack tip opening displacement (CTOD)* fracture tests. Bottom shell plates of AH36 steels were used and they proposed a fracture toughness (K_I) as $100 \text{ ksi}\sqrt{\text{in}}$ for this grade of steel as a reasonable lower bound value to use for subsequent critical crack size calculations.

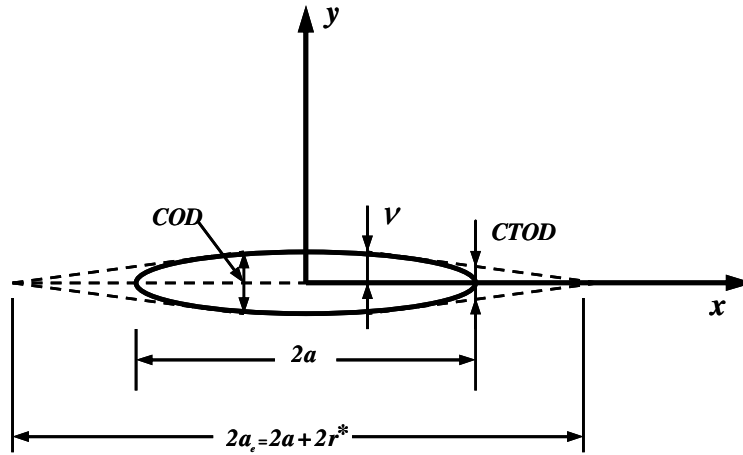


Fig. 7.10. Crack opening displacement and CTOD

In LEFM, the *crack opening displacement (COD)* as illustrated in Fig.7.10 is expressed by [54]:

$$COD = 2v = \frac{4\sigma}{E} \sqrt{a^2 - x^2} \quad (\text{Eq.7.10})$$

The maximum crack tip opening displacement occurs at the centre of the crack (at $x=0$) as follows:

$$COD_{\max} = \frac{4\sigma a}{E} \quad (\text{Eq.7.11})$$

If a plastic zone correction is considered, the COD is given by:

$$COD = \frac{4\sigma}{E} \sqrt{(a+r^*)^2 - x^2} \quad (\text{Eq.7.12})$$

The CTOD is then found for $x = a$ as follows:

$$CTOD \equiv \delta = \frac{4\sigma}{E} \sqrt{(a+r^*)^2 - a^2} \approx \frac{4\sigma}{E} \sqrt{2ar^*} = \frac{4}{\pi} \frac{K_I^2}{E\sigma_Y} \quad (\text{Eq.7.13})$$

7.5.2 Irwin's plastic zone correction

If the yield stress is applied normal to the crack plane ($\theta = 0$) in *Mode I* loading, Eq.7.1 can be reduced to:

$$\sigma_y = \frac{K_I}{\sqrt{2\pi r^*}} \quad (\text{Eq.7.14})$$

Fig. 7.11 is a schematic presentation of the change in the distribution of the y component of the stress caused by the localized plastic deformation in the vicinity of the crack tip.

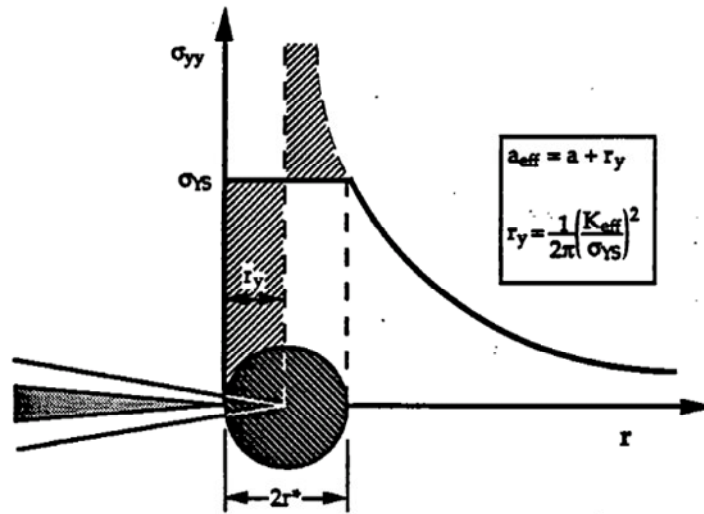


Fig. 7.11. Irwin plastic zone correction for plane stress condition [15]

Irwin [9, 11] modelled the effective stress intensity factor increases, K_I , by treating the crack as if it were slightly longer than its true physical length, given by:

$$K_I = \sigma f \sqrt{\pi(a+r_y)} \quad (\text{Eq.7.15})$$

The size of the plastic zone, $r_y = r^*$, at the crack tip for plane stress condition is defined by:

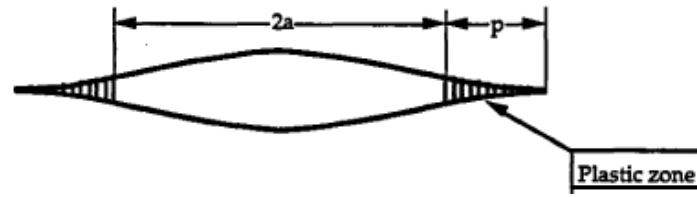
$$r_y = \frac{1}{2\pi} \left(\frac{K_I}{\sigma_Y} \right)^2 \quad (\text{Eq.7.16})$$

and for plane strain condition:

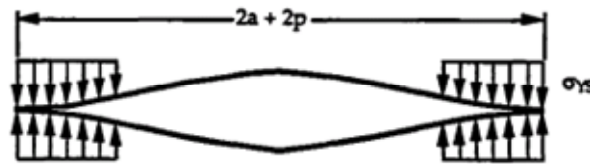
$$r_y = \frac{1}{6\pi} \left(\frac{K_I}{\sigma_Y} \right)^2 \quad (\text{Eq.7.17})$$

7.5.3 The Dugdale approach

Dugdale [69] assumed that all of the plastic deformation concentrates in a strip in front of the crack, the so-called *strip yield model*. The assumption of this model includes plane stress deformation and a non strain hardening material. The strip yield model consists of a through-thickness crack in an infinite plate that is subjected to a uniform tensile stress normal to the plane of the crack as illustrated in Fig.7.12. The crack is considered to have an effective length equal to $2a + 2p$. At each end of the crack there is a length p that is subjected to yield-point stresses that tend to close the crack, or, in reality, to prevent it from opening. Thus the length of the real crack would be $2a$.



a) Strip yield plastic zones



b) Assumed closure stresses in the strip yield zone

Fig.7.12. The strip yield model for a through crack [15]

Another way of looking at the behaviour of this model is to assume that yield zones of length p spread out from the tip of the real crack, a , as the loading is increased. Thus the displacement at the original crack tip, δ , which is the *COD*, increases as the real crack length increases or as the applied loading increases.

Burdenkin and Stone [74] used the strip yield model to estimate *CTOD* in an infinite plate with a through thickness crack, namely:

$$\delta = 8 \frac{\sigma_y a}{\pi E} \ln \left[\sec \left(\frac{\pi \sigma}{2 \sigma_y} \right) \right] \quad (\text{Eq.7.18})$$

where σ_y denotes yield strength of the material (ksi), a is half crack length (in), σ represents nominal applied stress (ksi) and E is modulus of elasticity of the material (ksi).

Using a series expansion for $\ln \left[\sec \left(\frac{\pi\sigma}{2\sigma_Y} \right) \right]$, this expression yields:

$$\delta = \frac{8\sigma_Y a}{\pi E} \left[\frac{1}{2} \left(\frac{\pi\sigma}{2\sigma_Y} \right)^2 + \frac{1}{12} \left(\frac{\pi\sigma}{2\sigma_Y} \right)^4 + \frac{1}{45} \left(\frac{\pi\sigma}{2\sigma_Y} \right)^6 + \dots \right] \quad (\text{Eq.7.19})$$

For nominal stress values less than σ_Y , representing small scale yielding, Eq.7.19 can be simplified to:

$$\delta = \frac{\pi a \sigma^2}{E \sigma_Y} = \frac{K_I^2}{\sigma_Y E} = \frac{G_I}{\sigma_Y} = \frac{J}{\sigma_Y} \quad (\text{Eq.7.20})$$

where G denotes strain energy release rate ($= \pi a \sigma^2 / E$) and J represents J integral value as discussed in the following section.

7.5.4 J-Integral approach

For elastic stress-strain fields, a surface-integral representation of a property related to the presence of a defect was derived by *Eshelby* [75], based on his earlier work [76]. He found that the integral vanished for a closed surface, embracing a homogeneous elastic material, even with allowance for anisotropy and finite deformation.

Günther [77] introduced similar approach of surface and line integrals with conservation properties, i.e. vanishing for closed surfaces of paths. *Cherepanov* [78], *Rice* [79] and *Hutchinson* [80] introduced a path-independent integral, so called *J-integral*, for plane elastostatic fields. It is a method of characterizing the stress-strain field around the tip of a crack by an integration path taken sufficiently far from the crack tip to be substituted for a path close to the crack-tip region. It has been extensively applied in fracture mechanics, especially in formulations of crack growth criteria. Path-independent integrals were also discussed by *Knowles and Sternberg* [81]. They studies two integrals for plane elastostatic fields, so called *L and M-Integral*. Interpretation of these integrals in terms of energy flux was subsequently made by *Budiansky and Rice* [82].

Shi, Sun et al. [83] studied the relationship between the *J-integral* and the *crack tip opening displacement (CTOD)*. The *J-integral* values are increased with the *CTOD* values when the load is increased. *Boothman et al.* [84] investigated *J-integrals* for semi-elliptical cracks in wide steel plates under tension.

The *J-integral* is a line or surface integral that enclosed crack front from one crack surface to the another along the arbitrary path around the tip of a crack as illustrated in Fig. 7.13.

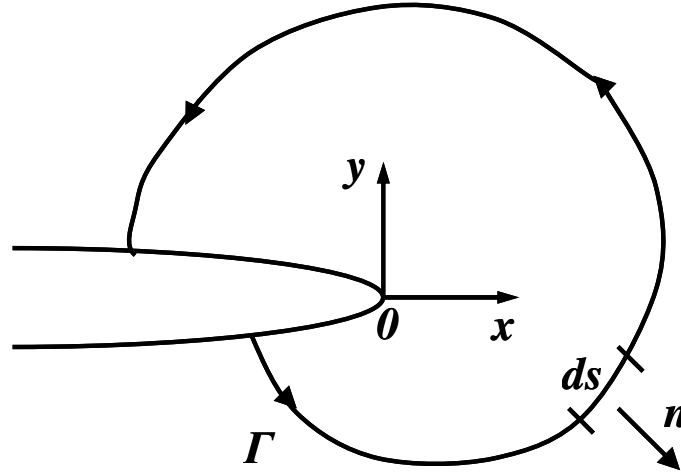


Fig. 7.13. Arbitrary contour around a crack tip

The path-independent integral of J , as illustrated by Fig.7.13 is given by [79]:

$$J = \int_{\Gamma} W dy - \int_{\Gamma} \left(t_x \frac{\partial u_x}{\partial x} + t_y \frac{\partial u_y}{\partial y} \right) ds \quad (\text{Eq.7.21})$$

- where Γ = arbitrary path surrounding crack tip
 W = the strain energy density = $\int \sigma_{ij} d\epsilon_{ij}$
 t_x = traction vector along x-axis (= $\sigma_x n_x + \tau_{xy} n_y$)
 t_y = traction vector along y-axis (= $\sigma_y n_y + \tau_{xy} n_x$)
 n = unit outward normal vector to path Γ
 ds = arc length along the path Γ

The crack tip with the path attached may be advanced by an increment, da , and the corresponding change in value of the J -integral is the amount of energy pouring through the path per unit increase in crack area, as characterized by da . For linear elastic conditions, the J -integral is identical to G , the energy release rate per unit increase in crack area. It can be said that the J -failure criteria for the linear elastic case is equivalent to the stress intensity factor, K_{Ic} , failure criterion. In case of the crack opening mode, it can be expressed by:

$$J_{Ic} = G_{Ic} = \frac{K_{Ic}^2}{E} = \delta\sigma_y \quad \text{for plain stress condition} \quad (\text{Eq.7.22})$$

$$J_{Ic} = G_{Ic} = \frac{1-\nu^2}{E} K_{Ic}^2 = \delta\sigma_y \quad \text{for plain strain condition} \quad (\text{Eq.7.23})$$

7.6 Crack propagation threshold and crack closure

McClintock [85] and *Frost* [86] noted a significant deceleration in fatigue-crack growth rates at low stresses. It shows the existence of a threshold for fatigue crack propagation, below which fatigue cracks should not propagate. The crack closure can be defined by direct physical contact between the two crack surfaces. *Ember* [87] found that fatigue-crack surface interfere with each other through closure mechanism. *Schmidt et al.* [88] found that crack closure may have a significant effect on the threshold behaviour. There are four crack closure mechanisms which may lead to crack closure as follows [47].

- Plastically induced closure caused by the presence of residual plastic deformation left in the wake of a propagating crack.
- Surface roughness-induced closure caused by deviations of the crack trajectory associated with micro-structural characteristics of the material (e.g. grain size and interlamellar spacing).
- Mode II induced closure caused by the displacement of the fatigue crack tip along shear planes
- Environmentally induced closure resulting from the build-up of corrosion products within the crack that wedge the crack surfaces

However, there are many factors which have an influence on the fatigue crack propagation threshold including such as stress history, mean stress, residual stress, yield strength, grain size, mode of crack tip opening, other material properties and temperature etc.

Barsom [89] proposed a threshold stress-intensity factors, ΔK_{th} , based on mild steel, low alloy steel, austenitic steel and other various steels, which are introduced in Section 7.9.

7.7 General concept of crack propagation

The subsequent life of structural components with cracks is governed by the rate of crack propagation. The presence of a fatigue crack can lead to loss of effectiveness of a structural element when the crack reaches a critical size. Normally the life of these structural components is determined by the fatigue-crack growth behaviour of the basic material and the imposed overall stress fields.

The fatigue-crack propagation behaviour for steel structures can be classified into three regions as illustrated in Fig. 7.14.

Stage I can be called crack initiation which is a vertical region in which the crack has initiated and grows very rapidly then decreases in crack growth rate. However if the stress intensity factor fluctuation value is below the threshold value ΔK_{th} , the fatigue crack should not propagate under cyclic-stress fluctuation. The initiation of cracks can only take place in the region of plastic deformation. As long as the strains are elastic,

even in the regions face of geometrical discontinuities and residual stresses, fatigue cracks do not start.

Stage II can be said steady-state crack propagation where a steady rate of crack growth is present. The crack is progressively increasing in length and does so over a reasonable range of stress intensity before entering region *III*. In this linear region of the log-log plot in Fig. 7.14 the growth can be represented by the well known *Paris-Erdogan* [90] formula. The *Paris-Erdogan formula* is fit to the linear portion of the da/dN versus stress intensity factor fluctuation ΔK . At relatively high ΔK levels the crack growth rate accelerates in each cycle. The formula is expressed by:

$$\frac{da}{dN} = C(\Delta K)^m \quad (\text{Eq.7.24})$$

$$\Delta K = \Delta\sigma Y(a)\sqrt{\pi a} \quad (\text{Eq.7.25})$$

where a = half the crack length
 N = number of cycles
 ΔK = stress-intensity-factor fluctuation
 $\Delta\sigma$ = stress range
 $Y(a)$ = geometric factor
 C, m = material constants

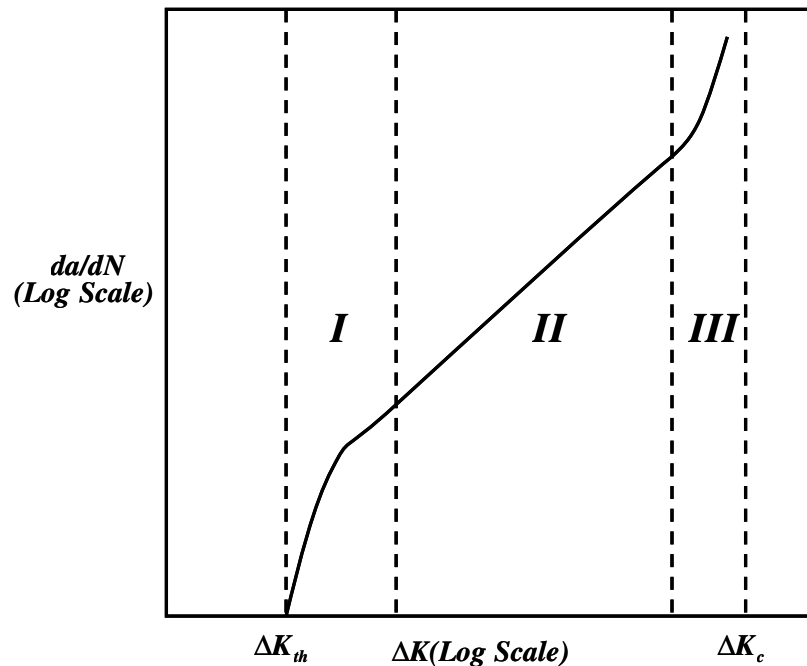


Fig. 7.14. A schematic of the fatigue crack growth rate curve

In *Stage III*, the fatigue crack growth per cycle is significantly higher than that predicted for *Stage II*. In this stage the fracture toughness of the material is reached and the crack is now unstable as its crack growth rate increases very rapidly with increasing stress concentration to failure which is accompanied by either ductile tearing or increment of brittle fracture in each cycle.

Forman *et al.* [91] proposed relevant equation for *Stage III*, given by:

$$\frac{da}{dN} = \frac{C(\Delta K)^m}{(1-R)K_C - \Delta K} \quad (\text{Eq.7.26})$$

where K_C is fracture toughness of the material and R is the K ratio defined by ($= K_{min} / K_{max}$).

7.8 Stress cycle and amplitude

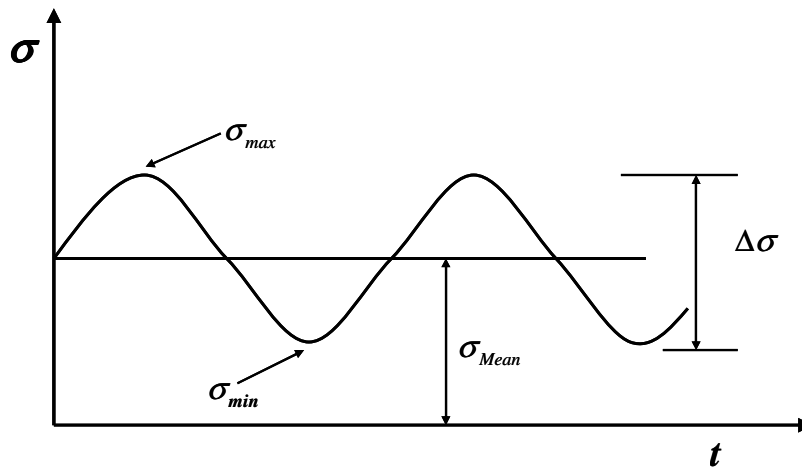


Fig. 7.15. Constant-amplitude loading

The prediction of fatigue crack propagation rates and propagation time of a cracked structure requires the input values of relevant crack propagation data, geometry factors and stress history etc. Actually most structural components are subjected to a variety of load histories either constant amplitude loading as shown in Fig. 7.15 or variable amplitude loading as illustrated in Fig. 7.16. Most ship and offshore structures suffer from variable amplitude random wave induced loading rather than constant amplitude loading. The load sequence on a ship is different in each loading and ballast voyage. The fluctuating loads on a ship occur from hogging and sagging response across various waves. In wave conditions, the buoyancy forces of ship are unevenly distributed, causing bending of ship, and shows the compression in the deck and tension in the keel during the sagging condition and vice-verse in a hogging condition. The loads on offshore structure depend on winds, currents and waves.

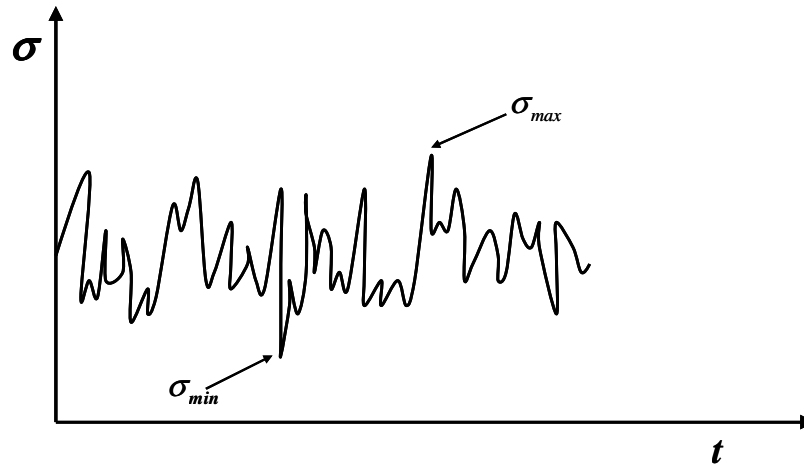


Fig. 7.16. Random stress loading

Barsom [92] proposed a single stress-intensity parameter that can be used to define the crack growth rate under both constant and variable-amplitude loading. The average fatigue crack growth rates per cycle, under variable-amplitude random sequence stress spectra can be expressed by:

$$\frac{da}{dN} = C (\Delta K_{rms})^m \quad (\text{Eq.7.27})$$

where the root mean-square value of the stress intensity factor, ΔK_{rms} is given by:

$$\Delta K_{rms} = \sqrt{\frac{\sum_{i=1}^k \Delta K_i^2}{n}} \quad (\text{Eq.7.28})$$

7.9 Parameters to calculate crack propagation

Due to an ability to tolerate large cracks for example by redundancy of a structure, good notch stress and ductility of modern ship steel and weld metal, ships can tolerate relatively large cracks without unstable fracture. Usually the fatigue cracking is not an immediate threat to the structural integrity of ship. If we can estimate crack propagate rates for ageing ships, we can develop a strategy for more efficient maintenance and inspection schedules.

There are several undefined parameters to calculate crack propagation which are the threshold stress-intensity factor ΔK_{th} and the material constants C , m .

7.9.1 Threshold stress-intensity factor, ΔK_{th}

Barsom [89] proposed a threshold stress-intensity factor, ΔK_{th} , based on mild steel, low alloy steel, austenitic steel and other various steels, and formulated by:

$$\Delta K_{th} = 6.4(1 - 0.85 R) \text{ ksi}\sqrt{\text{in}} \quad \text{for } R \geq 0.1 \quad (\text{Eq.7.29})$$

$$\Delta K_{th} = 5.5 \text{ ksi}\sqrt{\text{in}} \quad \text{for } R < 0.1 \quad (\text{Eq.7.30})$$

where R is stress ratio ($\sigma_{min} / \sigma_{max}$)

Dexter *et al.* [5] proposed the typical ΔK_{th} value as $3 \text{ MPa}\sqrt{\text{m}}$ for general ship structural steel.

7.9.2 Material constant, C and m

The form of Eq.7.24 can only be obtained from experimental test data. This means that the material parameters C and m are not the values which can be calculated from a mathematical or a theoretical model. Generally the equation can be derived by curve fitting through test data. The data can be plotted a straight line in a logarithmic plot. If we assume a straight line equation is $y = mx + b$, the test data can be represented by:

$$\log\left(\frac{da}{dN}\right) = m \log(\Delta K) + \log(C) \quad (\text{Eq.7.31})$$

Taking the anti-log of Eq.7.31 becomes the *Paris-Erdogan* equation given by Eq.7.24.

Dexter *et al.* [5] proposed the value of m as 3.0 as a typical value for steel. They also introduced different values of the constant C from various sources as follows:

- Fisher *et al.* [93] : $9.0 \times 10^{-12} \text{ MPa}\sqrt{\text{m}}$
- BS 7910 [94] : $16.5 \times 10^{-12} \text{ MPa}\sqrt{\text{m}}$
- BS 6493 [95] : $9.5 \times 10^{-12} \text{ MPa}\sqrt{\text{m}}$

Barsom *et al.* [47] introduced each different material parameter values for C and m under *Mode I* crack given by:

- Martensite steels : $C = 0.66 \times 10^{-8} \text{ ksi}\sqrt{\text{in}}$, $m = 2.25$
- Ferrite-Pearlite steels : $C = 3.6 \times 10^{-10} \text{ ksi}\sqrt{\text{in}}$, $m = 3.0$
- Austenitic stainless steel : $C = 3.0 \times 10^{-10} \text{ ksi}\sqrt{\text{in}}$, $m = 3.25$

Dobson *et al.* [25] suggested fatigue crack growth parameters for two different steel materials, HY-80 and carbon steel. They proposed that $C = 1.77 \times 10^{-9} \text{ ksi}\sqrt{\text{in}}$, $m = 2.54$ for HY-80 and $C = 2.54 \times 10^{-9} \text{ ksi}\sqrt{\text{in}}$, $m = 2.53$ for carbon steel material.

Garbatov and Soares [29] proposed the material parameters C and m based on different yield stress levels of typical ship structures as follows:

- $\sigma_y = 268 \text{ N/mm}^2$: $C = 8.85 \times 10^{-15} \text{ MPa}\sqrt{\text{m}}$, $m = 3.5$
- $\sigma_y = 312 \text{ N/mm}^2$: $C = 3.80 \times 10^{-13} \text{ MPa}\sqrt{\text{m}}$, $m = 3.0$

7.10 Prediction of crack propagation and fatigue life

The cracks on structural components grow their size as a function of time. To predict crack propagation for quasi-elastic condition at Stage II (LEFM), the most empirical relationship between the crack growth increment per cycle (da/dN) and parameters of stress range ($\Delta\sigma$) and the instantaneous crack length (a) can be the *Paris-Erdogan* equation as specified in Eq.7.24 and the stress intensity factor is described as Eq.7.25.

If we substitute the Eq.7.25 into Eq.7.24 and integrate equation we can obtain:

$$a(N) = \left[a_0^{1-(m/2)} + (1-(m/2)) C \Delta\sigma^m Y^m \pi^{(m/2)} N \right]^{\frac{1}{1-(m/2)}}, \quad m \neq 2 \quad (\text{Eq.7.32})$$

$$a(N) = a_0 \exp \left[C \Delta\sigma^2 Y^2 \pi N \right], \quad m = 2 \quad (\text{Eq.7.33})$$

The number of cycles (N) is defined as:

$$N = \nu_0 t \quad (\text{Eq.7.34})$$

where ν_0 is the mean zero up-crossing rate, t is time.

After substitution of Eq.7.34 in Eq.7.32, it becomes:

$$a(t) = \left[a_0^{1-\frac{m}{2}} + \left(1-\frac{m}{2}\right) C \Delta\sigma^m Y^m \pi^{(m/2)} \nu_0 t \right]^{\frac{1}{1-\frac{m}{2}}}, \quad m \neq 2 \quad (\text{Eq.7.35})$$

$$a(t) = a_0 \exp(C Y^2 \Delta\sigma^2 \pi \nu_0 t) \quad , \quad m = 2 \quad (\text{Eq.7.36})$$

Considering that the load can be described by the *Weibull* distribution, the stress range $\Delta\sigma^m$ can be written as [29]:

$$\Delta\sigma^m = \gamma_{\Delta\sigma}^m \Gamma \left[1 + \frac{m}{\alpha_{\Delta\sigma}} \right] \quad (\text{Eq.7.37})$$

where $\Gamma[]$ is the incomplete *Gamma function*, the scale parameter of the Weibull distribution of the stress range, $\gamma_{\Delta\sigma}$, is obtained from the shape parameter $\alpha_{\Delta\sigma}$ and a reference stress response $\Delta\sigma_0$, exceeded once in the corresponding reference number of the stress cycles N_0 which is determined as the N_0^{-1} probability level:

$$\gamma_{\Delta\sigma} = \frac{\Delta\sigma_0}{(\text{Ln}(N_0))^{\frac{1}{\alpha_{\Delta\sigma}}}} \quad (\text{Eq.7.38})$$

The definition of the fatigue limit state is given in terms of critical crack size a_{cr} . Replacing $a(t) = a_{cr}$ in Eq.7.35, one obtains the time T_p to crack propagation from the initial crack size a_0 to the critical size [29, 96]:

$$T_p = \frac{a_{cr}^{1-(m/2)} - a_0^{1-(m/2)}}{\left(1 - \frac{m}{2}\right) C \Delta\sigma^m Y^m \pi^{(m/2)} V_0} \quad (\text{Eq.7.39})$$

Consequently the total fatigue life for cracked structural components can be expressed the sum of the time T_i to crack initiation and the subsequent time T_p to crack propagation until critical size is reached, given by:

$$T_f = T_i + T_p \quad (\text{Eq.7.40})$$

7.11 Fracture control and inspection

Structural strength tends to decrease in a time dependant manner through the effects of corrosion and cracks. The total useful life of a structural component affected by variable loading amplitude is determined by the time required to initiate a crack and then to propagate the crack from subcritical size to a critical size. There are many factors which affect crack propagation and permissible residual strength, such as the magnitude and fluctuation of the applied stresses, fracture toughness of the material at a particular service temperature, plate thickness, crack size and shape, discontinuity at possible locations of fracture initiation, the magnitude of stress intensity factor, stress-corrosion susceptibility and the fatigue characteristics, etc.

It is very important to evaluate the critical crack size at design loads and to estimate the time or cycles to reach the critical crack size from existing crack size. Once critical crack size and amplitude of load can be decided, the inspection intervals on the basis of analysis results can be determined based on the most economic interval and reliability, probability of detection and safety of structure, etc.

Fig. 7.17 illustrates the time dependent crack growth curve from crack initiation size a_i through detected crack size a_o to the maximum permissible crack size a_p . It is apparent that cracks should be repaired and eliminated before they affect the strength

more than tolerable value. This means that any cracks must be discovered by means of periodical inspection before they reach the maximum permissible size.

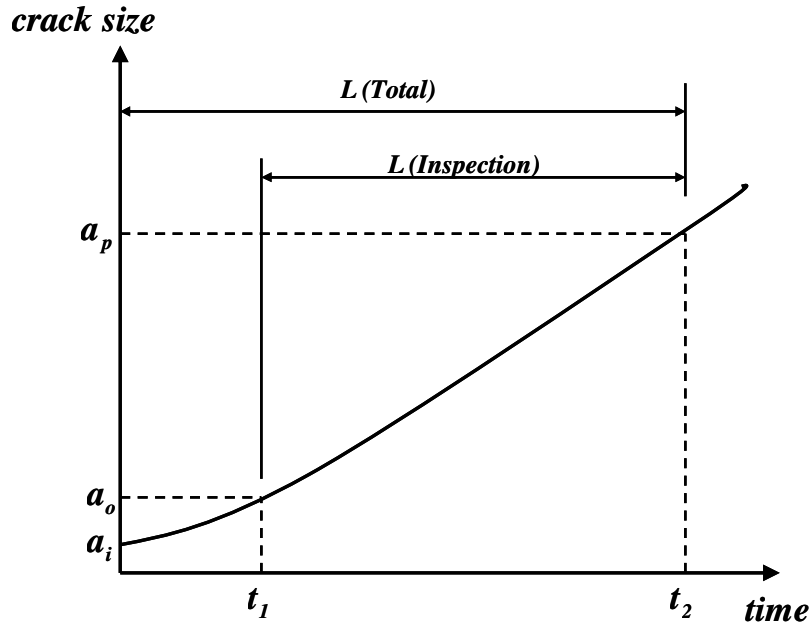


Fig. 7.17. Time dependant crack growth curve

However there is always the possibility to miss certain cracks during the inspection. If the inspection is carried out at time t_1 , undetected crack could grow to the maximum permissible size before the next inspection time t_2 . Therefore the proper inspection interval should be established and should be shorter than the period of crack growth from initial size to the maximum permissible size, $L(Inspection)$ as shown in Fig.7.17. Normally a sufficient number of inspections during the time $L(Inspection)$ can increase safety and reliability of structural components, however, on the contrary, it increases maintenance cost.

The actual detection of cracks, which are larger than the physically/realistically detectable size, is not a certainty. It will depend on many factors such as location of structural components, the skill of inspector, possible corrosion product inside cracks, view angles and inspection methods etc. The probability of detection should be less than 1 even for large cracks and can be expressed by [48]:

$$p = 1 - e^{-\{(a-a_0)/(\lambda-a_0)\}^\alpha} \quad (\text{Eq.7.41})$$

where a_0 is the crack size for which detection is absolutely impossible, α and λ are parameters determining the shape of the curve.

There is obviously the possibility that some certain cracks may not be detected during the inspection period and missed for several subsequent inspection periods. In this case, the cumulative probability of detection can be given by:

$$P = 1 - \prod_{i=1}^n (1 - p_i) \quad (\text{Eq.7.42})$$

Garbatov and Soares [29] proposed the probability of crack detection based on previous work by Packman *et al.* [97], given by:

$$P_d(t) = \begin{cases} 1 - \exp\left[-\frac{2a(t) - a_{d,0}}{\lambda_d}\right] & \text{if } 2a(t) > a_{d,0} \\ 0, & \text{if } 2a(t) \leq a_{d,0} \end{cases} \quad (\text{Eq.7.43})$$

where $\lambda_d = a_{d,0} / \ln(1 - k)$, $k = 0.95$, and $a_{d,0}$ is limit size of detection under which a crack will not be detected.

7.12 Prediction of stress intensity factors using finite element analysis

In previous sections, classical theories and recent research activities of the linear elastic fracture mechanics (LEFM) and the elastic plastic fracture mechanics (EPFM) approaches have been reviewed. Over past few decades the stress intensity factor (K) has been used for linear elastic fracture mechanics methods and which are strictly valid only for isotropic materials that behave in a perfectly linear elastic manner. When there is only a small amount of plastic deformation at the tip of the crack, linear elastic fracture mechanics (LEFM) gives a relatively good approximation of actual material behaviour. However if fracture is accompanied by considerable plastic deformation, then the elastic-plastic fracture mechanics method is used. Generally the *J-integral* and *CTOD* methods have been used as a tool and fracture criterion for nonlinear materials under elastic-plastic deformation. It is important to estimate the postulated cracks under given loading conditions.

Generally the LEFM based stress intensity factor (K) can be calculated by many existing formulae [58, 61] which are based on actual tensile specimen tests and numerical calculations. However the application of these formulae is restricted to standard shapes of problems and cannot cover all of crack patterns on ship's and marine structures. Actual tensile specimen tests also require a lot of cost and efforts to have a reliable stress intensity factor (K), J-Integral value or CTOD value. The finite element approach has now become more and more common and alternative solutions in linear elastic fracture mechanics and elastic fracture mechanic methods due to its relatively cheaper cost than actual test for complicated crack patterns. In this study, the finite element approach will be employed to investigate the effects of cracks on stress intensity factors, J-integral and CTOD values.

As indicated in Fig.4.3 in Chapter 4 and as illustrated in "Guidance Manual for Tanker Structure" by TSCF [98], the typical patterns of cracks on ship structures are single edge crack and centre crack on stiffened plate as illustrated in Fig. 5.6. Both

edge type cracks as illustrated in Fig.5.5 is a very unusual pattern of crack on marine structures, thus only single edge and centre cracks are considered in this studies.

As previously reviewed in Chapter 5, currently the most frequently used grades of steel for ship structures are mild steel with a yield stress, $\sigma_y = 235N/mm^2$ and higher strength steels with $\sigma_y = 315N/mm^2$ (LRS AH32, ABS HT32, DNV NV-32) and $\sigma_y = 355N/mm^2$ (LRS AH36, ABS HT36, DNV NV-36). If the material properties, such as yield stress, are different then the size of plastic deformation at the tip of the crack will be different under same loading conditions. However the LEFM based fracture mechanic method as indicated in Eq.7.7 does not have a parameter to represent material properties. This means that the calculation for LEFM based stress intensity factor (K) can be done by input parameters which are related to the size of the uniform tensile stress, crack size and plate width and LEFM based stress intensity factor (K) can only be used where the applied load is small and the amount of plastic deformation at the tip of the crack is small.

There have been some efforts to investigate the effects of different material properties on fracture toughness [15, 17, 23, 29]. However the effects of different crack sizes on stress intensity factors for commonly used steel for ship structures with a yield stress, $\sigma_y = 235N/mm^2$, $\sigma_y = 315N/mm^2$, $\sigma_y = 355N/mm^2$ have not been studied well, thus it is also valuable to find out the effects of different yield stresses on stress intensity factors by using FEM based elastic-plastic fracture mechanics approach.

In this study, numerical analyses have been carried out by the ANSYS [99] finite element computer software in order to model two-dimensional linear elastic and elastic-plastic analysis mode condition.

The work has been performed on a square (1m x 1m) unstiffened plate which has a single edge crack and centre crack under uniform tensile load. The effects of different crack sizes (a/W , from 0.05 to 0.4, where a is half crack size and W is plate breadth), loads ($10 N/mm^2$ to $100 N/mm^2$), and different yield stresses on the stress intensity factor (K) and J -integral and crack tip opening displacement (CTOD) values have been investigated. The calculated values are to be useful for the assessment of cracks and estimation of crack propagation for marine and offshore structures.

7.12.1 Finite element modelling details and methods for plate with a crack

7.12.1.1 Size and material properties

The full size of plate with crack is based on $1m \times 1m$ plate and a quarter of plate ($0.5m \times 0.5m$) is used for modelling and computational efficiency. Generally following material properties are assumed for this study:

$$\begin{aligned} \text{Young's modulus } (E) &= 209000 N/mm^2 \\ \text{Poisson's ratio } (\nu) &= 0.3 \end{aligned}$$

In order to consider the effect of different material yield stresses on the elastic plastic behaviour near the crack tip, three most commonly employed yield stresses (σ_y) of 235 N/mm^2 , 315 N/mm^2 and 355 N/mm^2 are used for this investigation.

7.12.1.2 Element type and K calculation

The recommended element type for a 2-D fracture model is the *PLANE2* (6-node triangular solid) or the *PLANE82* (8-noded quadrilateral elements) and in 3D is the *SOLID95* (20-noded brick) as illustrated in Fig. 7.18 with near tip mid-side nodes shifted to the quarter-point positions.

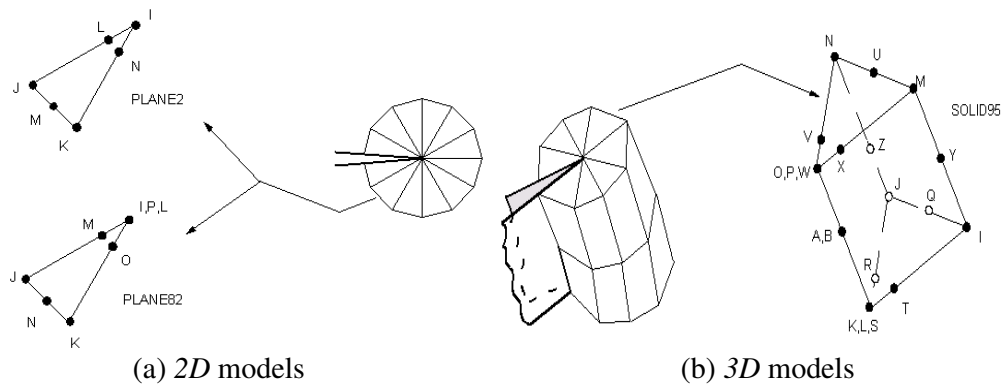


Fig. 7.18. Element type for 2D and 3D models

In ANSYS program, these elements around a crack tip are automatically generated by using *KSCON* command for 2-D model which allows to control the radius of the first row of elements and number of elements in the circumferential direction. For reasonable results, the first row of elements around the crack tip should have a radius of approximately $a/8$ or smaller. In the circumferential direction, roughly one element every 30 degree or 40 degree is recommended as illustrated in Fig. 7.19. However in a 3-D model the *KSCON* command can not be used and thus with 3D problems normal ANSYS mesh generation is required by defining number of elements around crack tip, number of elements around crack front, outer radius of crack-tip element, crack front radius and crack-front angle as shown in Fig. 7.20.

Generally the stress intensity factor (K) can be calculated by following procedure in ANSYS program:

- Define a local crack-tip or crack front coordinate system.
- Define a path along the crack face. The first node on the path should be the crack-tip node.
- Calculate K_I , K_{II} and K_{III} .

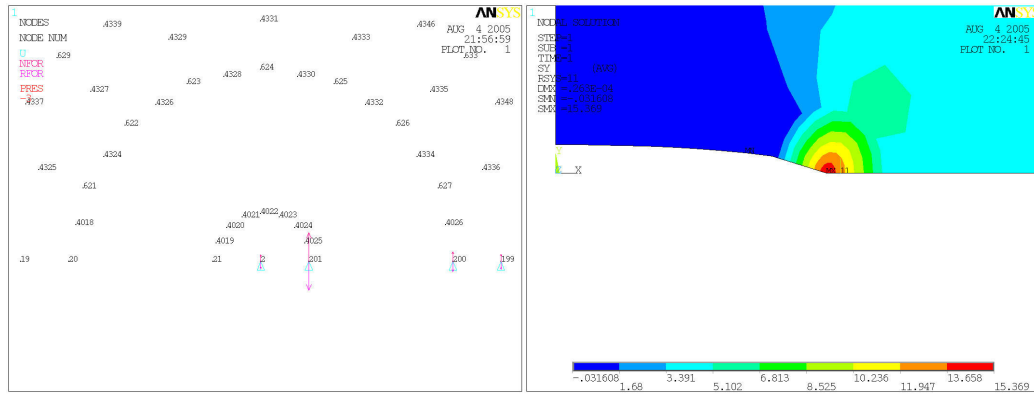


Fig. 7.19. Nodes and stress details around 2D crack tip

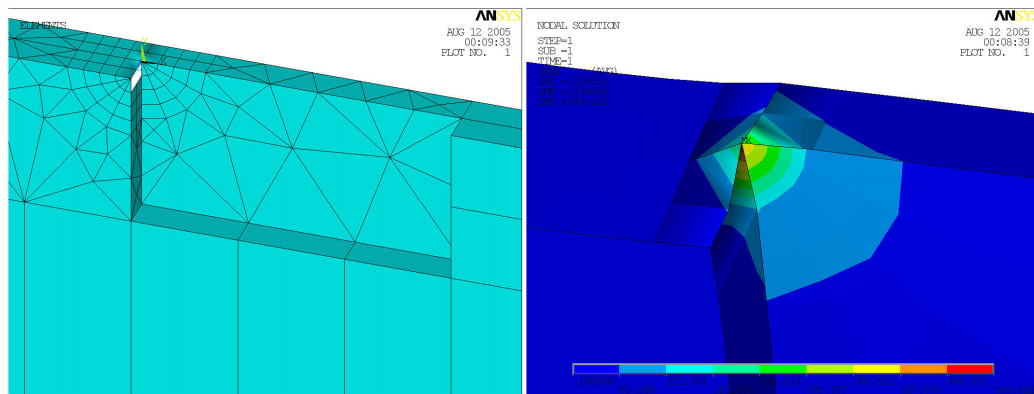


Fig. 7.20. Mesh details and stress details around 3D crack tip

The finite element modelling and calculation of stress intensity factor (K) are not an easy task for researchers and engineers who have not enough experience. As discussed in Section 5.5 in Chapter 5, creating a macro and using ANSYS Parametric Design Language (APDL) enables us to create our own custom ANSYS command, automate common tasks or even build our model in terms of parameters (variables) and more importantly reduce the time for building a model dramatically. In this studies, two(2) useful ANSYS macro programs have been created to reduce computational time and finite element modelling efforts and to calculate stress intensity factor (K) for 2 dimensional centre cracked plate modelling. The one is for automatic creation of geometry, mesh details, symmetric boundary condition and applying loads by simply input eight parameters which are material yield stress (arg1), half of crack length (arg2), half of plate breadth (arg3), half of plate length (arg4), number of mesh on cracked line (arg5) and uncracked line (arg6), the radius of the first row of elements around the crack tip (arg7) and maximum applied load (arg8). The other is for automatic calculation of stress intensity factor (K) for centre cracked plate by simply input six parameters which are crack tip node number (arg1), second node number for crack path (arg2), third node number for crack path (arg3), fourth (arg4), fifth (arg5) and sixth (arg6) node number to define crack tip coordinate system.

The developed macro program for automatic calculation of stress intensity factor (K) can be applied and extended to any other structural crack problems. The typical examples of *ANSYS* macro programs to create finite element model and to calculate stress intensity factor (K) are introduced in Appendix G and Fig. 7.21.

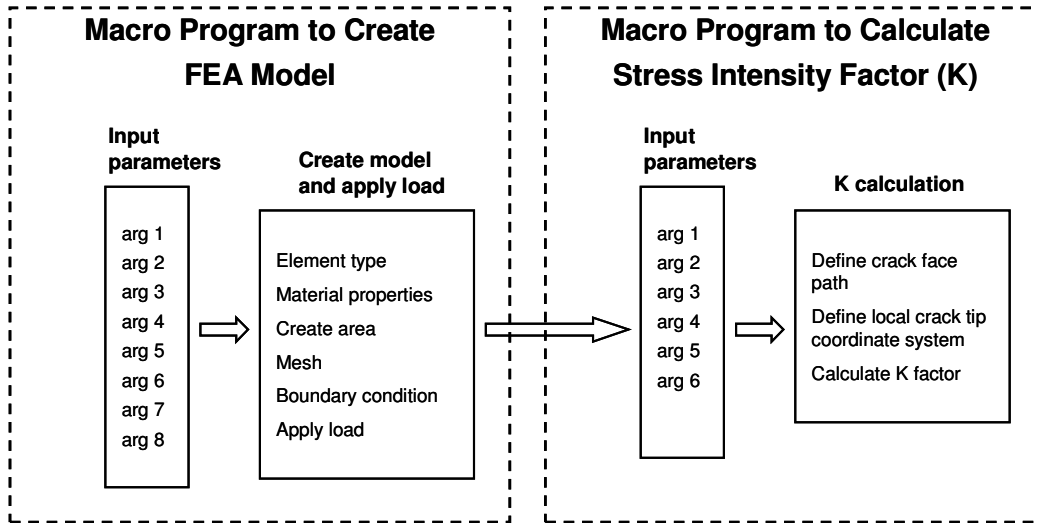


Fig. 7.21. Typical procedure of macro program for K calculation

7.12.1.3 Computation of J integral theory

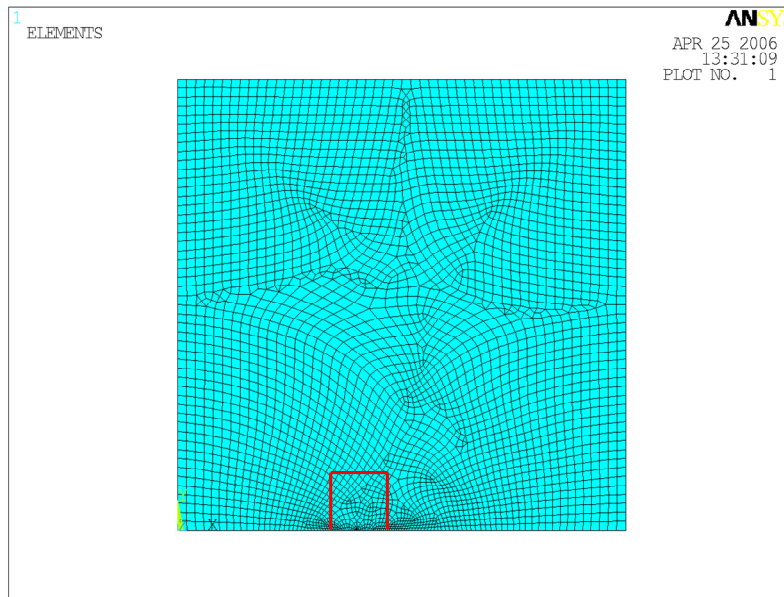


Fig. 7.22. J integral path based on 4 nodes

As defined in previous sections, the J -integral is a path independent line integral that measures the strength of the singular stresses and strains near the crack tip. In *ANSYS*, the computation of J value is much more complicated than the calculation of stress intensity factor (K) and J cannot compute directly by post processor commands. Thus

it is necessary to develop a macro by using the ANSYS Parametric Design Language (APDL), a scripting language that user can use to automate common tasks or even build model in terms of parameters (variables). But the procedure and the creation of macro program to calculate J-integral value is not an easy task for most of users. In this study, the source code for the J computation macro, which is based on 4 nodes path as illustrated in Fig.7.22, is developed. By using this program, the J computational value can be obtained in just two steps. The first step is to read in the desired set of results and define a path for the line integral (4 node path). The second step is to input a macro file name into input (command) menu.

The developed macro program for J computation can be applied and extended to any other structural crack problems. The typical procedure, which is combined with macro program to create finite element model, is illustrated in Fig. 7.23.

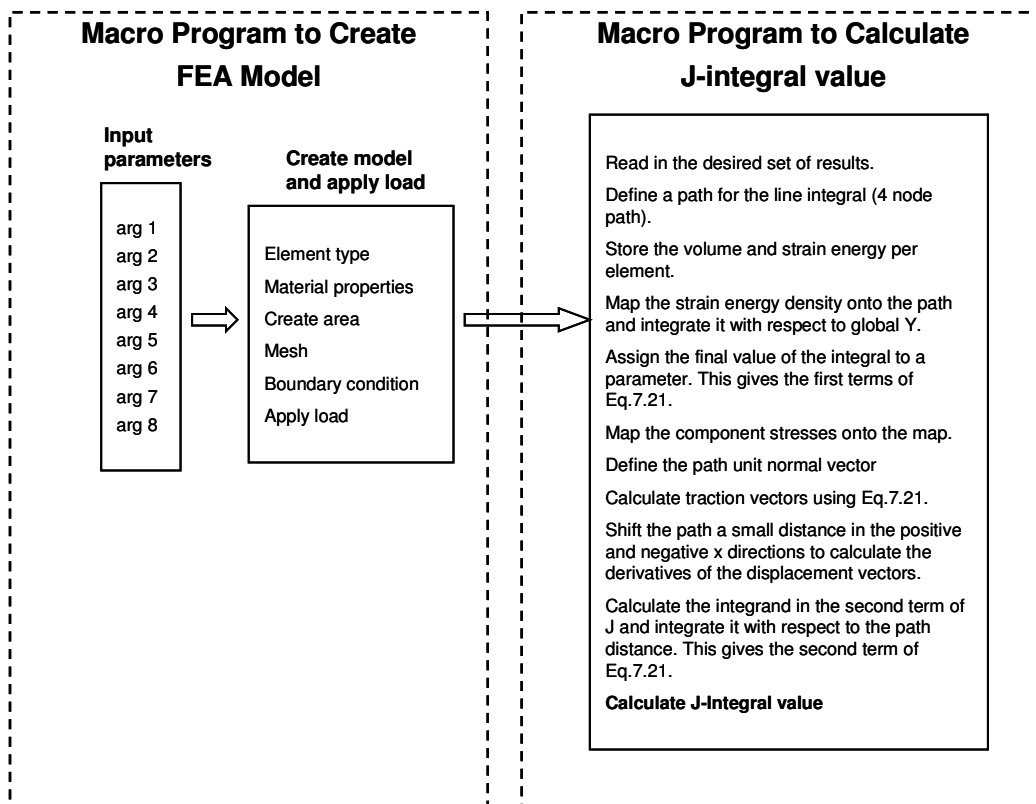


Fig. 7.23. Typical procedure of macro program for J computation

7.12.1.4 Computation of crack tip opening displacement (CTOD)

An alternative method to calculate strain energy rate G or J is to measure crack tip opening displacement (CTOD) as discussed in Section 7.5.1. The fracture would initiate when the strains in the crack-tip region reach a critical value, which can be characterized by a critical crack-tip opening displacement. In this study this

alternative method was also employed and the CTOD value is measured at 0.75mm from crack tip front.

7.12.2 Modelling results by LEFM

The procedure of evaluation and comparison of the results of finite element analyses with existing formulae, which are based on experimentation, is a very important step to validate the FEA results. In order to verify the correctness of FEA control and the results, some existing handbook formulae, which were proposed by *Broek* [48], *Tada et al.* [60] and *Isida* [62], are compared with K calculation results by ANSYS finite element analyses as shown in Table 7-1 and Fig. 7.24 for centre crack. A total of 250 cases of stress intensity factors are shown in Table 7-1, in which the centre crack size varies from 50mm to 400mm. Of these cases, 100 of them (50 cases are plain strain basis and another 50 cases are plain stress basis) have been performed to validate the accuracy of stress intensity factor from finite element analyses. Fig. 7.25 illustrates the von Mises stress distribution with 200mm centre crack length under 30 N/mm^2 tensile load. The results indicate that the Broek et al.'s formula produces the highest K values, and the K calculation by ANSYS program (plane strain) can predict stress intensity factor quite well and can be assumed as an average value of existing handbook solutions.

Table 7-1
Comparison of K calculation for plate with centre crack

σ (MPa)	2a/W	Stress Intensity Factor ($K = \text{MPa m}^{1/2}$)				
		Broek	Tada	Isida	ANSYS (P. strain)	ANSYS (P. stress)
10	0.05	2.83	2.81	2.82	2.82	2.56
20	0.05	5.67	5.61	5.64	5.64	5.13
30	0.05	8.50	8.42	8.47	8.48	7.70
40	0.05	11.34	11.23	11.29	11.28	10.27
50	0.05	14.17	14.03	14.11	14.10	12.83
60	0.05	17.01	16.84	16.93	16.92	15.40
70	0.05	19.84	19.65	19.75	19.74	17.97
80	0.05	22.68	22.45	22.58	22.56	20.53
90	0.05	25.51	25.26	25.40	25.38	23.09
100	0.05	28.35	28.07	28.22	28.20	25.67
10	0.10	4.07	3.99	3.99	4.03	3.67
20	0.10	8.13	7.97	7.98	8.06	7.33
30	0.10	12.20	11.96	11.97	12.08	11.00
40	0.10	16.27	15.95	15.96	16.11	14.66
50	0.10	20.34	19.93	19.96	20.14	18.33
60	0.10	24.40	23.92	23.95	24.17	21.99
70	0.10	28.47	27.91	27.94	28.20	25.66
80	0.10	32.54	31.90	31.93	32.22	29.32
90	0.10	36.61	35.88	35.92	36.25	32.99
100	0.10	40.67	39.87	39.91	40.28	36.65
10	0.20	6.18	5.74	5.64	5.93	5.39
20	0.20	12.36	11.48	11.29	11.86	10.79
30	0.20	18.54	17.23	16.93	17.78	16.18
40	0.20	24.72	22.97	22.58	23.71	21.58
50	0.20	30.90	28.71	28.22	29.64	28.97
60	0.20	37.08	34.45	33.86	35.56	32.38
70	0.20	43.26	40.19	39.51	41.49	37.76

80	0.20	49.45	45.94	45.15	47.42	43.15
90	0.20	55.63	51.68	50.80	53.34	48.54
100	0.20	61.81	57.42	56.44	59.27	53.93
10	0.30	8.94	7.26	6.91	7.73	7.03
20	0.30	17.88	14.52	13.83	15.45	14.06
30	0.30	26.82	21.78	20.74	23.18	21.09
40	0.30	35.77	29.04	27.65	30.90	28.12
50	0.30	44.71	36.30	34.56	38.63	35.15
60	0.30	53.65	43.56	41.48	46.35	42.18
70	0.30	62.59	50.82	48.39	54.07	49.21
80	0.30	71.53	58.08	55.30	61.80	56.23
90	0.30	80.47	65.34	62.21	69.52	63.26
100	0.30	89.41	72.59	69.13	77.24	70.29
10	0.40	13.47	8.79	7.98	9.66	8.79
20	0.40	26.93	17.58	15.96	19.32	17.58
30	0.40	40.40	26.37	23.95	28.97	26.37
40	0.40	53.86	35.16	31.93	38.63	35.15
50	0.40	67.33	43.95	39.91	48.28	43.94
60	0.40	80.80	52.75	47.89	57.94	52.72
70	0.40	94.26	61.54	55.87	67.59	61.51
80	0.40	107.73	70.33	63.86	77.24	70.29
90	0.40	121.20	79.12	71.84	86.90	79.07
100	0.40	134.66	87.91	79.82	96.55	87.86

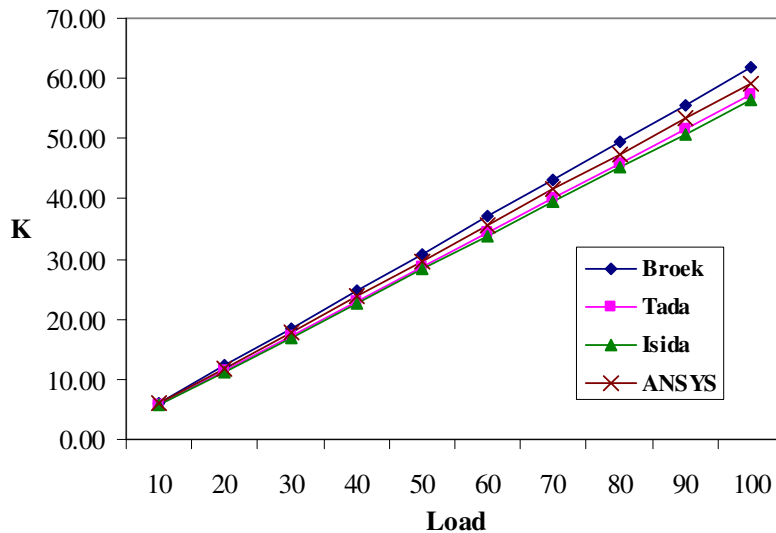


Fig. 7.24. K (Plain strain) values against different loads ($2a/W=0.2$)

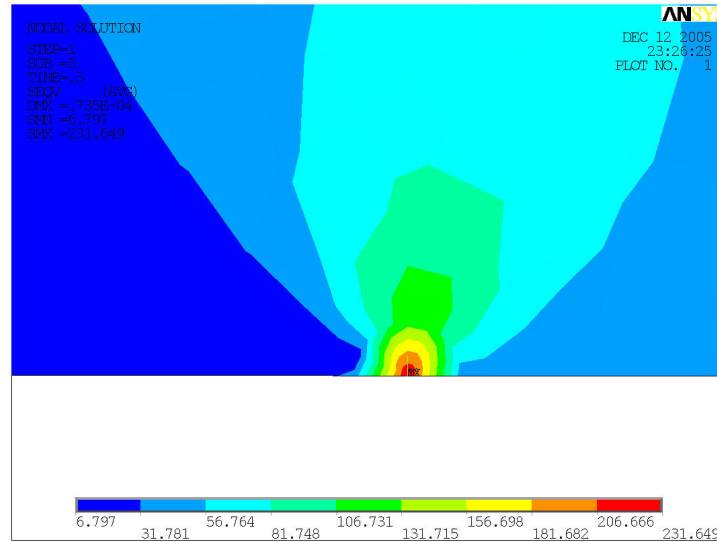


Fig. 7.25. The *von Mises* stress distribution near the crack tip ($2a=200\text{mm}$, $\sigma = 30 \text{ N/mm}^2$)

Table 7-2 indicates the comparison of K calculation for plate with a single edge crack based on formula from *Broek* [48], *Tada et al.* [60] and *Brown and Srawley* [63]. The results indicate that the stress intensity factors (K) from all the formulae are more or less the same, thus all of these formulae can be considered reliable to calculate stress intensity factors for plate with a single edge crack

Table 7-2

Comparison of K calculation for plate with single edge crack

σ (MPa)	$2a/W$	Stress Intensity Factor ($K = \text{MPa m}^{1/2}$)		
		Broek	Tada	Brown
10	0.05	3.14	3.15	3.14
20	0.05	6.28	6.29	6.28
30	0.05	9.42	9.44	9.42
40	0.05	12.56	12.58	12.56
50	0.05	15.70	15.73	15.70
60	0.05	18.84	18.87	18.84
70	0.05	21.98	22.02	21.96
80	0.05	25.12	25.17	25.12
90	0.05	28.26	28.31	28.26
100	0.05	31.40	31.46	31.40
10	0.10	4.49	4.50	4.49
20	0.10	8.98	8.99	8.98
30	0.10	13.46	13.49	13.46
40	0.10	17.95	17.98	17.95
50	0.10	22.44	22.48	22.44
60	0.10	26.93	26.97	26.93
70	0.10	31.42	31.47	31.41
80	0.10	35.90	35.96	35.90
90	0.10	40.39	40.46	40.39
100	0.10	44.88	44.96	44.88

10	0.20	6.64	6.65	6.63
20	0.20	13.27	13.29	13.27
30	0.20	19.91	19.94	19.90
40	0.20	26.54	26.58	26.54
50	0.20	33.18	33.23	33.17
60	0.20	39.81	39.88	39.81
70	0.20	46.45	46.52	46.44
80	0.20	53.09	53.17	53.08
90	0.20	59.72	59.81	59.71
100	0.20	66.36	66.46	66.35
10	0.30	8.68	8.70	8.68
20	0.30	17.37	17.39	17.36
30	0.30	26.05	26.09	26.05
40	0.30	34.74	34.79	34.73
50	0.30	43.42	43.48	43.41
60	0.30	52.11	52.18	52.09
70	0.30	60.79	60.87	60.78
80	0.30	69.48	69.57	69.46
90	0.30	78.16	78.27	78.14
100	0.30	86.85	86.96	86.82
10	0.40	10.87	10.88	10.86
20	0.40	21.74	21.76	21.73
30	0.40	32.61	32.64	32.59
40	0.40	43.47	43.52	43.46
50	0.40	54.34	54.41	54.32
60	0.40	65.21	65.29	65.19
70	0.40	76.08	76.17	76.05
80	0.40	86.95	87.05	86.92
90	0.40	97.82	97.93	97.78
100	0.40	108.68	108.81	108.65

7.12.3 Modelling results by EPFM

As previously specified, if fracture is accompanied by considerable plastic deformation near the crack tip, *elastic-plastic fracture mechanics (EPFM)* is used.

In this section, *J-integral* and *crack tip opening displacement (CTOD)* are investigated based on each of three different material properties which has a yield stress of 235 N/mm^2 , 315 N/mm^2 and 355 N/mm^2 .

Table 7-3 summarized the *J-integral* and *crack tip opening displacement (CTOD)* values based on ANSYS fracture modelling for a centre cracked plate under uniform tensile loads. Large scales of finite element modelling have been carried out in order to find out the effects of different material yield stresses, crack sizes and applied loads on J and CTOD values. J and CTOD values of a total of 300 cases have been calculated based on finite element modelling results, and are shown in Table 7-3, in which the centre crack size varies from 50mm to 400mm and the applied tensile stress (σ) ranges from 10 N/mm^2 to 100 N/mm^2 .

The comparisons between *Irwin's* plastic zone correction based on *Mode I* loading, which is introduced in Section 7.5.2 and current finite element fracture modelling results have been summarized in Appendix H. In Appendix H, the *J-integral* and *CTOD* value are converted to relevant *K* values in plane strain in accordance with Eq.7.20 and Eq.7.23.

Table 7-3
J-integral and crack tip opening displacement (CTOD) values

σ (MPa)	2a/W	SY235 (J) KJ/m ²	SY235 (CTOD) m	SY315 (J) KJ/m ²	SY315 (CTOD) m	SY355 (J) KJ/m ²	SY355 (CTOD) m
10	0.05	0.03433	0.0000106	0.03430	0.0000106	0.03431	0.0000106
20	0.05	0.13732	0.0000213	0.13722	0.0000212	0.13722	0.0000212
30	0.05	0.30897	0.0000319	0.30874	0.0000319	0.30875	0.0000319
40	0.05	0.54942	0.0000428	0.54887	0.0000425	0.54887	0.0000425
50	0.05	0.86007	0.0000558	0.85760	0.0000532	0.85760	0.0000532
60	0.05	1.24082	0.0000699	1.23640	0.0000656	1.23522	0.0000642
70	0.05	1.69141	0.0000842	1.68531	0.0000791	1.68337	0.0000771
80	0.05	2.21467	0.0001003	2.20410	0.0000932	2.20151	0.0000907
90	0.05	2.81665	0.0001202	2.79269	0.0001074	2.78945	0.0001048
100	0.05	3.49648	0.0001419	3.45141	0.0001221	3.44723	0.0001190
10	0.10	0.07073	0.0000152	0.07073	0.0000152	0.07073	0.0000152
20	0.10	0.28292	0.0000305	0.28292	0.0000305	0.28293	0.0000305
30	0.10	0.63675	0.0000463	0.63656	0.0000457	0.63657	0.0000457
40	0.10	1.13359	0.0000654	1.13194	0.0000617	1.13164	0.0000610
50	0.10	1.77328	0.0000857	1.77053	0.0000806	1.76943	0.0000786
60	0.10	2.55748	0.0001083	2.55200	0.0001006	2.55041	0.0000981
70	0.10	3.49228	0.0001367	3.47637	0.0001213	3.47410	0.0001182
80	0.10	4.57841	0.0001685	4.54624	0.0001442	4.54081	0.0001390
90	0.10	5.82376	0.0002057	5.76702	0.0001718	5.75351	0.0001621
100	0.10	7.23351	0.0002479	7.13786	0.0002020	7.11746	0.0001896
10	0.20	0.15340	0.0000225	0.15340	0.0000225	0.15341	0.0000225
20	0.20	0.61366	0.0000452	0.61361	0.0000450	0.61361	0.0000450
30	0.20	1.38230	0.0000736	1.38106	0.0000691	1.38068	0.0000678
40	0.20	2.45966	0.0001043	2.45731	0.0000980	2.45643	0.0000956
50	0.20	3.85222	0.0001441	3.84215	0.0001284	3.84061	0.0001249
60	0.20	5.56422	0.0001916	5.53952	0.0001638	5.53375	0.0001562
70	0.20	7.60414	0.0002479	7.55440	0.0002062	7.54272	0.0001943
80	0.20	9.98690	0.0003150	9.89016	0.0002544	9.86864	0.0002374
90	0.20	12.7298	0.0003935	12.5539	0.0003094	12.5163	0.0002858
100	0.20	15.8600	0.0004848	15.5460	0.0003716	15.4920	0.0003403
10	0.30	0.26056	0.0000293	0.26056	0.0000293	0.26057	0.0000293
20	0.30	1.04286	0.0000618	1.04226	0.0000587	1.04224	0.0000586
30	0.30	2.34877	0.0001013	2.34706	0.0000952	2.34638	0.0000928
40	0.30	4.18470	0.0001521	4.17538	0.0001348	4.17411	0.0001314
50	0.30	6.55995	0.0002163	6.53358	0.0001835	6.52691	0.0001738
60	0.30	9.48887	0.0002953	9.42838	0.0002424	9.41420	0.0002272
70	0.30	12.9962	0.0003914	12.8678	0.0003113	12.8390	0.0002884
80	0.30	17.11948	0.0005070	16.8651	0.0003918	16.8114	0.0003590
90	0.30	21.91526	0.0006457	21.4408	0.0004853	21.3430	0.0004401
100	0.30	27.46664	0.0008115	26.6169	0.0005921	26.4520	0.0005325
10	0.40	0.408090	0.0000367	0.40809	0.0000367	0.40809	0.0000367
20	0.40	1.633947	0.0000810	1.63289	0.0000760	1.63254	0.0000744
30	0.40	3.682490	0.0001374	3.67724	0.0001246	3.67622	0.0001213

40	0.40	6.568337	0.00002145	6.54616	0.00001826	6.54042	0.00001732
50	0.40	10.31335	0.00003141	10.2521	0.00002568	10.2377	0.00002403
60	0.40	14.95615	0.00004390	14.8084	0.00003466	14.7759	0.00003199
70	0.40	20.56088	0.00005935	20.2413	0.00004550	20.1707	0.00004143
80	0.40	27.22966	0.00007840	26.5792	0.00005817	26.4487	0.00005256
90	0.40	35.13470	0.00010179	33.8775	0.00007310	33.6350	0.00006532
100	0.40	44.56900	0.00013098	42.2010	0.00009057	41.7802	0.00008007

Figs. 7.26 to 7.28 and Figs. 7.29 to 7.31 illustrate the *J-Integral* and crack tip opening displacement (CTOD) values based on different material yield stresses, crack sizes, and applied loads.

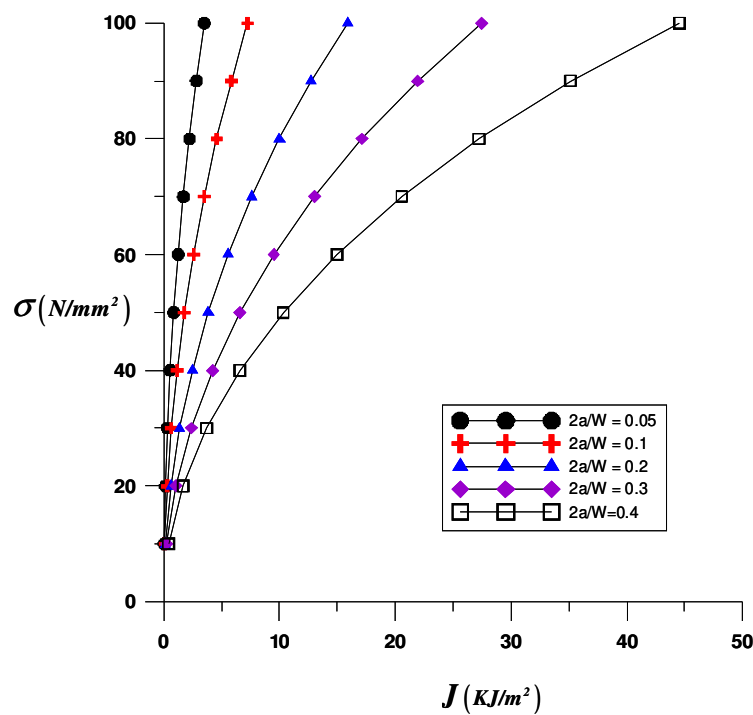


Fig. 7.26. *J-Integral* values with different crack sizes and loads ($\sigma_y = 235 \text{ N/mm}^2$)

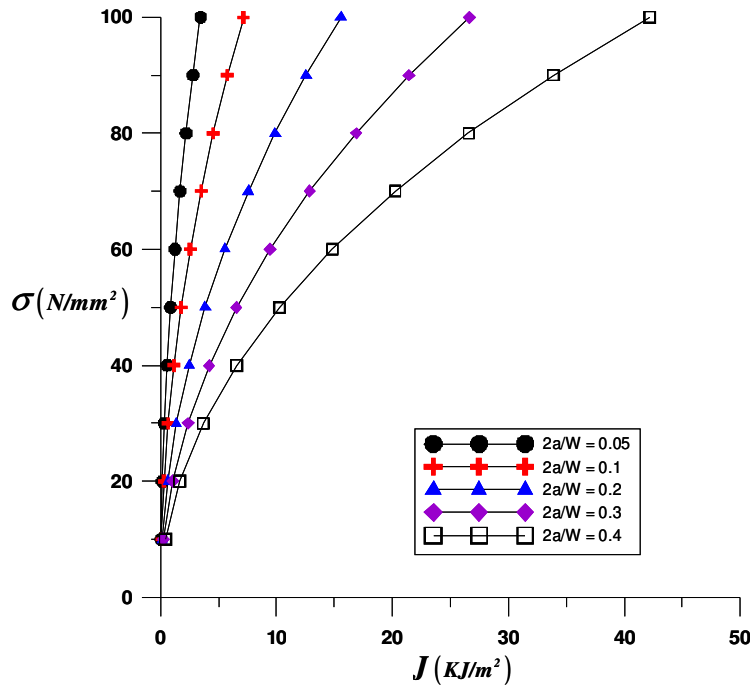


Fig. 7.27. *J-Integral* values with different crack size and loads ($\sigma_y = 315 \text{ N/mm}^2$)

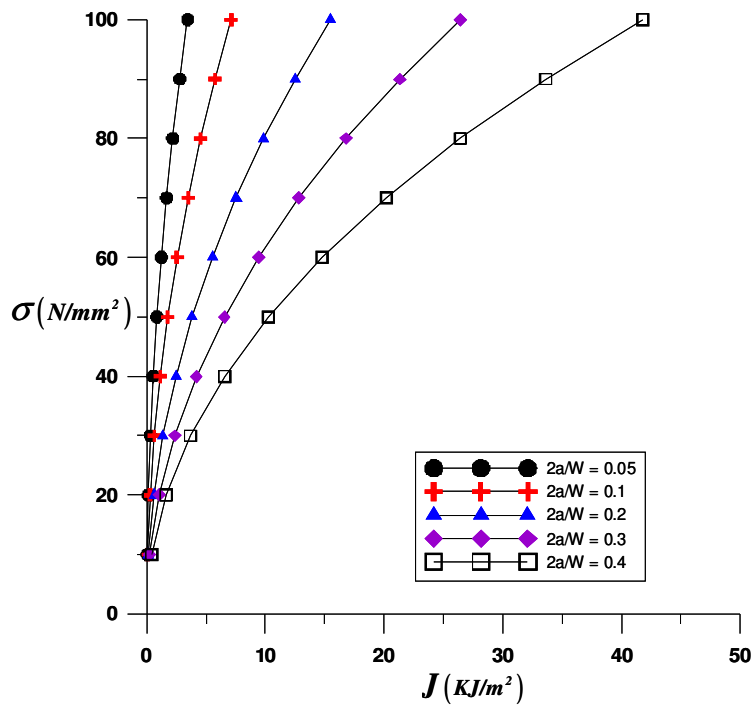


Fig. 7.28. *J-Integral* values with different crack size and loads ($\sigma_y = 355 \text{ N/mm}^2$)

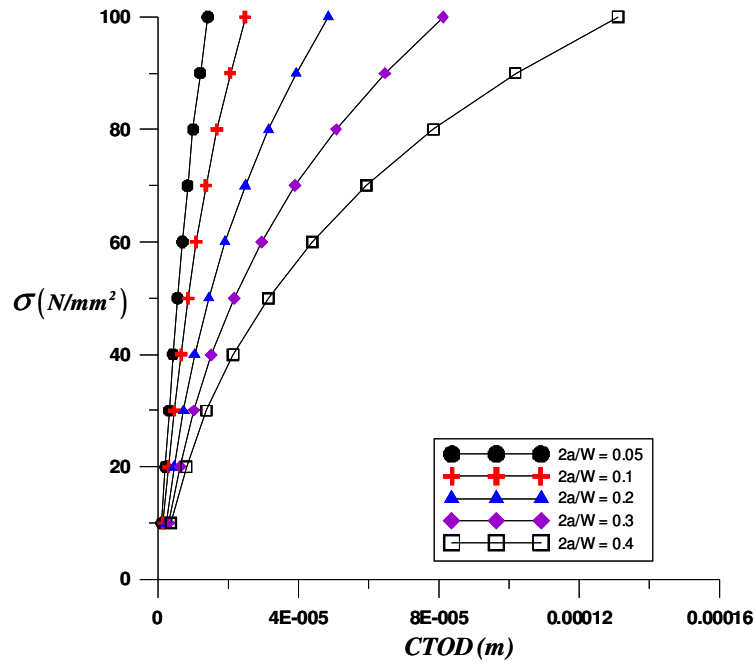


Fig. 7.29. CTOD values with different crack size and loads ($\sigma_y = 235$ N/mm²)

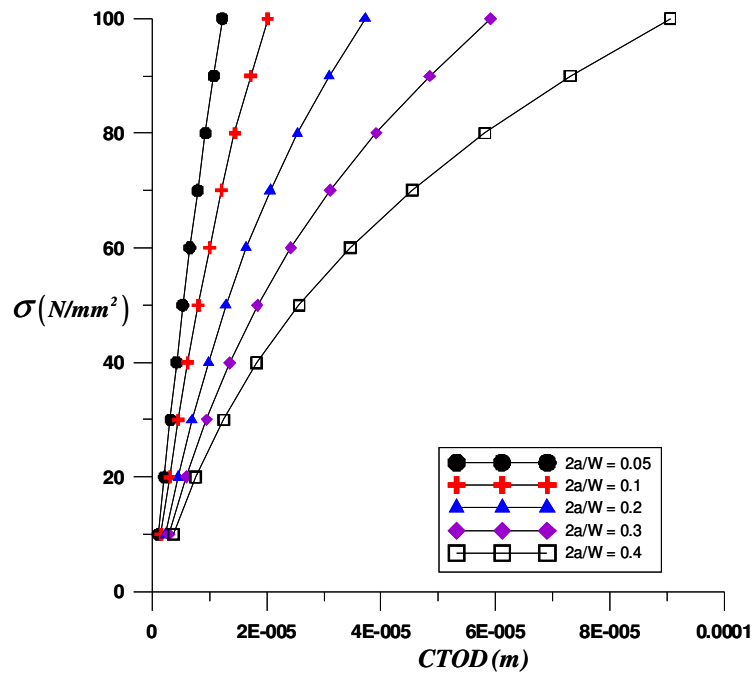


Fig. 7.30. CTOD values with different crack size and loads ($\sigma_y = 315$ N/mm²)

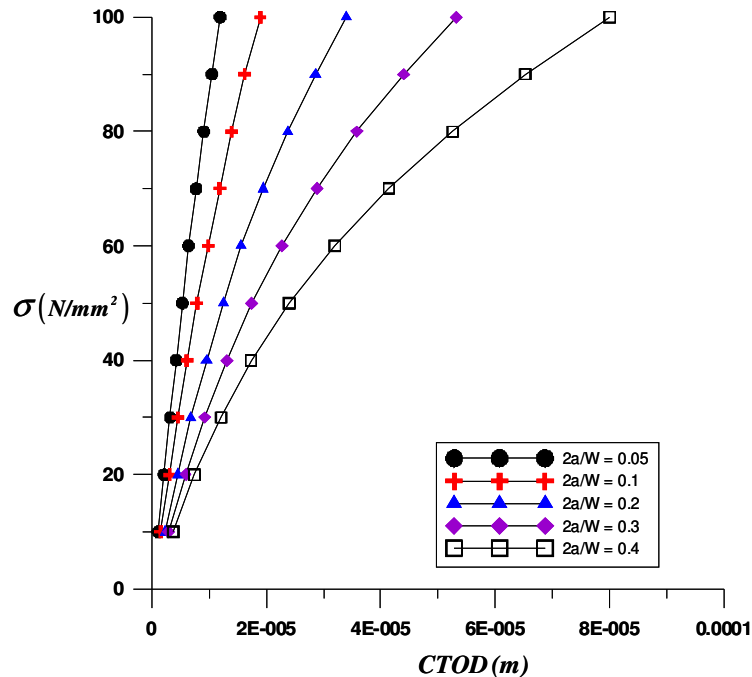


Fig. 7.31. CTOD values with different crack size and loads ($\sigma_y = 355 \text{ N/mm}^2$)

The results of *elastic-plastic fracture mechanics* methods are summarized in Section 7.13.

7.13 Concluding remarks

In this chapter historical background of fracture mechanic methods and current research activities in marine and offshore fields have been reviewed. Classical theory of the *linear elastic fracture mechanics (LEFM)* approach and the *elastic plastic fracture mechanics (EPFM)* approaches, which is based on *crack tip displacement method* and *J-integral method*, have been discussed. In addition, the general concept of crack propagation, prediction of crack propagation and fracture control and inspection have also been investigated.

Among others, the concept of the *linear elastic fracture mechanics (LEFM)* approach based on stress intensity factor (K) and the *elastic plastic fracture mechanics (EPFM)* approaches which are based on *crack tip displacement method* and *J-integral method* are applied to numerical computation for two-dimensional fracture problems in Section 7.12. The effects of crack size, loads and material properties on stress intensity factors, *J-Integral* and *crack tip opening displacement (CTOD)* values have been investigated through 100 cases of finite element analyses for *LEFM* approach and another 300 cases of finite element analyses for *EPFM* approach. The results can be summarized as follows:

- In this study, two(2) useful ANSYS macro programs have been created to reduce computational time and finite element modelling efforts and to calculate stress intensity factor (K) for 2 dimensional centre cracked plate modelling. One of them is for automatic creation of geometry, mesh details,

symmetric boundary conditions and applying loads by simply input eight parameters. The other is for automatic calculation of stress intensity factor (K) for centre cracked plate by simply input six parameters. The developed macro program for automatic calculation of stress intensity factor (K) can be applied and extended to any other structural crack problems.

- The computation of J value is much more complicated than the calculation of stress intensity factor (K). It cannot be computed directly by post processor commands of most of finite element programs. Thus it is necessary to develop a macro by using the ANSYS Parametric Design Language (APDL), a scripting language that can be used to automate common tasks or even to build models in terms of parameters (variables). But the procedure and the creation of a macro program to calculate J-integral value is not an easy task for most of user. In this study, the source code for the J computation macro, which is based on 4 nodes path as illustrated in Fig.7.22, is developed. By using this program, J value can be obtained in just two steps. The first step is to read in the desired set of results and define a path for the line integral (4 node path). The second step is to input a macro file name into input (command) menu. The developed macro program for J computation can be applied and extended to any other structural crack problems.
- Comparisons between the existing analytical formulae for *stress intensity factor (K)* of a centre cracked plate and ANSYS fracture finite element modelling results indicate that finite element modelling can predict stress intensity factor accurately. This means that finite element modelling can replace expensive actual test to find fracture toughness of various materials, so leads to save time, efforts and cost of actual test.
- Among the investigated analytical formulae, Broek's formulae gives the highest stress intensity factor (K). Whereas ANSYS finite element modelling results based on plane strain are about the average value of the existing formulae.
- If fracture is accompanied by considerable plastic deformation near the crack tip, then the elastic-plastic fracture mechanics method is recommended. In this Chapter, J-Integral and CTOD of three different material properties, namely a yield stress of 235 N/mm^2 , 315 N/mm^2 , 355 N/mm^2 , have been evaluated. The Higher yield strength of material shows smaller *J-Integral value* and *crack tip opening displacement (CTOD)* value than lower yield strength material. This is because the crack tip of lower yield strength material, such as mild steel, tends to yield earlier and have more plastic deformation around the crack tip than higher yield strength of material under same crack size and applied stress.
- The differences of *J-integral* values between mild steel and higher yield strength material are quite small, thus if the cracked structure has a mixed material properties then it is recommended to use lower yield stress material for finite element modelling in order to get more conservative *J* or *CTOD* values.
- If the crack size ($2a/W$) is as small as 0.05 and 0.1, the changing of *J* or *CTOD* values versus applied stress shows linear pattern and *J* and *CTOD* values are expected quite small. However if the crack size ($2a/W$) is larger than 0.2, the changing of *J* or *CTOD* values versus applied loads shows nonlinear pattern

and J and $CTOD$ values are to be steeply increased as increasing crack size, which is illustrated in Figs. 7.26 to 7.31.

- As indicated in Appendix H, the calculated J -integral values based on finite element modelling show slightly higher stress intensity factors than the Irwin's plastic zone correction based calculations.
- The calculated $CTOD$ values which is converted to stress intensity factors as indicated in Appendix H show large differences from J -integral based computation or the Irwin's plastic zone correction based calculations. Generally $CTOD$ obtained by finite element analyses shows higher stress intensity factor than handbook solutions at small crack size with small applied stresses ranges. But it shows less stress intensity factor at relatively large crack size and large applied stress ranges.

Pits and flaws near the crack tip will accelerate the crack propagation and tend to increase stress intensity factor. It is worth to investigate the effects of localized corrosion with different sizes and depths near the crack tip on stress intensity factor by using 3D finite element modelling.

There are two types of residual stresses exist in ship structures. The one is mechanical residual stress which is introduced through fabrication procedure, the other is welding induced residual stress. Welding residual stress is caused by the heat induced welding processes. The heat input through the welding processes to the plate gives a great influence of residual stresses in the plate and crack propagation. It is recommended to study the effects of heat induced welding process on the stress intensity factor, J -integral value and $CTOD$ value based on different material properties and on various structural details.

The optimum fracture control and maintenance plan depend on the consequence of a fracture and the time of crack initiation. In connection with the fatigue life assessment and methodologies which are described in Chapter 4, further research activities are recommended which consider both the first principle based spectral fatigue assessment methodology and elastic plastic fracture mechanics methodology based on different ship types and various structural details in order to establish the optimum fracture control plan, maintenance plan and reliability level of ageing ships.

In connection to Chapter 3, 4 and 5, it is also recommended to develop the methodology for the time-variant reliability assessment considering the effect of corrosion degradation and fatigue crack propagation on ultimate strength reduction in time dependent manner in order to justify the residual strength, to establish reliability and to develop the proper maintenance programme for ageing ship structures.

References (Chapter 7)

1. Ok, D. and Y. Pu. *Time-variant corrosion degradation, hull girder strength and fatigue assessment for ageing double hull tanker*. in *The 15th International Offshore and Polar Engineering Conference*. 2005. Seoul, Korea.
2. Ok, D. and Y. Pu, *Fatigue assessment for ageing double hull tanker*. 2005, MARSTRUCT EU Project (Project No. FP6-PLT-506141) Report MAR-W2-4-UNEW-2(1).
3. Garbatov, Y., et al., *Modeling Strength Degradation Phenomena*. 2005, MARSTRUCT EU Project (Project No. FP6-PLT-506141) Report MAR-R6-3-1-IST-1.
4. Garbatov, Y., et al. *Modelling Strength Degradation Phenomena and Inspections used for Reliability Assessment based Maintenance Planning*. in *The 25th International Conference on Offshore Mechanics and Arctic Engineering*. Hamburg, German, 4-9 June, 2006.
5. Dexter, R.J. and H.N. Mahmoud, *Predicting stable fatigue crack propagation in stiffened panels*. Ship Structure Committee, SSC-435, 2004.
6. Griffith, A.A., *The Phenomena of Rupture and Flaw in Solids*. Philosophical Transactions, Series A, 221, 1920: p. 163-198.
7. Irwin, G.R., *Fracture Dynamics*. In *Fracturing of Metals*. America Society of Metals, 1948: p. 147-166.
8. Orowan, E., *Fracture Strength of Solids*. In *report on Progress in Physics*. Physical Society of London, 1949. **Vol. 12**.
9. Irwin, G.R., *Onset of fast crack propagation in high strength steel and aluminum alloys*. Singapore Research Conference Proceedings, 1956. **2**: p. 289-305.
10. Westergaard, H.M., *Bearing pressures and cracks*. Transactions, ASME, Journal of Applied Mechanics, 1939: p. 6:49-53.
11. Irwin, G.R., *Analysis of Stresses and Strains Near the End of a Crack Transversing a Plate*. Transactions, ASME, Journal of Applied Mechanics, 1957. **Vol.24**: p. 361-364.
12. Poe, C.C., *"Fatigue crack propagation in stiffened panels"*, *Damage Tolerance in Aircraft Structures, ASTM STP 486*. American Society for Testing and Materials, 1971: p. 79-97.
13. Thayamballi, A.K., *Reliability of ship hull in the fracture and fatigue modes of failure*, in *Ph.D dissertation in engineering*. 1983, University of California.
14. Petershagen, H. and W. Fricke., *Fatigue crack propagation in plate panels with welded stiffeners*. IIW-Doc. XIII -1272-88, Technical University of Hamburg, 1988.
15. Anderson, T.L., *Elastic-plastic fracture mechanics*. Ship Structure Committee, SSC-345, 1990.
16. Sumpter, J.D.G., et al., *Fracture toughness of ship steels*. Royal Institution of Naval Architects, 1989. **131**: p. 169-186.
17. Sumpter, J.D.G. and A.J. Caudrey, *Recommended fracture toughness for ship hull steel and weld*. Marine Structures, 1995. **8**(4): p. 345-357.

18. Clarke, J.D., *Fatigue crack initiation and propagation in warship hulls*, in *Advances in Marine Structures-2*, C.S. Smith and R.S. Dow, Editors. 1991, Elsevier Science Publishers LTD.
19. Boukerrou, A. and R.A. Cottis, *Crack initiation in the corrosion fatigue of structural steels in salt solutions*. Corrosion Science, 1993. **35**(1-4 SU -): p. 577-585.
20. Tomita, Y., M. Matobat, and H. Kawabel, *Fatigue crack growth behavior under random loading model simulating real encountered wave condition*. Marine Structures, 1995. **8**(4): p. 407-422.
21. Xu, T. and R. Bea, *Load shedding of fatigue fracture in ship structures*. Marine Structures, 1997. **10**(1): p. 49-80.
22. Rokhlin, S.I., et al., *Effect of pitting corrosion on fatigue crack initiation and fatigue life*. Engineering Fracture Mechanics, 1999. **62**(4-5 SU -): p. 425-444.
23. Wistance, W., P.H. Pumpherey, and D.J. Howarth, *Materials qualification for the shipbuilding industry*. Charpy Centenary Conference, Poitiers, France, 2001.
24. Akpan, U.O., et al., *Risk assessment of aging ship hull structures in the presence of corrosion and fatigue*. Marine Structures, 2002. **15**(3): p. 211-231.
25. Dobson, W.G., et al., *Fatigue considerations in view of measured load spectra*. SSC-315, 1983.
26. Dexter, R.J. and P.J. Pilarski, *Crack propagation in welded stiffened panels*. Journal of Constructional Steel Research, 2002. **58**(5-8): p. 1081-1102.
27. Dexter, R.J., P.J. Pilarski, and H.N. Mahmoud, *Analysis of crack propagation in welded stiffened panels*. International Journal of Fatigue, 2003. **25**(9-11): p. 1169-1174.
28. British Standards Institute, *Guide on methods for assessing the acceptability of flaws in metallic structures*. BS 7910, 1999.
29. Garbatov, Y. and C. Guedes Soares, *Influence of steel strength on the fatigue reliability of welded structural components*. International Journal of Fatigue, 2004. **26**(7): p. 753-762.
30. Brossman, M.W. and J.A. Kies, *Energy release rates during fracturing of perforated plates*. Ship Structural Committee, SSC-98, 1955.
31. Dexter, R., J.Gentilcore, M. L, *Evaluation of ductile fracture models for ship structural details*. Ship Structural Committee, SSC-393, 1997.
32. Dinovitzer, A.S. and N. Pussegoda, *Fracture toughness of a ship structure*. Ship Structure Committee, SSC-430, 2003.
33. Francis, P.H., T.S. Cook, and A. Nagy, *Fracture behaviour characterization of ship steels and weldments*. Ship Structural Committee, SSC-276, 1978.
34. Glen, I.F., et al., *Fatigue resistant detail design guide for ship structures*. Ship Structure Committee, SSC-405, 1999.
35. Glen, I.F., et al., *Guide to damage tolerance analysis of marine structures*. Ship Structural Committee, SSC-409, 1999.
36. Hahn, G.T., R.G. Hoagland, and A.R. Resenfield, *Dynamic crack propagation and arrest in structural steels*. Ship Structural Committee, SSC-256, 1976.
37. Hawthorne, J.R. and F.J. Loss, *Fracture toughness characterization of shipbuilding steels*. Ship Structural Committee, SSC-248, 1975.
38. Kanninen, M., et al., *A Study of ship hull crack arrester systems*. Ship Structural Committee, SSC-265, 1977.

39. Kaufman, J.G. and M. Prager, *Marine structural steel toughness data bank*. Ship Structure Committee, SSC-352, 1991.
40. Mansour, A., et al., *Probability based ship design: Implementation of design guidelines*. Ship Structural Committee, SSC-392, 1996.
41. Pense, A.W., *Evaluation of fracture criteria for ship steels and weldments*. Ship Structural Committee, SSC-307, 1981.
42. Rolfe, S.T., D.M. Rhea, and B.O. Kuzmanovic, *Fracture control guidelines for welded ships hulls*. Ship Structure Committee, SSC-244, 1974.
43. Stambaugh, K.A. and W.A. Wood, *Ship fracture mechanisms - A Non-expert's guide for inspecting and determining the causes of significant ship fractures*. Ship Structure Committee, SSC-337, 1990.
44. Stambaugh, K.A. and W.A. Wood, *Ship Fracture Mechanism Investigation*. Ship Structural Committee, SSC-337 (Part 1), 1990.
45. Yee, R.D., et al., *Guide to damage tolerance analysis of marine structures*. Ship Structural Committee, SSC-402, 1997.
46. Carroll, L.B., S. Tiku, and A.S. Dinovitzer, *Rapid stress intensity factor solution estimation for ship structures applications*. Ship Structural Committee, SSC-429, 2003.
47. Barsom, J.M. and S.T. Rolfe, *Fracture and Fatigue Control in Structures: Applications of Fracture Mechanics*. Third Edition ed. 1999: ASTM.
48. Broek, D., *The practical use of fracture mechanics*. 2nd ed. 1988, AA Dordrecht, The Netherlands: Kluwer Academic Publishers.
49. Fricke, W., et al. *Technical Committee III.2, Fatigue and Fracture*. in *Proceeding of the 14th International Ship and Offshore Structures Congress*. 2000. Nagasaki, Japan: ISSC.
50. Dexter, R.J. and P.J. Pilarski, *Effect of Welded Stiffeners on Fatigue Crack Growth Rate*. Ship Structure Committee, SSC-413, 2000.
51. Brennan, F., et al. *Technical Committee III.2, Fatigue and Fracture*. in *Proceedings of the 15th International Ship and Offshore Structures Congress*. 2003. San Diego, USA: ISSC.
52. Barsom, J.M. and S.T. Rolfe, *Fracture and Fatigue Control in Structures: Applications of Fracture Mechanics*. Third Edition ed. 1977: ASTM.
53. Irwin, G.R., *Analysis of stresses and strains near the end of a crack transversing a plate*. Transactions, ASME, Journal of Applied Mechanics, 1957. **Volume 24**: p. 361-364.
54. Paik, J.K. and A.K. Thayamballi, *Ultimate Limit State Design of Steel Plated Design*. 2003: John Wiley & Sons Ltd.
55. Machida, S., *Ductile Fracture Mechanics*. 1984.
56. Paris, C.P. and G.C. Sih, *Stress Analysis of Cracks*. In *Fracture Toughness Testing and It's Applications*. ASTM STP No.381, 1965.
57. Tada, H., P.C. Paris, and G.R. Irwin, *The Stress Analysis of Cracks Handbook*. 1973.
58. Murakami, Y., *Stress intensity factors handbook*. 1987: Pergamon Books Ltd.
59. Janssen, M., J. Zuidema, and R.J.H. Wanhill, *Fracture Mechanics*. 2002: Delft University Press.
60. Tada, H., P.C. Paris, and G.R. Irwin, *The stress analysis of cracks handbook*. 1973.

61. Tada, H., P.C. Paris, and G.R. Irwin, *The Stress Analysis of Cracks Handbook*. 1997(Third Edition).
62. Isida, M., *Effect of width and length on stress intensity factors of internally cracked plates under various boundary conditions*. International Journal of Fracture, 1971. **Vol.7, No.3**: p. 301-316.
63. Brown, W.F. and J.E. Srawley, *Plane strain crack toughness testing of high strength metallic materials*. ASTM STP 410, 1966: p. 12.
64. Nisitani, H., *Tension of a strip with symmetric edge cracks or elliptical notches*. Trans. Japan Soc. Mech. Engrs., 1975. **Vol.49, No. 349**: p. 2518-2526.
65. Kitagawa, H. and R. Yuuki, *Analysis of arbitrarily shaped crack in a finite plate using conformal mapping, 1st Report - Construction of analysis procedure and its applicability*. Trans. Japan Soc. Mech. Engrs., 1977. **Vol.43, No.376**: p. 4354-4362.
66. Isida, M., H. Noguchi, and T. Yoshida, *Tention and bending of finite thickness plates with a semi-elliptical surface crack*. International Journal of Fracture, 1984. **Vol.26**: p. 157-188.
67. Newman, J.C., *An Improved Method of Collocation for the Stress Analysis of Cracked Plated with Various Shaped Boundaries*. NASA Technical Note, NASA TN D-6376, 1971.
68. Irwin, G.R. *Plastic zone near a crack and fracture toughness*. in *Sagamore Research Conference Proceeding*. 1961.
69. Dugdale, D.S., *Yielding of steel sheets containing slits*. Journal of the Mechanics and Physics of Solids, 1960. **8(2)**: p. 100-104.
70. Wells, A.A., *Unstable crack propagation in metals: cleavage and fast fracture*. Proceedings of the Crack Propagation Symposium, 1961. **Paper No.84**: p. 210-230.
71. Wells, A.A., *Application of fracture mechanics at and beyond general yield*. British Welding Research Association, 1963. **Report No. M13/63**.
72. Barenblatt, G.I., *The mathematical theory of equilibrium cracks in brittle fracture*. Advances in Applied Mechanics, 1962. **Vol. 7**: p.55-129.
73. Rolfe, S.T., A.E. Henn, and K.T. Hays, *Fracture mechanics methodology for fracture control in oil tanker*. United States Coast Guard, NVIC 15-91, Ch-1, 1991.
74. Burdenkin, F.M. and D.E.W. Stone, *The crack opening displacement approach to fracture mechanics in yielding materials*. Journal of Strain Analysis, 1966. **Vol.1**: p. 144-153.
75. Eshelby, J.D., *The determinate of the elastic field of an ellipsoidal inclusion and related problems*. Phil. Tras. Roy. Soc.(London), 1957. **A241**: p.376-396.
76. Eshelby, J.D., *The force on an elastic singularity*. Phil. Tras. Roy. Soc.(London), 1951. **A244**: p.87-112.
77. Günther, W., *Über einige Randintegrale der Elastomechanik*. Abh. Braunsch. Wiss. Ges., 1962. **14**: p. 53-72.
78. Cherepanov, G.P., *Crack propagation in continuous media*. J. Appl. Math. Mech., 1967. **31**: p. 503-512.
79. Rice, J.R., *A path independent integral and the approximation analysis of strain concentrations by notches and cracks*. Journal of Applied Mechanics, 1968. **35**: p. 379-386.

80. Hutchinson, J.W., *Singular behavior at the end of a tensile crack in a hardening material*. Journal of the Mechanics and Physics of Solids, 1968. **16**: p. 13-31.
81. Knowles, J.K. and E. Sternberg, *On a class of conservation laws in linearized and finite elastostatics*. Arch. Rat. Mech. Anal., 1972. **44**: p. 187-211.
82. Budiansky, B. and J.R. Rice, *Conservation laws and energy release rates*. Journal of Applied Mechanics, 1973. **26**: p. 201-203.
83. Shi, Y., et al., *Finite element analysis on relationships between the J-integral and CTOD for stationary cracks in welded tensile specimens*. International Journal of Pressure Vessels and Piping, 1998. **75**(3): p. 197-202.
84. Boothman, D.P., et al., *J-Estimation for semi-elliptical surface cracks in wide plates under direct tension*. Fatigue & Fracture of Engineering Materials & Structures, 1998(21): p. 333-346.
85. McClintock, F.A., *On the plasticity of the growth of fatigue cracks*, in *Fracture of Solids*. 1963, Wiley-Interscience: New York. p. 65.
86. Frost, N.E. *The growth of fatigue cracks*. in *Proceedings of the First International Conference on Fracture*. 1966. Sendai, Japan.
87. Ember, W., *"The significance of crack closure"*, *Damage Tolerance in Aircraft Structures*, ASTM STP 486. American Society for Testing and Materials, 1971: p. 230-242.
88. Schmidt, R.A. and P.C. Paris. *Threshold for fatigue crack propagation and effects of load ratio and frequency*. in *Progress in Flaw Growth and Fracture*, ASTM STP 536. 1973. Philadelphia: American Society for Testing and Materials, p.79.
89. Barsom, J.M., *Fatigue behavior of pressure-vessel steels*, in *Welding Research Council*. 1974: New York.
90. Paris, P.C. and F. Erdogan, *A Critical Analysis of Crack Propagation Laws*. Transactions, ASME, Journal of Basic Engineering, 1963. **Series D, 85, No.3**.
91. Forman, R.G., V.E. Kearney, and R.M. Engle, *Numerical analysis of crack propagation in cyclic-loaded structures*. Journal of Basic Engineering, 1967. **89**: p. 459-464.
92. Barsom, J.M. *Fatigue-Crack Growth under Variable-Amplitude Loading in ASTM A514 Grade B Steel*. in *ASTM STP 536, American Society for Testing and Materials*. 1973. Philadelphia.
93. Fisher, J.W.e.a., *Phase I: Final Report - "Development of Advanced Double Hull Concepts" Vol.3a, Structural Failure Modes:Fatigue, Final Report for Cooperative Agreement N00014-91-CA-0001*. 1993, Lehigh University: Bethlehem, PA.
94. BS7910, *Guide on methods for assessing the acceptability of flaws in metallic structures*. 1999, British Standards Institute: London.
95. BS6493, *Fatigue design and assessment for steel structures*. 1993.
96. Soares, C.G. and Y. Garbatov, *Fatigue reliability of the ship hull girder*. Marine Structures, 1996. **9**(3-4): p. 495-516.
97. Packman, P.F., et al., *Definition of fatigue cracks through non-destructive testing*. Journal of Materials, 1969. **4**(3): p. 666-700.
98. TSCF, *Guidance Manual for Tanker Structures*. Tanker Structure Co-Operative Forum, 1997.
99. ANSYS, *User's Manual (version 7.0)*. ANSYS Inc., 2003.

Chapter 8

Conclusions and Recommendations for Further Works

8.1 Conclusions

The principal objective of designing a ship is to reduce the risks of structural failure in order to ensure the safety of life, environment and property and to provide adequate durability of the hull structure for the design life [1]. There have been many records of casualties, which could lead to total losses or damage of various parts of the structure.

Structural strength of ageing ships tends to decrease with time through the effects of corrosion and fatigue induced cracks. Obviously severe general corrosion or localized corrosion over a large area will cause noticeable strength degradation and should be properly maintained and repaired based on a standard renewal or maintenance criteria. Fatigue induced cracks should also be properly monitored and repaired. Once crack is initiated, it might be propagated until it reaches a critical size. Finally fracture might occur when undesired and undetected cracks propagate to a critical size during ship's sailing through rough seas and heavy weather.

Structural designers and operators should always have a good understanding and knowledge of the causes of corrosion and fatigue cracks, the proper corrosion prevention methods, the corrosion rate estimate models, the fatigue and fatigue induced cracks and the location and extent of structural damage formed during operation of the structure and how it can affect the structural capacity in order to facilitate repair decisions for vessel's inspection and maintenance programme and to support a structural life extension decision later in life.

The overall researches presented in this thesis have been focused on the effects of corrosion and flaws on structural degradation in ageing ships. Finally some useful mathematical formulae and programs have been developed to evaluate strength degradation of ageing ships and to decide for immediate repair or future maintenance decision.

In Chapter 1, a general overview, background, objectives and structure of this thesis are presented.

In Chapter 2, factors which accelerate corrosion in marine structures such as the effects of high pressure tank cleaning washing, temperature changing due to cargo oil tank heating and the effects of clean inert gas system on structure degradation and corrosion rates have been investigated.

Especially, the effects of a clean inert gas system on corrosion prevention have not been studied well. In this research it is proposed that the clean inert gas system, either a high quality inert gas generator system or a N₂ generator system, can be used to

reduce corrosion degradation in marine structures in the areas such as ballast tanks and permanent void spaces and it has been found that high quality inert gas can be an effective economic solution considering appreciably reduced corrosion, maintenance, time out of service/trade, repair/steel replacement costs and improved re-sale value for the vessel, etc.

An approximate cost evaluation between a conventional boiler flue gas uptake inert gas system without inert gas supply to the double hull space and an inert gas generator with inert gas supply to the double hull space was investigated based on a typical AFRAMAX tanker. It is found that using clean inert gas to a marine structure will reduce overall maintenance cost considerably for replacement of steel structures, and possibly will reduce tank coating thickness for both new building ships and ageing ships.

In Chapter 3, various existing general corrosion models have been investigated and an average corrosion model based on *Melchers's* [2, 3], *Soares and Garvatov's* [4, 5], *Paik et al.'s* [6] and *Wang et al.'s* models [7] have been proposed. Some investigations on various pitting corrosion models and recommendations have also been carried out.

Time variant neutral axis position, section modulus at deck and section modulus at keel based on various existing general corrosion models for tanker structures have been investigated and compared. Finally some simplified formulas to estimate time variant vertical/horizontal section modulus degradation and associated stress changes at upper deck and keel are developed based on the selected double hull tanker. In addition, time-variant hull section modulus degradation is estimated when clean inert gas is applied for the double tanker. The results indicate the effectiveness of clean inert gas on control corrosion of marine and offshore structures, improvement of structural integrity and longitudinal strength in ageing double hull tankers. This means that a well designed clean inert gas system can minimize corrosion rates of structures and accordingly can minimize section modulus degradation over typical service life. Eventually the maintenance costs for ageing ships might remarkably be reduced compared to the structures which haven't clean inert gas provision.

In Chapter 4, the historical background and development of fatigue damage assessment methodologies and guidance of Classification Societies (IACS, DNV, ABS) have been reviewed.

Actual fatigue assessments of ship side shell longitudinal stiffeners in accordance with DNV guidance have been performed based on existing North Operating AFRAMAX shuttle tanker. In this assessment the effects of corrosion on fatigue life are considered, and several corrosion degradation models were used to assess the differences among them.

The results show that the accumulated fatigue life based on DNV model assuming 5 years effective corrosion protection period is noticeably shorter than that of the other

existing corrosion models. This is because that DNV recommendation has very conservative level of corrosion environment factor, D_{corr} , which is to be considered in final calculation of design life. In addition, the DNV guideline [8] uses fixed section modulus in their hull girder bending stress calculation whereas applied corrosion models use different section modulus values in each design life. Furthermore corrosion rates of local plate and stiffener in DNV guideline are more conservative than those of applied corrosion models (Wang's et al. and PW models) which is based on 30 years design life. This reveals that current corrosion margins in DNV guideline have adopted much higher values of corrosion degradation rates than actual statistics based existing corrosion models and data.

The results also show that the fatigue life of longitudinal stiffeners near the upper deck (stiffener no.43 ~ 46) is considerably shorter than for other locations. This is caused by a relatively higher vertical global stress range and small geometry property of stiffeners than at other locations. And also longitudinal stiffener no.32, which is located between the design load water line and the ballast load water line, shows the relatively short fatigue life than other locations.

In Chapter 5, a general review of existing formulae and recommendation to estimate elastic buckling strength and ultimate strength of unstiffened and stiffened plate have been investigated. Some recent research activities and guideline for the strength degradation due to localized corrosion have also been reviewed.

Obviously localized corrosion on a plate could reduce the strength of the plate. In this research, the ultimate strength of square plates with pitting corrosion has been investigated by using nonlinear finite element analyses. The effects of pitting corrosion width, depth, length and its transverse location on ultimate strength have been systematically studied. A total of 265 nonlinear finite element analyses have been carried out which is the full combination of two cases of transverse pitting locations, four cases of plate slenderness, four cases of pitting breadths, four cases of pitting lengths and two cases of pitting depths. The results can be summarized as follows:

- The length, breadth and depth of pit corrosion have weakening effects on the ultimate strength of the plates while plate slenderness has only marginal effect on strength reduction.
- The depth and width of the corrosion are the two dominant parameters. So this finding, to some extent, justifies the formula proposed by Paik, *et al.* [13-15], in which the corroded cross sectional area was chosen as the only parameter related to corrosion.
- Transverse location of pit corrosion is also an important factor determining the amount of strength reduction. When corrosion spreads transversely on both edges, it has the most deteriorating effect on strength.

The *Multi-Variable Regression Method* has been applied to derive empirical formulae to predict strength reduction due to pitting corrosion. The derived formulae are quite accurate. The formula for single side type pitting corrosion is slightly more accurate than that for both sides type pitting corrosion.

In addition, the *Artificial Neural Network (ANN) Method* is applied and some matrix based new formulae are derived to predict ultimate strength reduction of locally corroded plates. It is found out that the proposed formulae can accurately predict the ultimate strength reduction of locally corroded plates under uni-axial compression. The results can be summarized as follows:

- The number of *processing elements (PE)* in the hidden layer will not effect on the accuracy of ANN based output as long as there is an adequate number of epochs (more than 3000 epochs).
- The hyperbolic tangent (Tanh) activation function produces more accurate results than the logistic activation function.
- The ANN based empirical formulae show excellent accuracy to predict the ultimate strength reduction of unstiffened plates with localized corrosion under uniaxial compression. The formula for single side type pitting corrosion is slightly more accurate than that for both sides type pitting corrosion.

The formulae, which are derived by the *Multi-Variable Regression Method* and the *Artificial Neural Network (ANN) Method*, could be useful to determine structural integrity and residual strength of plates with localized corrosion during the initial design and on-site inspection and maintenance programme and could save considerable amount of time and efforts comparing with finite element analyses.

In Chapter 6, the effects of pitting corrosion on the ultimate strength of stiffened plates have been investigated by using nonlinear finite element analyses. The effects of different buckling modes based on half wave number, pitting corrosion width, transverse location and combined pitting corrosion on plate and web on ultimate strength have been studied. The results can be summarized as follows:

- The ultimate strength of stiffened plates shows remarkable decrease as the number of half sine waves of initial deflection increases.
- LRPASS and ULSAP programs produce the same ultimate strength regardless of the number of half wave. These programs could not consider the effect of the number of half wave. Of course they intend to produce the smallest value (the most critical one).
- Of these methods, LRPASS program proposes the most conservative ultimate strength.
- If the plate aspect ratio is same as the half wave number, the ultimate strength predicted by ULSAP is very close to those predicted by the finite element analyses ($\sigma_{ULT-FEM1}$ & $\sigma_{ULT-FEM2}$).
- In higher half wave numbers (3 and 4), which is closer to the plate aspect ratio, FORTRAN program controlled initial imperfection shape (perfect half sine wave) leads to a smaller ultimate strength than eigen buckling based initial imperfection shape.

- The ultimate strength of stiffened plates under the existing uniform corrosion models and IACS [1] corrosion allowance on the plate, web and flange is not remarkably reduced.
- The results show that the pitting corrosion on both edges at the longitudinally central location (number 4) has reduced the ultimate strength the most. This is probably due to the fact that stiffeners are served as support to the plate between them. The pitting corrosion along the stiffeners would effectively weaken the support of the stiffeners, so the strength is reduced much. On the other hand, the central area of a plate under uni-axial compression is usually less effective than those close to edges (stiffeners), so pitting corrosion in the central area would weaken the strength less than those close to edges. The strength reduction is only about 5% in the most critical case. Of course, the degree of corrosion in this example is fairly modest and is limited to only one plate. If the degree of corrosion is increased, the strength reduction would be expected to increase as well.
- In case of combined pitting corrosion on web and plate, the results show that the additional pitting corrosion on web will reduce ultimate strength further by 4 ~ 6 % compared to without pitting corrosion on the web. This is relatively small amount of reduction in ultimate strength of stiffened plates.

In Chapter 7, the historical background of fracture mechanic methods and current research activities in marine and offshore fields has been reviewed. Classical theory of the *linear elastic fracture mechanics (LEFM)* approach and the *elastic plastic fracture mechanics (EPFM)* approaches which is based on *crack tip displacement method* and *J-integral method* have been discussed. In addition, the general concept of crack propagation, prediction of crack propagation and fracture control and inspection are also been investigated.

Among others, the concept of the *linear elastic fracture mechanics (LEFM)* approach based on stress intensity factor (K) and the *elastic plastic fracture mechanics (EPFM)* approaches which are based on *crack tip displacement method* and *J-integral method* are applied to numerical computation for two-dimensional fracture problems. The effect of crack size, loads and material properties on stress intensity factors, *J-Integral* and *crack tip opening displacement (CTOD)* values have been investigated through 100 cases of finite element analyses for *LEFM* approach and another 300 cases of finite element analyses for *EPFM* approach. The results and achievements can be summarized as follows:

- In this study, two(2) useful ANSYS macro programs have been created to reduce computational time and finite element modelling efforts and to calculate stress intensity factor (K) for 2 dimensional centre cracked plate modelling. The one is for automatic creation of geometry, mesh details, symmetric boundary condition and applying loads by simply input eight parameters. The other is for automatic calculation of stress intensity factor (K) for centre cracked plate by simply input six parameters. The developed macro program for automatic calculation of stress intensity factor (K) can be applied and extended to any other structural crack problems.

- The computation of J value is much more complicate than the calculation of stress intensity factor (K) and J cannot compute directly by post processor commands of most of finite element programs. Thus it is necessary to develop a macro by using the ANSYS Parametric Design Language (APDL), a scripting language that user can use to automate common tasks or even build model in terms of parameters (variables). But the procedure and the creation of macro program to calculate J -integral value is not easy task for most of user who is using finite element program. In this study, the source code for the J computation macro which is based on 4 nodes path as illustrated in Fig.7.22 is developed. By using this program, the user can get the J computational value by just two steps. The first step is to read in the desired set of results and define a path for the line integral (4 node path). The second step is to input a macro file name into input (command) menu. The developed macro program for J computation can be applied and extended to any other structural crack problems.
- Some comparisons between existing handbook formulae for *stress intensity factor* (K) of centre cracked plate and ANSYS fracture finite element modelling results indicate that finite element modelling can predict stress intensity accurately. This means that finite element modelling can replace expensive actual test to find fracture toughness of various materials and leads to save time, efforts and cost of actual test.
- Among the handbook formulae, stress intensity factor (K) which is introduced in Broek [9] shows the highest values than other formulae. Whereas ANSYS finite element modelling results based on plane strain can be assumed as an average value of existing handbook formulae.
- If fracture is accompanied by considerable plastic deformation near the crack tip, then the elastic-plastic fracture mechanics method is recommended. In this Chapter, three different material properties based on yield stress of 235 N/mm^2 , 315 N/mm^2 , 355 N/mm^2 have been evaluated and investigated. The Higher yield strength of material shows lesser J -Integral value and crack tip opening displacement ($CTOD$) value than lower yield strength material. This is because the crack tip of lower yield strength material, such as mild steel, tends to yield earlier and have more plastic deformation around the crack tip than higher yield strength of material under same crack size and applied stress.
- The differences of J -integral values between mild steel and higher yield strength material are quite small, thus if the cracked structure has a mixed material properties then it is recommended to use lower yield stress material for finite element modelling in order to get more conservative J or $CTOD$ values.
- If the crack size ($2a/W$) is as small as 0.05 and 0.1, the changing of J or $CTOD$ values versus applied stress shows linear pattern and J and $CTOD$ values are expecting quite small. However if the crack size ($2a/W$) is larger than 0.2, the changing of J or $CTOD$ values versus applied loads shows nonlinear pattern and J and $CTOD$ values are to be steeply increased as increasing crack size as illustrated in Fig. 7.26 to Fig. 7.31.
- As indicated in Appendix H, the calculated J -integral values based on finite element modelling show slightly higher stress intensity factors than the Irwin's plastic zone correction based calculations.

- The calculated *CTOD* values which is converted to stress intensity factors as indicated in Appendix H show large differences from J-integral based computation or the Irwin's plastic zone correction based calculations. Generally *CTOD* based finite element analyses shows higher stress intensity factor than handbook solutions at small crack size with small applied stresses ranges. But it shows less stress intensity factor at relatively large crack size and large applied stress ranges.

8.2 Recommendations for further researches

This thesis broadly discussed many subjects such as corrosion effects, corrosion protection methods, corrosion rate estimate models, fatigue analyses of ship structures, buckling and ultimate strength of ship structures, effects of localized corrosion on strength degradation and its estimation, crack and crack propagation and fracture mechanics methodologies to assess structure degradation in ageing ship structures. However it is impossible to investigate in detail all the areas of interest during a PhD research period.

The proposals, investigations and methodologies reviewed and examined in this thesis will be useful to rationally evaluate suitable corrosion margins for marine structure during the design stage, to perform fatigue assessment under a corrosive environment, to estimate ultimate strength of corroded structures and to determine proper maintenance periods for double hull tankers as well as for other ship types. However there are still many areas which deserve further attention and investigation as follows:

- In Chapter 2, the effect of high pressure crude oil washing system is investigated. Normally crude oil washing will be performed by high pressure (5 ~ 12 bar) nozzles which are driven by cargo oil pumps or by a dedicated tank cleaning pump. Apparently high pressure tank cleaning system can cause deformation of corroded longitudinal stiffeners on upper deck and eventually will potentially have an effect on the strength and stiffness of ship structure. It is necessary to investigate the possible effect of high pressure tank cleaning machines on corroded stiffened plate components and subsequently on ultimate strength. Further research activities with actual tests onboard in order to evaluate the effects of high pressure tank cleaning washing, cargo oil tank heating and clean inert gas system on marine/offshore structures are recommended in order to verify effectiveness against corrosion for certain type and size of vessels.
- In Chapter 3, time variant neutral axis, section modulus at deck and section modulus at keel on various existing general corrosion models for tanker structures have been investigated and compared. Finally some simplified formulas to estimate time variant vertical/horizontal section modulus degradation and associated stress changes at upper deck and keel are developed based on the *AFRAMAX* double hull tanker. It is assumed that different size and tank structural details might have a different time variant section modulus degradation ratios and associated stress change at upper deck

and keel. Accordingly further research activities and investigation are required based on different sizes of double hull tankers.

In addition, it is recommended that further research activities and actual onboard tests are necessary to verify the effectiveness of clean inert gas against corrosion in double hull tanker structures.

- In Chapter 4, it is recommended that further research works are necessary to develop the first principle based spectral fatigue assessment methodology which considers annual degradation of corrosion on each structural member, time-variant vertical and horizontal section modulus degradation and time-variant stress change.
- In Chapter 5 and 6, finite element analyses have been carried out to investigate the effects of different material and geometry parameters such as plate slenderness, location, size and depth of pits on the ultimate strength of square plates under uni-axial compression. It is recommended further investigation of the effect of localized corrosion on plate with consideration of residual stresses and the effects of different locations, sizes and depths of pits on the ultimate strength of plate under lateral load, multi-loads and under shear have to be investigated.
- In Chapter 7, the effects of different crack sizes, loads and material properties on *stress intensity factor (K)* and *J-Integral* and *crack tip opening displacement (CTOD)* values have been discussed. Pits near the crack tip will accelerate the crack propagation and tend to increase stress intensity factor. It is worth to investigate the effects of different localized corrosion sizes and depths near the crack tip on stress intensity factor by using 3D finite element modelling.

There are two types of residual stresses exist in ship structures. The one is a mechanical residual stress which is introduced through fabrication procedure, the other is welding induced residual stress. Welding residual stress is caused by the heat induced welding processes. The heat input through the welding processes to the plate gives a great influence of residual stresses in the plate and crack propagation. It is recommended to study the effects of heat induced welding process on the stress intensity factor, J-integral value and CTOD value based on different material properties and on various structural details.

In addition, the optimum fracture control and maintenance plan depend on the consequence of a fracture and the time of crack initiation. In connection with the fatigue life assessment and methodologies which are described in Chapter 4, further research activities are recommended which consider both the first principle based spectral fatigue assessment methodology and elastic plastic fracture mechanics methodology based on different ship types and various structural details in order to establish the optimum fracture control plan, maintenance plan and reliability level of ageing ships.

In connection to Chapter 3, 4 and 5, it is also recommended to develop the methodology for the time-variant reliability assessment considering the effect of corrosion degradation and fatigue crack propagation on ultimate strength

reduction in time dependent manner in order to justify the residual strength, to establish reliability and to develop the proper maintenance programme for ageing ship structures.

References (Chapter 8)

1. IACS, *Common Structural Rules for Double Hull Oil Tankers*. 2006.
2. Melchers, R.E. *Probabilistic modelling of sea water corrosion of steel structures*. In: *Proceedings of the International Conference on Applications Statistics and Probability in Structural and Geotechnical Engineering(ICASP)*. 1995. Paris.
3. Melchers, R.E., *Corrosion uncertainty modelling for steel structures*. Journal of Constructional Steel Research, 1999. **52**(1 SU): p. 3-19.
4. Soares, C.G. and Y. Garbatov, *Reliability of maintained, corrosion protected plates subjected to non-linear corrosion and compressive loads*. Marine Structures, 1999. **12**(6): p. 425-445.
5. Soares, C.G. and Y. Garbatov, *Reliability of maintained ship hulls subjected to corrosion and fatigue under combined loading*. Journal of Constructional Steel Research, 1999b. **52**(1): p. 93-115.
6. Paik, J.K., et al., *A time-dependent corrosion wastage model for seawater ballast tank structures of ships*. Corrosion Science, 2004a. **46**(2 SU -): p. 471-486.
7. Wang, G., J. Spencer, and T. Elsayed, *Estimation of Corrosion Rates of Structural Members in Oil Tankers*. International Conference on Offshore Mechanics and Arctic Engineering, CANCUN, MEXICO, 2003c. **22nd**.
8. DNV, *Fatigue assessment of ship structures*. Det Norske Veritas, 2003. **Classification Note No 30.7**.
9. Broek, D., *The practical use of fracture mechanics*. 2nd ed. 1988, AA Dordrecht, The Netherlands: Kluwer Academic Publishers.

Author's Publications

- Duo Ok, Yongchang Pu, Atilla Incecik, “Artificial neural networks and their application to assessment of ultimate strength for plate elements with pitting corrosion”, Article was submitted for publication in journal (Ocean Engineering)
- Duo Ok, Yongchang Pu, Atilla Incecik, “Computation of ultimate strength of locally corroded unstiffened plates under uniaxial compression”, Article was submitted for publication in journal (Marine Structures)
- Duo Ok, Yongchang Pu, “Time-variant Corrosion Degradation, Hull Girder Strength and Fatigue Assessment for Ageing Double Hull Tankers”. In: 15th International Offshore and Polar Engineering Conference (ISOPE2005) 2005, Seoul, Korea
- Duo Ok, Yongchang Pu, “Corrosion Control Method by Using Clean Inert Gas to Ballast Tanks and Permanent Void Spaces in Marine and Offshore Structures”. In: 3rd International Marine Science and Technology for Environmental Sustainability Conference(ENSUS 2005) 2005, Newcastle upon Tyne, UK
- Garbatov, Y., Guedes Soares, C., Ok, D., Pu, Y., Rizzo, C., Rouhan A. and Parmentier, G.,”Modeling Strength Degradation Phenomena and Inspections used for Reliability Assessment based Maintenance Planning”, The 25th International Conference on OFFSHORE MECHANICS AND ARCTIC ENGINEERING, Hamburg, Germany, 4-9 June, 2006
- Garbatov, Y., Guedes Soares, C., Ok, D., Pu, Y., Rizzo, C., Rouhan A. and Parmentier, G.,”Modeling Strength Degradation Phenomena”, MARSTRUCT EU Project (Project No. FP6-PLT-506141) Report MAR-R6-3-IST-1, 6th September 2005
- Duo Ok, Yongchang Pu, “Fatigue Assessment for Ageing Double Hull Tanker”, MARSTRUCT EU Project (Project No. FP6-PLT-506141) Report MAR-W2-4-UNEW-2(1), May 2005
- Duo Ok, Yongchang Pu, “Time-Variant Corrosion Degradation Models in Double Hull Tanker”, MARSTRUCT EU Project (Project No. FP6-PLT-506141) Report MAR-W6-3-UNEW-03(1), March 2005
- Duo Ok, Yongchang Pu, “General and Pitting Corrosion Models”, MARSTRUCT EU Project (Project No. FP6-PLT-506141) Report MAR-W6-3-UNEW-02(1), March 2005
- Duo Ok, Yongchang Pu, “Types and Factors of Marine Corrosion”, MARSTRUCT EU Project (Project No. FP6-PLT-506141) Report MAR-W6-3-UNEW-01(1), March 2005
- Duo Ok, Yongchang Pu, “Corrosion and Crack Effects on Strength Degradation in Ageing Ship”. In: 4th Postgraduate Research Conference 2005, Newcastle upon Tyne, UK: School of Marine Science and Technology
- Duo Ok, Yongchang Pu, “Time-dependent reliability and ultimate strength of ageing ship”. In: 3rd Postgraduate Research Conference 2004, Newcastle upon Tyne, UK: School of Marine Science and Technology

Appendix A

Appendix A indicates the detail dimensions and geometries of ship side shell stiffeners in existing North Sea operating shuttle tanker. Table A-1 shows original designed geometric properties of shiplside longitudinal stiffeners in ballast tank and Table A-2 indicates geometric properties of shiplside longitudinal stiffeners considering deduction of corrosion allowance which is required by DNV 2004 Rules Pt.3, Ch.1, Sec.2, D200.

Z_s	= stiffener sectional modulus at top of flange
z	= distance above keel
b_{br}	= length of bracket side
t_p	= thickness of ship sideshell plate
h	= height of stiffener
t_w	= thickness of web
b_f	= width of flange
t_f	= thickness of flange
t_b	= thickness of bracket
t_{fr}	= thickness of transverse frame plating
z_{01}	= distance from neutral axis to top flange

Table A-1: Original designed geometric properties of shiplside longitudinal stiffener in ballast tank

Stiffener No.	Dimension (mm)	$Z_s (m^3)$	Z (m)	b_{br} (mm)	t_p (mm)	h (mm)	t_w (mm)	b_f (mm)	t_f (mm)	t_b (mm)	t_{fr} (mm)	Z_{01} (mm)
47	250 x 90 x 11/16 (L-type angle)	0.000526	20.5	450	15.5	250	11	90	16	13	15	216.3
46	250 x 90 x 11/16 (L-type angle)	0.000526	19.7	450	15.5	250	11	90	16	13	15	216.3
45	250 x 90 x 11/16 (L-type angle)	0.000527	18.9	450	16.0	250	11	90	16	13	15	217.5
44	300 x 90 x 11/16 (L-type angle)	0.000681	18.1	450	16.0	300	11	90	16	13	15	256.1
43	300 x 90 x 11/16 (L-type angle)	0.000681	17.3	450	16.0	300	11	90	16	13	15	256.1
42	380 x 120 x 12/20 (T-type angle)	0.001400	16.5	450	16.0	380	12	120	20	13	15	294.0
40	380 x 120 x 12/20 (T-type angle)	0.001400	14.9	450	16.0	380	12	120	20	13	15	294.0
39	380 x 120 x 12/20 (T-type angle)	0.001400	14.1	450	16.0	380	12	120	20	13	15	294.0
38	380 x 120 x 12/20 (T-type angle)	0.001400	13.3	450	16.0	380	12	120	20	13	15	294.0
37	380 x 120 x 12/20 (T-type angle)	0.001400	12.5	450	16.0	380	12	120	20	13	15	294.0
36	380 x 120 x 12/20 (T-type angle)	0.001400	11.7	450	16.0	380	12	120	20	13	15	294.0
34	380 x 120 x 12/20 (T-type angle)	0.001400	10.1	450	16.0	380	12	120	20	13	15	294.0
33	380 x 120 x 12/20 (T-type angle)	0.001400	9.3	450	16.0	380	12	120	20	13	15	294.0
32	380 x 120 x 12/20 (T-type angle)	0.001400	8.5	450	16.0	380	12	120	20	13	15	294.0
31	380 x 120 x 12/20 (T-type angle)	0.001400	7.7	450	16.0	380	12	120	20	13	15	294.0
30	380 x 120 x 12/20 (T-type angle)	0.001400	6.9	450	16.0	380	12	120	20	13	15	294.0
28	380 x 120 x 12/24 (T-type angle)	0.001566	5.3	450	16.0	380	12	120	24	13	15	286.5
27	380 x 120 x 12/24 (T-type angle)	0.001566	4.5	450	16.0	380	12	120	24	13	15	286.5
26	380 x 120 x 12/24 (T-type angle)	0.001566	3.7	450	16.0	380	12	120	24	13	15	286.5
25	380 x 120 x 12/24 (T-type angle)	0.001566	2.9	450	16.0	380	12	120	24	13	15	286.5
24	400 x 100 x 13/18 (L-type angle)	0.001232	2.1	450	16.0	400	13	100	18	13	16	320.8

Table A-2: Geometric properties of shiplside longitudinal stiffener in ballast tank considering corrosion allowance

Stiffener No.	Dimension (mm)	$Z_s (m^3)$	Z (m)	b_{br} (mm)	t_p (mm)	h (mm)	t_w (mm)	b_f (mm)	t_f (mm)	t_b (mm)	t_{fr} (mm)	Z_{01} (mm)
47	250 x 90 x 11/16 (L-type angle)	0.000405	20.5	450	12.5	250	8.0	90	13.0	10	12.0	216.5
46	250 x 90 x 11/16 (L-type angle)	0.000465	19.7	450	14.0	250	9.5	90	14.5	11.5	13.5	216.3
45	250 x 90 x 11/16 (L-type angle)	0.000467	18.9	450	14.5	250	9.5	90	14.5	11.5	13.5	217.6
44	300 x 90 x 11/16 (L-type angle)	0.000602	18.1	450	14.5	300	9.5	90	14.5	11.5	13.5	256.5
43	300 x 90 x 11/16 (L-type angle)	0.000602	17.3	450	14.5	300	9.5	90	14.5	11.5	13.5	256.5
42	380 x 120 x 12/20 (T-type angle)	0.001268	16.5	450	14.5	380	10.5	120	18.5	11.5	13.5	293.5
40	380 x 120 x 12/20 (T-type angle)	0.001268	14.9	450	14.5	380	10.5	120	18.5	11.5	13.5	293.5
39	380 x 120 x 12/20 (T-type angle)	0.001268	14.1	450	14.5	380	10.5	120	18.5	11.5	13.5	293.5
38	380 x 120 x 12/20 (T-type angle)	0.001268	13.3	450	14.5	380	10.5	120	18.5	11.5	13.5	293.5
37	380 x 120 x 12/20 (T-type angle)	0.001268	12.5	450	14.5	380	10.5	120	18.5	11.5	13.5	293.5
36	380 x 120 x 12/20 (T-type angle)	0.001268	11.7	450	14.5	380	10.5	120	18.5	11.5	13.5	293.5
34	380 x 120 x 12/20 (T-type angle)	0.001268	10.1	450	14.5	380	10.5	120	18.5	11.5	13.5	293.5
33	380 x 120 x 12/20 (T-type angle)	0.001268	9.3	450	14.5	380	10.5	120	18.5	11.5	13.5	293.5
32	380 x 120 x 12/20 (T-type angle)	0.001268	8.5	450	14.5	380	10.5	120	18.5	11.5	13.5	293.5
31	380 x 120 x 12/20 (T-type angle)	0.001268	7.7	450	14.5	380	10.5	120	18.5	11.5	13.5	293.5
30	380 x 120 x 12/20 (T-type angle)	0.001268	6.9	450	14.5	380	10.5	120	18.5	11.5	13.5	293.5
28	380 x 120 x 12/24 (T-type angle)	0.001435	5.3	450	14.5	380	10.5	120	22.5	11.5	13.5	285.3
27	380 x 120 x 12/24 (T-type angle)	0.001435	4.5	450	14.5	380	10.5	120	22.5	11.5	13.5	285.3
26	380 x 120 x 12/24 (T-type angle)	0.001435	3.7	450	14.5	380	10.5	120	22.5	11.5	13.5	285.3
25	380 x 120 x 12/24 (T-type angle)	0.001435	2.9	450	14.5	380	10.5	120	22.5	11.5	13.5	285.3
24	400 x 100 x 13/18 (L-type angle)	0.001107	2.1	450	14.5	400	11.5	100	16.5	11.5	14.5	320.8

Appendix B

Appendix B introduces a macro program which is created by author. In ANSYS program user can record a frequently used sequence of ANSYS commands in a macro program. Creating a macro by using ANSYS Parametric Design Language (APDL) enables user to create our own custom ANSYS command, automate common tasks or even build our model in terms of parameters (variables) and more importantly save time for building a model dramatically.

In this example, the input parameters are material yield stress (arg1), plate thickness (arg2), plate length (arg3), plate breadth (arg4), breadth of pit (arg5). By just input these five parameters user can automatically define element types and real constraint, define material properties, create model geometry, create nodes and elements by meshing, apply boundary condition (simply supported) and apply load (buckling load). Finally user can finish buckling analysis of unstiffend square plate by one step input command. Similarly user can extend this concept to nonlinear finite element analyses in order to get the ultimate strength of steel structures.

The concept of macro program is very useful and powerful in order to save modelling time and cost for both the beginners who wish to have reliable finite element results under the assistance of an expert without much knowing the complicate finite element program controls and the existing users who need to run many repeatable or similar finite element modelling.

arg1 = yield strength (N/mm²)

arg2 = plate thickness (mm)

arg3 = plate length (mm)

arg4 = plate breadth (mm)

arg5 = breadth of pit (mm)


```

ASBA, 1,P51X
rectang,0,arg3,0,arg5/2
rectang,0,arg3,arg4-(arg5/2),arg4
/AUTO,1
/REP,FAST
FLST,2,3,5,ORDE,3
FITEM,2,1
FITEM,2,-2
FITEM,2,4
AGLUE,P51X
CM,_Y,AREA
ASEL,,, 3
CM,_Y1,AREA
CMSEL,S,_Y
!*
CMSEL,S,_Y1
AATT, 1,, 1, 0, 1
CMSEL,S,_Y
CMDELE,_Y
CMDELE,_Y1
!*
FLST,5,2,5,ORDE,2
FITEM,5,1
FITEM,5,-2
CM,_Y,AREA
ASEL,,,P51X
CM,_Y1,AREA
CMSEL,S,_Y
!*
CMSEL,S,_Y1
AATT, 1,, 2, 0, 2
CMSEL,S,_Y
CMDELE,_Y
CMDELE,_Y1
!*
AESIZE,ALL,50,
MSHKEY,0
FLST,5,3,5,ORDE,2
FITEM,5,1
FITEM,5,-3
CM,_Y,AREA
ASEL,,,P51X
CM,_Y1,AREA
CHKMSH,'AREA'
CMSEL,S,_Y
!*
AMESH,_Y1
!*
CMDELE,_Y
CMDELE,_Y1
CMDELE,_Y2
!*
FINISH
/SOL
FLST,2,21,1,ORDE,8
FITEM,2,1
FITEM,2,24
FITEM,2,44

```

```
FITEM,2,64
FITEM,2,87
FITEM,2,107
FITEM,2,142
FITEM,2,-156
!*
/GO
D,P51X, , , , ,UY,UZ,ROTX,ROTZ, ,
FLST,2,21,1,ORDE,8
FITEM,2,2
FITEM,2,22
FITEM,2,-23
FITEM,2,65
FITEM,2,85
FITEM,2,-86
FITEM,2,127
FITEM,2,-141
!*
/GO
D,P51X, , , , ,UX,UY,UZ,ROTX,ROTZ,
FLST,2,21,1,ORDE,3
FITEM,2,85
FITEM,2,87
FITEM,2,-106
!*
/GO
D,P51X, , , , ,UY,UZ,ROTY,ROTZ, ,
FLST,2,21,1,ORDE,2
FITEM,2,1
FITEM,2,-21
!*
/GO
D,P51X, , , , ,UY,UZ,ROTY,ROTZ, ,
FINISH
/PREP7
FLST,4,21,1,ORDE,8
FITEM,4,1
FITEM,4,24
FITEM,4,44
FITEM,4,64
FITEM,4,87
FITEM,4,107
FITEM,4,142
FITEM,4,-156
CP,1,UX,P51X
FLST,4,21,1,ORDE,8
FITEM,4,2
FITEM,4,22
FITEM,4,-23
FITEM,4,65
FITEM,4,85
FITEM,4,-86
FITEM,4,127
FITEM,4,-141
CP,2,UX,P51X
FLST,4,21,1,ORDE,3
FITEM,4,85
FITEM,4,87
```

```
FITEM,4,-106
CP,3,UY,P51X
FLST,4,21,1,ORDE,2
FITEM,4,1
FITEM,4,-21
CP,4,UY,P51X
FINISH
/SOL
FLST,2,3,4,ORDE,3
FITEM,2,4
FITEM,2,10
FITEM,2,12
/GO
!*
SFL,P51X,PRES,0.01,
pstress,on
/sol
solve
finish
eplot
/SOLU
!*
ANTYPE,1
bucopt,subsp,1
/sol
solve
finish
/sol
expass,on
mxpand,1
outress,,all
/sol
solve
FINISH
```

Appendix C

Appendix C summarizes the results of 256 nonlinear finite element analyses based on higher tensile steel of 1m x 1m plate with a yield stress of 355 N/mm^2 with different geometry parameters such as plate slenderness, location, size and depth of pits on the ultimate strength of square plates.

- SE = single edge type pitting corrosion
- BE = both edges type pitting corrosion
- B = plate breadth
- t = plate thickness
- σ_c = ultimate strength of plate with localized corrosion
- σ_0 = ultimate strength of uncorroded plate
- x_1 = plate slenderness parameter (β)
- x_2 = the ratio of pit breadth to plate width
- x_3 = the ratio of pit length to plate length
- x_4 = the ratio of pit depth to plate thickness
- A_0 = uncorroded cross sectional area of plate
- A_r = cross sectional area of plate with corrosion.

Summary of FEA results for higher strength steel with pitting corrosion

No	FEM Input Variables						$\frac{A_0 - A_r}{A_0}$	σ_c	$\frac{\sigma_c}{\sigma_0}$
	Type	B/t	x_1	x_2	x_3	x_4	N/mm^2		
1	SE	41.7	1.719	0.1	0.25	0.25	0.975	278.27	0.991
2	SE	41.7	1.719	0.1	0.25	0.50	0.950	272.17	0.969
3	SE	50.0	2.061	0.1	0.25	0.25	0.975	252.70	0.992
4	SE	50.0	2.061	0.1	0.25	0.50	0.950	248.35	0.975
5	SE	62.5	2.576	0.1	0.25	0.25	0.975	229.63	0.991
6	SE	62.5	2.576	0.1	0.25	0.50	0.950	225.34	0.973
7	SE	41.7	1.719	0.1	0.50	0.25	0.975	272.81	0.972
8	SE	41.7	1.719	0.1	0.50	0.50	0.950	261.77	0.932
9	SE	50.0	2.061	0.1	0.50	0.25	0.975	246.62	0.968
10	SE	50.0	2.061	0.1	0.50	0.50	0.950	232.93	0.914
11	SE	62.5	2.576	0.1	0.50	0.25	0.975	222.74	0.961
12	SE	62.5	2.576	0.1	0.50	0.50	0.950	204.37	0.882
13	SE	41.7	1.719	0.1	0.75	0.25	0.975	268.48	0.956
14	SE	41.7	1.719	0.1	0.75	0.50	0.950	249.19	0.888
15	SE	50.0	2.061	0.1	0.75	0.25	0.975	241.68	0.948
16	SE	50.0	2.061	0.1	0.75	0.50	0.950	217.09	0.852
17	SE	62.5	2.576	0.1	0.75	0.25	0.975	218.34	0.942
18	SE	62.5	2.576	0.1	0.75	0.50	0.950	195.29	0.843
19	SE	41.7	1.719	0.1	1.00	0.25	0.975	254.76	0.907
20	SE	41.7	1.719	0.1	1.00	0.50	0.950	229.16	0.816
21	SE	50.0	2.061	0.1	1.00	0.25	0.975	240.27	0.943
22	SE	50.0	2.061	0.1	1.00	0.50	0.950	211.18	0.829
23	SE	62.5	2.576	0.1	1.00	0.25	0.975	216.42	0.934
24	SE	62.5	2.576	0.1	1.00	0.50	0.950	194.95	0.841
25	SE	41.7	1.719	0.2	0.25	0.25	0.950	275.83	0.982
26	SE	41.7	1.719	0.2	0.25	0.50	0.900	261.30	0.931
27	SE	50.0	2.061	0.2	0.25	0.25	0.950	251.07	0.985
28	SE	50.0	2.061	0.2	0.25	0.50	0.900	238.92	0.938
29	SE	62.5	2.576	0.2	0.25	0.25	0.950	227.96	0.984
30	SE	62.5	2.576	0.2	0.25	0.50	0.900	215.81	0.932
31	SE	41.7	1.719	0.2	0.50	0.25	0.950	265.15	0.944
32	SE	41.7	1.719	0.2	0.50	0.50	0.900	243.65	0.868
33	SE	50.0	2.061	0.2	0.50	0.25	0.950	238.10	0.934
34	SE	50.0	2.061	0.2	0.50	0.50	0.900	215.07	0.844
35	SE	62.5	2.576	0.2	0.50	0.25	0.950	213.60	0.922
36	SE	62.5	2.576	0.2	0.50	0.50	0.900	188.91	0.815
37	SE	41.7	1.719	0.2	0.75	0.25	0.950	256.00	0.912
38	SE	41.7	1.719	0.2	0.75	0.50	0.900	223.36	0.796
39	SE	50.0	2.061	0.2	0.75	0.25	0.950	229.18	0.899
40	SE	50.0	2.061	0.2	0.75	0.50	0.900	196.98	0.773
41	SE	62.5	2.576	0.2	0.75	0.25	0.950	207.29	0.895
42	SE	62.5	2.576	0.2	0.75	0.50	0.900	178.64	0.771
43	SE	41.7	1.719	0.2	1.00	0.25	0.950	252.38	0.899
44	SE	41.7	1.719	0.2	1.00	0.50	0.900	212.66	0.757
45	SE	50.0	2.061	0.2	1.00	0.25	0.950	226.23	0.888
46	SE	50.0	2.061	0.2	1.00	0.50	0.900	190.11	0.746
47	SE	62.5	2.576	0.2	1.00	0.25	0.950	205.77	0.888
48	SE	62.5	2.576	0.2	1.00	0.50	0.900	176.18	0.760
49	SE	41.7	1.719	0.3	0.25	0.25	0.925	274.11	0.976
50	SE	41.7	1.719	0.3	0.25	0.50	0.850	250.30	0.892

51	SE	50.0	2.061	0.3	0.25	0.25	0.925	249.95	0.981
52	SE	50.0	2.061	0.3	0.25	0.50	0.850	228.33	0.896
53	SE	62.5	2.576	0.3	0.25	0.25	0.925	227.06	0.980
54	SE	62.5	2.576	0.3	0.25	0.50	0.850	206.46	0.891
55	SE	41.7	1.719	0.3	0.50	0.25	0.925	260.01	0.926
56	SE	41.7	1.719	0.3	0.50	0.50	0.850	232.09	0.827
57	SE	50.0	2.061	0.3	0.50	0.25	0.925	233.22	0.915
58	SE	50.0	2.061	0.3	0.50	0.50	0.850	204.94	0.804
59	SE	62.5	2.576	0.3	0.50	0.25	0.925	208.94	0.902
60	SE	62.5	2.576	0.3	0.50	0.50	0.850	180.10	0.777
61	SE	41.7	1.719	0.3	0.75	0.25	0.925	248.53	0.885
62	SE	41.7	1.719	0.3	0.75	0.50	0.850	212.00	0.755
63	SE	50.0	2.061	0.3	0.75	0.25	0.925	222.62	0.874
64	SE	50.0	2.061	0.3	0.75	0.50	0.850	188.54	0.740
65	SE	62.5	2.576	0.3	0.75	0.25	0.925	201.27	0.869
66	SE	62.5	2.576	0.3	0.75	0.50	0.850	170.78	0.737
67	SE	41.7	1.719	0.3	1.00	0.25	0.925	243.99	0.869
68	SE	41.7	1.719	0.3	1.00	0.50	0.850	202.40	0.721
69	SE	50.0	2.061	0.3	1.00	0.25	0.925	219.11	0.860
70	SE	50.0	2.061	0.3	1.00	0.50	0.850	182.33	0.716
71	SE	62.5	2.576	0.3	1.00	0.25	0.925	199.32	0.860
72	SE	62.5	2.576	0.3	1.00	0.50	0.850	168.10	0.726
73	SE	41.7	1.719	0.4	0.25	0.25	0.900	272.80	0.972
74	SE	41.7	1.719	0.4	0.25	0.50	0.800	241.31	0.859
75	SE	50.0	2.061	0.4	0.25	0.25	0.900	249.15	0.978
76	SE	50.0	2.061	0.4	0.25	0.50	0.800	220.20	0.864
77	SE	62.5	2.576	0.4	0.25	0.25	0.900	226.49	0.978
78	SE	62.5	2.576	0.4	0.25	0.50	0.800	199.82	0.863
79	SE	41.7	1.719	0.4	0.50	0.25	0.900	256.38	0.913
80	SE	41.7	1.719	0.4	0.50	0.50	0.800	222.35	0.792
81	SE	50.0	2.061	0.4	0.50	0.25	0.900	229.97	0.902
82	SE	50.0	2.061	0.4	0.50	0.50	0.800	196.05	0.769
83	SE	62.5	2.576	0.4	0.50	0.25	0.900	206.19	0.890
84	SE	62.5	2.576	0.4	0.50	0.50	0.800	168.09	0.726
85	SE	41.7	1.719	0.4	0.75	0.25	0.900	243.39	0.867
86	SE	41.7	1.719	0.4	0.75	0.50	0.800	201.82	0.719
87	SE	50.0	2.061	0.4	0.75	0.25	0.900	218.64	0.858
88	SE	50.0	2.061	0.4	0.75	0.50	0.800	180.74	0.709
89	SE	62.5	2.576	0.4	0.75	0.25	0.900	198.21	0.856
90	SE	62.5	2.576	0.4	0.75	0.50	0.800	164.48	0.710
91	SE	41.7	1.719	0.4	1.00	0.25	0.900	238.29	0.849
92	SE	41.7	1.719	0.4	1.00	0.50	0.800	193.73	0.690
93	SE	50.0	2.061	0.4	1.00	0.25	0.900	214.85	0.843
94	SE	50.0	2.061	0.4	1.00	0.50	0.800	175.94	0.690
95	SE	62.5	2.576	0.4	1.00	0.25	0.900	196.11	0.847
96	SE	62.5	2.576	0.4	1.00	0.50	0.800	162.98	0.704
97	BE	41.7	1.719	0.1	0.25	0.25	0.975	278.25	0.991
98	BE	41.7	1.719	0.1	0.25	0.50	0.950	273.36	0.974
99	BE	50.0	2.061	0.1	0.25	0.25	0.975	252.63	0.991
100	BE	50.0	2.061	0.1	0.25	0.50	0.950	248.70	0.976
101	BE	62.5	2.576	0.1	0.25	0.25	0.975	229.56	0.991
102	BE	62.5	2.576	0.1	0.25	0.50	0.950	225.44	0.973
103	BE	41.7	1.719	0.1	0.50	0.25	0.975	273.03	0.972
104	BE	41.7	1.719	0.1	0.50	0.50	0.950	262.43	0.935
105	BE	50.0	2.061	0.1	0.50	0.25	0.975	246.86	0.969

106	BE	50.0	2.061	0.1	0.50	0.50	0.950	234.31	0.920
107	BE	62.5	2.576	0.1	0.50	0.25	0.975	222.96	0.962
108	BE	62.5	2.576	0.1	0.50	0.50	0.950	206.30	0.890
109	BE	41.7	1.719	0.1	0.75	0.25	0.975	268.94	0.958
110	BE	41.7	1.719	0.1	0.75	0.50	0.950	253.00	0.901
111	BE	50.0	2.061	0.1	0.75	0.25	0.975	242.18	0.950
112	BE	50.0	2.061	0.1	0.75	0.50	0.950	220.55	0.866
113	BE	62.5	2.576	0.1	0.75	0.25	0.975	218.37	0.943
114	BE	62.5	2.576	0.1	0.75	0.50	0.950	189.33	0.817
115	BE	41.7	1.719	0.1	1.00	0.25	0.975	267.54	0.953
116	BE	41.7	1.719	0.1	1.00	0.50	0.950	249.59	0.889
117	BE	50.0	2.061	0.1	1.00	0.25	0.975	241.05	0.946
118	BE	50.0	2.061	0.1	1.00	0.50	0.950	216.21	0.848
119	BE	62.5	2.576	0.1	1.00	0.25	0.975	217.51	0.939
120	BE	62.5	2.576	0.1	1.00	0.50	0.950	184.04	0.794
121	BE	41.7	1.719	0.2	0.25	0.25	0.950	274.90	0.979
122	BE	41.7	1.719	0.2	0.25	0.50	0.900	260.48	0.928
123	BE	50.0	2.061	0.2	0.25	0.25	0.950	250.14	0.982
124	BE	50.0	2.061	0.2	0.25	0.50	0.900	238.84	0.937
125	BE	62.5	2.576	0.2	0.25	0.25	0.950	226.92	0.979
126	BE	62.5	2.576	0.2	0.25	0.50	0.900	215.66	0.931
127	BE	41.7	1.719	0.2	0.50	0.25	0.950	264.21	0.941
128	BE	41.7	1.719	0.2	0.50	0.50	0.900	240.68	0.857
129	BE	50.0	2.061	0.2	0.50	0.25	0.950	237.77	0.933
130	BE	50.0	2.061	0.2	0.50	0.50	0.900	209.40	0.822
131	BE	62.5	2.576	0.2	0.50	0.25	0.950	212.73	0.918
132	BE	62.5	2.576	0.2	0.50	0.50	0.900	176.41	0.761
133	BE	41.7	1.719	0.2	0.75	0.25	0.950	255.03	0.908
134	BE	41.7	1.719	0.2	0.75	0.50	0.900	218.50	0.778
135	BE	50.0	2.061	0.2	0.75	0.25	0.950	228.70	0.897
136	BE	50.0	2.061	0.2	0.75	0.50	0.900	180.76	0.709
137	BE	62.5	2.576	0.2	0.75	0.25	0.950	205.14	0.885
138	BE	62.5	2.576	0.2	0.75	0.50	0.900	160.00	0.691
139	BE	41.7	1.719	0.2	1.00	0.25	0.950	251.87	0.897
140	BE	41.7	1.719	0.2	1.00	0.50	0.900	208.97	0.744
141	BE	50.0	2.061	0.2	1.00	0.25	0.950	226.03	0.887
142	BE	50.0	2.061	0.2	1.00	0.50	0.900	169.61	0.666
143	BE	62.5	2.576	0.2	1.00	0.25	0.950	203.66	0.879
144	BE	62.5	2.576	0.2	1.00	0.50	0.900	158.97	0.686
145	BE	41.7	1.719	0.3	0.25	0.25	0.925	271.85	0.968
146	BE	41.7	1.719	0.3	0.25	0.50	0.850	247.92	0.883
147	BE	50.0	2.061	0.3	0.25	0.25	0.925	247.83	0.973
148	BE	50.0	2.061	0.3	0.25	0.50	0.850	227.61	0.893
149	BE	62.5	2.576	0.3	0.25	0.25	0.925	224.42	0.969
150	BE	62.5	2.576	0.3	0.25	0.50	0.850	204.85	0.884
151	BE	41.7	1.719	0.3	0.50	0.25	0.925	255.58	0.910
152	BE	41.7	1.719	0.3	0.50	0.50	0.850	221.19	0.788
153	BE	50.0	2.061	0.3	0.50	0.25	0.925	228.12	0.895
154	BE	50.0	2.061	0.3	0.50	0.50	0.850	189.39	0.743
155	BE	62.5	2.576	0.3	0.50	0.25	0.925	202.08	0.872
156	BE	62.5	2.576	0.3	0.50	0.50	0.850	157.28	0.679
157	BE	41.7	1.719	0.3	0.75	0.25	0.925	242.57	0.864
158	BE	41.7	1.719	0.3	0.75	0.50	0.850	192.97	0.687
159	BE	50.0	2.061	0.3	0.75	0.25	0.925	215.13	0.844
160	BE	50.0	2.061	0.3	0.75	0.50	0.850	155.82	0.611

161	BE	62.5	2.576	0.3	0.75	0.25	0.925	193.03	0.833
162	BE	62.5	2.576	0.3	0.75	0.50	0.850	139.72	0.603
163	BE	41.7	1.719	0.3	1.00	0.25	0.925	237.34	0.845
164	BE	41.7	1.719	0.3	1.00	0.50	0.850	178.55	0.636
165	BE	50.0	2.061	0.3	1.00	0.25	0.925	211.00	0.828
166	BE	50.0	2.061	0.3	1.00	0.50	0.850	149.37	0.586
167	BE	62.5	2.576	0.3	1.00	0.25	0.925	191.43	0.826
168	BE	62.5	2.576	0.3	1.00	0.50	0.850	145.15	0.627
169	BE	41.7	1.719	0.4	0.25	0.25	0.900	269.33	0.959
170	BE	41.7	1.719	0.4	0.25	0.50	0.800	235.35	0.838
171	BE	50.0	2.061	0.4	0.25	0.25	0.900	246.02	0.965
172	BE	50.0	2.061	0.4	0.25	0.50	0.800	215.31	0.845
173	BE	62.5	2.576	0.4	0.25	0.25	0.900	222.71	0.961
174	BE	62.5	2.576	0.4	0.25	0.50	0.800	192.31	0.830
175	BE	41.7	1.719	0.4	0.50	0.25	0.900	248.20	0.884
176	BE	41.7	1.719	0.4	0.50	0.50	0.800	206.22	0.735
177	BE	50.0	2.061	0.4	0.50	0.25	0.900	220.12	0.864
178	BE	50.0	2.061	0.4	0.50	0.50	0.800	175.59	0.689
179	BE	62.5	2.576	0.4	0.50	0.25	0.900	193.72	0.836
180	BE	62.5	2.576	0.4	0.50	0.50	0.800	145.91	0.630
181	BE	41.7	1.719	0.4	0.75	0.25	0.900	231.88	0.826
182	BE	41.7	1.719	0.4	0.75	0.50	0.800	176.39	0.628
183	BE	50.0	2.061	0.4	0.75	0.25	0.900	203.59	0.799
184	BE	50.0	2.061	0.4	0.75	0.50	0.800	142.31	0.558
185	BE	62.5	2.576	0.4	0.75	0.25	0.900	182.72	0.789
186	BE	62.5	2.576	0.4	0.75	0.50	0.800	126.52	0.546
187	BE	41.7	1.719	0.4	1.00	0.25	0.900	224.78	0.801
188	BE	41.7	1.719	0.4	1.00	0.50	0.800	158.27	0.564
189	BE	50.0	2.061	0.4	1.00	0.25	0.900	198.07	0.777
190	BE	50.0	2.061	0.4	1.00	0.50	0.800	131.72	0.517
191	BE	62.5	2.576	0.4	1.00	0.25	0.900	181.23	0.782
192	BE	62.5	2.576	0.4	1.00	0.50	0.800	129.26	0.558
193	SE	45.5	1.875	0.1	0.50	0.25	0.975	259.89	0.971
194	SE	45.5	1.875	0.1	0.50	0.50	0.950	247.77	0.926
195	SE	55.6	2.291	0.1	0.50	0.25	0.969	234.66	0.967
196	SE	55.6	2.291	0.1	0.50	0.50	0.939	218.79	0.901
197	SE	45.5	1.875	0.1	1.00	0.25	0.975	253.61	0.948
198	SE	45.5	1.875	0.1	1.00	0.50	0.950	227.02	0.848
199	SE	55.6	2.291	0.1	1.00	0.25	0.969	228.53	0.941
200	SE	55.6	2.291	0.1	1.00	0.50	0.939	201.51	0.830
201	SE	45.5	1.875	0.2	0.50	0.25	0.950	251.77	0.941
202	SE	45.5	1.875	0.2	0.50	0.50	0.900	224.88	0.840
203	SE	55.6	2.291	0.2	0.50	0.25	0.939	225.84	0.930
204	SE	55.6	2.291	0.2	0.50	0.50	0.878	201.80	0.831
205	SE	45.5	1.875	0.2	1.00	0.25	0.950	239.05	0.893
206	SE	45.5	1.875	0.2	1.00	0.50	0.900	200.38	0.749
207	SE	55.6	2.291	0.2	1.00	0.25	0.939	215.43	0.887
208	SE	55.6	2.291	0.2	1.00	0.50	0.878	182.62	0.752
209	SE	45.5	1.875	0.3	0.50	0.25	0.925	246.73	0.922
210	SE	45.5	1.875	0.3	0.50	0.50	0.850	218.55	0.817
211	SE	55.6	2.291	0.3	0.50	0.25	0.908	220.93	0.910
212	SE	55.6	2.291	0.3	0.50	0.50	0.817	192.50	0.793
213	SE	45.5	1.875	0.3	1.00	0.25	0.925	231.26	0.864
214	SE	45.5	1.875	0.3	1.00	0.50	0.850	191.74	0.717
215	SE	55.6	2.291	0.3	1.00	0.25	0.908	208.76	0.860

216	SE	55.6	2.291	0.3	1.00	0.50	0.817	174.91	0.720
217	SE	45.5	1.875	0.4	0.50	0.25	0.900	243.21	0.909
218	SE	45.5	1.875	0.4	0.50	0.50	0.800	209.12	0.782
219	SE	55.6	2.291	0.4	0.50	0.25	0.878	217.98	0.898
220	SE	55.6	2.291	0.4	0.50	0.50	0.756	184.22	0.759
221	SE	45.5	1.875	0.4	1.00	0.25	0.900	226.28	0.846
222	SE	45.5	1.875	0.4	1.00	0.50	0.800	184.33	0.689
223	SE	55.6	2.291	0.4	1.00	0.25	0.878	205.10	0.845
224	SE	55.6	2.291	0.4	1.00	0.50	0.756	169.26	0.697
225	BE	45.5	1.875	0.1	0.50	0.25	0.975	260.12	0.972
226	BE	45.5	1.875	0.1	0.50	0.50	0.950	248.69	0.929
227	BE	55.6	2.291	0.1	0.50	0.25	0.969	234.88	0.968
228	BE	55.6	2.291	0.1	0.50	0.50	0.939	220.61	0.909
229	BE	45.5	1.875	0.1	1.00	0.25	0.975	254.38	0.951
230	BE	45.5	1.875	0.1	1.00	0.50	0.950	233.28	0.872
231	BE	55.6	2.291	0.1	1.00	0.25	0.969	229.05	0.943
232	BE	55.6	2.291	0.1	1.00	0.50	0.939	200.06	0.824
233	BE	45.5	1.875	0.2	0.50	0.25	0.950	251.23	0.939
234	BE	45.5	1.875	0.2	0.50	0.50	0.900	225.54	0.843
235	BE	55.6	2.291	0.2	0.50	0.25	0.939	225.40	0.928
236	BE	55.6	2.291	0.2	0.50	0.50	0.878	193.32	0.796
237	BE	45.5	1.875	0.2	1.00	0.25	0.950	239.42	0.895
238	BE	45.5	1.875	0.2	1.00	0.50	0.900	188.91	0.706
239	BE	55.6	2.291	0.2	1.00	0.25	0.939	214.35	0.883
240	BE	55.6	2.291	0.2	1.00	0.50	0.878	167.21	0.689
241	BE	45.5	1.875	0.3	0.50	0.25	0.925	242.04	0.905
242	BE	45.5	1.875	0.3	0.50	0.50	0.850	205.58	0.768
243	BE	55.6	2.291	0.3	0.50	0.25	0.908	215.21	0.886
244	BE	55.6	2.291	0.3	0.50	0.50	0.817	173.66	0.715
245	BE	45.5	1.875	0.3	1.00	0.25	0.925	223.85	0.837
246	BE	45.5	1.875	0.3	1.00	0.50	0.850	158.10	0.591
247	BE	55.6	2.291	0.3	1.00	0.25	0.908	200.48	0.826
248	BE	55.6	2.291	0.3	1.00	0.50	0.817	146.78	0.605
249	BE	45.5	1.875	0.4	0.50	0.25	0.900	234.31	0.876
250	BE	45.5	1.875	0.4	0.50	0.50	0.800	190.99	0.714
251	BE	55.6	2.291	0.4	0.50	0.25	0.878	206.87	0.852
252	BE	55.6	2.291	0.4	0.50	0.50	0.756	160.72	0.662
253	BE	45.5	1.875	0.4	1.00	0.25	0.900	210.77	0.788
254	BE	45.5	1.875	0.4	1.00	0.50	0.800	140.78	0.526
255	BE	55.6	2.291	0.4	1.00	0.25	0.878	188.64	0.777
256	BE	55.6	2.291	0.4	1.00	0.50	0.756	130.20	0.536

Appendix D

Appendix D summarizes the results of finite element analyses (FEA) and Multi-Variable Regression output using data obtained from finite element analyses in Appendix C. One of them is for the plates with pitting corrosion on one side (edge) of the plates, the other is for the plates with symmetrical pitting corrosion on two sides (edges). Four variables, x_1 , x_2 , x_3 and x_4 , have been chosen as independent variables, where the valid ranges of x_1 is 1.719 to 2.576, which corresponds to $B/t = 40$ to 62.5, x_2 is 0 to 0.4, x_3 is 0 to 1.0 and x_4 is 0 or 0.5. 128 sets of finite element analyses results for single edge type pitting corrosion on the plate and another 128 sets with both edges type pitting corrosion are used to derive the formulae. Following tables indicate all data which include the independent four (4) variables x_1 , x_2 , x_3 , x_4 .

- FEM_{SE} = the results of FEA based on the single edge type pitting corrosion
- FEM_{BE} = the results of FEA based on the both edges type pitting corrosion
- MRM_{SE} = Multi-Variable Regression output based on the single edge type pitting corrosion
- MRM_{BE} = Multi-Variable Regression output based on the both edges type pitting corrosion
- σ_C = ultimate strength of plate with localized corrosion
- σ_0 = ultimate strength of uncorroded plate
- x_1 = plate slenderness parameter (β)
- x_2 = the ratio of pit breadth to plate width
- x_3 = the ratio of pit length to plate length
- x_4 = the ratio of pit depth to plate thickness

FEA and Multi-Variable Regression output for plate with single edge pitting corrosion

No	B/t	x_1	x_2	x_3	x_4	σ_c	σ_0	FEM _{SE}	MRM _{SE}
1	41.7	1.719	0.1	0.25	0.25	278.27	280.76	0.991	1.041652
2	41.7	1.719	0.1	0.25	0.50	272.17	280.76	0.969	0.933152
3	50	2.061	0.1	0.25	0.25	252.70	254.82	0.992	1.036726
4	50	2.061	0.1	0.25	0.50	248.35	254.82	0.975	0.928226
5	62.5	2.576	0.1	0.25	0.25	229.63	231.67	0.991	1.029308
6	62.5	2.576	0.1	0.25	0.50	225.34	231.67	0.973	0.920808
7	41.7	1.719	0.1	0.50	0.25	272.81	280.76	0.972	1.000152
8	41.7	1.719	0.1	0.50	0.50	261.77	280.76	0.932	0.891652
9	50	2.061	0.1	0.50	0.25	246.62	254.82	0.968	0.995226
10	50	2.061	0.1	0.50	0.50	232.93	254.82	0.914	0.886726
11	62.5	2.576	0.1	0.50	0.25	222.74	231.67	0.961	0.987808
12	62.5	2.576	0.1	0.50	0.50	204.37	231.67	0.882	0.879308
13	41.7	1.719	0.1	0.75	0.25	268.48	280.76	0.956	0.958652
14	41.7	1.719	0.1	0.75	0.50	249.19	280.76	0.888	0.850152
15	50	2.061	0.1	0.75	0.25	241.68	254.82	0.948	0.953726
16	50	2.061	0.1	0.75	0.50	217.09	254.82	0.852	0.845226
17	62.5	2.576	0.1	0.75	0.25	218.34	231.67	0.942	0.946308
18	62.5	2.576	0.1	0.75	0.50	195.29	231.67	0.843	0.837808
19	41.7	1.719	0.1	1.00	0.25	254.76	280.76	0.907	0.917152
20	41.7	1.719	0.1	1.00	0.50	229.16	280.76	0.816	0.808652
21	50	2.061	0.1	1.00	0.25	240.27	254.82	0.943	0.912226
22	50	2.061	0.1	1.00	0.50	211.18	254.82	0.829	0.803726
23	62.5	2.576	0.1	1.00	0.25	216.42	231.67	0.934	0.904808
24	62.5	2.576	0.1	1.00	0.50	194.95	231.67	0.841	0.796308
25	41.7	1.719	0.2	0.25	0.25	275.83	280.76	0.982	1.008052
26	41.7	1.719	0.2	0.25	0.50	261.30	280.76	0.931	0.899552
27	50	2.061	0.2	0.25	0.25	251.07	254.82	0.985	1.003126
28	50	2.061	0.2	0.25	0.50	238.92	254.82	0.938	0.894626
29	62.5	2.576	0.2	0.25	0.25	227.96	231.67	0.984	0.995708
30	62.5	2.576	0.2	0.25	0.50	215.81	231.67	0.932	0.887208
31	41.7	1.719	0.2	0.50	0.25	265.15	280.76	0.944	0.966552
32	41.7	1.719	0.2	0.50	0.50	243.65	280.76	0.868	0.858052
33	50	2.061	0.2	0.50	0.25	238.10	254.82	0.934	0.961626
34	50	2.061	0.2	0.50	0.50	215.07	254.82	0.844	0.853126
35	62.5	2.576	0.2	0.50	0.25	213.60	231.67	0.922	0.954208
36	62.5	2.576	0.2	0.50	0.50	188.91	231.67	0.815	0.845708
37	41.7	1.719	0.2	0.75	0.25	256.00	280.76	0.912	0.925052
38	41.7	1.719	0.2	0.75	0.50	223.36	280.76	0.796	0.816552
39	50	2.061	0.2	0.75	0.25	229.18	254.82	0.899	0.920126
40	50	2.061	0.2	0.75	0.50	196.98	254.82	0.773	0.811626
41	62.5	2.576	0.2	0.75	0.25	207.29	231.67	0.895	0.912708
42	62.5	2.576	0.2	0.75	0.50	178.64	231.67	0.771	0.804208
43	41.7	1.719	0.2	1.00	0.25	252.38	280.76	0.899	0.883552
44	41.7	1.719	0.2	1.00	0.50	212.66	280.76	0.757	0.775052
45	50	2.061	0.2	1.00	0.25	226.23	254.82	0.888	0.878626
46	50	2.061	0.2	1.00	0.50	190.11	254.82	0.746	0.770126
47	62.5	2.576	0.2	1.00	0.25	205.77	231.67	0.888	0.871208
48	62.5	2.576	0.2	1.00	0.50	176.18	231.67	0.760	0.762708
49	41.7	1.719	0.3	0.25	0.25	274.11	280.76	0.976	0.974452
50	41.7	1.719	0.3	0.25	0.50	250.30	280.76	0.892	0.865952
51	50	2.061	0.3	0.25	0.25	249.95	254.82	0.981	0.969526
52	50	2.061	0.3	0.25	0.50	228.33	254.82	0.896	0.861026

53	62.5	2.576	0.3	0.25	0.25	227.06	231.67	0.980	0.962108
54	62.5	2.576	0.3	0.25	0.50	206.46	231.67	0.891	0.853608
55	41.7	1.719	0.3	0.50	0.25	260.01	280.76	0.926	0.932952
56	41.7	1.719	0.3	0.50	0.50	232.09	280.76	0.827	0.824452
57	50	2.061	0.3	0.50	0.25	233.22	254.82	0.915	0.928026
58	50	2.061	0.3	0.50	0.50	204.94	254.82	0.804	0.819526
59	62.5	2.576	0.3	0.50	0.25	208.94	231.67	0.902	0.920608
60	62.5	2.576	0.3	0.50	0.50	180.10	231.67	0.777	0.812108
61	41.7	1.719	0.3	0.75	0.25	248.53	280.76	0.885	0.891452
62	41.7	1.719	0.3	0.75	0.50	212.00	280.76	0.755	0.782952
63	50	2.061	0.3	0.75	0.25	222.62	254.82	0.874	0.886526
64	50	2.061	0.3	0.75	0.50	188.54	254.82	0.740	0.778026
65	62.5	2.576	0.3	0.75	0.25	201.27	231.67	0.869	0.879108
66	62.5	2.576	0.3	0.75	0.50	170.78	231.67	0.737	0.770608
67	41.7	1.719	0.3	1.00	0.25	243.99	280.76	0.869	0.849952
68	41.7	1.719	0.3	1.00	0.50	202.40	280.76	0.721	0.741452
69	50	2.061	0.3	1.00	0.25	219.11	254.82	0.860	0.845026
70	50	2.061	0.3	1.00	0.50	182.33	254.82	0.716	0.736526
71	62.5	2.576	0.3	1.00	0.25	199.32	231.67	0.860	0.837608
72	62.5	2.576	0.3	1.00	0.50	168.10	231.67	0.726	0.729108
73	41.7	1.719	0.4	0.25	0.25	272.80	280.76	0.972	0.940852
74	41.7	1.719	0.4	0.25	0.50	241.31	280.76	0.859	0.832352
75	50	2.061	0.4	0.25	0.25	249.15	254.82	0.978	0.935926
76	50	2.061	0.4	0.25	0.50	220.20	254.82	0.864	0.827426
77	62.5	2.576	0.4	0.25	0.25	226.49	231.67	0.978	0.928508
78	62.5	2.576	0.4	0.25	0.50	199.82	231.67	0.863	0.820008
79	41.7	1.719	0.4	0.50	0.25	256.38	280.76	0.913	0.899352
80	41.7	1.719	0.4	0.50	0.50	222.35	280.76	0.792	0.790852
81	50	2.061	0.4	0.50	0.25	229.97	254.82	0.902	0.894426
82	50	2.061	0.4	0.50	0.50	196.05	254.82	0.769	0.785926
83	62.5	2.576	0.4	0.50	0.25	206.19	231.67	0.890	0.887008
84	62.5	2.576	0.4	0.50	0.50	168.09	231.67	0.726	0.778508
85	41.7	1.719	0.4	0.75	0.25	243.39	280.76	0.867	0.857852
86	41.7	1.719	0.4	0.75	0.50	201.82	280.76	0.719	0.749352
87	50	2.061	0.4	0.75	0.25	218.64	254.82	0.858	0.852926
88	50	2.061	0.4	0.75	0.50	180.74	254.82	0.709	0.744426
89	62.5	2.576	0.4	0.75	0.25	198.21	231.67	0.856	0.845508
90	62.5	2.576	0.4	0.75	0.50	164.48	231.67	0.710	0.737008
91	41.7	1.719	0.4	1.00	0.25	238.29	280.76	0.849	0.816352
92	41.7	1.719	0.4	1.00	0.50	193.73	280.76	0.690	0.707852
93	50	2.061	0.4	1.00	0.25	214.85	254.82	0.843	0.811426
94	50	2.061	0.4	1.00	0.50	175.94	254.82	0.690	0.702926
95	62.5	2.576	0.4	1.00	0.25	196.11	231.67	0.847	0.804008
96	62.5	2.576	0.4	1.00	0.50	162.98	231.67	0.704	0.695508
97	45.5	1.875	0.1	0.50	0.25	259.89	267.57	0.971	0.997897
98	45.5	1.875	0.1	0.50	0.50	247.77	267.57	0.926	0.889397
99	55.6	2.291	0.1	0.50	0.25	234.66	242.77	0.967	0.991903
100	55.6	2.291	0.1	0.50	0.50	218.79	242.77	0.901	0.883403
101	45.5	1.875	0.1	1.00	0.25	253.61	267.57	0.948	0.914897
102	45.5	1.875	0.1	1.00	0.50	227.02	267.57	0.848	0.806397
103	55.6	2.291	0.1	1.00	0.25	228.53	242.77	0.941	0.908903
104	55.6	2.291	0.1	1.00	0.50	201.51	242.77	0.830	0.800403
105	45.5	1.875	0.2	0.50	0.25	251.77	267.57	0.941	0.964297
106	45.5	1.875	0.2	0.50	0.50	224.88	267.57	0.840	0.855797
107	55.6	2.291	0.2	0.50	0.25	225.84	242.77	0.930	0.958303

108	55.6	2.291	0.2	0.50	0.50	201.80	242.77	0.831	0.849803
109	45.5	1.875	0.2	1.00	0.25	239.05	267.57	0.893	0.881297
110	45.5	1.875	0.2	1.00	0.50	200.38	267.57	0.749	0.772797
111	55.6	2.291	0.2	1.00	0.25	215.43	242.77	0.887	0.875303
112	55.6	2.291	0.2	1.00	0.50	182.62	242.77	0.752	0.766803
113	45.5	1.875	0.3	0.50	0.25	246.73	267.57	0.922	0.930697
114	45.5	1.875	0.3	0.50	0.50	218.55	267.57	0.817	0.822197
115	55.6	2.291	0.3	0.50	0.25	220.93	242.77	0.910	0.924703
116	55.6	2.291	0.3	0.50	0.50	192.50	242.77	0.793	0.816203
117	45.5	1.875	0.3	1.00	0.25	231.26	267.57	0.864	0.847697
118	45.5	1.875	0.3	1.00	0.50	191.74	267.57	0.717	0.739197
119	55.6	2.291	0.3	1.00	0.25	208.76	242.77	0.860	0.841703
120	55.6	2.291	0.3	1.00	0.50	174.91	242.77	0.720	0.733203
121	45.5	1.875	0.4	0.50	0.25	243.21	267.57	0.909	0.897097
122	45.5	1.875	0.4	0.50	0.50	209.12	267.57	0.782	0.788597
123	55.6	2.291	0.4	0.50	0.25	217.98	242.77	0.898	0.891103
124	55.6	2.291	0.4	0.50	0.50	184.22	242.77	0.759	0.782603
125	45.5	1.875	0.4	1.00	0.25	226.28	267.57	0.846	0.814097
126	45.5	1.875	0.4	1.00	0.50	184.33	267.57	0.689	0.705597
127	55.6	2.291	0.4	1.00	0.25	205.10	242.77	0.845	0.808103
128	55.6	2.291	0.4	1.00	0.50	169.26	242.77	0.697	0.699603

FEA and Multi-Variable Regression output for plate with both edges pitting corrosion

No	B/t	x_1	x_2	x_3	x_4	σ_c	σ_0	FEM _{BE}	MRM _{BE}
1	41.7	1.719	0.1	0.25	0.25	278.25	280.76	0.991	1.09955
2	41.7	1.719	0.1	0.25	0.50	273.36	280.76	0.974	0.95555
3	50	2.061	0.1	0.25	0.25	252.63	254.82	0.991	1.085388
4	50	2.061	0.1	0.25	0.50	248.7	254.82	0.976	0.941388
5	62.5	2.576	0.1	0.25	0.25	229.56	231.67	0.991	1.06406
6	62.5	2.576	0.1	0.25	0.50	225.44	231.67	0.973	0.92006
7	41.7	1.719	0.1	0.50	0.25	273.03	280.76	0.972	1.04455
8	41.7	1.719	0.1	0.50	0.50	262.43	280.76	0.935	0.90055
9	50	2.061	0.1	0.50	0.25	246.86	254.82	0.969	1.030388
10	50	2.061	0.1	0.50	0.50	234.31	254.82	0.920	0.886388
11	62.5	2.576	0.1	0.50	0.25	222.96	231.67	0.962	1.00906
12	62.5	2.576	0.1	0.50	0.50	206.3	231.67	0.890	0.86506
13	41.7	1.719	0.1	0.75	0.25	268.94	280.76	0.958	0.98955
14	41.7	1.719	0.1	0.75	0.50	253	280.76	0.901	0.84555
15	50	2.061	0.1	0.75	0.25	242.18	254.82	0.950	0.975388
16	50	2.061	0.1	0.75	0.50	220.55	254.82	0.866	0.831388
17	62.5	2.576	0.1	0.75	0.25	218.37	231.67	0.943	0.95406
18	62.5	2.576	0.1	0.75	0.50	189.33	231.67	0.817	0.81006
19	41.7	1.719	0.1	1.00	0.25	267.54	280.76	0.953	0.93455
20	41.7	1.719	0.1	1.00	0.50	249.59	280.76	0.889	0.79055
21	50	2.061	0.1	1.00	0.25	241.05	254.82	0.946	0.920388
22	50	2.061	0.1	1.00	0.50	216.21	254.82	0.848	0.776388
23	62.5	2.576	0.1	1.00	0.25	217.51	231.67	0.939	0.89906
24	62.5	2.576	0.1	1.00	0.50	184.04	231.67	0.794	0.75506
25	41.7	1.719	0.2	0.25	0.25	274.9	280.76	0.979	1.03925
26	41.7	1.719	0.2	0.25	0.50	260.48	280.76	0.928	0.89525
27	50	2.061	0.2	0.25	0.25	250.14	254.82	0.982	1.025088
28	50	2.061	0.2	0.25	0.50	238.84	254.82	0.937	0.881088
29	62.5	2.576	0.2	0.25	0.25	226.92	231.67	0.979	1.00376
30	62.5	2.576	0.2	0.25	0.50	215.66	231.67	0.931	0.85976
31	41.7	1.719	0.2	0.50	0.25	264.21	280.76	0.941	0.98425
32	41.7	1.719	0.2	0.50	0.50	240.68	280.76	0.857	0.84025
33	50	2.061	0.2	0.50	0.25	237.77	254.82	0.933	0.970088
34	50	2.061	0.2	0.50	0.50	209.4	254.82	0.822	0.826088
35	62.5	2.576	0.2	0.50	0.25	212.73	231.67	0.918	0.94876
36	62.5	2.576	0.2	0.50	0.50	176.41	231.67	0.761	0.80476
37	41.7	1.719	0.2	0.75	0.25	255.03	280.76	0.908	0.92925
38	41.7	1.719	0.2	0.75	0.50	218.5	280.76	0.778	0.78525
39	50	2.061	0.2	0.75	0.25	228.7	254.82	0.897	0.915088
40	50	2.061	0.2	0.75	0.50	180.76	254.82	0.709	0.771088
41	62.5	2.576	0.2	0.75	0.25	205.14	231.67	0.885	0.89376
42	62.5	2.576	0.2	0.75	0.50	160	231.67	0.691	0.74976
43	41.7	1.719	0.2	1.00	0.25	251.87	280.76	0.897	0.87425
44	41.7	1.719	0.2	1.00	0.50	208.97	280.76	0.744	0.73025
45	50	2.061	0.2	1.00	0.25	226.03	254.82	0.887	0.860088
46	50	2.061	0.2	1.00	0.50	169.61	254.82	0.666	0.716088
47	62.5	2.576	0.2	1.00	0.25	203.66	231.67	0.879	0.83876
48	62.5	2.576	0.2	1.00	0.50	158.97	231.67	0.686	0.69476
49	41.7	1.719	0.3	0.25	0.25	271.85	280.76	0.968	0.97895
50	41.7	1.719	0.3	0.25	0.50	247.92	280.76	0.883	0.83495

Appendix D: Summary of FEA results and Multi-Variable Regression Output

51	50	2.061	0.3	0.25	0.25	247.83	254.82	0.973	0.964788
52	50	2.061	0.3	0.25	0.50	227.61	254.82	0.893	0.820788
53	62.5	2.576	0.3	0.25	0.25	224.42	231.67	0.969	0.94346
54	62.5	2.576	0.3	0.25	0.50	204.85	231.67	0.884	0.79946
55	41.7	1.719	0.3	0.50	0.25	255.58	280.76	0.910	0.92395
56	41.7	1.719	0.3	0.50	0.50	221.19	280.76	0.788	0.77995
57	50	2.061	0.3	0.50	0.25	228.12	254.82	0.895	0.909788
58	50	2.061	0.3	0.50	0.50	189.39	254.82	0.743	0.765788
59	62.5	2.576	0.3	0.50	0.25	202.08	231.67	0.872	0.88846
60	62.5	2.576	0.3	0.50	0.50	157.28	231.67	0.679	0.74446
61	41.7	1.719	0.3	0.75	0.25	242.57	280.76	0.864	0.86895
62	41.7	1.719	0.3	0.75	0.50	192.97	280.76	0.687	0.72495
63	50	2.061	0.3	0.75	0.25	215.13	254.82	0.844	0.854788
64	50	2.061	0.3	0.75	0.50	155.82	254.82	0.611	0.710788
65	62.5	2.576	0.3	0.75	0.25	193.03	231.67	0.833	0.83346
66	62.5	2.576	0.3	0.75	0.50	139.72	231.67	0.603	0.68946
67	41.7	1.719	0.3	1.00	0.25	237.34	280.76	0.845	0.81395
68	41.7	1.719	0.3	1.00	0.50	178.55	280.76	0.636	0.66995
69	50	2.061	0.3	1.00	0.25	211	254.82	0.828	0.799788
70	50	2.061	0.3	1.00	0.50	149.37	254.82	0.586	0.655788
71	62.5	2.576	0.3	1.00	0.25	191.43	231.67	0.826	0.77846
72	62.5	2.576	0.3	1.00	0.50	145.15	231.67	0.627	0.63446
73	41.7	1.719	0.4	0.25	0.25	269.33	280.76	0.959	0.91865
74	41.7	1.719	0.4	0.25	0.50	235.35	280.76	0.838	0.77465
75	50	2.061	0.4	0.25	0.25	246.02	254.82	0.965	0.904488
76	50	2.061	0.4	0.25	0.50	215.31	254.82	0.845	0.760488
77	62.5	2.576	0.4	0.25	0.25	222.71	231.67	0.961	0.88316
78	62.5	2.576	0.4	0.25	0.50	192.31	231.67	0.830	0.73916
79	41.7	1.719	0.4	0.50	0.25	248.2	280.76	0.884	0.86365
80	41.7	1.719	0.4	0.50	0.50	206.22	280.76	0.735	0.71965
81	50	2.061	0.4	0.50	0.25	220.12	254.82	0.864	0.849488
82	50	2.061	0.4	0.50	0.50	175.59	254.82	0.689	0.705488
83	62.5	2.576	0.4	0.50	0.25	193.72	231.67	0.836	0.82816
84	62.5	2.576	0.4	0.50	0.50	145.91	231.67	0.630	0.68416
85	41.7	1.719	0.4	0.75	0.25	231.88	280.76	0.826	0.80865
86	41.7	1.719	0.4	0.75	0.50	176.39	280.76	0.628	0.66465
87	50	2.061	0.4	0.75	0.25	203.59	254.82	0.799	0.794488
88	50	2.061	0.4	0.75	0.50	142.31	254.82	0.558	0.650488
89	62.5	2.576	0.4	0.75	0.25	182.72	231.67	0.789	0.77316
90	62.5	2.576	0.4	0.75	0.50	126.52	231.67	0.546	0.62916
91	41.7	1.719	0.4	1.00	0.25	224.78	280.76	0.801	0.75365
92	41.7	1.719	0.4	1.00	0.50	158.27	280.76	0.564	0.60965
93	50	2.061	0.4	1.00	0.25	198.07	254.82	0.777	0.739488
94	50	2.061	0.4	1.00	0.50	131.72	254.82	0.517	0.595488
95	62.5	2.576	0.4	1.00	0.25	181.23	231.67	0.782	0.71816
96	62.5	2.576	0.4	1.00	0.50	129.26	231.67	0.558	0.57416
97	45.5	1.875	0.1	0.50	0.25	260.12	267.57	0.972	1.038066
98	45.5	1.875	0.1	0.50	0.50	248.69	267.57	0.929	0.894066
99	55.6	2.291	0.1	0.50	0.25	234.88	242.77	0.968	1.020833
100	55.6	2.291	0.1	0.50	0.50	220.61	242.77	0.909	0.876833
101	45.5	1.875	0.1	1.00	0.25	254.38	267.57	0.951	0.928066
102	45.5	1.875	0.1	1.00	0.50	233.28	267.57	0.872	0.784066
103	55.6	2.291	0.1	1.00	0.25	229.05	242.77	0.943	0.910833

104	55.6	2.291	0.1	1.00	0.50	200.06	242.77	0.824	0.766833
105	45.5	1.875	0.2	0.50	0.25	251.23	267.57	0.939	0.977766
106	45.5	1.875	0.2	0.50	0.50	225.54	267.57	0.843	0.833766
107	55.6	2.291	0.2	0.50	0.25	225.4	242.77	0.928	0.960533
108	55.6	2.291	0.2	0.50	0.50	193.32	242.77	0.796	0.816533
109	45.5	1.875	0.2	1.00	0.25	239.42	267.57	0.895	0.867766
110	45.5	1.875	0.2	1.00	0.50	188.91	267.57	0.706	0.723766
111	55.6	2.291	0.2	1.00	0.25	214.35	242.77	0.883	0.850533
112	55.6	2.291	0.2	1.00	0.50	167.21	242.77	0.689	0.706533
113	45.5	1.875	0.3	0.50	0.25	242.04	267.57	0.905	0.917466
114	45.5	1.875	0.3	0.50	0.50	205.58	267.57	0.768	0.773466
115	55.6	2.291	0.3	0.50	0.25	215.21	242.77	0.886	0.900233
116	55.6	2.291	0.3	0.50	0.50	173.66	242.77	0.715	0.756233
117	45.5	1.875	0.3	1.00	0.25	223.85	267.57	0.837	0.807466
118	45.5	1.875	0.3	1.00	0.50	158.1	267.57	0.591	0.663466
119	55.6	2.291	0.3	1.00	0.25	200.48	242.77	0.826	0.790233
120	55.6	2.291	0.3	1.00	0.50	146.78	242.77	0.605	0.646233
121	45.5	1.875	0.4	0.50	0.25	234.31	267.57	0.876	0.857166
122	45.5	1.875	0.4	0.50	0.50	190.99	267.57	0.714	0.713166
123	55.6	2.291	0.4	0.50	0.25	206.87	242.77	0.852	0.839933
124	55.6	2.291	0.4	0.50	0.50	160.72	242.77	0.662	0.695933
125	45.5	1.875	0.4	1.00	0.25	210.77	267.57	0.788	0.747166
126	45.5	1.875	0.4	1.00	0.50	140.78	267.57	0.526	0.603166
127	55.6	2.291	0.4	1.00	0.25	188.64	242.77	0.777	0.729933
128	55.6	2.291	0.4	1.00	0.50	130.2	242.77	0.536	0.585933

Appendix E

Appendix E summarizes the results of finite element analyses (FEA), input parameters and output values based on Tanh activation function for Artificial Neural Networks approach. One of them is for the plates with pitting corrosion on single edge of the plates, the other is for the plates with symmetrical pitting corrosion on both edges. Four variables, x_1 , x_2 , x_3 and x_4 , have been chosen as independent variables, where the valid ranges of x_1 is 1.719 to 2.576, which corresponds to $B/t = 40$ to 62.5, x_2 is 0 to 0.4, x_3 is 0 to 1.0 and x_4 is 0 or 0.5. 136 sets of finite element analyses results for single edge type pitting corrosion on the plate and another 137 sets with both edges type pitting corrosion are used to derive the formulae. Following tables indicate all data which include the independent four (4) variables x_1 , x_2 , x_3 , x_4 .

FEM_{SE} = the results of FEA based on the single edge type pitting corrosion

FEM_{BE} = the results of FEA based on the both edges type pitting corrosion

ANN Output = ANN output based on Tanh activation function

σ_C = ultimate strength of plate with localized corrosion

σ_0 = ultimate strength of uncorroded plate

x_1 = plate slenderness parameter (β)

x_2 = the ratio of pit breadth to plate width

x_3 = the ratio of pit length to plate length

x_4 = the ratio of pit depth to plate thickness

ANN inputs and outputs for plate with single edge type pitting corrosion

No	B/t	X ₁	X ₂	X ₃	X ₄	σ_c	σ_0	FEM _{SE}	ANN Output
1	45.5	1.875221	0.3	0.5	0.5	218.55	267.57	0.816796	0.810783
2	41.7	1.718609	0.3	0.25	0.5	250.3	280.76	0.891509	0.909122
3	50	2.060682	0.4	1	0.5	175.94	254.82	0.690448	0.69855
4	45.5	1.875221	0.1	1	0.5	227.02	267.57	0.848451	0.833355
5	62.5	2.575853	0.1	1	0.25	216.42	231.67	0.934174	0.934576
6	50	2.060682	0.3	1	0.25	219.11	254.82	0.859862	0.862344
7	41.7	1.718609	0.3	1	0.25	243.99	280.76	0.869034	0.863671
8	50	2.060682	0.3	0.25	0.5	228.33	254.82	0.896044	0.899414
9	45.5	1.875221	0.4	1	0.5	184.33	267.57	0.688904	0.699097
10	45.5	1.875221	0.3	1	0.25	231.26	267.57	0.864297	0.863046
11	50	2.060682	0.2	1	0.25	226.23	254.82	0.887803	0.889382
12	50	2.060682	0.4	0.25	0.5	220.2	254.82	0.864139	0.853028
13	50	2.060682	0.1	0.25	0.5	248.35	254.82	0.97461	0.983121
14	55	2.27	0	0	0	243.81	243.81	1	1.002078
15	62.5	2.575853	0.2	0.25	0.5	215.81	231.67	0.931541	0.927029
16	41.7	1.718609	0.4	1	0.25	238.29	280.76	0.848732	0.845652
17	62.5	2.575853	0.2	0.75	0.5	178.64	231.67	0.771097	0.770719
18	55.6	2.291479	0.4	1	0.5	169.26	242.77	0.697203	0.697955
19	41.7	1.718609	0.2	0.25	0.25	275.83	280.76	0.982441	0.989906
20	41.7	1.718609	0.2	1	0.5	212.66	280.76	0.757444	0.758114
21	50	2.060682	0.2	0.5	0.5	215.07	254.82	0.844008	0.846997
22	41.7	1.718609	0.3	0.75	0.25	248.53	280.76	0.885204	0.879516
23	55.6	2.29	0	0	0	242.77	242.77	1	1.001895
24	55.6	2.291479	0.1	1	0.25	228.53	242.77	0.941344	0.935468
25	41.7	1.718609	0.3	0.75	0.5	212	280.76	0.755093	0.740081
26	62.5	2.575853	0.1	0.5	0.5	204.37	231.67	0.88216	0.897532
27	45.5	1.875221	0.2	0.5	0.5	224.88	267.57	0.840453	0.857546
28	50	2.060682	0.4	0.5	0.25	229.97	254.82	0.90248	0.910009
29	41.7	1.718609	0.1	0.75	0.5	249.19	280.76	0.887555	0.864867
30	45.5	1.875221	0.1	0.5	0.25	259.89	267.57	0.971297	0.966387
31	62.5	2.575853	0.4	1	0.25	196.11	231.67	0.846506	0.841803
32	50	2.060682	0.2	1	0.5	190.11	254.82	0.746056	0.756055
33	45.5	1.875221	0.2	0.5	0.25	251.77	267.57	0.94095	0.937223
34	50	2.060682	0.4	0.75	0.25	218.64	254.82	0.858017	0.860747
35	62.5	2.575853	0.2	0.75	0.25	207.29	231.67	0.894764	0.901118
36	62.5	2.575853	0.1	0.25	0.5	225.34	231.67	0.972677	0.970747
37	55.6	2.291479	0.2	0.5	0.25	225.84	242.77	0.930263	0.928798
38	62.5	2.575853	0.3	0.25	0.5	206.46	231.67	0.891181	0.879506
39	62.5	2.575853	0.2	0.25	0.25	227.96	231.67	0.983986	0.971109
40	55.6	2.291479	0.2	1	0.5	182.62	242.77	0.752235	0.754801
41	50	2.060682	0.3	0.5	0.5	204.94	254.82	0.804254	0.800006
42	55.6	2.291479	0.3	0.5	0.25	220.93	242.77	0.910038	0.906339
43	62.5	2.575853	0.3	0.5	0.25	208.94	231.67	0.901886	0.899302
44	45.5	1.87	0	0	0	267.57	267.57	1	1.005415
45	41.7	1.718609	0.3	0.5	0.5	232.09	280.76	0.826649	0.820179
46	40	1.65	0	0	0	287.48	287.48	1	1.006958
47	41.7	1.718609	0.3	0.5	0.25	260.01	280.76	0.926093	0.923987
48	55.6	2.291479	0.4	0.5	0.5	184.22	242.77	0.758825	0.75935
49	50	2.060682	0.1	0.75	0.5	217.09	254.82	0.851935	0.859174
50	41.7	1.718609	0.4	0.5	0.5	222.35	280.76	0.791958	0.787857
51	50	2.060682	0.2	0.75	0.25	229.18	254.82	0.89938	0.904317

52	62.5	2.575853	0.1	0.25	0.25	229.63	231.67	0.991194	0.985326
53	55.6	2.291479	0.3	1	0.5	174.91	242.77	0.720476	0.717207
54	45.5	1.875221	0.1	0.5	0.5	247.77	267.57	0.926001	0.923033
55	60	2.47	0	0	0	235.33	235.33	1	1.000208
56	55.6	2.291479	0.4	0.5	0.25	217.98	242.77	0.897887	0.901341
57	41.7	1.718609	0.2	1	0.25	252.38	280.76	0.898917	0.890729
58	62.5	2.575853	0.1	0.5	0.25	222.74	231.67	0.961454	0.95969
59	55.6	2.291479	0.2	1	0.25	215.43	242.77	0.887383	0.888515
60	50	2.060682	0.3	0.5	0.25	233.22	254.82	0.915234	0.912921
61	41.7	1.718609	0.1	0.75	0.25	268.48	280.76	0.956262	0.949454
62	62.5	2.575853	0.3	0.75	0.25	201.27	231.67	0.868779	0.872071
63	50	2.060682	0.4	0.25	0.25	249.15	254.82	0.977749	0.976076
64	41.7	1.718609	0.4	1	0.5	193.73	280.76	0.69002	0.699616
65	41.7	1.718609	0.3	1	0.5	202.4	280.76	0.7209	0.719528
66	62.5	2.575853	0.2	0.5	0.5	188.91	231.67	0.815427	0.821297
67	45.5	1.875221	0.4	0.5	0.25	243.21	267.57	0.908958	0.917406
68	41.7	1.718609	0.4	0.75	0.5	201.82	280.76	0.718835	0.716737
69	62.5	2.575853	0.2	0.5	0.25	213.6	231.67	0.922001	0.924078
70	41.7	1.718609	0.2	0.5	0.5	243.65	280.76	0.867823	0.866768
71	41.7	1.718609	0.3	0.25	0.25	274.11	280.76	0.976314	0.982942
72	50	2.060682	0.4	1	0.25	214.85	254.82	0.843144	0.843982
73	62.5	2.575853	0.3	0.75	0.5	170.78	231.67	0.737169	0.727948
74	55.6	2.291479	0.3	1	0.25	208.76	242.77	0.859909	0.861518
75	50	2.060682	0.2	0.75	0.5	196.98	254.82	0.773016	0.777822
76	62.5	2.575853	0.1	0.75	0.25	218.34	231.67	0.942461	0.945914
77	62.5	2.575853	0.4	0.75	0.5	164.48	231.67	0.709975	0.705938
78	62.5	2.575853	0.3	0.5	0.5	180.1	231.67	0.777399	0.773777
79	62.5	2.575853	0.4	0.5	0.5	168.09	231.67	0.725558	0.746973
80	41.7	1.718609	0.1	0.5	0.5	261.77	280.76	0.932362	0.929373
81	62.5	2.575853	0.3	1	0.25	199.32	231.67	0.860362	0.860559
82	55.6	2.291479	0.1	1	0.5	201.51	242.77	0.830045	0.830284
83	41.7	1.718609	0.4	0.25	0.25	272.8	280.76	0.971648	0.982175
84	62.5	2.575853	0.4	0.25	0.25	226.49	231.67	0.977641	0.962983
85	50	2.060682	0.4	0.75	0.5	180.74	254.82	0.709285	0.711383
86	41.7	1.718609	0.2	0.5	0.25	265.15	280.76	0.944401	0.940863
87	45.5	1.875221	0.2	1	0.5	200.38	267.57	0.748888	0.757138
88	41.7	1.718609	0.4	0.25	0.5	241.31	280.76	0.859489	0.861191
89	50	2.060682	0.1	0.5	0.25	246.62	254.82	0.96782	0.964345
90	50	2.060682	0.1	0.5	0.5	232.93	254.82	0.914096	0.91573
91	50	2.060682	0.2	0.25	0.25	251.07	254.82	0.985284	0.983353
92	50	2.060682	0.1	0.25	0.25	252.7	254.82	0.99168	0.993215
93	50	2.060682	0.3	1	0.5	182.33	254.82	0.715525	0.718063
94	41.7	1.718609	0.1	1	0.25	254.76	280.76	0.907394	0.937304
95	62.5	2.575853	0.4	0.5	0.25	206.19	231.67	0.890016	0.891738
96	41.7	1.718609	0.1	1	0.5	229.16	280.76	0.816213	0.834586
97	62.5	2.575853	0.1	1	0.5	194.95	231.67	0.841499	0.828311
98	45.5	1.875221	0.3	1	0.5	191.74	267.57	0.716598	0.718824
99	41.7	1.718609	0.2	0.75	0.5	223.36	280.76	0.795555	0.784229
100	50	2.060682	0.1	1	0.25	240.27	254.82	0.942901	0.936199
101	62.5	2.575853	0.2	1	0.5	176.18	231.67	0.760478	0.753368
102	50	2.060682	0.2	0.25	0.5	238.92	254.82	0.937603	0.946005
103	50	2.060682	0.3	0.25	0.25	249.95	254.82	0.980888	0.975758
104	50	2.060682	0.2	0.5	0.25	238.1	254.82	0.934385	0.933242
105	45.5	1.875221	0.2	1	0.25	239.05	267.57	0.893411	0.890101
106	50	2.060682	0.1	1	0.5	211.18	254.82	0.828742	0.831955

107	45.5	1.875221	0.1	1	0.25	253.61	267.57	0.947827	0.936794
108	62.5	2.575853	0.2	1	0.25	205.77	231.67	0.888203	0.887484
109	50	2.060682	0.4	0.5	0.5	196.05	254.82	0.769367	0.770462
110	62.5	2.575853	0.4	0.75	0.25	198.21	231.67	0.855557	0.855199
111	62.5	2.58	0	0	0	231.67	231.67	1	0.999144
112	41.7	1.718609	0.2	0.75	0.25	256	280.76	0.911811	0.906947
113	50	2.060682	0.3	0.75	0.25	222.62	254.82	0.873636	0.87603
114	41.7	1.72	0	0	0	280.76	280.76	1	1.006491
115	41.7	1.718609	0.4	0.75	0.25	243.39	280.76	0.866897	0.86573
116	45	1.85	0	0	0	269.02	269.02	1	1.005565
117	41.7	1.718609	0.1	0.5	0.25	272.81	280.76	0.971684	0.968276
118	45.5	1.875221	0.4	0.5	0.5	209.12	267.57	0.781552	0.779827
119	62.5	2.575853	0.4	1	0.5	162.98	231.67	0.703501	0.697324
120	62.5	2.575853	0.3	1	0.5	168.1	231.67	0.725601	0.716262
121	41.7	1.718609	0.4	0.5	0.25	256.38	280.76	0.913164	0.923837
122	41.7	1.718609	0.1	0.25	0.5	272.17	280.76	0.969404	0.988878
123	55.6	2.291479	0.1	0.5	0.25	234.66	242.77	0.966594	0.962084
124	50	2.06	0	0	0	254.82	254.82	1	1.003908
125	62.5	2.575853	0.3	0.25	0.25	227.06	231.67	0.980101	0.961324
126	41.7	1.718609	0.2	0.25	0.5	261.3	280.76	0.930688	0.954996
127	50	2.060682	0.1	0.75	0.25	241.68	254.82	0.948434	0.947909
128	55.6	2.291479	0.1	0.5	0.5	218.79	242.77	0.901223	0.907137
129	55.6	2.291479	0.2	0.5	0.5	201.8	242.77	0.831239	0.834731
130	45.5	1.875221	0.4	1	0.25	226.28	267.57	0.845685	0.84486
131	50	2.060682	0.3	0.75	0.5	188.54	254.82	0.739895	0.734166
132	45.5	1.875221	0.3	0.5	0.25	246.73	267.57	0.922114	0.918745
133	55.6	2.291479	0.3	0.5	0.5	192.5	242.77	0.792932	0.787464
134	62.5	2.575853	0.1	0.75	0.5	195.29	231.67	0.842966	0.852379
135	62.5	2.575853	0.4	0.25	0.5	199.82	231.67	0.86252	0.836662
136	55.6	2.291479	0.4	1	0.25	205.1	242.77	0.844833	0.842965

ANN inputs and outputs for plate with both edges type pitting corrosion

No	B/t	x_1	x_2	x_3	x_4	σ_c	σ_0	FEM _{BE}	ANN Output
1	45.5	1.875221	0.3	0.5	0.25	242.04	267.57	0.904586	0.902854
2	50	2.060682	0.2	0.75	0.5	180.76	254.82	0.709363	0.726759
3	50	2.060682	0.1	0.75	0.5	220.55	254.82	0.865513	0.869289
4	45.5	1.875221	0.1	0.5	0.25	260.12	267.57	0.972157	0.967677
5	50	2.060682	0.2	1	0.5	169.61	254.82	0.665607	0.697157
6	62.5	2.575853	0.2	0.75	0.5	160	231.67	0.690638	0.672959
7	50	2.060682	0.1	0.5	0.5	234.31	254.82	0.919512	0.922374
8	62.5	2.575853	0.4	0.25	0.25	222.71	231.67	0.961324	0.934022
9	62.5	2.575853	0.1	0.25	0.5	225.44	231.67	0.973108	0.952507
10	62.5	2.575853	0.3	0.75	0.25	193.03	231.67	0.833211	0.834836
11	41.7	1.718609	0.2	0.25	0.25	274.9	280.76	0.979128	0.980557
12	50	2.060682	0.3	0.25	0.25	247.83	254.82	0.972569	0.971129
13	50	2.060682	0.1	1	0.25	241.05	254.82	0.945962	0.956658
14	62.5	2.575853	0.4	0.75	0.25	182.72	231.67	0.788708	0.774954
15	41.7	1.718609	0.3	0.75	0.5	192.97	280.76	0.687313	0.658473
16	41.7	1.718609	0.4	0.5	0.5	206.22	280.76	0.734506	0.717648
17	62.5	2.575853	0.1	1	0.5	184.04	231.67	0.794406	0.783999
18	50	2.060682	0.2	0.5	0.25	237.77	254.82	0.93309	0.928888
19	62.5	2.575853	0.3	1	0.25	191.43	231.67	0.826305	0.817006
20	62.5	2.575853	0.3	0.75	0.5	139.72	231.67	0.603099	0.597561
21	45.5	1.875221	0.2	1	0.25	239.42	267.57	0.894794	0.904927
22	41.7	1.718609	0.2	0.75	0.25	255.03	280.76	0.908356	0.898653
23	41.7	1.718609	0.4	1	0.25	224.78	280.76	0.800613	0.793812
24	41.7	1.718609	0.2	0.75	0.5	218.5	280.76	0.778245	0.762693
25	45.5	1.875221	0.2	0.5	0.25	251.23	267.57	0.938932	0.932296
26	62.5	2.575853	0.3	0.5	0.5	157.28	231.67	0.678897	0.687798
27	50	2.060682	0.1	1	0.5	216.21	254.82	0.848481	0.847311
28	41.7	1.718609	0.4	1	0.5	158.27	280.76	0.56372	0.572916
29	50	2.060682	0.4	0.75	0.5	142.31	254.82	0.558473	0.590957
30	62.5	2.575853	0.4	0.75	0.5	126.52	231.67	0.546122	0.575389
31	41.7	1.718609	0.2	0.25	0.5	260.48	280.76	0.927767	0.946011
32	55.6	2.291479	0.2	0.5	0.25	225.4	242.77	0.928451	0.924868
33	50	2.060682	0.3	0.5	0.25	228.12	254.82	0.89522	0.899646
34	50	2.060682	0.1	0.75	0.25	242.18	254.82	0.950396	0.962336
35	41.7	1.718609	0.1	0.75	0.25	268.94	280.76	0.9579	0.965705
36	62.5	2.575853	0.1	1	0.25	217.51	231.67	0.938879	0.933637
37	62.5	2.575853	0.3	0.25	0.5	204.85	231.67	0.884232	0.852014
38	41.7	1.718609	0.2	0.5	0.5	240.68	280.76	0.857245	0.864936
39	41.7	1.718609	0.3	0.5	0.25	255.58	280.76	0.910315	0.90541
40	50	2.060682	0.4	1	0.25	198.07	254.82	0.777294	0.783944
41	62.5	2.575853	0.1	0.5	0.25	222.96	231.67	0.962403	0.960895
42	62.5	2.575853	0.2	0.5	0.5	176.41	231.67	0.761471	0.776526
43	50	2.060682	0.1	0.25	0.5	248.7	254.82	0.975983	0.964698
44	41.7	1.718609	0.4	0.25	0.25	269.33	280.76	0.959289	0.960797
45	41.7	1.718609	0.1	0.5	0.25	273.03	280.76	0.972468	0.969148
46	45.5	1.875221	0.3	0.5	0.5	205.58	267.57	0.768322	0.759095
47	41.7	1.718609	0.3	1	0.5	178.55	280.76	0.635952	0.619092
48	45.5	1.875221	0.3	1	0.25	223.85	267.57	0.836604	0.84386
49	62.5	2.575853	0.4	1	0.25	181.23	231.67	0.782277	0.769122
50	50	2.060682	0.4	0.25	0.5	215.31	254.82	0.844949	0.845806
51	55.6	2.291479	0.1	1	0.25	229.05	242.77	0.943486	0.94784

52	45.5	1.875221	0.3	1	0.5	158.1	267.57	0.590873	0.611059
53	55.6	2.291479	0.1	0.5	0.25	234.88	242.77	0.9675	0.963652
54	41.7	1.718609	0.4	0.75	0.5	176.39	280.76	0.628259	0.608145
55	50	2.060682	0.2	0.5	0.5	209.4	254.82	0.821757	0.833621
56	41.7	1.72	0	0	0	280.76	280.76	1	1.002552
57	41.7	1.718609	0.1	0.75	0.5	253	280.76	0.901126	0.892919
58	45.5	1.875221	0.4	0.5	0.5	190.99	267.57	0.713795	0.704942
59	55.6	2.291479	0.3	1	0.25	200.48	242.77	0.825802	0.829595
60	50	2.060682	0.2	0.25	0.5	238.84	254.82	0.937289	0.93385
61	41.7	1.718609	0.2	1	0.5	208.97	280.76	0.744301	0.729914
62	50	2.060682	0.1	0.5	0.25	246.86	254.82	0.968762	0.965896
63	62.5	2.575853	0.3	1	0.5	145.15	231.67	0.626538	0.590719
64	55.6	2.291479	0.3	0.5	0.5	173.66	242.77	0.715327	0.716955
65	62.5	2.58	0	0	0	231.67	231.67	1	1.00911
66	62.5	2.575853	0.2	1	0.25	203.66	231.67	0.879095	0.87126
67	55	2.27	0	0	0	243.81	243.81	1	1.00681
68	62.5	2.575853	0.2	0.75	0.25	205.14	231.67	0.885484	0.891293
69	41.7	1.718609	0.4	0.25	0.5	235.35	280.76	0.83826	0.865316
70	62.5	2.575853	0.3	0.25	0.25	224.42	231.67	0.968705	0.962568
71	50	2.060682	0.3	1	0.25	211	254.82	0.828035	0.838318
72	45.5	1.875221	0.1	0.5	0.5	248.69	267.57	0.929439	0.931408
73	50	2.060682	0.3	1	0.5	149.37	254.82	0.586178	0.603187
74	50	2.060682	0.3	0.5	0.5	189.39	254.82	0.743231	0.740578
75	62.5	2.575853	0.1	0.25	0.25	229.56	231.67	0.990892	0.983359
76	62.5	2.575853	0.4	0.5	0.25	193.72	231.67	0.836189	0.850066
77	50	2.06	0	0	0	254.82	254.82	1	1.005188
78	45.5	1.875221	0.2	1	0.5	188.91	267.57	0.706021	0.714887
79	45	1.85	0	0	0	269.02	269.02	1	1.003554
80	50	2.060682	0.3	0.75	0.5	155.82	254.82	0.61149	0.630134
81	62.5	2.575853	0.1	0.5	0.5	206.3	231.67	0.890491	0.888858
82	55.6	2.29	0	0	0	242.77	242.77	1	1.006963
83	41.7	1.718609	0.3	1	0.25	237.34	280.76	0.845348	0.847386
84	50	2.060682	0.2	0.75	0.25	228.7	254.82	0.897496	0.8957
85	41.7	1.718609	0.3	0.25	0.25	271.85	280.76	0.968265	0.97469
86	45.5	1.875221	0.1	1	0.5	233.28	267.57	0.871847	0.865546
87	50	2.060682	0.4	0.5	0.5	175.59	254.82	0.689075	0.689443
88	41.7	1.718609	0.3	0.75	0.25	242.57	280.76	0.863976	0.843006
89	41.7	1.718609	0.1	1	0.5	249.59	280.76	0.88898	0.878837
90	41.7	1.718609	0.1	0.25	0.5	273.36	280.76	0.973643	0.970229
91	55.6	2.291479	0.4	0.5	0.25	206.87	242.77	0.852123	0.868355
92	55.6	2.291479	0.2	0.5	0.5	193.32	242.77	0.796309	0.809426
93	62.5	2.575853	0.4	1	0.5	129.26	231.67	0.557949	0.57203
94	41.7	1.718609	0.1	0.25	0.25	278.25	280.76	0.99106	0.984471
95	45.5	1.87	0	0	0	267.57	267.57	1	1.00371
96	55.6	2.291479	0.3	0.5	0.25	215.21	242.77	0.886477	0.89503
97	45.5	1.875221	0.2	0.5	0.5	225.54	267.57	0.84292	0.851276
98	62.5	2.575853	0.1	0.75	0.25	218.37	231.67	0.942591	0.955722
99	45.5	1.875221	0.4	1	0.25	210.77	267.57	0.787719	0.789549
100	62.5	2.575853	0.3	0.5	0.25	202.08	231.67	0.872275	0.887615
101	50	2.060682	0.2	0.25	0.25	250.14	254.82	0.981634	0.979354
102	62.5	2.575853	0.2	0.25	0.25	226.92	231.67	0.979497	0.976514
103	55.6	2.291479	0.4	1	0.25	188.64	242.77	0.777032	0.776826
104	50	2.060682	0.1	0.25	0.25	252.63	254.82	0.991406	0.984061
105	55.6	2.291479	0.4	1	0.5	130.2	242.77	0.53631	0.569204
106	55.6	2.291479	0.3	1	0.5	146.78	242.77	0.604605	0.595932

107	55.6	2.291479	0.1	1	0.5	200.06	242.77	0.824072	0.820917
108	60	2.47	0	0	0	235.33	235.33	1	1.008312
109	40	1.65	0	0	0	287.48	287.48	1	1.002018
110	41.7	1.718609	0.2	1	0.25	251.87	280.76	0.897101	0.909369
111	55.6	2.291479	0.4	0.5	0.5	160.72	242.77	0.662026	0.669974
112	41.7	1.718609	0.3	0.25	0.5	247.92	280.76	0.883032	0.90488
113	50	2.060682	0.3	0.75	0.25	215.13	254.82	0.844243	0.842021
114	62.5	2.575853	0.2	0.25	0.5	215.66	231.67	0.930893	0.908572
115	45.5	1.875221	0.4	1	0.5	140.78	267.57	0.526143	0.570597
116	45.5	1.875221	0.1	1	0.25	254.38	267.57	0.950704	0.962383
117	62.5	2.575853	0.2	0.5	0.25	212.73	231.67	0.918246	0.920146
118	41.7	1.718609	0.1	0.5	0.5	262.43	280.76	0.934713	0.938039
119	55.6	2.291479	0.1	0.5	0.5	220.61	242.77	0.90872	0.909049
120	50	2.060682	0.4	0.75	0.25	203.59	254.82	0.798956	0.805058
121	62.5	2.575853	0.4	0.5	0.5	145.91	231.67	0.629818	0.646975
122	55.6	2.291479	0.2	1	0.25	214.35	242.77	0.882934	0.887857
123	62.5	2.575853	0.1	0.75	0.5	189.33	231.67	0.81724	0.822709
124	41.7	1.718609	0.4	0.75	0.25	231.88	280.76	0.825901	0.817365
125	41.7	1.718609	0.1	1	0.25	267.54	280.76	0.952914	0.966463
126	41.7	1.718609	0.2	0.5	0.25	264.21	280.76	0.941053	0.935292
127	41.7	1.718609	0.3	0.5	0.5	221.19	280.76	0.787826	0.774268
128	50	2.060682	0.4	0.5	0.25	220.12	254.82	0.863825	0.879206
129	50	2.060682	0.2	1	0.25	226.03	254.82	0.887018	0.898339
130	50	2.060682	0.3	0.25	0.5	227.61	254.82	0.893219	0.886654
131	50	2.060682	0.4	0.25	0.25	246.02	254.82	0.965466	0.952544
132	50	2.060682	0.4	1	0.5	131.72	254.82	0.516914	0.569146
133	62.5	2.575853	0.2	1	0.5	158.97	231.67	0.686192	0.653756
134	41.7	1.718609	0.4	0.5	0.25	248.2	280.76	0.884029	0.890158
135	62.5	2.575853	0.4	0.25	0.5	192.31	231.67	0.830103	0.804831
136	55.6	2.291479	0.2	1	0.5	167.21	242.77	0.688759	0.676209
137	45.5	1.875221	0.4	0.5	0.25	234.31	267.57	0.875696	0.885794

Appendix F

Appendix F introduces a useful MATLAB program in order to calculate the ultimate strength of plate with localized corrosion. Total five(5) input parameters are required that is the ultimate strength of uncorroded plate and x_1, x_2, x_3, x_4 .

Sigma_C = ultimate strength of plate with localized corrosion

Sigma_O = ultimate strength of uncorroded plate

x_1 = plate slenderness parameter (β)

x_2 = the ratio of pit breadth to plate width

x_3 = the ratio of pit length to plate length

x_4 = the ratio of pit depth to plate thickness

```
clc
disp('%%%%%%%%%%%%%%%%%%%%%%%%%%%%%%%%%%%%%%%%%%%%%%%%%%%%%%%%%%%%%%%%%%%%%%%%')
disp('%% ARTIFICIAL NEURAL NETWORK BASED ULTIMATE STRENGTH CALCULATION %%')
disp('%% (PLATE WITH PITTING CORROSION FOR SINGLE EDGE) %%')
disp('%% BY DUO OK, UNIVERSITY OF NEWCASTLE UPON TYNE %%')
disp('%% 2 NOVEMBER 2005 %%')
disp('%%%%%%%%%%%%%%%%%%%%%%%%%%%%%%%%%%%%%%%%%%%%%%%%%%%%%%%%%%%%%%%%%%%%%%%%')

disp('Ultimate strength of uncorroded plate (N/mm2)')
Sigma_O=231.67

disp('plate slenderness parameter')
x1=2.576

disp('Pit breadth ratio ( = pit breadth / plate breadth)')
x2=0.1

disp('Pit length ratio (= pit length / plate length)')
x3=1.0

disp('Pit depth ratio (= pit depth / plate thickness)')
x4=0.25

xf1=(1.9441*x1)-4.1078
xf2=(4.5000*x2)-0.8999
xf3=(1.7999*x3)-0.8999
xf4=(3.5999*x4)-0.8999

x=[xf1;xf2;xf3;xf4]
w1=[0.0282 0.0496 0.3851 0.7093
    -0.0115 -0.6978 -0.1098 -1.6504
    -0.0183 -2.0535 -0.3542 -0.3978
    -0.2708 0.5036 -2.1643 0.6909];
w2=[-0.1755 1.0057 0.3621 0.6168];
b1=[-0.2751; 1.8543; -0.4064; -1.0153];
b2=[0.1681];
X=[1;x];
W1=[b1 w1];
W2=[b2 w2];
f=tanh(W2*[1;tanh(W1*X)])
X
W1
W2
Y=f

disp('Ultimate strength of Plate with Pitting Corrosion (N/mm2)')
Sigma_C=((Y+4.8860)/5.7860)*Sigma_O
```

```
clc
disp('%%%%%%%%%%%%%%%%%%%%%%%%%%%%%%%%%%%%%%%%%%%%%%%%%%%%%%%%%%%%%%%%%%%%%%%%')
disp('%% ARTIFICIAL NEURAL NETWORK BASED ULTIMATE STRENGTH CALCULATION %%')
disp('%% (PLATE WITH PITTING CORROSION FOR BOTH EDGES) %%')
disp('%% BY DUO OK, UNIVERSITY OF NEWCASTLE UPON TYNE %%')
disp('%% 2 NOVEMBER 2005 %%')
disp('%%%%%%%%%%%%%%%%%%%%%%%%%%%%%%%%%%%%%%%%%%%%%%%%%%%%%%%%%%%%%%%%%%%%%%%%')

disp('Ultimate strength of uncorroded plate (N/mm2)')
Sigma_O=254.82

disp('plate slenderness parameter')
x1=2.060

disp('Pit breadth ratio ( = pit breadth / plate breadth)')
x2=0.2

disp('Pit length ratio (= pit length / plate length)')
x3=0.5

disp('Pit depth ratio (= pit depth / plate thickness)')
x4=0.25

xf1=(2.0896*x1)-4.4912
xf2=(4.5000*x2)-0.8999
xf3=(1.7999*x3)-0.8999
xf4=(3.5999*x4)-0.8999

x=[xf1;xf2;xf3;xf4]
w1=[-0.3056 -0.7707 -1.0947 -0.6146
    -0.1769 0.5681 -1.9262 0.5216
    -0.1755 -0.9780 -1.0876 -0.0798
    0.2109 1.1998 -0.4158 -0.8671];
w2=[0.9123 -0.6682 0.8597 0.5669];
b1=[1.5899; 1.1090; -0.0856; -0.4588];
b2=[0.7260];
X=[1;x];
W1=[b1 w1];
W2=[b2 w2];
f=tanh(W2*[1;tanh(W1*X)])
X
W1
W2
Y=f

disp('Ultimate strength of Plate with Pitting Corrosion (N/mm2)')
Sigma_C=((Y+3.0658)/3.9658)*Sigma_O
```

Appendix G

Appendix G introduces useful ANSYS macro programs. The one is for automatic creation of geometry, mesh details, symmetric boundary condition and applying loads by simply input eight parameters as follows:

- arg1 = material yield stress
- arg2 = half of crack length
- arg3 = half of plate breadth
- arg4 = half of plate length
- arg5 = number of mesh on cracked line
- arg6 = number of mesh on uncracked line
- arg7 = the radius of the first row of elements around the crack tip
- arg8 = maximum applied load

The other is for automatic calculation of stress intensity factor (K) for centre cracked plate by simply input six parameters as follows:

- arg1 = crack tip node number
- arg2 = second node number for crack path
- arg3 = third node number for crack path
- arg4 = fourth node number for crack path to define crack tip coordinate system
- arg5 = fifth node number for crack path to define crack tip coordinate system
- arg6 = sixth node number for crack path to define crack tip coordinate system

```
!!! pl_ccrak.mac Revision(1.0)
!!! Revision history : 1st create (4th August 2005)
!!! Last modified : 4th August 2005
!!! macro name : pl_ccrak.mac
!!! Author      : Duo Ok
!!!           : Marine Science & Technology
!!!           : University of Newcastle upon Tyne, UK
!!!           : du-o.ok@ncl.ac.uk / okduo8173@yahoo.co.uk
!
!/com *****
!/com Calculation of Stress Intensity Factor (K) for Centre Cracked Plate
!/com (Create Geometry & Apply Load - Non Linear )
!/com
!/com *****
!/com
!/com Solid 82, Plane 82 model
!/com Boundary condition : symmetric condition for left & bottom line
!/com                      (1/4 Quarter model)
!/com ARGUMENTS
!/com
!/com arg1 : Yield stress (N/mm2)
!/com arg2 : half crack length = a (m)
!/com arg3 : plate half breadth = 0.5W (m)
!/com arg4 : plate half length = L/2 (m)
!/com arg5 : Number of mesh on cracked line
!/com arg6 : Number of mesh on uncracked line = (100-arg5)
!/com arg7 : The radius of the first row of elements around the crack tip (m)
!/com arg8 : Maximum applied load (MPa)
!/com *****
!/com *****
!!!Element type / solid 82
/PREP7
!*
ET,1,PLANE82
!*
KEYOPT,1,3,2
KEYOPT,1,5,0
KEYOPT,1,6,0
!*
!!! Material property
!*
MPTEMP,,,,,,,,
MPTEMP,1,0
MPDATA,EX,1,,209000
MPDATA,PRXY,1,,0.3
TB,BISO,1,1,2,
TBTEMP,0
TBDATA,,arg1,,,,
TBDE,BISO,1,,,
TB,BISO,1,1,2,
TBTEMP,0
TBDATA,,arg1,0,,,,
!!! Input keypoint
K,1,0,0,,
K,3,arg2,0,,
K,4,arg3,0,,
K,5,arg3,arg4,,
K,6,0,arg4,,
```

```
!!!Line
L,1,3
L,4,3
L,5,4
L,5,6
L,6,1
!!!Line numbering
!*
LPLOT
!!! Line mesh
!! L5(Left)/L3(Right)
FLST,5,2,4,ORDE,2
FITEM,5,3
FITEM,5,5
CM,_Y,LINE
LSEL,,,P51X
CM,_Y1,LINE
CMSEL,_,_Y
!*
LESIZE,_Y1,,,100,0.1,,,,1
!*
!! L4(Top)
FLST,5,1,4,ORDE,1
FITEM,5,4
CM,_Y,LINE
LSEL,,,P51X
CM,_Y1,LINE
CMSEL,_,_Y
!*
LESIZE,_Y1,,,10,,,,,1
!*
!! L1(Bottom Cracked Line)
FLST,5,1,4,ORDE,1
FITEM,5,1
CM,_Y,LINE
LSEL,,,P51X
CM,_Y1,LINE
CMSEL,_,_Y
!*
LESIZE,_Y1,,,arg5,0.1,,,,1
!*
!! L2 (Bottom Uncracked line)
FLST,5,1,4,ORDE,1
FITEM,5,2
CM,_Y,LINE
LSEL,,,P51X
CM,_Y1,LINE
CMSEL,_,_Y
!*
LESIZE,_Y1,,,arg6,0.1,,,,1
!*
/AUTO,1
/REP,FAST
!!! Create the concentration keypoint
!*
KSCON,3,arg7,1,8,0,
!!! Create area
/AUTO,1
```

```
/REP,FAST
A,1,3,4,5,6
!!! Mesh
MSHKEY,0
CM,_Y,AREA
ASEL,,,,,1
CM,_Y1,AREA
CHKMSH,'AREA'
CMSEL,S,_Y
!*
AMESH,_Y1
!*
CMDELE,_Y
CMDELE,_Y1
CMDELE,_Y2
!*
!!! Apply boundary condition
/AUTO,1
/REP,FAST
FINISH
/SOL
FLST,2,2,4,ORDE,2
FITEM,2,2
FITEM,2,5
DL,P51X,,SYMM
!!! Apply Load
FLST,2,1,4,ORDE,1
FITEM,2,4
/GO
!*
SFL,P51X,PRES,arg8,
/SOL
ANTYPE,0
NLGEOM,1
NSUBST,10
OUTRES,ALL,1
AUTOTS,0
TIME,1
!!! Solving
/STATUS,SOLU
SOLVE
```

```
!!! pl_kcal.mac Revision(1.0)
!!! Revision history : 1st create (4th August 2005)
!!! Last modified : 4th August 2005
!!! macro name : pl_kcal.mac
!!! Author      : Duo Ok
!!!           : Marine Science & Technology
!!!           : University of Newcastle upon Tyne, UK
!!!           : du-o.ok@ncl.ac.uk / ockduo@yahoo.co.kr
!
!/com *****
!/com Calculation of Stress Intensity Factor (K) for Cracked Plate
!/com (Plane strain & Plane stress )
!/com
!/com *****
!/com
!/com Solid 82, Plane 82 model
!/com Boundary condition : symmetric condition for left & bottom line
!/com (1/4 Quarter model)
!/com ARGUMENTS
!/com
!/com arg1 : Node number 1 for crack face path (crack tip node)
!/com arg2 : Node number 2 for crack face path
!/com arg3 : Node number 3 for crack face path
!/com arg4 : Node number 4 to define local crack tip coordinate system (crack tip node)
!/com arg5 : Node number 5 to define local crack tip coordinate system (crack tip right)
!/com arg6 : Node number 6 to define local crack tip coordinate system (crack tip up)
!/com *****
!/com *****
!!! Post processing for K cal
!!! Define crack face path
FINISH
/POST1
FLST,2,3,1
FITEM,2,arg1    !! arg1
FITEM,2,arg2    !!arg2
FITEM,2,arg3    !!arg3
!*
PATH,K1,3,30,20,
PPATH,P51X,1
PATH,STAT
!*
!!! Define local crack tip coordinate system
!*
CS,11,0,arg4,arg5,arg6,1,1,
!!! Activate the local crack tip coordinate system
CSYS,11,
!!! To activate the crack tip coordinate system as results coordinate system
!*
RSYS,11
AVPRIN,0,0
AVRES,2
/EFACET,1
LAYER,0
FORCE,TOTAL
!*
!!! Calculate K Factor (Plane strain)
KCALC,0,1,0,1
```

Appendix H

Appendix H is summarized the *J-integral* and *crack tip opening displacement (CTOD)* values based on ANSYS fracture modelling for centre cracked plate under uniform tensile loads (Mode I). The effects of three different material properties which has yield stress of 235 N/mm^2 , 315 N/mm^2 and 355 N/mm^2 on stress intensity factors have been investigated.

The comparisons between *Irwin's* plastic zone correction and current finite element fracture modelling results of the *J-integral* and *CTOD* values, which are converted to relevant K values in plane strain in accordance with Eq.7.20 and Eq.7.23, are done in order to find out the effects of different material yield stresses, crack sizes and applied loads on *J* and *CTOD* values.

Total 300 cases of *J* and *CTOD* values based on finite element modelling results are shown in the Appendix H, which are corresponding to material yield stresses of 235 N/mm^2 , 315 N/mm^2 and 355 N/mm^2 , and centre crack sizes from 50mm to 400mm and applied tensile stress (σ) ranges from 10 N/mm^2 to 100 N/mm^2 .

Stress Intensity factor (K) for Centre Cracked Plate ($\sigma_y = 235 \text{ N/mm}^2$)

σ (MPa)	2a/W	SY235 (Irwin's plastic zone correction – K) $\text{MPa} \sqrt{\text{m}}$	SY235 (J Integral-K) $\text{MPa} \sqrt{\text{m}}$	SY235 (CTOD-K) $\text{MPa} \sqrt{\text{m}}$
10	0.05	2.807	2.808	7.579
20	0.05	5.616	5.616	10.718
30	0.05	8.431	8.423	13.127
40	0.05	11.253	11.233	15.209
50	0.05	14.086	14.054	17.363
60	0.05	16.932	16.881	19.432
70	0.05	19.792	19.709	21.328
80	0.05	22.671	22.553	23.273
90	0.05	25.570	25.434	25.475
100	0.05	28.491	28.337	27.679
10	0.10	3.987	4.030	9.075
20	0.10	7.978	8.061	12.834
30	0.10	11.977	12.093	15.814
40	0.10	15.987	16.135	18.800
50	0.10	20.012	20.181	21.513
60	0.10	24.055	24.235	24.177
70	0.10	28.120	28.320	27.163
80	0.10	32.211	32.427	30.163
90	0.10	36.332	36.572	33.319
100	0.10	40.485	40.759	36.584
10	0.20	5.743	5.935	11.020
20	0.20	11.492	11.871	15.631
30	0.20	17.252	17.817	19.934
40	0.20	23.030	23.767	23.733
50	0.20	28.831	29.744	27.896
60	0.20	34.661	35.748	32.160
70	0.20	40.525	41.790	36.582
80	0.20	46.430	47.892	41.232
90	0.20	52.380	54.071	46.089
100	0.20	58.381	60.353	51.156
10	0.30	7.260	7.735	12.585
20	0.30	14.530	15.476	18.273
30	0.30	21.815	23.225	23.387
40	0.30	29.126	31.001	28.657
50	0.30	36.470	38.815	34.170
60	0.30	43.855	46.683	39.922
70	0.30	51.289	54.633	45.964
80	0.30	58.781	62.704	52.310
90	0.30	66.338	70.945	59.035
100	0.30	73.968	79.424	66.183
10	0.40	8.792	9.681	14.074
20	0.40	17.597	19.371	20.914
30	0.40	26.425	29.081	27.232
40	0.40	35.289	38.840	34.029
50	0.40	44.199	48.669	41.176
60	0.40	53.168	58.608	48.676
70	0.40	62.207	68.718	56.598
80	0.40	71.327	79.081	65.050
90	0.40	80.539	89.829	74.120
100	0.40	89.854	101.174	84.081

Stress Intensity factor (K) for Centre Cracked Plate ($\sigma_y = 315 \text{ N/mm}^2$)

σ (MPa)	2a/W	SY315 (Irwin's plastic zone correction – K) $\text{MPa} \sqrt{m}$	SY315 (J Integral-K) $\text{MPa} \sqrt{m}$	SY315 (CTOD-K) $\text{MPa} \sqrt{m}$
10	0.05	2.807	2.087	8.774
20	0.05	5.618	5.614	12.409
30	0.05	8.439	8.420	15.198
40	0.05	11.272	11.227	17.549
50	0.05	14.122	14.034	19.622
60	0.05	16.993	16.851	21.791
70	0.05	19.890	19.674	23.931
80	0.05	22.816	22.499	25.968
90	0.05	25.776	25.325	27.885
100	0.05	28.773	28.154	29.726
10	0.10	3.988	4.030	10.507
20	0.10	7.982	8.061	14.859
30	0.10	11.988	12.091	18.198
40	0.10	16.013	16.123	21.133
50	0.10	20.063	20.165	24.154
60	0.10	24.144	24.209	26.988
70	0.10	28.262	28.256	29.624
80	0.10	32.422	32.313	32.305
90	0.10	36.630	36.393	35.264
100	0.10	40.893	40.489	38.233
10	0.20	5.743	5.935	12.759
20	0.20	11.497	11.871	18.043
30	0.20	17.270	17.809	22.367
40	0.20	23.071	23.756	26.631
50	0.20	28.912	29.705	30.479
60	0.20	34.800	35.668	34.428
70	0.20	40.746	41.653	38.631
80	0.20	46.757	47.660	42.905
90	0.20	52.845	53.696	47.316
100	0.20	59.016	59.753	51.853
10	0.30	7.261	7.735	14.571
20	0.30	14.537	15.471	20.624
30	0.30	21.840	23.217	26.251
40	0.30	29.185	30.967	31.234
50	0.30	36.585	38.737	36.439
60	0.30	44.054	46.534	41.883
70	0.30	51.604	54.363	47.459
80	0.30	59.249	62.236	53.241
90	0.30	67.002	70.173	59.255
100	0.30	74.874	78.186	65.452
10	0.40	8.794	9.681	16.294
20	0.40	17.608	19.365	23.452
30	0.40	26.461	29.061	30.032
40	0.40	35.373	38.774	36.355
50	0.40	44.363	48.524	43.109
60	0.40	53.450	58.318	50.080
70	0.40	62.653	68.182	57.373
80	0.40	71.989	78.131	64.876
90	0.40	81.477	88.208	72.723
100	0.40	91.135	98.449	80.947

Stress Intensity factor (K) for Centre Cracked Plate ($\sigma_y = 355 \text{ N/mm}^2$)

σ (MPa)	2a/W	SY355 (Irwin's plastic zone correction – K) $\text{MPa} \sqrt{\text{m}}$	SY355 (J Integral-K) $\text{MPa} \sqrt{\text{m}}$	SY355 (CTOD-K) $\text{MPa} \sqrt{\text{m}}$
10	0.05	2.807	2.807	9.315
20	0.05	5.617	5.614	13.173
30	0.05	8.435	8.420	16.134
40	0.05	11.262	11.227	18.630
50	0.05	14.103	14.034	20.829
60	0.05	16.961	16.843	22.882
70	0.05	19.838	19.662	25.074
80	0.05	22.739	22.486	27.204
90	0.05	25.667	25.311	29.234
100	0.05	28.624	28.137	31.159
10	0.10	3.987	4.030	11.154
20	0.10	7.980	8.061	15.775
30	0.10	11.982	12.091	19.319
40	0.10	15.999	16.121	22.308
50	0.10	20.036	20.159	25.318
60	0.10	24.097	24.202	28.294
70	0.10	28.187	28.247	31.055
80	0.10	32.310	32.293	33.673
90	0.10	36.472	36.351	36.361
100	0.10	40.677	40.431	39.320
10	0.20	5.743	5.935	13.544
20	0.20	11.494	11.871	19.155
30	0.20	17.260	17.807	23.517
40	0.20	23.049	23.752	27.922
50	0.20	28.869	29.699	31.923
60	0.20	34.726	35.650	35.688
70	0.20	40.629	41.621	39.804
80	0.20	46.584	47.608	43.995
90	0.20	52.599	53.615	48.279
100	0.20	58.681	59.649	52.680
10	0.30	7.261	7.735	15.468
20	0.30	14.533	15.471	21.875
30	0.30	21.827	23.214	27.514
40	0.30	29.154	30.962	32.734
50	0.30	36.524	38.717	37.647
60	0.30	43.949	46.499	43.043
70	0.30	51.438	54.302	48.493
80	0.30	59.002	62.137	54.108
90	0.30	66.651	70.013	59.902
100	0.30	74.395	77.943	65.894
10	0.40	8.793	9.681	17.298
20	0.40	17.602	19.363	24.637
30	0.40	26.442	29.057	31.457
40	0.40	35.328	38.757	37.585
50	0.40	44.276	48.490	44.270
60	0.40	53.301	58.254	51.074
70	0.40	62.417	68.063	58.121
80	0.40	71.639	77.939	65.462
90	0.40	80.981	87.891	72.980
100	0.40	90.458	97.957	80.798

